Coherent Frequency Conversion from Microwave to Optical Fields in an Erbium Doped Y_2SiO_5 Crystal: Towards the Single Photon Regime

UNIVERSITY
of
OTAGO
SAPERE AUDE
Te Whare Wānanga o Otāgo
NEW ZEALAND

Xavier Fernandez Gonzalvo

Department of Physics
University of Otago

This dissertation is submitted for the degree of
Doctor of Philosophy

February 2017

Per al pare i la mare.

Acknowledgements

First of all, I would like to thank my supervisor, Assoc. Prof. Jevon Longdell. I really value your expertise. I have learnt so many things from you. Lots and lots of physics in many different areas, lots of electronics, some programming and even a bit of sailing! I would also like to thank my co-supervisors, Prof. Rob Ballagh and Dr. Mikkel Andersen. Your advice and your experienced words have been really useful, especially towards the end of my PhD. Another very important person to thank is Dr. Yu-Hui Chen (Stephen), who was also involved in the frequency conversion project. Thanks a lot for your help, Stephen, in particular with the theoretical aspects of the project and of course thanks a lot for all the work you have done with the microwave resonators. Next I would like to thank Dr. Sebastian Horvath. Even though you joined the project during my last months in Dunedin you brought with you some needed fresh air, and I learnt to look at what I was doing in a different, more useful way. On the other end of the time line I would like to thank Dr. Luke Taylor, who had been in the lab for a while when I arrived, and who offered a very helping hand from day one. And of course, I would also like to thank everyone else who has been at LTJ. Hamish, Maddy, Jelena, Gavin, Lewis, Mark, Matt and all the undergrads. Thanks a lot for the fun times, and for making LTJ such a pleasant group to work in!

Another very important person to thank is Peter Stroud, our mechanical engineer in the Department. I think none of the experiments I did during my PhD would have been possible without your work. Building a cryostat together was a very interesting and rewarding experience, and one from which I learnt so much. What a good piece of work, the Kraken! Many, many thanks also to the people in the electronics workshop. Peter McCabe, Barbara Buchanan and Miles Thayer, thanks a lot for all your help with anything wire related, and for taking care of our burnt instruments every now and again. And in general, thanks a lot to everyone in the Depratment of Physics, from the administrative staff to all the students, postdocs and researchers around. I have had a really good time during my stay.

Outside of the Department I would like to sincerely thank Sven Rogge and Chunming Yin at UNSW for hosting us during one of our first experiments and for all the help they provided. Also, thanks a lot to Brent Pooley at the Department of Geology for cutting and polishing the mirror that we used for our optical cavity experiments. That was really helpful.

Finally, I would like to thank my parents, who have been so helpful and supportive during the hardest times. Thank you so much. Also thanks a lot to Nora and Gyula for hosting me during my writing days. Köszönöm szépen. And last, but definitely not least, thanks a lot to my partner, Júlia. This would have been a completely different experience had you not been there. Nagyon puszi, Julim.

Abstract

In the context of quantum information technologies superconducting qubits (SQs) are very attractive devices for the manipulation of quantum states, and present themselves as one of our best candidates to build a quantum processor. They couple naturally to microwave photons, for which suitable quantum memories or a long distance propagation channel don't exist. A way around these limitations is to turn these microwave photons into optical ones by building a quantum frequency converter: a device by which the frequency of a photon can be changed while preserving its non-classical correlations. Then, optical fibres could be used to link distant SQ-based devices together, facilitating the creation of a network of quantum computers. Moreover, SQs could then be coupled to quantum memories compatible with photons at optical frequencies, which are the most well developed kind of quantum memories at the present time.

This thesis explores the possibility to convert single microwave photons into optical photons using erbium doped in a yttrium orthosilicate crystal (Er^{3+}:$\mathrm{Y_2SiO_5}$). Er^{3+}:$\mathrm{Y_2SiO_5}$ is a good candidate because it has a naturally occurring optical transition near 1536 nm close to the point where silica optical fibres show their minimum loss. A microwave transition can be found in two different ways: one way is to use the 167 isotope of erbium, which is the only stable isotope that shows hyperfine splitting as it has non-zero nuclear spin. The hyperfine structure of the ground state of $^{167}\mathrm{Er}^{3+}$:$\mathrm{Y_2SiO_5}$ spans over about 5 GHz. The other possibility is to use the other stable isotopes of erbium and Zeeman split their ground state using an external magnetic field. A microwave transition near 5 GHz can be achieved with moderate magnetic fields due to the high g-factors of Er^{3+}:$\mathrm{Y_2SiO_5}$.

The physical process of interest is a three wave mixing process involving two fields at optical frequencies and one field at microwave frequencies. In order to boost the efficiency of the frequency conversion process the Er^{3+}:$\mathrm{Y_2SiO_5}$ crystal is placed inside a microwave and an optical resonator. The problem is first explored from the theoretical point of view, where a nonlinear coefficient $\Lambda^{(2)}$ is derived (analogous to the $\chi^{(2)}$ often used in nonlinear optics), and the interaction between cavity modes and the nonlinear medium is studied. It is predicted that with a sample cooled down to millikelvin temperatures total frequency conversion between microwave and optical fields can be achieved.

A preliminary hole burning spectroscopy experiment is performed with the objective of reconstructing the hyperfine structure of the excited state of $^{167}\mathrm{Er}^{3+}$:$\mathrm{Y}_2\mathrm{SiO}_5$, but the complexity of the problem makes it too difficult to achieve this goal. Then a series of experiments are shown, aimed at determining whether or not frequency conversion at the single photon level is achievable using the even isotopes of erbium in a magnetic field. These experiments are based in the Raman heterodyne spectroscopy technique, which is used in combination with electron paramagnetic resonance and optical absorption spectroscopy. In all experiments the sample is cooled down to cryogenic temperatures near 4 K. A first experiment shows that the frequency conversion process exists in Er^{3+}:$\mathrm{Y}_2\mathrm{SiO}_5$, in a setup where only a microwave resonator is used, but not an optical one. A second experiment is performed in a similar setup, this time presenting a quantitative study of the properties of the frequency conversion process, and its comparison with the theoretical model previously derived. A third experiment is performed, which incorporates an optical cavity to the system. The interaction between the erbium ions and the optical cavity introduces a whole new range of experimental complications, which are studied and discussed. Then, the frequency conversion signal is studied anew, showing an unexpected highly non-linear scaling behaviour with the input powers. A hypothesis explaining this unexpected behaviour is given, referring to stray optical absorption in the inhomogeneous line of Er^{3+}:$\mathrm{Y}_2\mathrm{SiO}_5$ (and in particular $^{167}\mathrm{Er}^{3+}$:$\mathrm{Y}_2\mathrm{SiO}_5$), which can be bleached out under certain circumstances due to spectral hole burning effects. The overall maximum frequency conversion efficiency observed is of 3×10^{-4} per Watt of pump laser power. While this value is still far from the target several ways of improvement are proposed, including cooling down the system to millikelvin temperatures, increasing the dopant concentration and modifying the geometry of the resonators.

Table of contents

Chapter 1

Introduction and Outline

This thesis forms part of a greater effort: converting microwave photons into optical photons, one by one. The motivation for doing so resides in the flourishing fields of quantum computation and quantum communication. In the last decades there have been incredible amounts of effort and resources put into making quantum computers a reality. These devices hold the promise of a computational advantage over classical computers. This advantage arises from the very nature of the quantum world, and the laws of Quantum Mechanics. Many different systems have been proposed to build the various components of a quantum computer. In analogy to classical computers these components are, perhaps not exhaustively, quantum memories, quantum processors and quantum wires[1]. As of today, one of our best candidates to implement quantum processors are superconducting qubits. These devices couple naturally to microwave photons. On the other hand, one of our best candidates for a quantum wire are optical fibres, the idea being to propagate quantum information encoded into optical photons over long distances. Quantum wires become particularly relevant when it comes to creating a network of quantum computers, or simply connecting one quantum computer to another distant one. Additionally, most of our best quantum memories work in the optical domain too, so there is a clear mismatch between the frequencies that our different candidates work at. Having a device capable of interconverting microwave and optical photons while preserving their relevant quantum properties intact is therefore very appealing, because then hypothetical quantum computers based on superconducting qubits could be connected to one another using optical fibres, and quantum memories for light could be used to store information. This is the end goal of the bigger project that encompasses my thesis: to build a Quantum Frequency Converter between microwaves and optical fields.

---

[1] What is meant by quantum wire here is a quantum communication channel, or a transmission line for quantum information, but not necessarily a wire. As a matter of fact, traditional wires do a rather poor job when it comes to transmitting quantum information.

The aim of this thesis is to explore a possible avenue towards building such a device. In our approach we use an erbium doped yttrium orthosilicate crystal (Er^{3+}:Y_2SiO_5, or Er:YSO for short). This material can provide the necessary nonlinear effects between microwave and optical fields in order to perform frequency conversion. One of the most meaningful parameters of a frequency conversion device is it's efficiency, i.e. how many photons come out at the target frequency for every photon that goes in at the original frequency. Ideally this number is one, meaning total conversion with no loss, although values of a few percent already would make a frequency converter a useful device. In order to achieve high conversion efficiencies our proposal incorporates an optical and a microwave resonator, which enhances the interaction between the microwave and optical fields and the Er:Y_2SiO_5 crystal, thus boosting up the conversion efficiency.

The goals of this thesis are, first of all, to provide a theoretical background discussing whether or not efficient quantum frequency conversion is achievable using Er:Y_2SiO_5 in a microwave and an optical cavities. Then, to show experimentally that the frequency conversion process in Er^{3+}:Y_2SiO_5 exists, and study it's properties, in particular providing quantitative measurements of the conversion efficiency. This step will be performed using a microwave resonator, but not an optical one, as this simplifies the experiment greatly while still providing meaningful results. The third goal is to include an optical cavity and quantify what level of enhancement one can obtain from it. The final outcome of this thesis should be a solid discussion as to whether Er^{3+}:Y_2SiO_5 is a good system for performing frequency conversion between microwave and optical fields at the single photon level.

Outline

The outline of this thesis goes as follows. I will start by presenting an overview of the fields of quantum computation and quantum communication in Ch. 2, which will put our work into context. I will explain where the necessity of quantum frequency conversion devices arises from, with a particular focus in microwave to optical converters, and I will present a list of the different approaches to solve this problem up to date, discussing each one of them. Chapter 3 will be dedicated to rare earths and rare earth ion doped crystals. The properties of Er^{3+}:Y_2SiO_5 and why it is a potentially good candidate for performing microwave to optical quantum frequency conversion will be explained here. In Ch. 4 I will explain the theoretical proposal that initially motivated this project. This was a paper published by Williamson et al. in 2014. However, the theory presented there had some limitations that I wanted to overcome, so I developed an alternative one. Explaining this theory will comprise most of Ch. 4. The rest of the thesis from then on will be devoted to the experimental work we performed. First of all, in Ch. 5, I will present the three main experimental techniques that we used in our experiments. These are Raman heterodyne spectroscopy, electron paramagnetic resonance, and optical absorption spectroscopy. Chapter 6 is dedicated to some of the first experiments that we did, where we explored the viability of using the 167 isotope of erbium. This isotope has a property that the rest of stable isotopes don't have: non-zero nuclear spin, and therefore it exhibits hyperfine splittings in its energy levels. We aimed at determining the hyperfine structure of the excited state of $^{167}\mathrm{Er}^{3+}{:}\mathrm{Y}_2\mathrm{SiO}_5$ using hole burning spectroscopy. The large number of levels involved made the spectra difficult to assign, and we were ultimately unable to determine the excited state hyperfine levels. However, the data will be useful to test theoretical models that are being developed by other people in our group. Chapters 7, 8 and 9 are dedicated to frequency conversion experiments in $\mathrm{Er}^{3+}{:}\mathrm{Y}_2\mathrm{SiO}_5$. In Ch. 7 I will describe the first of such experiments, and the qualitative behaviour of the frequency conversion process will be discussed. Chapter 8 describes the next evolutionary step from this experiment. In these first two experiments a microwave resonator was used in order to boost the efficiency of the frequency conversion process, but not an optical one. In Ch. 9 I will talk about the third iteration of our experiment, which includes an optical resonator. Some of the changes that this implied were unforeseen, and some interesting behaviours will be discussed. Finally, I will close with Ch. 10 where the main conclusions from my work will be extracted and the future perspectives of the experiment will be discussed.

Chapter 2

Quantum Frequency Conversion for Quantum Information Processes

2.1 Quantum Information Technologies

Quantum information processing has attracted a lot of interest in the scientific community in the last couple of decades, and a lot of resources have been put into making it a reality [1]. The field of quantum information and quantum computation brings concepts from different fields together: quantum mechanics, computer science, information theory and cryptography. Quantum information is sometimes thought as in contrast with classical information. However, it would be wrong to think about quantum computation and quantum communication as future, better replacements for their classical counterparts. One should not think of them as opposites, but rather as complimentary to one another, as the very nature of quantum and classical information is different, so they are suitable to solve different kinds of problems.

In classical information the basic unit of information is called a bit, which can be in either of two states, usually labelled 0 and 1. The quantum counterpart of the classical bit is the quantum bit, or *qubit* for short. The main difference between bits and qubits is that the latter ones, apart from 0 and 1, can be in a linear combination between these two states, also known as a *superposition state*. This is usually expressed in the Dirac notation as

$$|\Phi\rangle = \alpha\,|0\rangle + \beta\,|1\rangle\,, \tag{2.1}$$

where α and β are complex numbers. This virtually confers the qubit an infinite number of states in which it can be, as the coefficients in front of states $|0\rangle$ and $|1\rangle$ can be chosen arbitrarily as long as their modulus square adds up to one ($|\alpha|^2 + |\beta|^2 = 1$), which means that states need to be normalised. The concept of quantum superposition is rather unintuitive. By measuring a classical bit one can know exactly in which state that bit is. Either 0, or 1. The result of measuring a quantum bit is also binary. In the previous example measuring in the $|0\rangle$—$|1\rangle$ *basis* will also yield either 0 or 1, but such a measurement does not tell us in what state the qubit was before the measurement. What is truly happening when a qubit is measured in the $|0\rangle$—$|1\rangle$ basis is that the qubit *collapses* into either the state $|0\rangle$ or the state $|1\rangle$. Then, if the qubit collapses into $|0\rangle$ we assign a measurement value of 0 and if it collapses into state $|1\rangle$ we assign a measurement value of 1[1]. The outcome of measuring a qubit is probabilistic, and the probability of getting either 0 or 1 will depend on the particular superposition state of the qubit before the measurement. Measuring in the $|0\rangle$—$|1\rangle$ basis the probability to get 0 is $|\alpha|^2$ while the probability to get 1 is $|\beta|^2$. The actual initial state of a qubit (i.e. the values of α and β) can only be inferred by taking multiple measurements of many identically prepared qubits and working out the statistics, and even then the true state of the qubit will only be obtained (with arbitrary precision) in the limit of taking an infinite number of measurements. The requirement of an infinite number of identically prepared copies of the same qubit is an important one, as measuring the same qubit multiple times does not add any new information, since after the first measurement the qubit collapses into either of the measurement basis states, and will therefore always give the same result in successive measurements performed in the same basis. It is not without a certain level of irony that a qubit can be in an infinite number of states, yet we can only get two possible results when observing it, or that if we want to know it's complete state with absolute precision we need to perform an infinite number of measurements. These seemingly ironical properties are the source behind the "wizardry" of quantum information and its associated technologies, and all the goodness that comes with them.

But what benefits can we obtain from quantum devices that we can not get from classical ones? In the last decades there has been a tremendous amount of effort and resources invested into making quantum devices a reality, and into finding different applications for these devices. Some of the applications found for quantum computing devices stay at the level of scientific curiosities, but some others could have a great impact in human society as we know it nowadays. In the following paragraphs I will give some examples of the later ones, dividing quantum information technologies into two groups: quantum computation and quantum communication technologies. However it is quite possible that the most exciting quantum devices are yet to be even imagined, as quantum technologies are still in a relative state of infancy, and the quantum technological boom, if it is to occur, is yet to arrive.

---

[1] Assigning the values 0 and 1 is completely arbitrary, as these are just labels. What matters is that the outcome of measuring a qubit is always binary. In fact, there is an infinite number of possible measurement bases that one could use. For example measuring in the $(|0\rangle + |1\rangle)/\sqrt{2}$—$(|0\rangle - |1\rangle)/\sqrt{2}$ will force the qubit to collapse into either state $(|0\rangle + |1\rangle)/\sqrt{2}$ or state $(|0\rangle - |1\rangle)/\sqrt{2}$. Then, if we wish, we can assign a measurement value of 0 to the first possible outcome and of 1 to the second one.

In the field of computation (classical or quantum) mathematical algorithms are classified as either being *efficient* or as being *inefficient*. This classification has to do with how much time does an algorithm require to get a solution for the problem it solves, as related to the size, or the number of variables involved in the problem. It is a scaling property. An efficient algorithm runs in a time that scales polynomially (or faster) with the size of the problem. An inefficient algorithm, in contrast, requires an amount of time that scales superpolynomially (e.g. exponentially) with the size of the problem. For many problems of interest even the best classical algorithms to date can only offer inefficient solutions. For some of these problems quantum algorithms have very cleverly been designed to offer efficient solutions. Many of the quantum algorithms that outperform their classical counterparts have very niche applications, but there are a handful of quantum algorithms that would be useful in a broader way if we could implement them in practice, as it will be discussed in the following paragraphs.

An example of a useful quantum algorithm outperforming classical ones is the quantum search algorithm, also known as Grover's algorithm [2]. It solves the problem of finding a particular element in an unsorted list. Any classical algorithm trying to find a particular element in an unsorted list of N elements will need to access that list a number of times proportional to N. Grover's algorithm makes use of the fact that quantum mechanical systems can be in a superposition of states to simultaneously examine multiple elements. By adjusting the phases of different quantum operations it is possible to make successful search results to constructively interfere while unsuccessful ones interfere in a random manner. This allows the quantum search algorithm to find the desired element by accessing the list a number of times proportional to $\sqrt{N}$ instead of N. While a quadratic enhancement in computational effort is not the most impressive result given by a quantum algorithm as compared to a classical one the range of applications of quantum search algorithms is enormous, as databases are ubiquitous in the modern world.

Other well known examples of useful quantum algorithms are Shor's algorithms for prime number factorisation and discrete logarithm computations [3]. These algorithms, as many other quantum algorithms, make use of the quantum Fourier transform, whose classical counterpart is the discrete Fourier transform. While the computation of the classical discrete Fourier transform requires $\mathcal{O}(N2^N)$ operations its quantum analogue can be performed in $\mathcal{O}(N^2)$ steps, where N is the number of qubits[2]. This represents an exponential enhancement. The importance of prime number factorisation and discrete logarithms is found in the field of cryptography. Because these operations are *hard* to perform in a classical computer they are at the heart of many encryption algorithms, such as the ones used in credit card purchases and

---

[2] The number of different quantum states for a system with N qubits is 2^N, and so the vector defining the state of the system has $n = 2^N$ components. Therefore, the classical discrete Fourier transform for a vector of length n requires $\mathcal{O}[n \log(n)]$ operations, while the quantum Fourier transform requires $\mathcal{O}[\log^2(n)]$ operations.

internet banking. Having a quantum computer capable of performing this kind of algorithm would render the most widely used encryption systems useless.

Another important application of quantum computation is quantum simulation [1]. Because of the nature of quantum mechanical systems, performing simulations to predict their behaviour is a very resource consuming task using classical computers. This is because given a system of N quantum mechanical elements it takes $\mathcal{O}(c^N)$ bits of classical memory to define its state (where c is some constant). Using a quantum computer it would take $\mathcal{O}(kN)$ qubits to do the same thing (where k is some other constant, not necessarily equal to c). It makes sense that simulating quantum mechanical systems is much better done using quantum mechanical systems rather than classical ones. The applications of quantum simulation are numerous. Quantum simulation would not only be useful to the field of physics, but also to all the other fields where quantum effects play an important role, like material sciences, electronics, and chemistry.

The other group of applications for quantum information systems is the one related to quantum communication technologies. Here the properties of quantum mechanical systems are used to ensure secure transfer of information between two parties. I suggested earlier that quantum computers could be used to break some of the most widely used encryption systems. Perhaps it is not surprising that an answer to that potential threat is also found in quantum mechanics, in what's known as quantum key distribution. A notable quantum key distribution protocol is the BB84 protocol [4] (as it was proposed by Charles Bennett and Gilles Brassard in 1984), which was the first one of its kind. Other protocols have been proposed since then. The key points that these protocols exploit are the fact that quantum states can not be cloned [5, 6] and the fact that the measurement process collapses the quantum state in one of the measurement basis' states. This makes it possible to conceive a communication protocol in which a potential eavesdropper trying to intercept the message could be detected. In fact, the way in which quantum key distribution works is by sending encryption and decryption keys between two parties. These keys are the ones being sent using a quantum communication channel, which makes it is possible to tell if the message containing the key has been intercepted or not. If it has, a new key is sent, and otherwise the sent key is used. This process is repeated until a key is successfully transmitted without being eavesdropped. Once both parties share the same secret encryption key the encrypted message can be sent using classical communication.

These are only a few of the proposed applications for quantum information technologies. It is possible that, as with many other scientific advances, the most exciting and wild possibilities will only be discovered once the technologies involved have properly matured. One of the reasons that makes it hard for scientists to think about applications for quantum computers, for instance, is the fact that we haven't been able to build one.

Building quantum information devices has indeed proven to be a very challenging quest. I like to divide quantum devices into three groups, in direct analogy with their classical counterparts. *Quantum processors* will be required to perform logical operations over quantum bits of information. In any complex system this information will need to be stored, so *quantum memories* will be necessary. For many of the projected applications short time memories will be sufficient, as opposed to permanent memories used for data storage (these would be useful too, but much harder to realise). Finally, we will need a way to move information from one place to another, so we will need a *quantum wire*. Using these components one can envisage things like the quantum internet [7], where quantum information is processed and stored in different nodes and shared between one another using quantum channels. The challenge is to find a suitable physical platform to build these components.

To transmit quantum information from one place to another photons seem to be one of our best candidates[3]. These can be propagated through free space (e.g. for satellite communication) or using optical fibres. It would still require a considerable amount of effort to use optical fibres for long range quantum communication, as photon-encoded qubits decohere due to loss more and more the further they travel through an optical fibre. A possible solution is a quantum repeater, as proposed by Lu-Ming Duan, Mikhail Lukin, Juan Ignacio Cirac and Peter Zoller in what is known as the DLCZ protocol [9]. In their proposal quantum repeaters substitute the classical repeaters found in nowadays telecommunications networks. These quantum repeaters are used to distribute entanglement over long distances, which is the fundamental resource of most quantum communication protocols. The reason why classical repeaters can not be used in quantum communication is because what a classical repeater does is to take an input signal and amplify it, or in other words: make a stronger/bigger copy of it. Due to the no-cloning theorem this method of operation would not work with quantum bits, as it is impossible to make multiple replicas of a quantum state.

A big disadvantage of using photons is that they do not interact with one another. The implications of this is that multi-qubit quantum gates are very hard to realise in a system that only uses photons[4]. Different systems using natural and artificial atoms could be used to build quantum processors [11]. These systems couple naturally to photons, which are used both

---

[3] Another possible candidate are rare earth doped crystals. These posses coherence times as long as several hours, and it has been proposed that physical transportation of rare earth doped crystals could be a better solution than propagating information using photons in optical fibres [8]. However, this would be technically very challenging, as the crystal would need to be kept at cryogenic temperatures during the whole trip, as well as electromagnetically and possibly mechanically isolated from the environment.

[4] In 2001 E. Knill,R. Laflamme and G.J. Milburn presented a theoretical proposal known as the KLM protocol [10] in which projective measurements are used to introduce an effective interaction between photons, thus making it possible to implement quantum gates using only linear optical elements. However, the technical requirements to implement the KLM protocol are very demanding.

to control the system and to extract information from it. However, they all work at different frequencies, so connecting them to one another can not be done in a direct way.

A similar situation is found with quantum memories. Different systems capable of storing quantum information have been proposed and demonstrated [12–20], each with its own advantages and inconveniences. However, while most of them can be coupled to electromagnetic radiation they can't be used together with other devices because they all work at different frequencies.

To overcome this issue hybrid quantum systems have been proposed [21, 22]. Hybrid systems combine more than one quantum system in a single device making use of the advantages and strengths of each of them. A step further, or perhaps a sidestep, would be to have an intermediate device in which the frequency of the output photons from one of the elements in the network is converted to match the frequency of the input photons of the next element. This is the goal of Quantum Frequency Conversion (QFC) [23], which is explained in more detail in the following section.

2.2 Quantum Frequency Conversion

Different quantum systems can be used to implement different components in a quantum network. The different nodes of such a network could be connected to one another using optical fibres. Photons are an appealing quantum information carrier because they interact weakly with the environment. Silica optical fibres have a transmission peak around 1550 nm, at the so-called telecommunications C-band. One of the attractive things of using optical fibres to build a quantum network is that a big amount of infrastructure is already there at the present time; these are the optical fibres used for the internet. However, most useful quantum systems can not be directly connected to a fibre network, as they tend to work at wavelengths different from those in the C-band. A solution to this problem is to use a device capable of converting the frequency of the output photonic qubit of a given quantum device to a frequency suitable to be transmitted along a fibre. Such a device needs to leave the qubit's quantum properties of interest unperturbed. In other words: QFC needs to preserve the non-classical correlations of the incoming photon. In a similar way, the frequency of a photonic qubit coming from an optical fibre would need to be converted to the frequency of the receiving quantum device, so QFC needs to be performed in a reversible way. In general, the requirements for useful QFC are that the process needs to be coherent, efficient, and free of noise. These three conditions ensure that the non-classical correlations will be preserved during the frequency conversion process.

There are a number of ways to achieve QFC. In all cases it is going to happen through some sort of nonlinear process, as linear processes preserve frequency. The most common ways of achieving QFC make use of the $\chi^{(2)}$ or $\chi^{(3)}$ nonlinearity of certain nonlinear materials. Other approaches exist, but in many cases one can define an effective nonlinearity and describe the conversion process in a standard nonlinear optics way.

Any QFC process needs to be tailored to the specific requirements of the input and the output photons. Naturally, different physical systems will be suitable for different types of QFC. For applications related to building the quantum internet (or any sort of reasonably sized quantum network) there is quite a long list of physical systems that one would like to interact with. From neutral atoms in optical traps to superconducting circuits, passing through trapped ions, quantum dots and doped crystals. QFC devices would make these very different systems compatible with one another.

QFC has been demonstrated in the past on different occasions. Frequency conversion between optical frequencies of a member of a time-bin entangled photon pair was reported in Ref. [24], showing that entanglement was preserved after the frequency conversion process. Later on frequency conversion of single photons was demonstrated using four-wave mixing in a Bragg-scattering photonic crystal fibre [25]. QFC interfacing an optical quantum memory and telecom photons was shown for the first time in Ref. [26]. In that experiment QFC was achieved in an optically thick cold of rubidium gas. In Ref. [27] QFC between optical and telecom photons was shown using a periodically poled lithium niobate (PPLN) crystal. The use of nonlinear crystals has the attraction that on-chip implementation is much more feasible than for example using atomic clouds. In that experiment the photons converted were about a picosecond long. QFC of optical light emitted from a single quantum emitter (or quantum dot) to the telecom band was shown in Ref. [28]. QFC from a quantum dot source emiting in the near infrared to visible wavelengths was reported in Ref. [29]. In Ref. [30] optical photons coming from a rubidium quantum memory were converted to the telecom band using a nonlinear crystal waveguide. In that experiment the converted photons were about 10 ns long (in general, the longer the photon the more sensitive you are to the background noise, as time filtering becomes less effective). All these experiments involved frequencies in the optical domain. Another interesting part of the electromagnetic spectrum is the microwave domain. Experiments in the microwave regime are much harder than in the optical one because in general microwaves interact much more weakly with atoms than optical photons do, but as I will outline in the following section there is a lot of potential in the microwave domain too, and indeed a lot of effort is being put in the realisation of microwave based quantum systems.

2.3 Microwave to Optical Quantum Frequency Conversion

Superconducting qubits (SQs) are notable quantum systems that have generated a lot of interest in recent years [31–33]. SQs are macroscopic objects (with sizes ranging from nanometre to millimetre scales) that despite their size exhibit quantum properties, like discrete energy levels, superposition and entanglement. In their most basic form they consist of a loop of superconducting wire broken by a capacitor, and a *Josephson junction*. A loop of wire (an inductance) attached to a capacitor forms an LC resonant circuit, the behaviour of which is analogous to that of a harmonic oscillator. In such a system, the canonical conjugate variables (analogous to position and momentum for a harmonic oscillator) are the flux Φ in the inductor and the charge Q in the capacitor, obeying the commutation relationship $[\Phi, Q] = i\hbar$.

However, a harmonic oscillator is of little use for quantum computation. What we want for quantum computation, instead, is an effective two level atom with which a qubit can be implemented. The reason why a harmonic oscillator is not suitable is because in a harmonic oscillator the different energy levels are all equidistant, making the transition frequencies degenerate. Therefore one will address many different states when using photons of a particular single frequency, instead of addressing only two states. To get around the harmonic oscillator behaviour a nonlinearity is introduced in the inductance of the superconducting LC circuit. This comes from what is known as a Josephson junction, which creates a nonlinearity so big that it's effects can be seen with single photons. A Josephson junction is formed by having a thin insulating layer in between two superconductors. The insulator layer needs to be thin enough to allow Cooper pairs (electron pairs that give rise to superconductivity) to tunnel through it coherently. This is typically a few nanometers. A voltage difference applied between the two superconducting halves of a Josephson junction induces a time dependent phase difference in the current through the junction. This time varying phase difference, in turn, gives rise to a nonlinear inductance. The nonlinearity introduced by the Josephson junction breaks the degeneracy of the frequency differences between energy levels, giving rise to an effective artificial atom.

SQs have many desirable qualities for implementing quantum computers. To start with, they are manufactured components. This means that, in contrast with, for example, neutral atoms, their properties can be tailored to a specific application, offering a lot of freedom and a wider range of potential applications. The quantum states of SQs are very sensitive to AC and DC electromagnetic fields, which makes it easy to interact with them and to couple them strongly to resonant cavities. They are small, and they can be built on a chip. This is a very important property, as one of the requirements for implementing quantum computers is that of scalability of the various components. Their technical capabilities are also quite impressive. The longest coherence times achieved with SQs are on the order of $100\,\mu$s [34]. Single- and two-qubit gate times of 1 or 2 ns have also been reported [35]. These two facts combined allow the possibility of performing thousands of operations before the qubit decoheres. Qubit readout fidelities of 98% have been reported in Ref. [36]. Coupling between SQs can be made strong, and furthermore this coupling can be tuned and switched on and off at will electronically [37, 38]. It is important to note that not all of these great features of SQs can be achieved at once (or at least so far), but the flexibility in their capabilities appears nevertheless to be very promising.

However, SQs have their inconveniences too, and experiments with them are challenging. SQs usually have transition frequencies in the microwave regime, of about 5-10 GHz. Environmental thermal radiation is present at these frequencies for a very wide range of temperatures, which takes the form of noise in SQ experiments. In order to minimise thermal population of the excited state of a SQ the device typically needs to be cooled down to temperatures below 100 mK. This requires dilution refrigerators, which are non-trivial machines. On top of that, SQs interact strongly with electromagnetic fields. This is both desirable and inconvenient. Strong interactions means that accessing them and performing operations on them is easy, but at the same time they become very sensitive to external noise. For this reason SQ experiments need to be shielded inside a Faraday cage, which is often provided by the metallic body of the cryostat they sit in. In addition, performing experiments with SQs often requires magnetic shielding from the environment. Furthermore, multiple filtering and attenuation stages need to be added to the wires used to talk to them, often requiring several stages at the different temperature phases of the cryostat.

The fact that SQs interact with microwave photons makes it particularly infeasible to connect them directly to any sort of long range network. This is because, as mentioned earlier, the temperatures at which thermal noise starts to appear at these frequencies are very low. Using microwaves to communicate quantum information from one point to another would require the whole length of the transmission line to be cooled down to millikelvin temperatures, which sounds really impractical with nowadays technologies. For this reason, and given the very promising features of SQs, it would be highly desirable to have a system capable of performing QFC between microwave and visible or telecom photons, which could then be coupled to optical fibres for which propagation losses and decoherence is low. At the same time this would allow the use of optical quantum memories [12–16], which are currently more advanced than their microwave counterpart [17–20].

As discussed in the previous section QFC between optical frequencies has been proved in several occasions. Recently, QFC has also been demonstrated between microwave frequencies [39], but so far QFC between optical and microwave fields has remained a challenge for the scientific community.

Several proposals for implementing microwave to optical QFC have been suggested. These include optomechanical resonators [40–45], nonlinear crystals [46–50], Brillouin scattering with magnons [51–53], Rydberg gasses [54–56] and rare earth ion doped crystals [57–59]. Most of these proposals make use of optical and microwave resonators, that are used to magnify the efficiency of the frequency conversion process.

Optomechanical approaches [40–45] rely on using mechanical resonators to couple microwave and optical fields. Simplistically speaking, these systems can be thought as if one of the mirrors from a microwave and an optical resonator were glued together back to back, and coupled to a mechanical resonator, which effectively acts as an interaction channel between the two resonators. These kinds of approaches have shown bidirectional coherent conversion with photon number efficiencies as high as 10% [44]. The downside of these kind of schemes is that in order to achieve low noise frequency conversion it would be desirable to cool the mechanical resonator down to its ground state, which is currently challenging due to the low (kHz) frequencies at which they operate.

A different approach is to use conventional nonlinear materials to build resonantly enhanced modulators [46–50]. In this case the refractive index of an optically transparent material is modulated by a microwave field, giving rise to symmetric sidebands at the microwave frequency around the optical carrier. It is possible to get rid of one of the sidebands by cleverly manipulating the optical resonator's transmission spectrum. Photon number conversion efficiencies of the order of 0.1% have been shown, with bandwidths larger than 1 MHz. The challenges with this kind of implementation is achieving high enough nonlinearities in the materials used, and keeping the conversion process single-sideband.

Another avenue is to use Brillouin scattering between magnons (collective electron spin excitations) and photons in ferrimagnetic insulators like yttrium iron garnet (YIG) [51–53]. In these systems a spherical sample of YIG is used to build a whispering gallery mode resonator that supports two optical modes. At the same time, the YIG sphere is capable of sustaining a magnetisation resonant mode at microwave frequencies. This is a very recent field of investigation, and no conclusive results regarding QFC between microwave and optical fields have been reported yet, as the efficiencies they can achieve at the moment are extremely low.

Rydberg gasses have been suggested as a different alternative [54–56]. The specific proposed implementations are diverse. One option would be to use hyperfine transitions to store the microwave excitation, which would then be retrieved as an optical photon. Another option would be to implement a six-wave mixing process where some of the frequencies involved are optical and some are in the microwave regime, in such a way that one gets microwave to optical frequency conversion. The microwave transitions in Rydberg gasses are electric dipole transitions as opposed to magnetic dipole transitions as in most of the other systems. This translates into a stronger coupling with the microwave photons, providing the advantage that in some of the proposed schemes resonant cavities are not required in order to achieve high conversion efficiencies, so the conversion process is much more broadband. The highest speculated conversion efficiencies are as high as 90%, but so far no experimental demonstration has been reported.

Last, but not least, it has been proposed as a way to achieve QFC between microwave and optical fields to use rare earth doped crystals [57–59]. Rare earth doped crystals can possess long coherence times and narrow inhomogeneous linewidths, and exhibit high nonlinearities around these. The aim in this kind of experiments is to find a Δ-like energy level structure (a three level structure where the three different transitions are allowed) where one of the transitions has a microwave frequency while the other two are in the optical domain. By coherently driving the microwave and one of the optical transitions one can generate a field at the frequency of the other optical transition, thus converting the microwave photon into an optical one. A particularly well suited material towards this end is erbium doped yttrium orthosilicate (Er^{3+}:Y_2SiO_5). The reason is that Er^{3+}:Y_2SiO_5 has a natural optical transition in the telecom band at around 1536 nm. Furthermore, microwave transitions of a few GHz can be achieved by either using the hyperfine levels of one of its isotopes or by Zeeman splitting the degenerate ground and/or excited states of the other isotopes. Additionally, since the g-factors observed in Er^{3+}:Y_2SiO_5 are large, this could be achieved using only moderate magnetic field strengths (below 1 T). This kind of approach is the main topic of my thesis, and it will be explained in more detail in what follows.

Chapter 3

Rare Earth Ion Doped Crystals

The rare earths series is comprised of the following elements, in order of appearance in the periodic table: scandium (Sc), yttrium (Y), lanthanum (La), cerium (Ce), praseodymium (Pr), neodymium (Nd), promethium (Pm), samarium (Sm), europium (Eu), gadolinium (Gd), terbium (Tb), dysprosium (Dy), holmium (Ho), erbium (Er), thulium (Tm), ytterbium (Yb) and lutetium (Lu). This is, the lanthanide group (La-Lu) together with Sc and Y. The name "rare earths" is highly misleading, as they are neither that rare, nor are they "earths" [60]. They are not rare in the sense that their abundance is quite large. For example, the most common rare earth (Ce) is about six times more abundant than lead, while the least common rare earth element (Lu) is about two hundred times more abundant than gold [60]. Rare earths are called "rare" because by the time most of them were discovered, in the 19th century, there was only one deposit of rare earth elements known, in Ytterby (Sweden) [60]. The reason why they are called "earths" is because they were first extracted from oxides, and in French and in German (the major scientific languages during the 19th century in Europe) the words for an oxide of an element are literally translated to English as "earth".

Rare earth elements are widely used in many different applications, ranging from relatively low tech applications to high tech ones. Among the long list of rare earth element applications one can find things like metal alloys, pigmentation, glass additives, automotive catalysts, ceramics, polishing powders, batteries, permanent magnets, nuclear control rods, photographic filters, high temperature superconductors, phosphors, lasers and a long etcetera, most of these having in turn their own applications. The list of applications of rare earth permanent magnets alone, for instance, is already huge. It is often their unique optical, magnetic or chemical properties what makes them useful. In particular, the optical properties of rare earths can be exploited for building solid state lasers, fibre lasers and fibre amplifiers [61], which are widely used in the field of telecommunications, but are also useful for more scientific oriented applications such as building classical and quantum memories for light amongst others.

3.1 Atomic Properties and Doped Crystals

The most common oxidation state of rare earths is 3+, although some can also have 2+ or 4+ oxidation states, when that leads to a full, half full or empty 4f shell depending on which particular atomic species is ionised. The elements in the lanthanide series (note the exclusion of Sc and Y) share very similar atomic properties. The main difference amongst them in terms of the electronic structure is how many electrons they possess in the 4f shell. From La which has none up to Lu which has fourteen, filling up the whole 4f shell.

In order to make use of the very narrow optical transitions that rare earth ions can exhibit at low temperatures it is common to dope them into crystals. The host crystal usually contains Y^{3+} or La^{3+}, which is partially substituted by the rare earth element to study. The substitution ratio, or concentration, is often given in parts per million (ppm), and it indicates how many host ions are substituted by dopant ions. Typical dopant concentrations range from a few to a few thousand ppm, which results in small ion-ion interactions and a small perturbation of the host crystal lattice.

A remarkable fact of the 4f shell in the lanthanide ions is that it is effectively electrically shielded by the 5s, 6s and 5p shells. These shells are filled completely and their radial distribution probability peak is further out than that of the 4f shell, as shown in Fig. 3.1 for the case of Pr^{3+}. The 4f-4f are the lowest energy electronic transitions in most lanthanides. La and Lu are an exception to this, since their 4f shell is either completely empty or completely full. Because of the screening from the outer shells the 4f-4f transitions' behaviour is very similar to that of a free atom, and these transitions tend to have very narrow linewidths even when the ions are embedded in a crystalline structure. Because of this, rare earth ion doped crystals are sometimes thought of as frozen atomic coulds, where the dopant ions behave as free ions yet their spatial position is fixed.

The energy level structure of the 4f electrons in free rare earth ions arises mainly from the Coulomb interaction between electrons, and the spin-orbit coupling. The spin orbit coupling interaction splits the Coulomb energy terms into $2S + 1$ multiplets, where S is the total spin of the electrons. The spin-orbit multiplets are labelled as ${}^{2S+1}L_J$, where L is the total orbital angular momentum of the electrons and J is the total angular momentum ($\vec{J} = \vec{L} + \vec{S}$). Conventionally, the different values of $L = 0, 1, 2, 3...$ are denoted by S, P, D, F... which historically stood for sharp, principal, diffuse and fundamental due to the shapes of their corresponding spectral lines [63]. The ${}^{2S+1}L_J$ notation may suggest that L, S and J are all good quantum numbers, but because the spin-orbit coupling is strong L and S are not (meaning that for a given energy state L and S are not well defined). However, since the free ion is spherically symmetric J is a good quantum number. In spite of this fact, the ${}^{2S+1}L_J$ notation is still used to refer to the different energy levels, for lack of a better way.

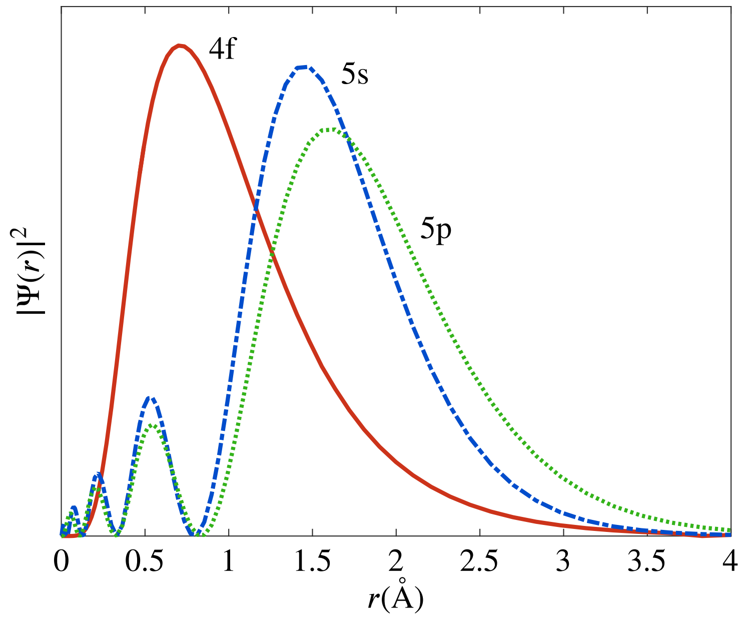

Figure 3.1: Radial probability density of electrons in the 4f, 5s and 5p shells for Pr^{3+}. The data utilised to plot this figure has been taken from Ref. [62].

For rare earth ions embedded in a crystalline structure the spin-orbit multiplets are further split by the crystal field. Depending on the point symmetry of the host crystal at the dopant site the crystal field splitting will lift the spin-orbit degeneracy to a lesser or higher degree. For the case of non-Kramers ions, which are those with an even number of valence electrons, this degeneracy can be lifted completely for sufficiently low symmetry sites. For the case of Kramers ions, which are those with an odd number of valence electrons, the spin-orbit degeneracy can be lifted up to $J+1/2$ Kramers doublets. The degeneracy of the Kramers doublets can be broken into Zeeman levels by applying a magnetic field. For ions that have a nuclear spin I different from zero each of the crystal field levels is split via the hyperfine and quadrupole interactions into $2I + 1$ levels. A diagram of these splittings and their typical orders of magnitudes is shown in Fig. 3.2.

The principal decay mechanism across crystal field levels of a ${}^{2S+1}L_J$ manifold is via phonon emission, which is a very fast process. Another factor that determines the population density on each energy state is temperature. The spectral distribution of thermal radiation states is determined by the product k_BT, where k_B is the Boltzmann constant and T is the temperature of the crystal. If we define the angular frequency of a transition linking the energy level i and the lowest energy state as ω_{i0}, all energy levels with $\hbar\omega_{i0} < k_BT$ (where $\hbar$ is the reduced Planck constant) will be populated. This means that in general, at cryogenic temperatures, only the lowest crystal field level will contain a meaningful atomic population.

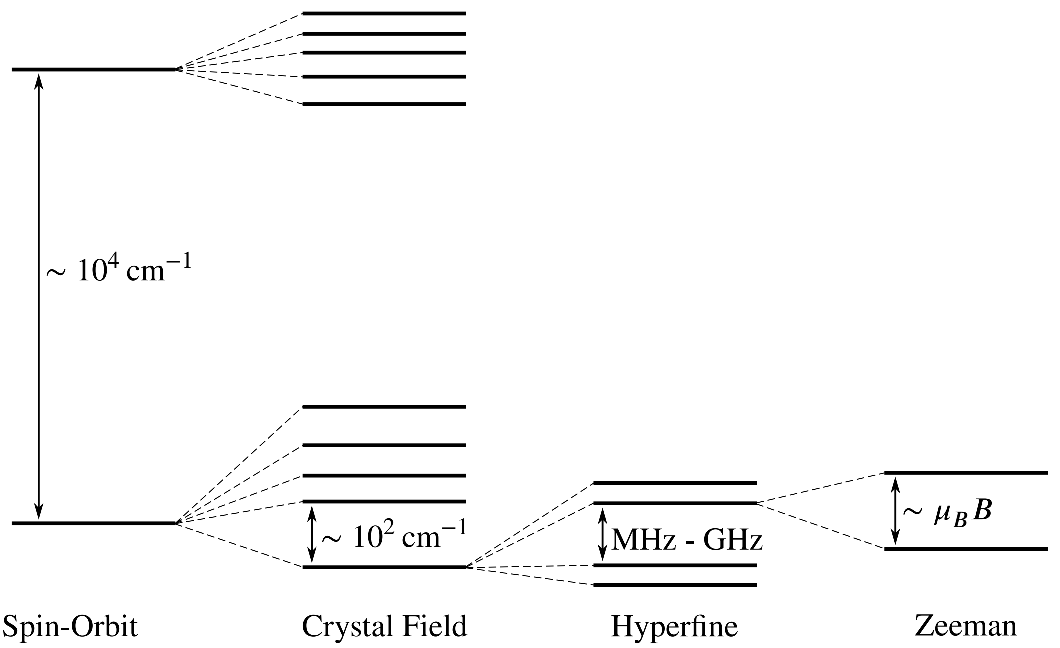

Figure 3.2: Different contributions to the splitting of the energy level in rare earth ion doped crystals. Note that the ~ $\mu_B B$ Zeeman splitting only applies to Kramers ions.

3.2 Homogeneous and Inhomogeneous Broadening

Rare earth transitions are generally characterised by two different linewidths in their spectral absorption profile. The homogeneous linewidth is associated to a single dopant, while the inhomogeneous linewidth is associated to the whole collective of dopants inside the crystal.

The homogeneous linewidth is the same for all ions, and its minimum possible linewidth is determined by the population decay rate, although this limit is rarely achieved. The actual linewidth of the homogeneous line is given by the inverse of the coherence time T_2. The coherence time will in general depend on the temperature of the sample. At room temperature absorption and emission of phonons will result in a broader homogeneous line. At temperatures near 4 K the effect of phonons is in most cases negligible for optical transitions. Other effects can contribute to the homogeneous broadening, such as spin flips due to neighbouring atoms. In order to minimise this it is desirable to use a host crystal whose atoms have low magnetic moments, like silicates. Another option is to apply an external magnetic field to polarise the spins inside the sample and stop them from flipping around. Similarly, dopant-dopant interaction can broaden the homogeneous line. This process can be minimised by decreasing the dopant concentration in the crystal. Typical homogeneous linewidths range from less than a kHz up to several MHz, although linewidths as narrow as 60 Hz have been reported in Er^{3+}:Y_2SiO_5 [64].

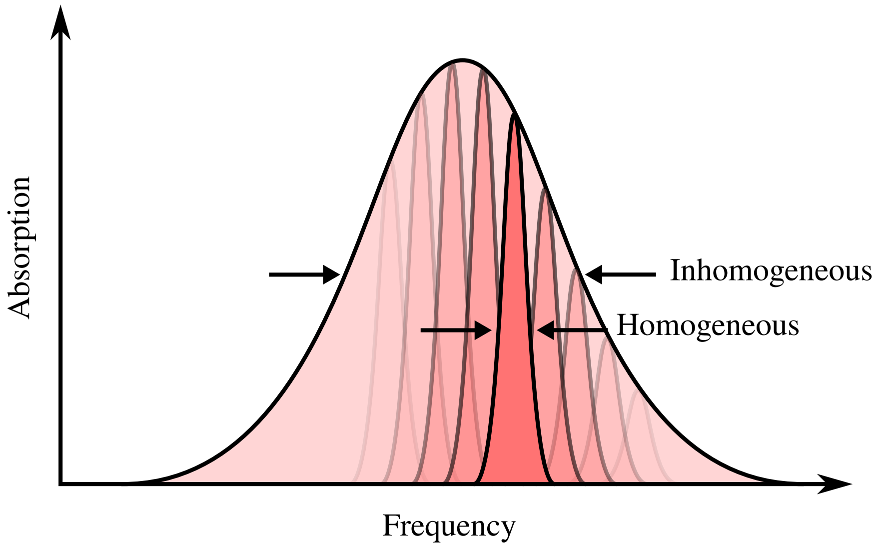

Figure 3.3: Inhomogeneous line arising from the homogeneous profile of a collection of ions with different central frequencies.

The inhomogeneous line is the combination of the homogeneous lines of all the dopants in the sample. Because the host crystal will in general be imperfect each ion will see a slightly different environments around itself. This induces a different frequency shift for different ions, giving rise to a broadening of the collective spectral line (see Fig. 3.3). These crystal inhomogeneities are often caused by strain in the crystal. This means that different crystals grown in different ways can have different inhomogeneous broadenings. The inhomogeneous broadening of a given crystal will in general also change if mechanical stress is applied to the crystal, and sometimes this effect can be permanent (e.g. if the crystal has been hit or dropped). Another factor presumed to affect the inhomogeneous linewidth is the concentration of ions, as the higher the dopant number the higher the disorder in the crystal will be. The inhomogeneous linewidth of rare earth ion doped crystals can vary quite a lot for different dopants in different crystals. This can range from a few hundreds of MHz to several hundreds of GHz. The lineshape typically resembles a Gaussian function. Using low-strain, isotopically pure crystals inhomogeneous linewidths as narrow as 16 MHz have been observed in isotopically purified $^{170}\mathrm{Er}^{3+}$:$^{7}\mathrm{LiYF}_4$ [65].

3.3 Spectral Hole Burning

Spectral hole burning is an effect that arises from the combination of homogeneous and inhomogeneous broadening in the absorption spectrum of a rare earth doped crystal. A spectral hole is a dip in the inhomogeneous absorption profile. This can be achieved by using a narrow band light source, like a laser, to (either permanently or temporarily) “bleach” away some of the absorption. If the spectral width of the laser is narrower than the inhomogeneous line then the laser can be set on resonance with only a subgroup, or a class of ions in the crystal. The effect of the laser will be to transfer population from the ground state to some excited state, which then may decay into a different ground state. Since the ground state is being vacated less absorption is observed at that particular frequency. This process works in the exact same way as – and can in fact be considered a form of – optical pumping, but it only affects a portion of the ions.

The minimum width of the spectral hole will be given by the convolution between the homogeneous linewidth of the ions and the spectral width of the laser. The lifetime of the hole will be given by the decay time back to the initial state of the atomic population that has been pumped to other energy levels. In the case of a two level atom this would be the lifetime of the excited state. In the case where there are intermediate states the lifetime of the spectral hole will depend on the decay times of all the states involved in the process. Some rare earth ions have very long lived intermediate states, which can give rise to spectral hole lifetime of the order of several weeks [61]. Further than this, photoionisation [66] and ion displacement in deuterated samples [67] can give rise to persistent hole burning, where the spectral holes will remain as long as the sample is kept cold.

In a rich energy level structure a spectral hole usually comes accompanied by a collection of side holes and anti-holes, as shown in the four level example in Fig. 3.4. The central hole arises from removing population from a particular energy level. This population will be stored in some other energy level, which will give rise to an increase in absorption for a transition starting from that level, creating a side anti-hole. At the same time, other transitions starting from the energy level that has had its population removed will have a decreased level of absorption, which creates a side hole. The spectral distance between side holes and anti-holes and the central hole will be given by the energy separation between the different energy levels involved. Spectral hole burning spectroscopy is a powerful tool for determining the energy levels of rare earth ions in a crystal.

Experimentally, this can be measured using a pump-probe scheme. A pump laser beam is used to burn a hole in the inhomogeneous absorption profile. Then, a weak probe laser beam is scanned over the inhomogeneous line, which is used to measure how the absorption profile has changed. If the experiment is conducted using pulses of light it is possible to measure the lifetime of the spectral features by varying the time delay between the pump and the probe pulse.

A picture of how such a measurement works for the case of an atom with two ground states and two excited states is shown in Fig. 3.4. The pump beam moves the atomic population from

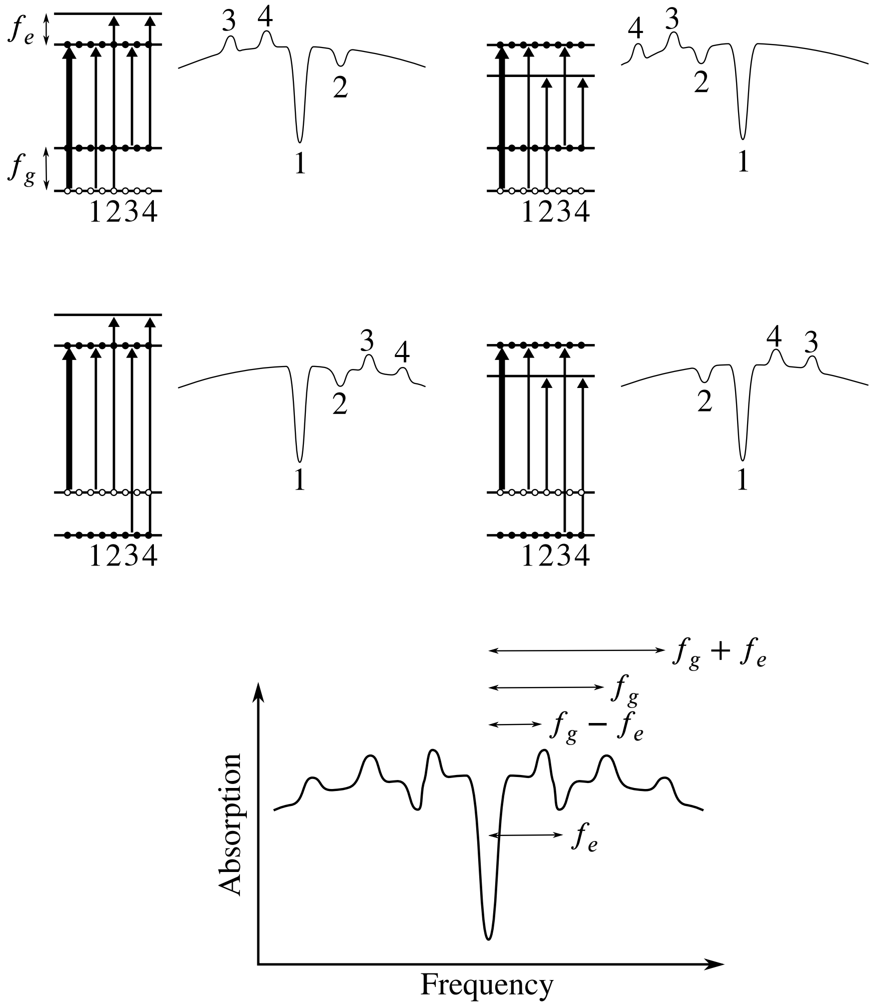

Figure 3.4: Spectral hole burning in a four level atom giving rise to a collection of side holes and anti-holes. The frequency difference between these features is directly related to the frequency difference between energy levels. The thick arrows show the transition that the pump is on resonance with for each class of ions, while the thin arrows show the different transitions that the probe will be on resonance with when it's frequency is scanned.

one of the ground states to one of the excited states. These two states will be different for different classes of ions in the inhomogeneous line. The population is then stored either in the excited state or in the other ground state, or a combination of both. This will depend on the decay rates of these states, the majority of the population being in the longer lived one. This population shift is represented with empty circles for the level being emptied or full circles for the levels being filled. When a probe beam is scanned across the inhomogeneous profile a difference in absorption will be observed at frequencies 1, 2, 3 and 4 as noted in the picture, giving rise to side holes and anti-holes. The total observed effect will be the combination of the different contributions from the different ion classes, as seen at the bottom of the figure. In the example shown the lifetime of the upper ground state is assumed to be large. If the lifetime of the excited state levels was longer than that of the ground states then the side anti-holes would become side holes.

3.4 Er^{3+}:Y_2SiO_5 as a Candidate for Frequency Conversion

Yttrium orthosilicate (Y_2SiO_5, or just YSO) is the host crystal that we will be interested in, and the one that we used in all the experiments described in Ch. 6, 7, 8 and 9. Y_2SiO_5 has a monoclinic biaxial crystal structure, belonging to the C_{2h}^6 symmetry group. Its unit cell is defined by the parameters $a = 1.041\,\mathrm{nm}$, $b = 0.6726\,\mathrm{nm}$, $c = 1.249\,\mathrm{nm}$ and $\tilde{\beta} = 102.65°$ ($\tilde{\beta}$ is the angle between the a and c axes). The standard coordinate system used is based in three orthogonal optical extinction axes labelled D_1, D_2 and b [68].

Y^{3+} ions occupy two inequivalent crystallographic sites of C_1 symmetry in Y_2SiO_5, labelled site 1 and site 2 [69]. Additionally, for each crystallographic site there are four subclasses of sites with different orientations related by C_2 rotation and by inversion, due to the crystal C_{2h}^6 symmetry. Under the effect of an arbitrarily oriented magnetic field the subclasses related by inversion will behave identically, while the subclasses related by C_2 rotation will behave differently. This gives rise to two magnetically inequivalent subclasses for each crystallographic site, which I will label subclass I and subclass II as in Ref. [70]. For magnetic fields oriented along the b axis of the crystal or along the $D_1 - D_2$ plane this magnetic inequivalence is lifted and the two subclasses become degenerate. When the crystal is doped Er^{3+} ions substitute Y^{3+} ions in similar amounts in site 1 and in site 2. The ground and first excited spin-orbit states of erbium are labelled $^4I_{15/2}$ and $^4I_{13/2}$ respectively. The transition between these states in Er^{3+}:Y_2SiO_5 occurs at 1536.478 nm for site 1 and at 1538.903 nm for site 2 in vacuum [70].

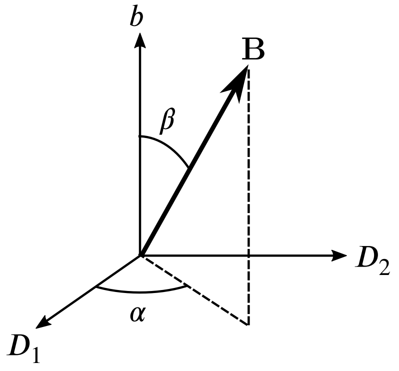

Figure 3.5: Convention utilised to define the angles α and β referring to the direction of the magnetic field $\vec{B}$ with respect to the crystal axes D_1, D_2 and b.

Due to its optical transitions in the telecommunications band Er^{3+}:Y_2SiO_5 is a very attractive material for quantum information and communication technologies. For these applications long coherence times are often desirable. As it has been said earlier, one of the sources of decoherence is the interaction between the nuclear spins of the different atoms in the crystal. In this regard Y_2SiO_5 is a particularly good host, as its constituents have either small magnetic moments (-0.137μ_N for ^{89}Y) or low natural abundance for their magnetic isotopes (4.7% for ^{29}Si with -0.554μ_N and 0.04% for ^{17}O with -1.89μ_N, where μ_N is the nuclear magneton).

Erbium appears in nature in six different stable isotopes: ^{162}Er, ^{164}Er, ^{166}Er, ^{167}Er, ^{168}Er and ^{170}Er. The even isotopes have no nuclear spin, and they appear with a total natural abundance of 77.05%. The only stable odd isotope, ^{167}Er, has a natural abundance of 22.95%, and it has nuclear spin $I = 7/2$.

At cryogenic temperatures only the lowest crystal field level of Er^{3+}:Y_2SiO_5 will be populated. As a consequence the system can be described by an effective spin half Hamiltonian. This spin Hamiltonian takes the following form:

$$H = \mu_B \mathbf{B} \cdot \mathbf{g} \cdot \mathbf{S} + \mathbf{I} \cdot \mathbf{A} \cdot \mathbf{S} + \mathbf{I} \cdot \mathbf{Q} \cdot \mathbf{I} - \mu_N g_N \mathbf{B} \cdot \mathbf{I}, \tag{3.1}$$

where μ_B is the Bohr magneton, and μ_N is the nuclear magneton. $\mathbf{B}$ is an externally applied magnetic field, $\mathbf{S}$ and $\mathbf{I}$ are the electron and nuclear spin operators. $\mathbf{g}$ is the g-factor matrix and g_N is the nuclear g-factor ($g_N = -0.1618$ for Er^{3+} ions). $\mathbf{A}$ is the hyperfine interaction matrix, and $\mathbf{Q}$ is the electric quadrupole matrix. For the even isotopes, since $I = 0$, Eq. (3.1) reduces to

$$H = \mu_B \mathbf{B} \cdot \mathbf{g} \cdot \mathbf{S}. \tag{3.2}$$

In our endeavour of converting microwave photons into optical ones we want an atomic level structure in which we can find a Δ system configuration, consisting of three energy levels coupled to one another in such a way that two of the transitions have optical frequencies and the other one has a frequency belonging to the microwave regime. As mentioned earlier, Er^{3+}:Y_2SiO_5 has a natural transition in the optical telecommunications band, which is extremely convenient as light at these frequencies is readily compatible with silica optical fibres. The hyperfine structure of $^{167}Er^{3+}$:Y_2SiO_5 consists of sixteen energy levels spanned across a ~5 GHz range, which is particularly suitable for our needs. For the even isotopes, transitions of a few GHz can be obtained by Zeeman splitting the Kramers doublet states using only moderate magnetic fields, of the order of a few hundreds of mT. This presents two possible avenues, as shown in Fig. 3.6. The first one is to use the hyperfine structure of the ^{167}Er isotope at zero magnetic fields. Working at zero magnetic fields is particularly desirable not only because it simplifies the experimental requirements significantly, but most importantly because it allows the use of superconducting materials for building microwave resonators (superconductors and magnetic fields are not particularly good friends). Working at zero magnetic field, however, one looses the freedom to tune the frequency of the microwave transition. Another drawback of using the ^{167}Er isotope is that the energy level structure of the $^4I_{15/2}$ ground state has not been particularly well determined at zero magnetic fields, and the energy level structure of the $^4I_{13/2}$ excited state is mostly unknown. The second avenue is to use the even isotopes of erbium in an externally applied magnetic field. This has the disadvantage that superconductors can not be used for building the microwave cavities, but on the other hand it offers much more freedom regarding what microwave frequencies one can use, as this will be determined by the magnetic field strength and not by the nature of the hyperfine interaction. Additionally, working with two ground and two excited states is a much easier job than working with sixteen ground states and sixteen excited states, especially when the energies of these are unknown. There is an inconvenient in building a quantum frequency converter that requires magnets, which is the incompatibility of superconducting qubits and magnetic fields. However, one can always devise a setup in which the half that contains the superconducting qubit is magnetically shielded from the half that contains the quantum frequency converter, and microwave photons are transported between the qubit and the converter using waveguides.

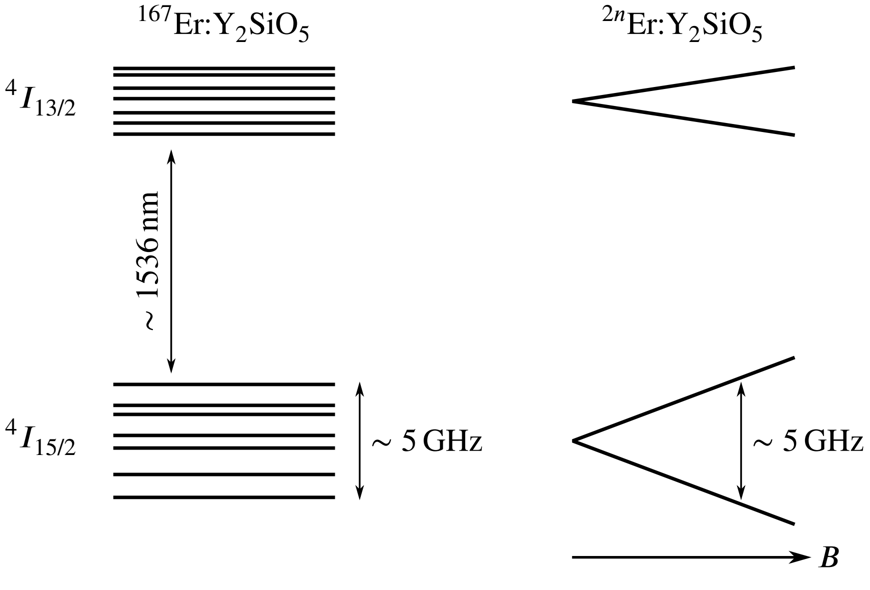

Figure 3.6: Schematic representation of the energy levels of the stable odd and even isotopes of Er^{3+}:Y_2SiO_5, showing two possibilities to perform microwave to optical frequency conversion depending on which parity isotopes are used. For the odd isotope hyperfine transitions near 5 GHz can be found in the ground state. For the even isotopes the ground state can be Zeeman split using an applied magnetic field.

During my thesis I first explored the feasibility of using the ^{167}Er isotope. In order to do that we tried to reconstruct the hyperfine structure of the $^4I_{13/2}$ excited state using hole burning spectroscopy, as it will be described in Ch. 6. However this turned out to be more difficult than

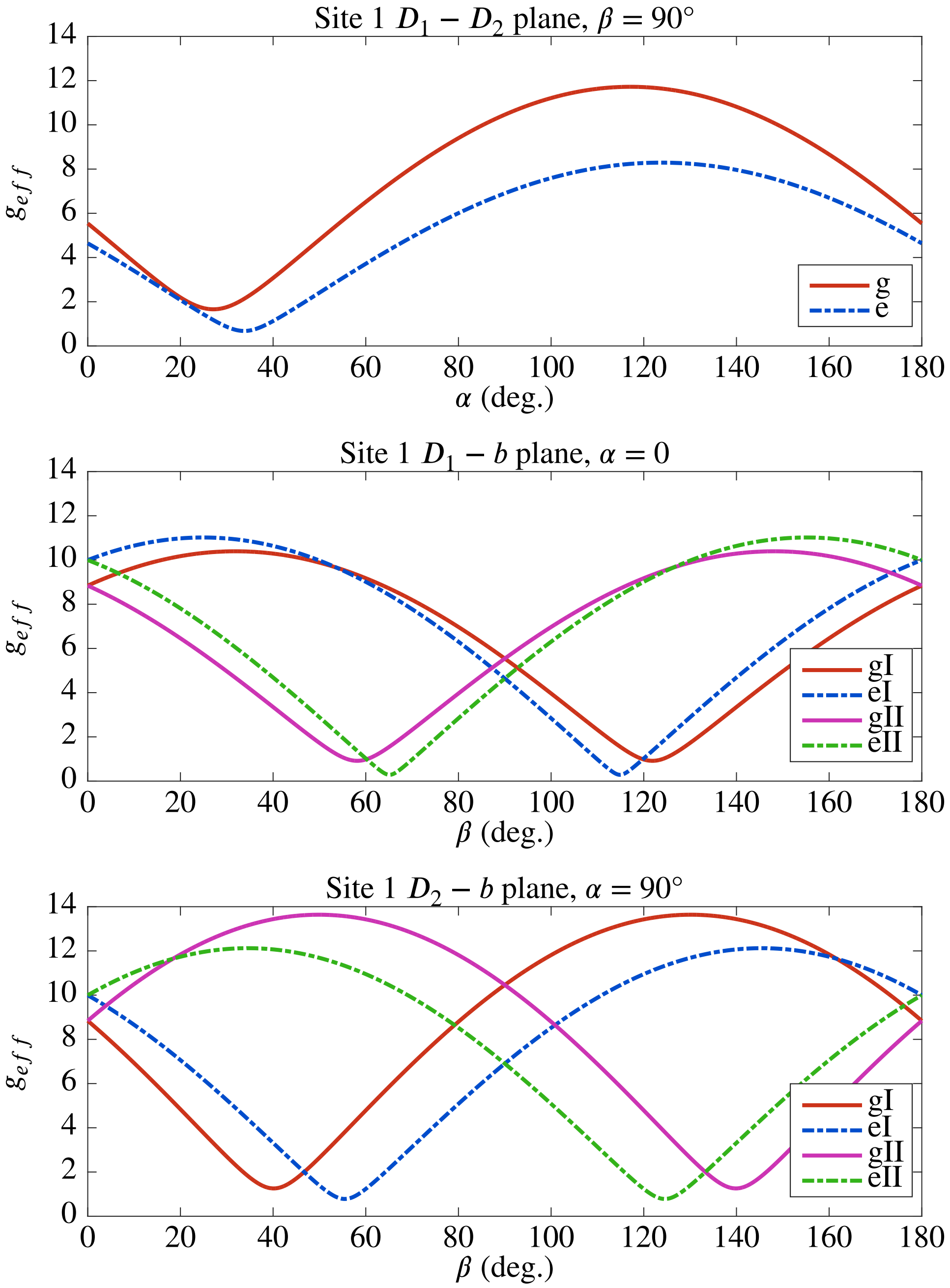

Figure 3.7: Effective g-factors for site 1 in Er^{3+}:Y_2SiO_5 for different orientations of the magnetic field, as reported in Ref. [70]. The results shown are for the ground (g) and the excited (e) states, and for the magnetically inequivalent subclasses I and II. The angle α is measured from D_1 to the projection of $\mathbf{B}$ in the $D_1 - D_2$ plane and the angle β is measured from the crystal axis b to $\mathbf{B}$, as shown in Fig. 3.5.

anticipated and our efforts were redirected into using the even isotopes in a magnetic field. In the following paragraphs I will summarise some of the optical spectroscopic properties of the even isotopes of erbium in Y_2SiO_5, in particular when a magnetic field is applied (although some of this can also be applied to the 167 isotope, like the g-factors).

Back to the g-factor in Eq. (3.2), it is a three by three matrix. For a given direction of the magnetic field Eq. (3.2) can be rewritten as

$$H = \mu_B B g_{eff} S. \tag{3.3}$$

Note that g_{eff} is a scalar and that B and S refer to the modulus of the vectors $\mathbf{B}$ and $\mathbf{S}$. The value of g_{eff} will then depend on the orientation of $\mathbf{B}$ with respect to the crystal axes. In general, g will be different for the ground and the excited states, and it will also be different for ions of the magnetically inequivalent subclasses I and II. This gives four different g matrices, which were determined by Sun et al. in Ref. [70]. Their results have been reproduced in Fig. 3.7, following the angle convention of Fig. 3.5.

The optical transitions between the $^4I_{15/2}$ and the $^4I_{13/2}$ energy states have an electric dipole and a magnetic dipole contribution. By diagonalising the spin Hamiltonian in Eq. (3.2) one can attempt to calculate the transition strengths associated with the magnetic dipole part of the optical transition. To do so one can diagonalise the ground and the excited state spin Hamiltonians and then check the overlap between the different eigenstates of each Hamiltonian. Formally

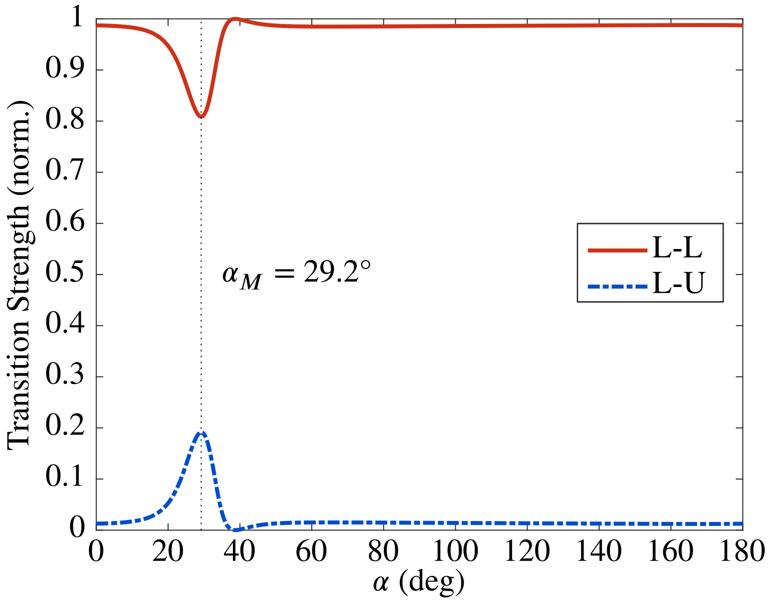

Figure 3.8: Normalised magnetic dipole contribution to the transition strength for like-to-like (L-L) and like-to-unlike (L-U) transitions as a function of magnetic field orientation in the $D_1 - D_2$ plane.

speaking, this shouldn't necessarily provide any good result, as the spin Hamiltonians for the ground and the excited states are completely disconnected from one another. However, the results obtained seem to agree relatively well with reality [71]. Knowing the transition strength is important, as it will determine the efficiency of the three wave mixing process that will allow us to convert microwaves into optical photons. What we want is to maximise the product of the like-to-like (e.g. bottom ground state to bottom excited state) times the like-to-unlike (e.g. bottom ground state to top excited state) transition strengths. It will be also desirable to work with a magnetic field in the $D_1 - D_2$ plane in order to break the magnetic inequivalence between subclasses I and II. Fig. 3.8 shows the normalised magnetic dipole contribution to the transition strength for like-to-like and like-to-unlike transitions under this condition. The optimal angle for the magnetic field α_M is found to be near 29.2°. Note that this is not necessarily the absolute best angle as the dependency of the electric dipole contribution to the transition strength is unknown. However, it gives a good indication of where this maximum may be.

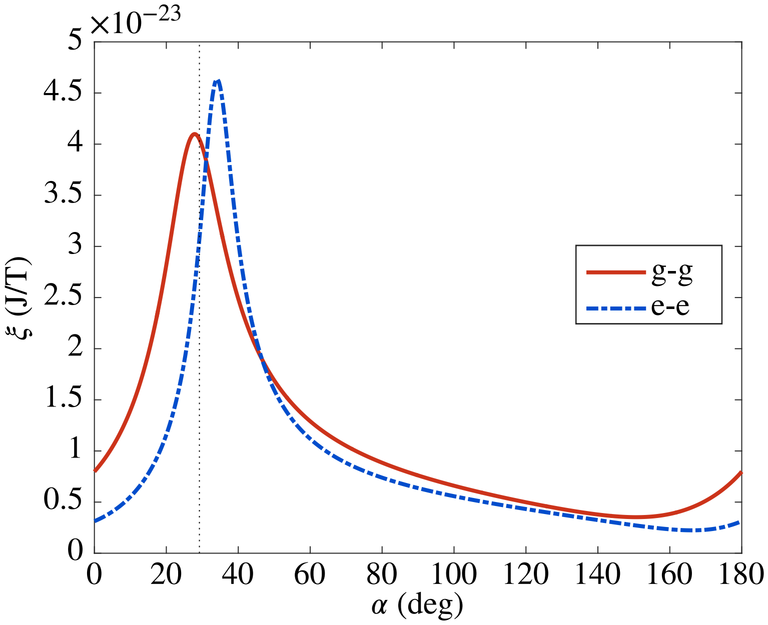

Figure 3.9: Magnetic transition dipole moment between the Zeeman split levels in the ground (g-g) and the excited (e-e) state as a function of the magnetic field orientation in the $D_1 - D_2$ plane.

In our experiments the microwaves will be applied as an AC magnetic field oscillating along the b axis of the crystal. The transition dipole moment ξ of the microwave transition in the ground and in the excited state can be calculated from the spin Hamiltonian (3.2). The conversion efficiency will be proportional to ξ as it will be seen in Ch. 4. A calculation of ξ for several angles of the externally applied magnetic field is presented in Fig. 3.9. It makes sense that the highest microwave transition dipole moments occur for similar angles as the highest optical transition strengths for like-to-unlike transitions, as both of these require some sort of mixing between bottom and top sublevels.

To summarise, the most relevant properties that make Er^{3+}:$\mathrm{Y_2SiO_5}$ suitable for microwave to optical quantum frequency conversion are its natural optical and microwave transition frequencies at zero and low magnetic fields, narrow linewidths and high transition dipole moments for said transitions, and narrow inhomogeneous optical linewidths at low temperatures. In Ch. 4 the effective nonlinearity between optical and microwave fields will be calculated from first principles, and the dependency of the effective nonlinear coefficient with the aforementioned quantities will be shown explicitly.

Chapter 4

Quantum Frequency Conversion in Er^{3+}:Y_2SiO_5: Theory

In this chapter I will talk about the theory behind the project of quantum frequency conversion between microwave and optical fields, based in the properties of Er^{3+}:Y_2SiO_5 discussed in Ch. 3. I will start with a short summary of the original theory that motivated the project, developed by Lewis Williamson, Yu-Hui Chen and Jevon Longdell, and published in 2014 [57]. Then I will move on to the derivation of the theory that I developed, which is meant to overcome some of the limitations of that presented in [57]. This derivation is based on using the nonlinear optics concept of effective nonlinearity of a medium, which can be calculated from the atomic properties of the sample as it will be shown. The advantage is that providing an effective value for the nonlinear coefficient makes it easier to compare our results with other approaches to the problem of converting microwave photons into optical ones.

My derivation consists of three main parts. First I will derive the nonlinear coefficient from first principles, using only the atomic properties of our atoms. Then I will write down the Hamiltonian that governs the dynamics of optical and microwave cavity modes in a nonlinear medium, and to finish I will use the input-output formalism to work out the dynamics of this system. At the end of this chapter I will talk about conversion efficiencies, making a comparison with the case of single pass optics, and finally I will discuss the feasibility of achieving unit efficiency.

4.1 Derivation from Cavity Quantum Electrodynamics

Our approach to quantum frequency conversion between microwaves and optical fields using Er^{3+}:Y_2SiO_5 crystals was first studied by Williamson et al. in Ref. [57], which I will briefly describe in this section. In that paper a collection of N three level atoms at zero temperature is considered. The simplification of working at zero temperature is a reasonable approximation when working with samples at millikelvin temperatures, because at these temperatures thermal radiation at microwave frequencies (a few gigahertz) is negligible, but this is not the case when working at temperatures near 4 K. This collection of three level atoms interacts with an optical cavity mode of frequency ω_a, a microwave cavity mode of frequency ω_b and a coherent driving field of frequency ω_Ω. The coupling strengths between the kth atom and the optical and microwave resonators are $g_{o,k}$ and $g_{\mu,k}$ respectively, and for that atom the coherent driving field has a Rabi frequency Ω_k. The fields are detuned from the atomic transitions but are kept in triple resonance with one another, so that the condition $\omega_a = \omega_b + \omega_\Omega$ is satisfied, as seen in Fig. (4.1). The optical and the microwave detunings for the kth atom are given by $\Delta_{o,k}$ and $\Delta_{\mu,k}$ respectively. Working off resonance means that one does not need to consider absorption of the input fields (microwaves in particular) by the atoms. Additionally, working off resonance greatly simplifies the problem at hand because one can adiabatically eliminate the second and third atomic levels.

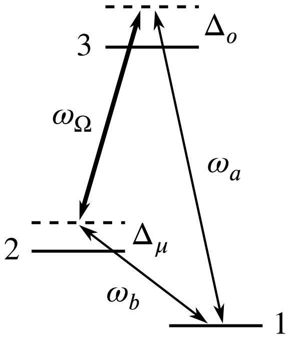

Figure 4.1: Energy level diagram of a single atom showing the different fields and detunings.

The Hamiltonian of such a system can be written in the rotating frame as:

$$H = \hbar \sum_k \left(\Delta_{o,k}\sigma_{33,k} + \Delta_{\mu,k}\sigma_{22,k}\right) + \hbar \sum_k \left(\Omega_k \sigma_{32,k} + h.c.\right) \tag{4.1}$$

$$+ \hbar \sum_k \left(g_{\mu,k}\sigma_{21,k} b + h.c.\right) + \hbar \sum_k \left(g_{o,k}\sigma_{31,k} a + h.c.\right), \tag{4.2}$$

where a and b are the annihilation operators for the optical and microwave fields respectively and $\sigma_{ij} \equiv |i\rangle\langle j|$.

When the detunings of the fields are large compared to the Rabi frequencies and the atom-cavity couplings ($|\Delta_{i,k}| >> |g_{i,k}|$ and $|\Delta_{\mu,k}\Delta_{o,k}| >> |\Omega_k|^2$) one can adiabatically eliminate the excited state of the atoms [72, 73], which yields the following Hamiltonian:

$$H = \hbar \sum_k \left(-\frac{\Delta_{\mu,k}|g_{o,k}|^2}{\Delta_{o,k}\Delta_{\mu,k} - |\Omega_k|^2} a^\dagger a - \frac{\Delta_{o,k}|g_{\mu,k}|^2}{\Delta_{o,k}\Delta_{\mu,k} - |\Omega_k|^2} b^\dagger b \right. \tag{4.3}$$

$$\left. + \frac{\Omega_k g_{\mu,k} g^*_{o,k}}{\Delta_{o,k}\Delta_{\mu,k} - |\Omega_k|^2} a^\dagger b + \frac{\Omega^*_k g^*_{\mu,k} g_{o,k}}{\Delta_{o,k}\Delta_{\mu,k} - |\Omega_k|^2} b^\dagger a \right). \tag{4.4}$$

The first two terms of the Hamiltonian in Eq. 4.3 describe the off-resonance interaction between the atoms and the cavities, which translates into a frequency shift of the cavities' frequencies (see Appendix A). We can ignore these terms as they can be easily compensated for by tuning the two resonance frequencies of the resonators. The third and fourth terms describe a linear interaction between the microwave and the optical modes. Taking into account the conditions set by the adiabatic elimination approximation we can rewrite Eq. 4.3 as

$$H = \hbar \sum_k \frac{g_{\mu,k} g_{o,k} \Omega_k}{\Delta_{\mu,k}\Delta_{o,k}} \left(a^\dagger b + b^\dagger a \right) \equiv \hbar S \left(a^\dagger b + b^\dagger a \right), \tag{4.5}$$

where the terms in the sum have been grouped into S on the right hand side.

To proceed from here one looks at the input-output formalism [74] in order to write an expression relating each of the output fields a_{out} and b_{out} with the input fields a_{in} and b_{in}. I will not show this derivation in detail here, but a similar procedure is done in Sec. 4.2.5. Once these expressions have been found the conversion efficiency η can be found by calculating $|a_{out}/b_{in}|^2$. This yields the following expression:

$$\eta(\omega) = \left| \frac{4iS\sqrt{\kappa_\mu \kappa_o}}{4|S|^2 + (\kappa_\mu - 2i\omega)(\kappa_o - 2i\omega)} \right|^2 \tag{4.6}$$

where κ_μ and κ_o are the microwave and optical cavity decay rates respectively. From the previous expression one can see that there is an impedance matching condition

$$4|S|^2 = \kappa_\mu \kappa_o \tag{4.7}$$

which, if satisfied, yields total conversion between microwave and optical fields on resonance ($\omega = 0$):

$$b_{out}(t) = a_{in}(t) \tag{4.8}$$

$$a_{out}(t) = b_{in}(t). \tag{4.9}$$

To get an intuitive understanding of what Eq. (4.7) means it is convenient to first assume that all the atoms have identical properties. This means, amongst other things, that phase matching and mode overlapping are ignored for the moment. Under these approximations Eq. (4.7) can be rewritten as

$$\sqrt{\frac{Ng_\mu^2}{\kappa_\mu \Delta_\mu}} \times \sqrt{\frac{Ng_o^2}{\kappa_o \Delta_o}} \times \frac{2\Omega}{\sqrt{\Delta_\mu \Delta_o}} = 1. \tag{4.10}$$

This new condition appears as the product of three terms being equal to one. Looking at the first term, the fact that the microwave cavity needs to be detuned from the microwave resonance implies that Δ_μ needs to be bigger than the inhomogeneous linewidth of the microwave transition (γ_μ). This means in turn that the first term in Eq. (4.10) is bounded above by the microwave cooperativity factor $\sqrt{Ng_\mu^2/\kappa_\mu \gamma_\mu}$. Using the same argument the second term in Eq. (4.10) will be bounded above by the optical cooperativity factor. The third term is bounded to be smaller than one due to the adiabatic elimination condition introduced earlier. If the product of the three needs to be equal to one this means that either the first or the second terms (or both) need to be greater than one, which means that in order to achieve efficient microwave-optical conversion it is necessary that one or both of the cavities operate in the strong coupling regime.

In a more realistic scenario one can incorporate the effects of phase matching and imperfect mode overlapping into a combined filling factor F, defined as

$$F \equiv \frac{1}{\sqrt{V_\mu V_o}} \left| \int_{V_c} \chi(\mathbf{r}) \psi(\mathbf{r}) \phi(\mathbf{r}) \mathrm{d}^3\mathbf{r} \right|, \tag{4.11}$$

where V_c is the crystal volume, V_μ and V_o are the mode volumes of the microwave and the optical cavities respectively, and $\chi(\mathbf{r})$, $\psi(\mathbf{r})$ and $\phi(\mathbf{r})$ are the mode functions for the microwave and two optical modes respectively. Additionally to F one can introduce a parameter α which takes into account the spectroscopic properties of the different ions in the crystal:

$$\alpha \equiv \sqrt{\frac{\mu_0}{\hbar^2 \epsilon_0}} d_{31} \mu_{21} \bar{N} \int_{\delta_{\mu,0}}^{\infty} \frac{D_\mu(\delta_\mu)}{\delta_\mu} \mathrm{d}\delta_\mu \int_{\delta_{o,0}}^{\infty} \frac{D_o(\delta_o)}{\delta_o} \mathrm{d}\delta_o, \tag{4.12}$$

where d_{31} and μ_{21} are the electric dipole moment and the magnetic dipole moment for the 1 to 3 and 2 to 1 transitions respectively, $\bar{N}$ is the number density of ions in the crystal, and $D_\mu(\delta_\mu)$ and $D_o(\delta_o)$ are the inhomogeneous broadening spectral distribution functions for the microwave and optical transitions respectively, which are assumed to be Gaussian. The lower limits in the integrals should be chosen far from the mean of the Gaussian distributions, but need to be chosen greater than zero to avoid breaking the adiabatic approximation at $\delta = 0$.

With these two newly defined quantities an impedance matching parameter can be written as

$$R \equiv \frac{2|S|}{\sqrt{\kappa_\mu \kappa_o}} = \Omega \alpha F \sqrt{Q_\mu Q_o}, \tag{4.13}$$

where Ω is the peak Rabi frequency of the driving field and Q_μ and Q_o are the quality factors of the microwave and optical resonators respectively. Note that R^2 is nothing else than the quotient between the left and the right hand sides of Eq. (4.7). Complete photon conversion is then possible for $R = 1$. The culminating point of Ref. [57] is showing that for a realistic set of parameters R can be made greater than one, and therefore total conversion between microwave and optical fields using erbium doped crystals is theoretically possible (if R can be made > 1 then going to $R = 1$ is only a matter of adjusting down the power of the driving field).

The results in reference [57] provide a very valuable starting point and are the motivator behind my PhD project, but the theory presented there has some limitations. For a start, it is assumed that all the atoms start in the ground state, which is the same as assuming that the crystal will be at zero temperature. While this may be a good approximation when working at millikelvin temperatures in a dilution fridge it is far from reality when working near 4 K in a liquid helium cryostat. Another limitation is the negligence of the second excited state of an erbium atom in a magnetic field (excluding the ^{167}Er) which will give some contribution in the conversion process. The third one is the requirement of being off-resonance with the atomic transitions and requiring low driving fields, albeit this is a much more circumventable factor experimentally. A further inconvenience of the theory presented in [57] is the fact that it is not straightforward to compare its results with other approaches towards microwave to optical conversion.

4.2 Derivation from Nonlinear Optics

To avoid some of the limitations of the theory presented in the previous section I developed an alternative theory that is based on calculating a nonlinear coefficient that mixes two optical and a microwave fields in a medium, in this case, a crystal doped with erbium. The size of this nonlinear coefficient will naturally depend on the spectroscopic properties of the erbium ions. Once this is obtained the next step is to work out the interaction of three fields in a nonlinear medium inside a resonator. I split the derivation in three parts: 1. calculate the nonlinear coefficient of the medium, 2. write down the Hamiltonian governing the dynamics of the fields inside a resonator and 3. calculate the dynamical properties that spring out from said Hamiltonian and work out the relation between input and output fields. Recipes can be found in the literature to perform each of these steps [75, 76, 74], but some thought is required to adapt them to our particular case.

4.2.1 Nonlinear Optics at a Glance

Nonlinear optics is the part of optics that deals with the behaviour of light in nonlinear media, where the total dielectric polarization of the medium **P** responds nonlinearly to the electric field **E** inside the medium. The relationship between **P** and **E** is often parametrised as

$$\mathbf{P}(t) = \epsilon_0 \chi^{(1)} \mathbf{E}(t) + \epsilon_0 \chi^{(2)} \mathbf{E}^2(t) + \epsilon_0 \chi^{(3)} \mathbf{E}^3(t) + \ldots, \tag{4.14}$$

where ϵ_0 is the dielectric permittivity of vacuum and the coefficients $\chi^{(n)}$ are the nth order susceptibilities of the medium. In many situations all of these coefficients are negligible except for $\chi^{(1)}$, and linear optics apply, but in other cases the higher order terms need to be taken into account, giving rise to very interesting physical phenomena like frequency mixing between different electromagnetic fields. The particular process we are interested in is frequency up-conversion, where an input field at frequency ω_1 interacts with a second field at frequency ω_2 (often referred to as the pump) to be converted into an output field at frequency $\omega_3 = \omega_2 \pm \omega_1$, where $\omega_3 > \omega_1$. This process can be performed in media where $\chi^{(2)} \neq 0$, and it can happen in two different ways: sum frequency generation (SFG, where $\omega_3 = \omega_2 + \omega_1$) and difference frequency generation (DFG, where $\omega_3 = \omega_2 - \omega_1$). Figure (4.2) shows these two processes schematically. In the case of SFG two input photons at frequencies ω_1 and ω_2 are absorbed by the medium and a photon at frequency $\omega_3 = \omega_2 + \omega_1$ is emitted. In the case of DFG there are

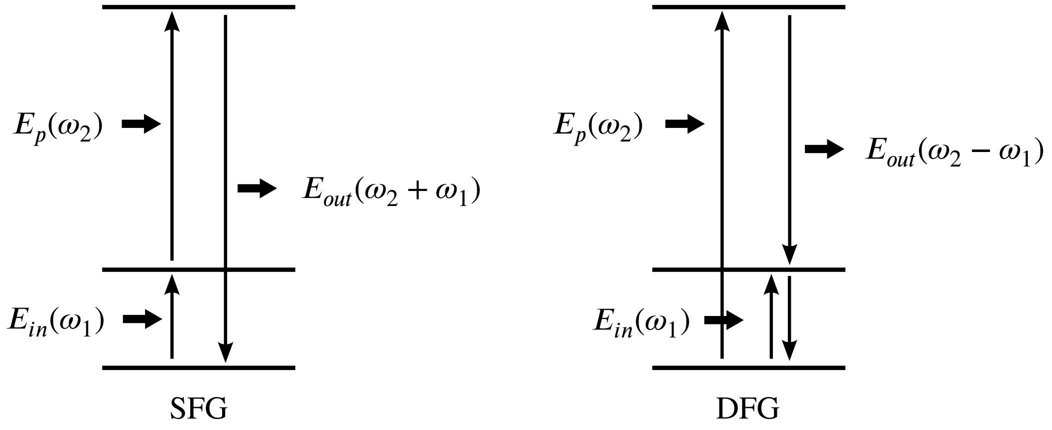

Figure 4.2: Frequency up-conversion via sum frequency generation (SFG) and difference frequency generation (DFG) in a nonlinear medium.

also two input photons at frequencies ω_1 and ω_2, but in this case the presence of the photon at ω_1 stimulates the photon at ω_2 to split into two photons, one at frequency $\omega_3 = \omega_2 - \omega_1$ and another one at frequency ω_1. In either case the ratio between the converted field $\mathrm{E}_{out}(\omega_2 \pm \omega_1)$ and the input field $\mathrm{E}_{in(\omega_1)}$ is proportional to $\chi^{(2)}$, so the power ratio between these fields is proportional to $|\chi^{(2)}|^2$.

4.2.2 Energy Levels and Other Parameters

In this section I will present the energy level structure of our system of interest, and I will describe some of the relevant parameters involved in the calculations later on. In our experiments we will have an Er^{3+}:$\mathrm{Y_2SiO_5}$ crystal inside a magnetic field. We will only be interested in the even isotopes of erbium. Their relevant energy level structure is presented in Fig. 4.3, showing the Zeeman split $^4I_{15/2}$ and $^4I_{13/2}$ energy levels. For a magnetic field aligned in the D_1-D_2 plane of the crystal with an angle $\alpha \simeq \alpha_M$ (see Fig. 3.8) a splitting of ~5 GHz in the ground state can be achieved for a magnetic field strength of around 0.15 T. The four transitions between ground and excited states are around 1536 nm.

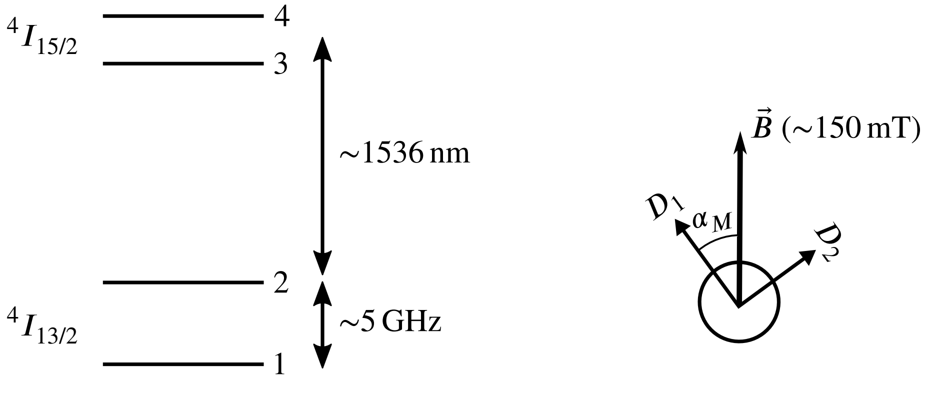

Figure 4.3: Energy level structure for the even isotopes of Er^{3+}:$\mathrm{Y_2SiO_5}$ under the effect of an external magnetic field aligned in the D_1-D_2 plane with an angle α_M as per Fig. 3.8. A microwave transition between levels 1 and 2 of 5 GHz can be obtained for a magnetic field strength of ~0.15 T.

The particular values for the different parameters involved in the later calculations are chosen to match the experimental conditions of the experiments presented in Chs. 8 and 9 unless otherwise specified. These values are presented in Tab. 4.1. The optical and microwave inhomogeneous broadenings have been measured in the experiments presented in Ch. 8. The decoherence rate for the optical transitions was measured in Ref. [77]. The decoherence rate for the microwave transition is taken to be limited by the inhomogeneous broadening linewidth. The electric dipole moment for the optical transitions has been obtained from the optical absorption measurements presented in Ch. 8. Finally, the magnetic transition dipole moments for the microwave transitions have been calculated from diagonalising the spin Hamiltonians of the ground and the excited states of Er^{3+}:Y_2SiO_5, as explained in Ch. 3.

Symbol	Name	Magnitude	Units
$\delta_{inh,o}$	optical inhomogeneous broadening	0.4	GHz
$\delta_{inh,m}$	microwave inhomogeneous broadening	35	MHz
$\gamma_{41}, \gamma_{42}, \gamma_{31}, \gamma_{31}$	decoherence rate	0.1	MHz/2π
γ_{21}	”	35	MHz/2π
μ_{31}, μ_{42}	electric transition dipole moment	2.6×10^{-32}	C·m
μ_{41}, μ_{32}	C·m	1.7×10^{-32}	”
ξ_{21}	magnetic transition dipole moment	$4.3\mu_B$	-
ξ_{43}	”	$1.2\mu_B$	-

Table 4.1: Values of the Er^{3+}:Y_2SiO_5 parameters used in the calculations of $\Lambda^{(2)}$, chosen to match the experimental conditions of the experiments in Chs. 8 and 9 (sample temperature ~4 K, magnetic field ~150 mT). The magnetic transition dipole moments are given in terms of the Bohr magneton.

4.2.3 Effective Nonlinearity

In the usual nonlinear optics case where three electric fields are mixed the different components of the polarisation of the medium can be expressed in terms of the nonlinear tensor $\chi^{(2)}_{ijk}$ as

$$P_i = \epsilon_0 \sum_{jk} \chi^{(2)}_{ijk} E_j E_k, \tag{4.15}$$

where i, j and k are spatial coordinate indices. In our case we have two electric fields and a magnetic field mixing with each other, so I will define a magneto-electric nonlinear coefficient $\Lambda^{(2)}$ and write the polarisation vector as

$$P_i = \epsilon_0 \sum_{jk} \Lambda^{(2)}_{ijk} B_j E_k. \tag{4.16}$$

While $\chi^{(2)}$ is usually expressed in units of m/V the corresponding units for $\Lambda^{(2)}$ are 1/T. In order to compare the magnitude of a given $\Lambda^{(2)}$ with a given $\chi^{(2)}$ one needs to divide $\Lambda^{(2)}$ by the speed of light, because of the relationship between the electric and magnetic fields in an electromagnetic wave $E = cB$.

Before starting the derivation of $\Lambda^{(2)}$ a very important point needs to be made. When using $\chi^{(2)}$ or $\Lambda^{(2)}$ to calculate the polarisation of the medium in a second order frequency conversion process we are effectively taking Eq. 4.14 and neglecting all the higher order terms. In many cases this is a good approximation, because the higher order nonlinear coefficients ($\chi^{(3)}$, $\chi^{(4)}$, etc.) are much smaller than the second order term in most situations. However, this approximation starts to break down when the applied fields shift the atomic population between the different energy levels. In our case this is going to happen when the fields are set on resonance with the atomic transitions, and because the inhomogeneous line of Er^{3+}:Y_2SiO_5 is so narrow this will happen even for very low powers. What this means is that the theory developed here will only give accurate results when the involved fields are off resonance with the atomic transitions, and their associated Rabi frequencies are low compared to the relevant detunings. Note that this is the same condition imposed in Ref. [57] that allowed to adiabatically eliminate the higher energy levels (see Sec. 4.1).

A derivation of the usual second order nonlinear coefficient $\chi^{(2)}$ from first principles can be found in [75]. I will follow that derivation closely, making the required changes where appropriate. I will start with a Hamiltonian describing an atom interacting with an electromagnetic field. I will use that to write down the equations of motion for the density matrix operator, and calculate the atomic dipole moment, which I will relate with the components of the nonlinear polarization oscillating at the frequency of interest. From that relationship I will finally extract a value for $\Lambda^{(2)}$. A fair amount of detail will be given in this derivation.

The Hamiltonian for an atom sitting in an electromagnetic field in the semiclassical approximation can be written as

$$H = H_0 + V, \tag{4.17}$$

where H_0 represents the Hamiltonian of the free atom and V accounts for the interaction energy of the atom with the external field. This interaction is considered to be a perturbative term of the total Hamiltonian, in the sense that the matrix elements of V are much smaller than those of H_0.

In our case, the microwave transition is a magnetic dipole transition and it will be taken as such. One of the characteristics of the microwave resonators that we use is that the electric and the magnetic fields inside them are spatially separated. Because the microwave transition is a magnetic dipole transition we have designed our resonators so that the sample sits inside the region filled by the magnetic field. The optical transitions, in contrast, are a mixture between electric dipole and magnetic dipole. For the case of optical light this distinction is less important, as optical resonators are not able to spatially separate the electric field from the magnetic field. For this reason I will consider the optical transitions as if they were electric dipole only, even though this is not technically correct. Doing this has some implications. One of them is the simplification of most of the expressions in the remainder of the chapter, as we only need to consider one field for the optical frequencies instead of two, and this is part of the reason why I want to make this simplification. Another implication is that we would have to be very careful when taking values from the published literature for the optical transition's electric dipole moment, as they may give wrong results in the formalism I'm using. To avoid this we will measure the optical transition electric dipole moments ourselves, in the understanding that when performing these measurements the transition will also be treated as an electric dipole transition only. What this means is that the values for the transition electric dipole moments that we will measure will not be the "real" values from the most rigorous point of view. However they will still give the right results when calculating $\Lambda^{(2)}$ as long as the criteria about the transition type we are dealing with doesn't change between measurements and calculations. A value for the optical transitions electric dipole moment can be obtained from optical absorption measurements as it will be explained in Ch. 8. With this clarification made we can write the interaction part of the Hamiltonian as

$$V = -\vec{\mu} \cdot \tilde{\vec{E}} - \vec{\xi} \cdot \tilde{\vec{B}}, \tag{4.18}$$

where $\tilde{\vec{E}}$ and $\tilde{\vec{B}}$ are the external electric and magnetic fields[1], and $\vec{\mu}$ and $\vec{\xi}$ are the electric and magnetic dipole moment operators of the atom.

Next we write the equation of motion for the density matrix ρ_{nm} of our system as

$$\dot{\rho}_{nm} = -\frac{i}{\hbar}\left[H, \rho\right]_{nm} - \gamma_{nm}\left(\rho_{nm} - \rho_{nm}^{(eq)}\right), \tag{4.19}$$

where the second therm is a phenomenologically added damping term. What this term tells us is that, in the absence of any applied field, each component of the density matrix relaxes to its equilibrium state $\rho_{nm}^{(eq)}$ at a rate given by γ_{nm}. We will assume that for a system in thermal equilibrium the different energy levels may contain some population. However, no coherent superposition between the energy eigenstates will exist, as thermal relaxation and/or excitation is an incoherent process. In this case

$$\rho_{nm}^{(eq)} = 0 \quad \text{for} \quad n \neq m. \tag{4.20}$$

The commutator in Eq. (4.19) will split into two terms according to Eq. (4.17). By taking E_n as the eigenenergies of the unperturbed Hamiltonian we can write

$$\left[H_0, \rho\right]_{nm} = \left(E_n - E_m\right)\rho_{nm} \equiv \hbar\omega_{nm}\rho_{nm}, \tag{4.21}$$

where ω_{nm} is the frequency of the transition going from state m to state n, in angular frequency units.

---

[1] Here the "~" on top of $\vec{E}$ and $\vec{B}$ is used to denote that the fields have not been specifically decomposed into their different frequency components.

We are going to seek a perturbative solution of Eq. (4.19). To do so we replace V for λV, where λ is a parameter ranging between 0 and 1. Then we look for a solution of the form

$$\rho_{nm} = \rho_{nm}^{(0)} + \lambda \rho_{nm}^{(1)} + \lambda^2 \rho_{nm}^{(2)} + \cdots . \tag{4.22}$$

If Eq. (4.22) is to be a solution of Eq. (4.19) for any value of λ, then the coefficients of each power of λ must satisfy Eq. (4.19) separately, so we get the set of equations

$$\dot{\rho}_{nm}^{(0)} = -i\omega_{nm}\rho_{nm}^{(0)} - \gamma_{nm}\left(\rho_{nm}^{(0)} - \rho_{nm}^{(eq)}\right), \tag{4.23}$$

$$\dot{\rho}_{nm}^{(1)} = -i\left(\omega_{nm} + \gamma_{nm}\right)\rho_{nm}^{(1)} - \frac{i}{\hbar}\left[V, \rho^{(0)}\right]_{nm}, \tag{4.24}$$

$$\dot{\rho}_{nm}^{(2)} = -i\left(\omega_{nm} + \gamma_{nm}\right)\rho_{nm}^{(2)} - \frac{i}{\hbar}\left[V, \rho^{(1)}\right]_{nm}, \tag{4.25}$$

$$\cdots$$

This set of equations can be solved iteratively. The solution for the zero-th order equation in the steady state is already known to be

$$\rho_{nm}^{(0)} = \rho_{nm}^{(eq)} . \tag{4.26}$$

The solutions for the N-th order term can be shown to be

$$\rho_{nm}^{(N)} = -\frac{i}{\hbar}\int_{-\infty}^{t}\left[V(t'), \rho^{(N-1)}\right]_{nm} e^{(i\omega_{nm}+\gamma_{nm})(t'-t)}\,\mathrm{d}t'. \tag{4.27}$$

In order to calculate $\Lambda^{(2)}$ we are going to need to solve the equation for $\rho_{nm}^{(2)}$, for which we will need $\rho_{nm}^{(1)}$, which we can get from Eqs. (4.27), (4.26) and (4.18). Noting that the commutator

$$\left[V, \rho^{(0)}\right]_{nm} = -\left(\rho_{mm}^{(0)} - \rho_{nn}^{(0)}\right)\left[\vec{\mu}_{nm}\cdot\vec{\tilde{E}} + \vec{\xi}_{nm}\cdot\vec{\tilde{B}}\right] \tag{4.28}$$

we can then write

$$\begin{aligned}\rho_{nm}^{(1)}(t) = {} & \frac{i}{\hbar}\left(\rho_{mm}^{(0)} - \rho_{nn}^{(0)}\right)e^{-(i\omega_{nm}+\gamma_{nm})t}\vec{\mu}_{nm}\cdot\int_{-\infty}^{t}\vec{\tilde{E}}e^{(i\omega_{nm}+\gamma_{nm})t'}\,\mathrm{d}t' \\ & + \frac{i}{\hbar}\left(\rho_{mm}^{(0)} - \rho_{nn}^{(0)}\right)e^{-(i\omega_{nm}+\gamma_{nm})t}\vec{\xi}_{nm}\cdot\int_{-\infty}^{t}\vec{\tilde{B}}e^{(i\omega_{nm}+\gamma_{nm})t'}\,\mathrm{d}t'.\end{aligned} \tag{4.29}$$

At this point we wish to split the electric and the magnetic fields into frequency components:

$$\tilde{\vec{E}}(t) = \sum_p \vec{E}(\omega_p) e^{-i\omega_p t}, \tag{4.30}$$

$$\tilde{\vec{B}}(t) = \sum_p \vec{B}(\omega_p) e^{-i\omega_p t}. \tag{4.31}$$

Introducing these expressions into (4.29) and calculating the integrals we get

$$\rho^{(1)}_{nm}(t) = \frac{1}{\hbar}\left(\rho^{(0)}_{mm} - \rho^{(0)}_{nn}\right) \sum_p \frac{\left(\vec{\mu}_{nm}\cdot\vec{E}(\omega_p) + \vec{\xi}_{nm}\cdot\vec{B}(\omega_p)\right) e^{-i\omega_p t}}{(\omega_{nm} - \omega_p) - i\gamma_{nm}}. \tag{4.32}$$

We can calculate $\rho^{(2)}_{nm}(t)$ in a similar way, first noting that the commutator

$$\begin{aligned}
\left[V, \rho^{(1)}\right]_{nm} = &-\frac{1}{\hbar}\sum_\nu \left(\rho^{(0)}_{mm} - \rho^{(0)}_{\nu\nu}\right) e^{-i(\omega_p+\omega_q)t} \\
&\times \sum_{pq} \frac{\left[\vec{\mu}_{n\nu}\cdot\vec{E}(\omega_q) + \vec{\xi}_{n\nu}\cdot\vec{B}(\omega_q)\right]\left[\vec{\mu}_{\nu m}\cdot\vec{E}(\omega_p) + \vec{\xi}_{\nu m}\cdot\vec{B}(\omega_p)\right]}{(\omega_{\nu m} - \omega_p) - i\gamma_{\nu m}} \\
&+\frac{1}{\hbar}\sum_\nu \left(\rho^{(0)}_{\nu\nu} - \rho^{(0)}_{nn}\right) e^{-i(\omega_p+\omega_q)t} \\
&\times \sum_{pq} \frac{\left[\vec{\mu}_{n\nu}\cdot\vec{E}(\omega_p) + \vec{\xi}_{n\nu}\cdot\vec{B}(\omega_p)\right]\left[\vec{\mu}_{\nu m}\cdot\vec{E}(\omega_q) + \vec{\xi}_{\nu m}\cdot\vec{B}(\omega_q)\right]}{(\omega_{n\nu} - \omega_p) - i\gamma_{n\nu}}.
\end{aligned} \tag{4.33}$$

Introducing this into Eq. (4.27) yields

$$\begin{aligned}
\rho^{(2)}_{nm}(t) = &\sum_\nu \sum_{pq} e^{-i(\omega_p+\omega_q)t} \\
&\times \left\{ \frac{\rho^{(0)}_{mm} - \rho^{(0)}_{\nu\nu}}{\hbar^2} \frac{\left[\vec{\mu}_{n\nu}\cdot\vec{E}(\omega_q) + \vec{\xi}_{n\nu}\cdot\vec{B}(\omega_q)\right]\left[\vec{\mu}_{\nu m}\cdot\vec{E}(\omega_p) + \vec{\xi}_{\nu m}\cdot\vec{B}(\omega_p)\right]}{\left[(\omega_{nm} - \omega_p - \omega_q) - i\gamma_{nm}\right]\left[(\omega_{\nu m} - \omega_p) - i\gamma_{\nu m}\right]} \right. \\
&\left. + \frac{\rho^{(0)}_{\nu\nu} - \rho^{(0)}_{nn}}{\hbar^2} \frac{\left[\vec{\mu}_{n\nu}\cdot\vec{E}(\omega_p) + \vec{\xi}_{n\nu}\cdot\vec{B}(\omega_p)\right]\left[\vec{\mu}_{\nu m}\cdot\vec{E}(\omega_q) + \vec{\xi}_{\nu m}\cdot\vec{B}(\omega_q)\right]}{\left[(\omega_{nm} - \omega_p - \omega_q) - i\gamma_{nm}\right]\left[(\omega_{n\nu} - \omega_p) - i\gamma_{n\nu}\right]} \right\} \\
\equiv &\sum_\nu \sum_{pq} K_{nm\nu} e^{-i(\omega_p+\omega_q)t},
\end{aligned} \tag{4.34}$$

where the term K_{nmv} has been defined for later convenience.

According to the density matrix formulation of quantum mechanics the expectation value of the atomic electric dipole moment of a single atom will be given by

$$\langle \tilde{\vec{\mu}}(t) \rangle = \sum_{nm} \rho_{nm}(t) \vec{\mu}_{mn}, \tag{4.35}$$

where $\vec{\mu}_{mn} = -e \langle n | \, \mathbf{r} \, | m \rangle$, $-e$ being the electron charge and $\mathbf{r}$ being the position operator for the electron. We can separate $\langle \tilde{\vec{\mu}} \rangle$ into its different frequency components as

$$\langle \tilde{\vec{\mu}}(t) \rangle = \sum_{r} \langle \vec{\mu}(\omega_r) \rangle \, e^{-i\omega_r t}. \tag{4.36}$$

Inserting (4.34) into (4.35) we see that

$$\langle \tilde{\vec{\mu}}(t) \rangle = \sum_{nmv} \sum_{pq} K_{nmv} \vec{\mu}_{mn} e^{-i(\omega_p + \omega_q)t} \tag{4.37}$$

Then, by comparing with (4.36), the complex amplitude of the component of $\langle \tilde{\vec{\mu}}(t) \rangle$ oscillating at a frequency $\omega_p + \omega_q$ will be given by

$$\left\langle \vec{\mu}(\omega_p + \omega_q) \right\rangle = \sum_{nmv} \sum_{(pq)} K_{nmv} \vec{\mu}_{mn}, \tag{4.38}$$

where the parenthesis (pq) below the second summation implies that the sum is performed over all frequencies ω_p and ω_q while keeping the sum $\omega_p + \omega_q$ constant. Then, the amplitude of the total nonlinear polarization oscillating at a frequency $\omega_p + \omega_q$ is given by

$$\vec{P}^{(2)}(\omega_p + \omega_q) = \bar{N} \left\langle \vec{\mu}(\omega_p + \omega_q) \right\rangle = \bar{N} \sum_{nmv} \sum_{(pq)} K_{nmv} \vec{\mu}_{mn}, \tag{4.39}$$

where $\bar{N}$ is the atomic density of atoms in units of $1/volume$. At this point we introduce the second order nonlinear magneto-electric susceptibility $\Lambda^{(2)}$ through the equation

$$P_i^{(2)}(\omega_p + \omega_q) = \epsilon_0 \sum_{jk} \sum_{(pq)} \Lambda_{ijk}^{(2)}(\omega_p + \omega_q, \omega_q, \omega_p) B_j(\omega_q) E_k(\omega_p). \tag{4.40}$$

Note that in writing $\Lambda_{ijk}^{(2)} = \Lambda_{ijk}^{(2)}(\omega_p + \omega_q, \omega_q, \omega_p)$ the first variable $(\omega_p + \omega_q)$ is redundant with the second and the third ones (ω_q, ω_p). This has been written in this way to make it explicit that $\Lambda^{(2)}$ is the nonlinear coefficient for a process that involves three frequencies, one of which is the sum of the other two. Inserting the expression for K_{nmv} in Eq. (4.39) we get

$$
\begin{aligned}
P_i^{(2)}(\omega_p+\omega_q) = {} & \frac{\bar{N}}{\hbar^2}\sum_{nmv}\sum_{(pq)}\mu^i_{mn} \\
& \times\Bigg\{\left(\rho^{(0)}_{mm}-\rho^{(0)}_{vv}\right)\frac{\left[\vec{\mu}_{nv}\cdot\vec{E}(\omega_q)+\vec{\xi}_{nv}\cdot\vec{B}(\omega_q)\right]\left[\vec{\mu}_{vm}\cdot\vec{E}(\omega_p)+\vec{\xi}_{vm}\cdot\vec{B}(\omega_p)\right]}{\left[(\omega_{nm}-\omega_p-\omega_q)-i\gamma_{nm}\right]\left[(\omega_{vm}-\omega_p)-i\gamma_{vm}\right]} \\
& -\left(\rho^{(0)}_{vv}-\rho^{(0)}_{nn}\right)\frac{\left[\vec{\mu}_{nv}\cdot\vec{E}(\omega_p)+\vec{\xi}_{nv}\cdot\vec{B}(\omega_p)\right]\left[\vec{\mu}_{vm}\cdot\vec{E}(\omega_q)+\vec{\xi}_{vm}\cdot\vec{B}(\omega_q)\right]}{\left[(\omega_{nm}-\omega_p-\omega_q)-i\gamma_{nm}\right]\left[(\omega_{nv}-\omega_p)-i\gamma_{nv}\right]}\Bigg\}.
\end{aligned}
\tag{4.41}
$$

Now we will substitute the scalar products of dipole moments and fields, in order of appearance, by $\sum_j \mu^j_{nv}E_j(\omega_q)$, $\sum_j \xi^j_{nv}B_j(\omega_q)$, $\sum_k \mu^k_{vm}E_k(\omega_p)$ and $\sum_k \xi^k_{vm}B_k(\omega_p)$ in the first term, and $\sum_k \mu^k_{nv}E_k(\omega_p)$, $\sum_k \xi^k_{nv}B_k(\omega_p)$, $\sum_j \mu^j_{vm}E_j(\omega_q)$ and $\sum_j \xi^j_{vm}B_j(\omega_q)$ in the second term. Here we are merely writing the scalar products of the different vectors as the sum of the products of their components. In doing so, then, i, j and k are spatial indices in Cartesian coordinates. In addition to this decomposition we will neglect the crossed terms containing $\vec{E}(\omega_q)\cdot\vec{E}(\omega_p)$ and $\vec{B}(\omega_q)\cdot\vec{B}(\omega_p)$, as they refer to processes in which we are not interested. We can then rewrite the previous equation as

$$
\begin{aligned}
P_i^{(2)}(\omega_p+\omega_q) = {} & \frac{\bar{N}}{\hbar^2}\sum_{nmv}\sum_{(pq)}\sum_{jk}B_j(\omega_q)E_k(\omega_p) \\
& \Bigg\{\left(\rho^{(0)}_{mm}-\rho^{(0)}_{vv}\right)\frac{\mu^i_{mn}\xi^j_{nv}\mu^k_{vm}}{\left[(\omega_{nm}-\omega_p-\omega_q)-i\gamma_{nm}\right]\left[(\omega_{vm}-\omega_p)-i\gamma_{vm}\right]} \\
& -\left(\rho^{(0)}_{vv}-\rho^{(0)}_{nn}\right)\frac{\mu^i_{mn}\xi^j_{nm}\mu^k_{nv}}{\left[(\omega_{nm}-\omega_p-\omega_q)-i\gamma_{nm}\right]\left[(\omega_{nv}-\omega_p)-i\gamma_{nv}\right]}\Bigg\}. \\
& +\frac{\bar{N}}{\hbar^2}\sum_{nmv}\sum_{(pq)}\sum_{jk}E_j(\omega_q)B_k(\omega_p) \\
& \Bigg\{\left(\rho^{(0)}_{mm}-\rho^{(0)}_{vv}\right)\frac{\mu^i_{mn}\mu^j_{nv}\xi^k_{vm}}{\left[(\omega_{nm}-\omega_p-\omega_q)-i\gamma_{nm}\right]\left[(\omega_{vm}-\omega_p)-i\gamma_{vm}\right]} \\
& -\left(\rho^{(0)}_{vv}-\rho^{(0)}_{nn}\right)\frac{\mu^i_{mn}\mu^j_{nm}\xi^k_{nv}}{\left[(\omega_{nm}-\omega_p-\omega_q)-i\gamma_{nm}\right]\left[(\omega_{nv}-\omega_p)-i\gamma_{nv}\right]}\Bigg\}
\end{aligned}
\tag{4.42}
$$

Because p, q, j and k are dummy indices within each set of summatories we can replace them at will. A particularly useful substitution is to exchange p with q and j with k in the second summatory set. Doing so we find

$$
\begin{aligned}
P_i^{(2)}(\omega_p+\omega_q) = \frac{\bar{N}}{\hbar^2} \sum_{nm\nu} \sum_{(pq)} \sum_{jk} & B_j(\omega_q) E_k(\omega_p) \\
\times \Bigg\{ \left(\rho_{mm}^{(0)} - \rho_{\nu\nu}^{(0)}\right) & \Bigg[\frac{\mu_{mn}^i \xi_{n\nu}^j \mu_{\nu m}^k}{\left[(\omega_{nm}-\omega_p-\omega_q)-i\gamma_{nm}\right]\left[(\omega_{\nu m}-\omega_p)-i\gamma_{\nu m}\right]} \\
& + \frac{\mu_{mn}^i \xi_{\nu m}^j \mu_{n\nu}^k}{\left[(\omega_{nm}-\omega_p-\omega_q)-i\gamma_{nm}\right]\left[(\omega_{\nu m}-\omega_q)-i\gamma_{\nu m}\right]} \Bigg] \\
- \left(\rho_{\nu\nu}^{(0)} - \rho_{nn}^{(0)}\right) & \Bigg[\frac{\mu_{mn}^i \xi_{\nu m}^j \mu_{n\nu}^k}{\left[(\omega_{nm}-\omega_p-\omega_q)-i\gamma_{nm}\right]\left[(\omega_{n\nu}-\omega_p)-i\gamma_{n\nu}\right]} \\
& + \frac{\mu_{mn}^i \xi_{n\nu}^j \mu_{\nu m}^k}{\left[(\omega_{nm}-\omega_p-\omega_q)-i\gamma_{nm}\right]\left[(\omega_{n\nu}-\omega_q)-i\gamma_{n\nu}\right]} \Bigg] \Bigg\} .
\end{aligned}
\tag{4.43}
$$

Finally, comparing Eq. (4.43) with Eq. (4.40) we see that

$$
\begin{aligned}
\Lambda_{ijk}^{(2)}(\omega_p+\omega_q, \omega_q, \omega_p) = \frac{\bar{N}}{\epsilon_0 \hbar^2} \sum_{nm\nu} & \\
\Bigg\{ \left(\rho_{mm}^{(0)} - \rho_{\nu\nu}^{(0)}\right) & \Bigg[\frac{\mu_{mn}^i \xi_{n\nu}^j \mu_{\nu m}^k}{\left[(\omega_{nm}-\omega_p-\omega_q)-i\gamma_{nm}\right]\left[(\omega_{\nu m}-\omega_p)-i\gamma_{\nu m}\right]} \\
& + \frac{\mu_{mn}^i \xi_{\nu m}^j \mu_{n\nu}^k}{\left[(\omega_{nm}-\omega_p-\omega_q)-i\gamma_{nm}\right]\left[(\omega_{\nu m}-\omega_q)-i\gamma_{\nu m}\right]} \Bigg] \\
- \left(\rho_{\nu\nu}^{(0)} - \rho_{nn}^{(0)}\right) & \Bigg[\frac{\mu_{mn}^i \xi_{\nu m}^j \mu_{n\nu}^k}{\left[(\omega_{nm}-\omega_p-\omega_q)-i\gamma_{nm}\right]\left[(\omega_{n\nu}-\omega_p)-i\gamma_{n\nu}\right]} \\
& + \frac{\mu_{mn}^i \xi_{n\nu}^j \mu_{\nu m}^k}{\left[(\omega_{nm}-\omega_p-\omega_q)-i\gamma_{nm}\right]\left[(\omega_{n\nu}-\omega_q)-i\gamma_{n\nu}\right]} \Bigg] \Bigg\} .
\end{aligned}
\tag{4.44}
$$

In order to get a better understanding of what Eq. (4.44) is telling us we will next examine the different terms in the summation over $nm\nu$. We look at the different denominators and consider only the resonant cases, for which the sums of frequencies in between parenthesis are equal to zero. Imposing the condition of resonance will then determine the subindices of the different ω_{ij} terms, based on the frequencies ω_p and ω_q. In some cases we will run into contradictory conclusions, e.g. m wants to be equal to one in the first parenthesis, but equal to two in the second one. To get an intuitive feeling let's consider now the simplified case in which we have two energy levels in the ground state but only one in the excited state. In this case we have a microwave transition from level 1 to level 2 and two optical transitions from level 2 to level 3 as well as from level 1 to level 3. We assign ω_q to the magnetic field and ω_p to the electric field as in Eq. (4.39). On resonance, $\omega_q = \omega_{21}$ and $\omega_p = \omega_{32}$, and only one set of subindices makes sense: $m = 1$, $n = 3$ and $\nu = 2$. Then, only two terms survive in the summation. One of them is proportional to

$$\propto -\left(\rho_{11}^{(0)} - \rho_{22}^{(0)}\right) \frac{\mu_{13}^{i} \xi_{21}^{j} \mu_{32}^{k}}{\gamma_{31}\gamma_{21}} \tag{4.45}$$

while the other one is proportional to

$$\propto \left(\rho_{22}^{(0)} - \rho_{33}^{(0)}\right) \frac{\mu_{13}^{i} \xi_{21}^{j} \mu_{32}^{k}}{\gamma_{31}\gamma_{32}}. \tag{4.46}$$

We can see that the effective nonlinearity is proportional to the population difference between the different energy levels, as we would expect. It is also proportional to the transition dipole moments of the different transitions, also as expected. It is important to notice, though, that the two surviving terms have opposite signs, which can be interpreted as a coherent destructive interference. For a certain value of the population differences $\Lambda^{(2)}$ will vanish. Namely, when

$$\frac{\rho_{11}^{(0)} - \rho_{22}^{(0)}}{\rho_{22}^{(0)} - \rho_{33}^{(0)}} = \frac{\gamma_{21}}{\gamma_{32}} \tag{4.47}$$

$\Lambda^{(2)}$ will be equal to zero. Note that, in thermal equilibrium, in order to have any meaningful population in the excited state we require temperatures of the order of 10^6 K. Because this is so, we can approximate $\rho_{33}^{(0)} \approx 0$. We can see in this case that if $\rho_{11}^{(0)} = \rho_{22}^{(0)}$ then $\Lambda^{(2)}$ vanishes. At 4 K, and for a 5 GHz microwave transition, $\rho_{22}^{(0)}/\rho_{11}^{(0)} \approx 0.95$. At room temperature this turns into $\rho_{22}^{(0)}/\rho_{11}^{(0)} \approx 0.992$, while at 10 mK $\rho_{22}^{(0)}/\rho_{11}^{(0)} \approx 3 \times 10^{-11}$. It is quite clear then that temperature will have a great effect in determining the value of $\Lambda^{(2)}$.

The result in Eq. (4.44) allows us to calculate the contribution to $\Lambda^{(2)}$ for a particular set of ions with a particular set of transition frequencies ω_{nm}. What we want to do next is to calculate the contribution of all the ions in the crystal by integrating over the optical and the microwave inhomogeneous lines. The plots in Fig. (4.4) show the absolute value and the complex angle θ of $\Lambda^{(2)}$ for a given set of parameters (see Tab. 4.1), and for an input laser and microwave frequencies tuned to the center of the inhomogeneous lines and at 4 K. For comparison, a plot

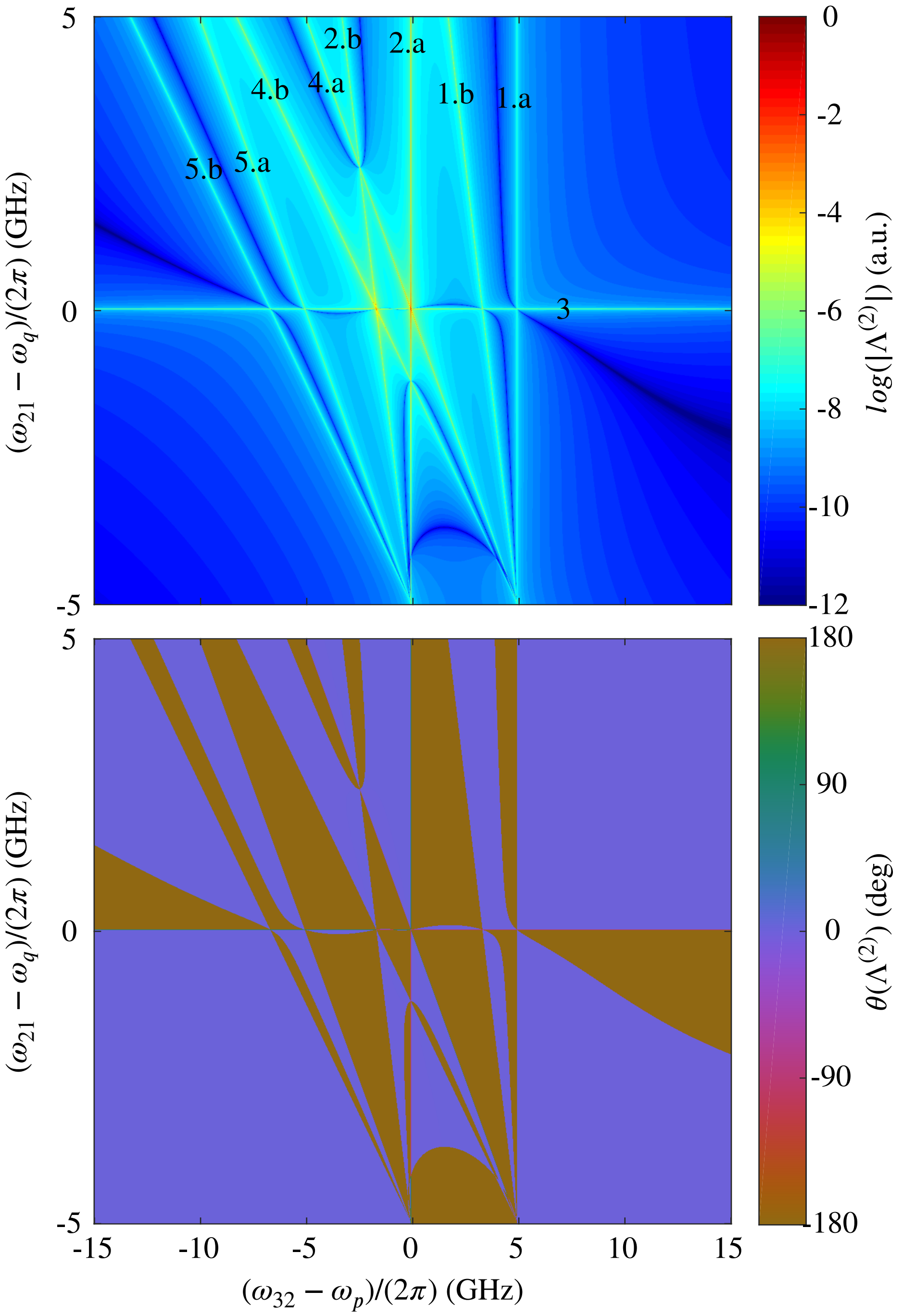

Figure 4.4: Contribution to the absolute value of $\Lambda^{(2)}$ and complex angle θ at 4 K for each ion as a function of its resonant frequencies ω_{32} and ω_{21} for an input optical (ω_p) and microwave (ω_q) frequencies on resonance with the center of the inhomogeneous lines, and for a given set of parameters as described in Tab. 4.1. The meaning of the different lines is explained in Fig. 4.5. The contribution from ions in the lowest and highest ground states is shown separately in Fig. 4.6.

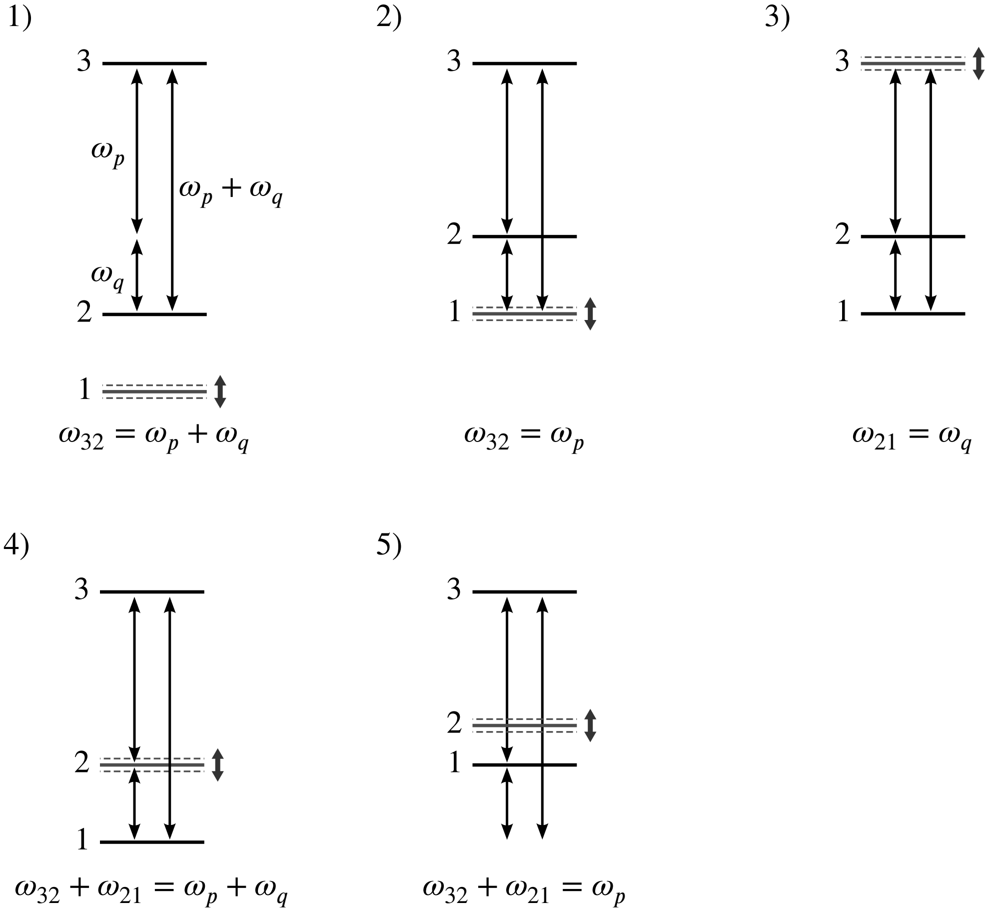

Figure 4.5: Atomic energy levels and input fields giving rise to the different lines in Fig. (4.4). Since in Er^{3+}:Y_2SiO_5 under the presence of a magnetic field there are two nondegenerate excited states, lines 1, 2, 4 and 5 are doubled. The lines labelled with "a" correspond to situations in which the lowest excited state is involved, while the lines labelled with "b" correspond to situations in which the highest excited state is involved.

with the contributions to $\Lambda^{(2)}$ coming from ions in the lower and in the upper ground states is shown in Fig. 4.6.

The remaining step in order to get the total value of $\Lambda^{(2)}$ is to integrate over a double Gaussian domain, as we are assuming that both the optical and the microwave inhomogeneous lines have a Gaussian profile. In any realistic case these Gaussians will be narrow compared with the limits of the vertical and horizontal axes in Fig. 4.4. The value chosen for the full width at half maximum (FWHM) of the optical inhomogeneous line is 0.4 GHz, and for the microwave inhomogeneous linewidth it is 35 MHz. Only a small fraction of what is shown in Fig. 4.4 needs to be integrated. It can be seen in Fig. 4.4 that $\Lambda^{(2)}$ is a very featured function. Each one of the bright lines (the lines where $\Lambda^{(2)}$ is large) correspond to a physical situation in which one of the three involved fields is on resonance with some atomic transition, as described in Fig. 4.5. The

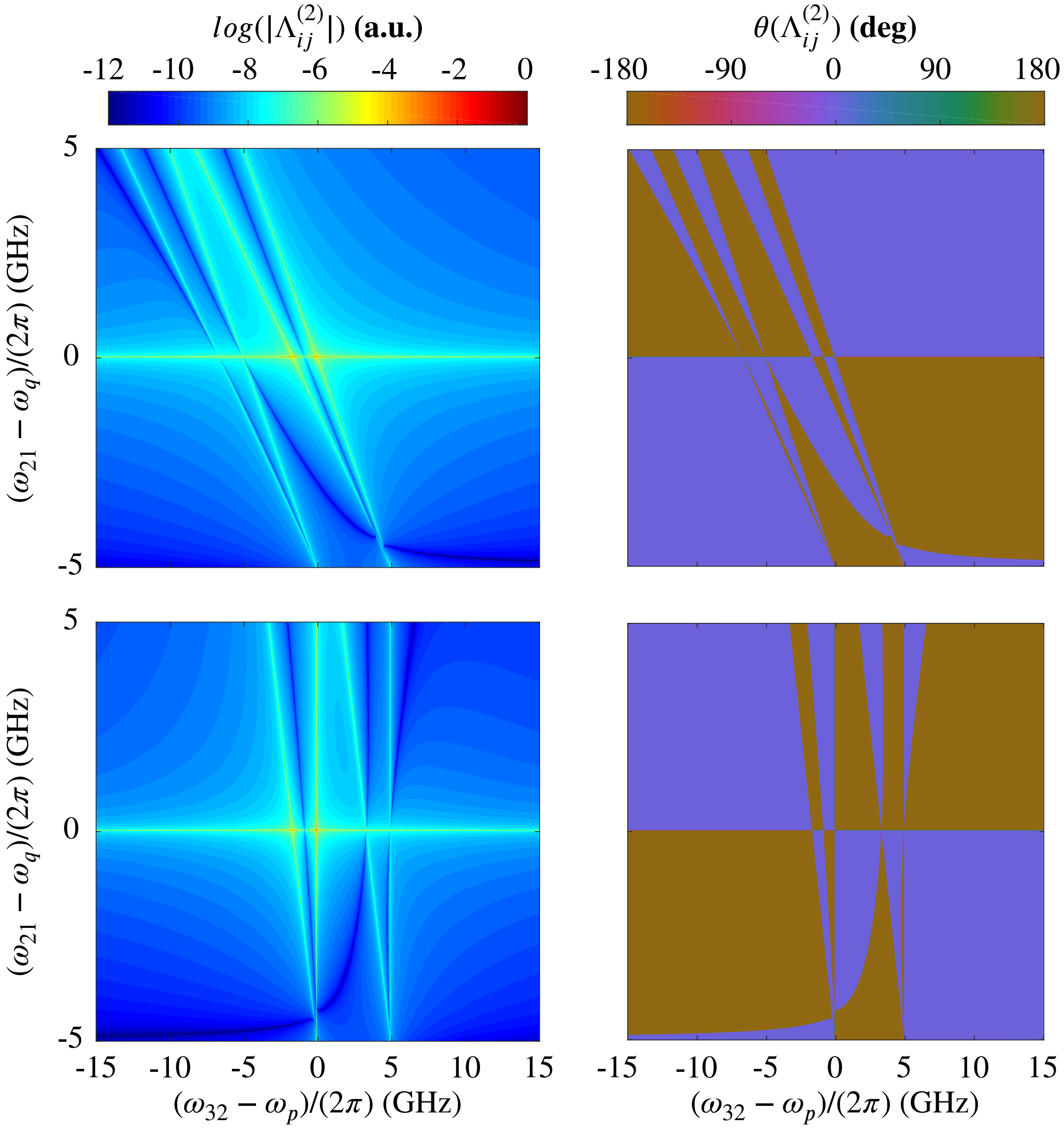

Figure 4.6: Contribution to the absolute value and complex angle of $\Lambda^{(2)}$ from ions in the lower ground state (top) and in the higher ground state (bottom) of Er^{3+}:Y_2SiO_5.

dark lines correspond to situations like the ones explained earlier and exemplified in Eq. (4.47), where the contribution to $\Lambda^{(2)}$ by the population in some of the energy levels is cancelled out by the contribution from the population in some other levels. It is also interesting to see in the plot of θ at which points $\Lambda^{(2)}$ changes sign. Another thing to notice about $\Lambda^{(2)}$ is how narrow its features are. The resolution in Fig. 4.4 isn't enough to give a good understanding of how sharp the different lines are. Their width is related to γ_{ij}, which is on the order of 0.1 MHz for the optical transitions. This makes numerical integration a hard task, as the available integration

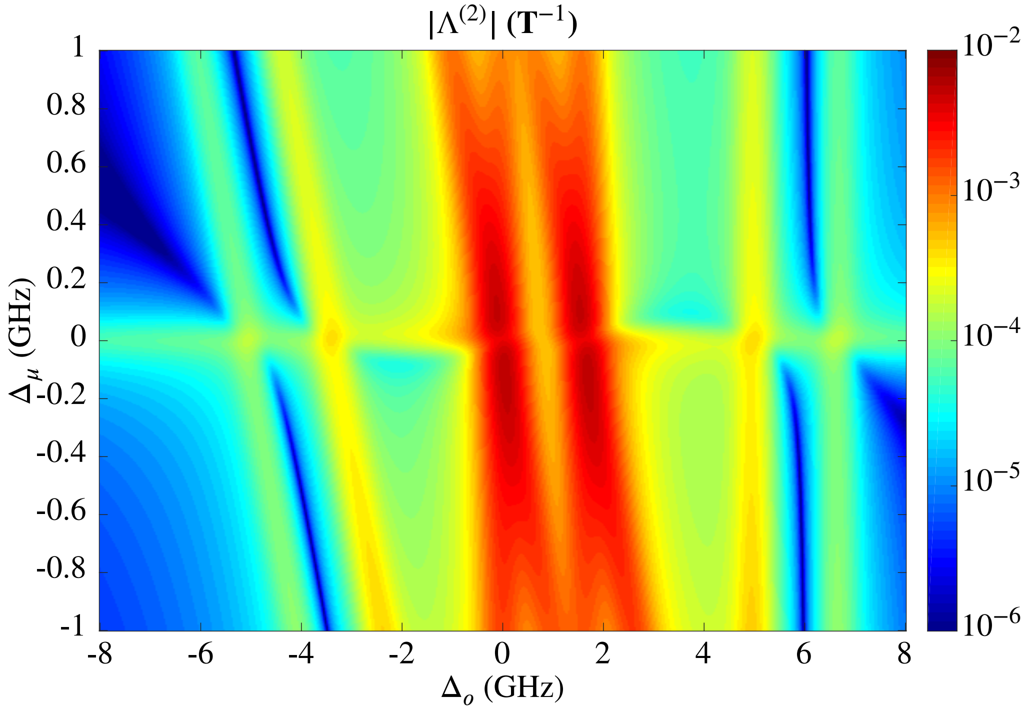

Figure 4.7: Value of $\Lambda^{(2)}$ integrated over the ingomogeneous optical and microwave lines for the set of parameters described in Tab. 4.1 at 4 K, as a function of optical (Δ_o) and microwave (Δ_m) detunings from the center of the inhomogeneous line. The calculation of $\Lambda^{(2)}$ only takes into account the SFG up-conversion process. The DFG process gives rise to a similar pattern but shifted 5 GHz upwards in the horizontal axis.

subroutines have a hard time identifying and dealing with such narrow features. It is explained in Appendix B how this problem was solved.

Next we want to calculate the integral of $\Lambda^{(2)}$ for different values of the optical and microwave detunings with respect to the center of the inhomogeneous lines. This is a relatively long process that requires several days of computational time, as each point requires a 2D integration of the function depicted in Fig. 4.4. The results are shown in Fig. 4.7 for a temperature of 4 K and in Fig. 4.8 for a temperature of 10 mK. The parameters used for these calculations are detailed in Tab. 4.1, and have been chosen to match the experimental conditions of the experiments presented in Chs. 8 and 9.

An important note needs to be made here: $\Lambda^{(2)}$ calculated in this way only accounts for the SFG process shown in Fig. 4.2. Because all of my experiments rely on heterodyne detection (See Ch. 5) we can't distinguish between SFG and DFG. The $\Lambda^{(2)}$ pattern corresponding to the DFG process can be easily obtained by shifting the SFG pattern upwards in the horizontal axis by an amount equal to ω_{21} at the center of the inhomogeneous line (ca. 5 GHz for the case shown in Fig. 4.7).

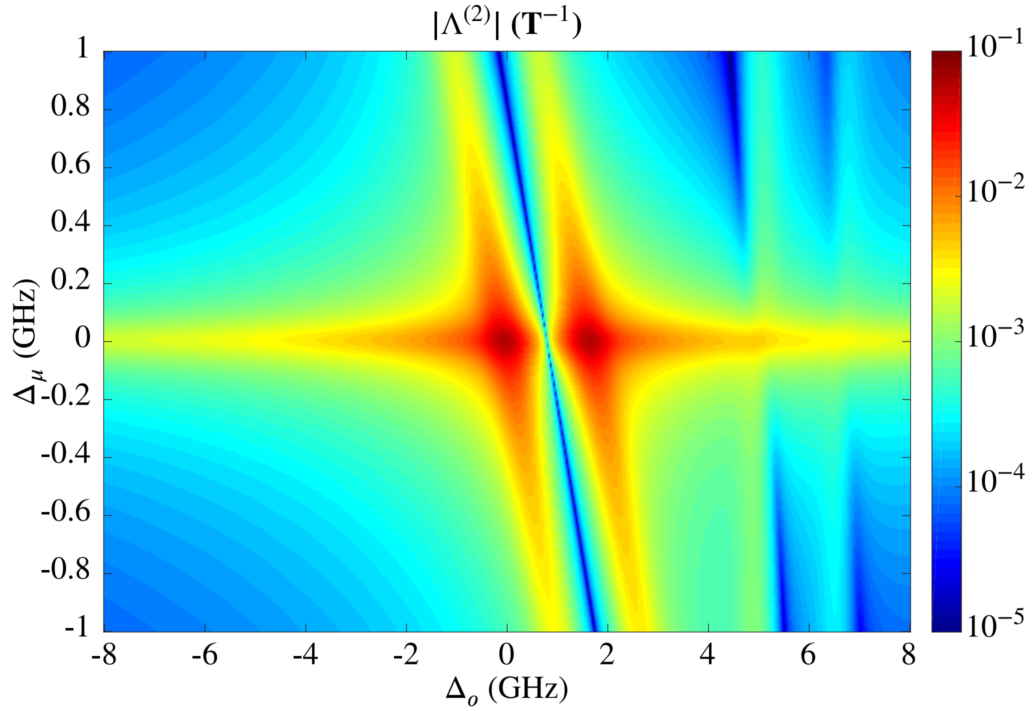

Figure 4.8: Value of $\Lambda^{(2)}$ integrated over the inhomogeneous optical and microwave lines using the same parameters as in Fig. 4.7 but at a temperature of 10 mK.

4.2.4 Hamiltonian for an Optical and a Microwave Cavity in a Nonlinear Medium

In this section I will derive the Hamiltonian describing the interaction between optical and microwave cavity modes in a nonlinear medium. This derivation is based in the theory presented by Ilchenko et al. in Ref. [76]. There are two subtle differences in our case. In Ref. [76] frequency conversion between microwave and optical fields is achieved by the presence of two input electric fields in a second order nonlinear medium, while in our case we have an electric and a magnetic field as inputs. We will need to adjust the nonlinear coefficient to this case, as explained in Sec. 4.2.3. The second difference is the type of resonators that we are using in our experiments (see Chs. 7, 8 and 9). Ilchenko's theory is based in using whispering gallery mode optical resonators, while we are using Fabry-Perot resonators. Our microwave resonators are also of a different nature. From the fundamental point of view, however, both problems are very similar.

Our system is described by the following Hamiltonian (note that this Hamiltonian is totally disconnected from that of Sec. 4.2.3):

$$H_{sys} = H_0 + V. \tag{4.48}$$

Here, H_0 is the free part of the Hamiltonian:

$$H_0 = \hbar\omega_0 a_0^\dagger a_0 + \hbar\omega_+ a_+^\dagger a_+ + \hbar\omega_- a_-^\dagger a_- + \hbar\omega_\Omega a_\Omega^\dagger a_\Omega \tag{4.49}$$

where ω_0 is a given mode of the optical resonator and $\omega_\pm$ are the next adjacent modes with higher (+) or lower (-) frequency. ω_Ω is the resonance frequency of the microwave resonator, and a_i are the annihilation operators of the corresponding modes, obeying the usual commutation relationships.

The interaction part of the Hamiltonian can be written as

$$V = -\int_{V_c} \vec{E} \cdot \vec{P}\, \mathrm{d}^3\vec{r}, \tag{4.50}$$

where the integral is performed over the volume of the crystal V_c, $\vec{E}$ represents the electric field and $\vec{P}$ represents the polarisation of the medium. Using Eq. (4.16) we can rewrite the interaction part of the Hamiltonian as

$$V = -\epsilon_0 \sum_{ijk} \int_{V_c} E_i \Lambda_{ijk}^{(2)} B_j E_k\, \mathrm{d}^3\vec{r}. \tag{4.51}$$

At this point I will drop the spatial indices ijk and substitute them by frequency indices $(+, -, 0$ and $\Omega)$. Note that there isn't a one to one correlation between spatial and frequency indices, so $\Lambda_{ijk}^{(2)}$ needs to be calculated individually for each set of frequency indices, which can be done once the directions of the involved fields have been chosen. Doing this change of indices makes it necessary to take into account all the spatial considerations in the calculation of $\Lambda^{(2)}$, but it helps to keep track of what frequency is associated to what field. Since we are only interested in the frequency components of the polarization that give rise to either up- or down-converted light I will rewrite the previous expression in the following form:

$$V = -\epsilon_0 \int_{V_c} E_+ \Lambda_{+\Omega 0}^{(2)} B_\Omega E_0\, \mathrm{d}^3\vec{r} - \epsilon_0 \int_{V_c} E_- \Lambda_{-\Omega 0}^{(2)} B_\Omega E_0\, \mathrm{d}^3\vec{r}, \tag{4.52}$$

where $E_{\pm,0}$ and B_Ω represent the electric and magnetic fields at frequencies $\omega_{\pm,0}$ and ω_Ω respectively, and $\Lambda_{\pm\Omega 0}^{(2)}$ accounts for the effective nonlinearity associated with each of the sidebands.

Now we want to introduce the expressions for the quantised electric and magnetic fields, which we write in the following way:

$$E_s = \sqrt{\frac{\hbar\omega_s}{2\epsilon_s V_s}}\left(\psi_s a_s - \psi_s^* a_s^\dagger\right) \tag{4.53}$$

$$B_\Omega = \sqrt{\frac{\hbar\omega_\Omega \mu_\Omega}{2V_\Omega}}\left(\psi_\Omega a_\Omega + \psi_\Omega^* a_\Omega^\dagger\right) \tag{4.54}$$

where the subindex s can take the values $+$, $-$ or 0. ϵ_s and μ_Ω are the electric permittivity and magnetic permeability of the corresponding modes ($\epsilon_s = \epsilon_0\epsilon_{r,s}$, $\mu_\Omega = \mu_0\mu_{r,\Omega}$), and V_s and V_Ω are the mode volumes of the different modes, defined as

$$V_s \equiv \frac{\displaystyle\int \epsilon_s E_s E_s^* \mathrm{d}V}{\max\left(\epsilon_s E_s E_s^*\right)} \tag{4.55}$$

and similarly for V_Ω. The wavefunctions ψ_s and ψ_Ω are dimensionless and normalised, such that

$$\int \psi_s^* \psi_s \, \mathrm{d}^3\vec{r} = V_s\,, \quad \int \psi_\Omega^* \psi_\Omega \, \mathrm{d}^3\vec{r} = V_\Omega. \tag{4.56}$$

Inserting (4.53) and (4.54) into (4.52) yields a collection of terms in which three creation and annihilation operators multiply each other. From all these terms the only ones that conserve energy are $a_+^\dagger a_\Omega a_0 + h.c.$ for SFG and $a_-^\dagger a_\Omega^\dagger a_0 + h.c.$ for DFG processes ($h.c.$ meaning the hermitian conjugate terms). The interaction part of the Hamiltonian in (4.52) then takes the form

$$\begin{aligned} V = {} & \epsilon_0 \left(\frac{\hbar^3}{8}\frac{\omega_+\omega_\Omega\omega_0}{V_+V_\Omega V_0}\frac{\mu_0}{\epsilon_0^2}\right)^{\frac{1}{2}} \Lambda^{(2)}_{+\Omega 0} \int_{V_c} \sqrt{\frac{\mu_{r,\Omega}}{\epsilon_{r,+}}} \left(\psi_+^*\psi_\Omega\psi_0 a_+^\dagger a_\Omega a_0 + \psi_+\psi_\Omega^*\psi_0^* a_+ a_\Omega^\dagger a_0^\dagger\right) \mathrm{d}^3\vec{r} \\ & + \epsilon_0 \left(\frac{\hbar^3}{8}\frac{\omega_-\omega_\Omega\omega_0}{V_-V_\Omega V_0}\frac{\mu_0}{\epsilon_0^2}\right)^{\frac{1}{2}} \Lambda^{(2)}_{-\Omega 0} \int_{V_c} \sqrt{\frac{\mu_{r,\Omega}}{\epsilon_{r,-}}} \left(\psi_-^*\psi_\Omega^*\psi_0 a_-^\dagger a_\Omega^\dagger a_0 + \psi_-\psi_\Omega\psi_0^* a_- a_\Omega a_0^\dagger\right) \mathrm{d}^3\vec{r}. \end{aligned} \tag{4.57}$$

If we assume all the optical fields to be in the same transverse spatial mode the four integrals of the different wavefunctions will give the same result, which will be an overlapping volume $\tilde{V}$ between the optical and the microwave modes. The effects of phase matching will come naturally from the calculation of these integrals. Then, we can finally write the interaction part of our Hamiltonian as

$$V = \hbar\left(g_+ a_+^\dagger a_\Omega a_0 + g_+^* a_+ a_\Omega^\dagger a_0^\dagger\right) + \hbar\left(g_- a_-^\dagger a_\Omega^\dagger a_0 + g_-^* a_- a_\Omega a_0^\dagger\right), \tag{4.58}$$

where

$$g_\pm = \left(\frac{\hbar}{8}\omega_\pm \omega_\Omega \omega_0 \frac{\tilde{V}^2}{V_\pm V_\Omega V_0}\mu_0\right)^{\frac{1}{2}} \Lambda^{(2)}_{\pm\Omega 0}. \tag{4.59}$$

4.2.5 Input Output Theory

Now that we have written the Hamiltonian of our system in a convenient way we are ready to study its dynamical properties. To this end we will look at the input-output theory of Quantum Electro-Dynamics. My reference point in the literature will be [74], although similar derivations can be found elsewhere.

We want to study the behaviour of our system in the presence of a surrounding bath, and the interactions between the two. To account for this we write the total Hamiltonian

$$H = H_{sys} + H_{bath} + H_{int} \tag{4.60}$$

where

$$H_{bath} = \hbar \int_{-\infty}^{\infty} \omega b^\dagger(\omega) b(\omega)\, \mathrm{d}\omega \tag{4.61}$$

is the bath Hamiltonian, and

$$H_{int} = i\hbar \int_{-\infty}^{\infty} \kappa(\omega)\left[b^\dagger(\omega) a_0 - b(\omega) a_0^\dagger\right] \mathrm{d}\omega \tag{4.62}$$

$$+\, i\hbar \int_{-\infty}^{\infty} \kappa(\omega)\left[b^\dagger(\omega) a_+ - b(\omega) a_+^\dagger\right] \mathrm{d}\omega \tag{4.63}$$

$$+\, i\hbar \int_{-\infty}^{\infty} \kappa(\omega)\left[b^\dagger(\omega) a_- - b(\omega) a_-^\dagger\right] \mathrm{d}\omega \tag{4.64}$$

$$+\, i\hbar \int_{-\infty}^{\infty} \kappa(\omega)\left[b^\dagger(\omega) a_\Omega - b(\omega) a_\Omega^\dagger\right] \mathrm{d}\omega \tag{4.65}$$

is the interaction Hamiltonian between the system and the surrounding bath (not to be confused with the interaction Hamiltonians V defined in Sec. 4.2.3 or Sec. 4.2.4), where $\kappa(\omega)$ is the coupling constant between our system and the bath. Note that all the terms in H_{int} containing the operators a_o, a_+, a_- and a_Ω are independent from one another. In order to keep things clean and simple in the following lines I will derive a series of equations for a generic operator a, which will apply to any of the aforementioned operators. We will recover the subindices later on, when they become relevant again.

We can derive and integrate the equation of motion for the bath operators as

$$\dot{b}(\omega) = \frac{i}{\hbar}\left[H, b(\omega)\right] = -i\omega b(\omega) + \kappa(\omega) a \tag{4.66}$$

$$\rightarrow b(\omega) = b_0(\omega) e^{-i\omega(t-t_0)} + \kappa(\omega) \int_{t_0}^{t} a(t') e^{-i\omega(t-t')}\, \mathrm{d}t' \tag{4.67}$$

where $b_0(\omega)$ is the value of $b(\omega)$ at $t = t_0$. On the other hand the equation of motion for a can be written as

$$\dot{a}(\omega) = \frac{i}{\hbar}\left[H, a\right] = \frac{i}{\hbar}\left[H_{sys}, a\right] - \int_{-\infty}^{\infty} \kappa(\omega) b(\omega)\, \mathrm{d}\omega. \tag{4.68}$$

At this point we define an “in” field as

$$b_{in}(t) \equiv \frac{1}{\sqrt{2\pi}} \int b_0(\omega) e^{-i\omega(t-t_0)}\, \mathrm{d}\omega \tag{4.69}$$

which is valid for $t_0 < t$. We also make here what is known as the first Markov approximation, which considers the coupling constant as independent of frequency:

$$\kappa(\omega) = \sqrt{\frac{\gamma}{2\pi}}, \tag{4.70}$$

where γ is a decay rate. Using this we can derive

$$\dot{a} = \frac{i}{\hbar}\left[H_{sys}, a\right] - \sqrt{\gamma} b_{in}(t) - \frac{\gamma}{2} a(t). \tag{4.71}$$

We can write an “out” field in a similar way as we have written b_{in}, as

$$b_{out}(t) \equiv \frac{1}{\sqrt{2\pi}} \int b_1(\omega) e^{-i\omega(t-t_1)} a(t')\, \mathrm{d}t' \tag{4.72}$$

where $t_1 > t$ and $b_1(\omega)$ corresponds to $b(\omega)$ at $t = t_1$. In a similar way as before we can now write the equation of motion of a as

$$\dot{a} = \frac{i}{\hbar}\left[H_{sys}, a\right] - \sqrt{\gamma} b_{out}(t) + \frac{\gamma}{2} a(t). \tag{4.73}$$

Combining (4.71) and (4.73) we get the input-output relationship

$$b_{out}(t) - b_{in}(t) = \sqrt{\gamma} a(t). \tag{4.74}$$

Given a known H_{sys} Eqs. (4.71) and (4.74) allow us to derive and solve the equations of motion for the field operators inside a cavity coupled to an external bath. However, in any realistic case, losses other than coupling will be present (e.g. optical absorption in the sample due to YSO and resistive losses in the microwave resonator). In order to include this in our model we consider instead a cavity with two output ports, where one port is coupled to the input and output fields $b(t)$ and the other one is coupled to a loss channel $\tilde{b}(t)$. In such a situation Eqs. (4.71) and (4.74) take the following form:

$$\dot{a}(t) = \frac{i}{\hbar}\left[H_{sys}, a\right] - \frac{1}{2}\left(\gamma + \tilde{\gamma}\right) a(t) - \sqrt{\gamma} b_{in}(t) - \sqrt{\tilde{\gamma}} \tilde{b}_{in}(t) \tag{4.75}$$

$$b_{out}(t) - b_{in}(t) = \sqrt{\gamma} a(t) \tag{4.76}$$

$$\tilde{b}_{out}(t) - \tilde{b}_{in}(t) = \sqrt{\tilde{\gamma}} a(t) \tag{4.77}$$

By inserting Eqs. (4.48), (4.49) and (4.58) into (4.75) the different equations of motion for the different intracavity fields can be derived. When doing so, we will consider the optical pump field to be a classical field, so we make the substitution $a_o(t) \rightarrow \alpha$ where α is a complex number. Consequently, we will not write an equation of motion for such field, and we will only be concerned about the dynamics of $a_{\pm}(t)$ and $a_{\Omega}(t)$:

$$\dot{a}_+(t) = -i\omega_+ a_+ - ig_+ \alpha a_\Omega - \frac{1}{2}\left(\gamma_+ + \tilde{\gamma}_+\right) a_+ - \sqrt{\gamma_+} b_{in+} - \sqrt{\tilde{\gamma}_+} \tilde{b}_{in+} \tag{4.78}$$

$$\dot{a}_-(t) = -i\omega_- a_- - ig_- \alpha a_\Omega^\dagger - \frac{1}{2}\left(\gamma_- + \tilde{\gamma}_-\right) a_- - \sqrt{\gamma_-} b_{in-} - \sqrt{\tilde{\gamma}_-} \tilde{b}_{in-} \tag{4.79}$$

$$\dot{a}_\Omega(t) = -i\omega_\Omega a_\Omega - ig_+^* \alpha^* a_+ - ig_- \alpha a_-^\dagger - \frac{1}{2}\left(\gamma_\Omega + \tilde{\gamma}_\Omega\right) a_\Omega - \sqrt{\gamma_\Omega} b_{\Omega in} - \sqrt{\tilde{\gamma}_\Omega} \tilde{b}_{\Omega in} \tag{4.80}$$

This system of equations can be simplified by writing each of our fields as the product of an amplitude that varies slowly in time and a fast oscillating component at the frequency of the input fields:

$$a_+(t) = A_+(t) e^{-i(\omega_p + \omega_m)t} \tag{4.81}$$

$$a_-(t) = A_-(t) e^{-i(\omega_p - \omega_m)t} \tag{4.82}$$

$$a_\Omega(t) = A_\Omega(t) e^{-i\omega_m t} \tag{4.83}$$

$$\alpha(t) = \mathscr{A} e^{-i\omega_p t} \tag{4.84}$$

where ω_p is the frequency of the input optical pump field and ω_m is the frequency of the input microwave field (in general different from ω_o and ω_Ω, the frequencies of the cavity modes). We can write a similar set of equations for the b_{in} fields. In addition, we define the following quantities:

$$\Gamma_+ \equiv i\left(\omega_+ - \omega_p - \omega_m\right) + \frac{1}{2}\left(\gamma_+ + \tilde{\gamma}_+\right) \tag{4.85}$$

$$\Gamma_- \equiv i\left(\omega_- - \omega_p + \omega_m\right) + \frac{1}{2}\left(\gamma_- + \tilde{\gamma}_-\right) \tag{4.86}$$

$$\Gamma_\Omega \equiv i\left(\omega_\Omega - \omega_m\right) + \frac{1}{2}\left(\gamma_\Omega + \tilde{\gamma}_\Omega\right) \tag{4.87}$$

Then we can rewrite the set of equations (4.78-4.80) as:

$$\dot{A}_+(t) = -\Gamma_+ A_+(t) - i g_+ \mathscr{A} A_\Omega(t) - \sqrt{\gamma_+} B_{in+}(t) - \sqrt{\tilde{\gamma}_+} \tilde{B}_{in+}(t) \tag{4.88}$$

$$\dot{A}_-(t) = -\Gamma_- A_-(t) - i g_- \mathscr{A} A_\Omega^\dagger(t) - \sqrt{\gamma_-} B_{in-}(t) - \sqrt{\tilde{\gamma}_-} \tilde{B}_{in-}(t) \tag{4.89}$$

$$\dot{A}_\Omega(t) = -\Gamma_\Omega A_\Omega(t) - i g_+^* \mathscr{A}^* A_+(t) - i g_- \mathscr{A} A_-^\dagger(t) - \sqrt{\gamma_\Omega} B_{\Omega in}(t) - \sqrt{\tilde{\gamma}_\Omega} \tilde{B}_{\Omega in}(t) \tag{4.90}$$

This system of equations can be straightforwardly solved in the steady state. We write it in a matrix form as $\dot{X} = MX + Q$, where the vector X has six components equal to A_+, A_-, A_Ω and their corresponding adjoint operators. Then we set $\dot{X} = 0$, invert M and find the solution as $X = -M^{-1}Q$. Then in order to calculate the size of the generated sidebands as a function of the input fields we can take the solutions for A_+ and A_- and introduce them into Eq. (4.74) to finally obtain:

$$\begin{aligned} B_{out+} = \sqrt{\gamma_+}\Bigg[& \frac{\Gamma_\Omega \Gamma_-^* - |\mathscr{A}|^2|g_-|^2}{-\Gamma_+|\mathscr{A}|^2|g_-|^2 + \Gamma_-^*|\mathscr{A}|^2|g_+|^2 + \Gamma_\Omega\Gamma_+\Gamma_-^*}\left(-\sqrt{\gamma_+}B_{in+} - \sqrt{\tilde{\gamma}_+}\tilde{B}_{in+}\right) \\ & - \frac{\mathscr{A}^2 g_- g_+}{-\Gamma_+|\mathscr{A}|^2|g_-|^2 + \Gamma_-^*|\mathscr{A}|^2|g_+|^2 + \Gamma_\Omega\Gamma_+\Gamma_-^*}\left(-\sqrt{\gamma_-}B_{in-}^\dagger - \sqrt{\tilde{\gamma}_-}\tilde{B}_{in-}^\dagger\right) \\ & - \frac{i\mathscr{A} g_+ \Gamma_-^*}{-\Gamma_+|\mathscr{A}|^2|g_-|^2 + \Gamma_-^*|\mathscr{A}|^2|g_+|^2 + \Gamma_\Omega\Gamma_+\Gamma_-^*}\left(-\sqrt{\gamma_\Omega}B_{\Omega in} - \sqrt{\tilde{\gamma}_\Omega}\tilde{B}_{\Omega in}\right)\Bigg] \\ & + B_{in+} \end{aligned} \tag{4.91}$$

$$\begin{aligned} B_{out-} = \sqrt{\gamma_-}\Bigg[& \frac{\mathscr{A}^2 g_- g_+}{-\Gamma_+^*|\mathscr{A}|^2|g_-|^2 + \Gamma_-|\mathscr{A}|^2|g_+|^2 + \Gamma_\Omega^*\Gamma_+^*\Gamma_-}\left(-\sqrt{\gamma_+}B_{in+}^\dagger - \sqrt{\tilde{\gamma}_+}\tilde{B}_{in+}^\dagger\right) \\ & + \frac{\Gamma_\Omega^*\Gamma_+^* + |\mathscr{A}|^2|g_+|^2}{-\Gamma_+^*|\mathscr{A}|^2|g_-|^2 + \Gamma_-|\mathscr{A}|^2|g_+|^2 + \Gamma_\Omega^*\Gamma_+^*\Gamma_-}\left(-\sqrt{\gamma_-}B_{in-} - \sqrt{\tilde{\gamma}_-}\tilde{B}_{in-}\right) \\ & - \frac{i\mathscr{A}g_-\Gamma_+^*}{-\Gamma_+^*|\mathscr{A}|^2|g_-|^2 + \Gamma_-|\mathscr{A}|^2|g_+|^2 + \Gamma_\Omega^*\Gamma_+^*\Gamma_-}\left(-\sqrt{\gamma_\Omega}B_{\Omega in}^\dagger - \sqrt{\tilde{\gamma}_\Omega}\tilde{B}_{\Omega in}^\dagger\right)\Bigg] \\ & + B_{in-} \end{aligned} \tag{4.92}$$

The previous set of equations might seem too convoluted to be able to extract any meaningful information from it, at least at first sight. In order to get an intuitive yet still realistic view of what's going on we can simplify them by neglecting most of the input fields. The justification for doing this is that B_{in+}, $\tilde{B}_{in+}$, B_{in-}, $\tilde{B}_{in-}$, and $\tilde{B}_{\Omega in}$ will be vacuum (or thermal) states. By setting them all to zero we are approaching the classical limit in which we neglect vacuum fluctuation contributions to the motion of our system. Doing so we can rewrite Eqs. (4.91) and (4.92) in a much more tractable way:

$$B_{out+} \simeq \frac{i\mathscr{A}g_+}{-\frac{\Gamma_+}{\Gamma_-^*}|\mathscr{A}|^2|g_-|^2 + |\mathscr{A}|^2|g_+|^2 + \Gamma_\Omega\Gamma_+}\sqrt{\gamma_+\gamma_\Omega}B_{\Omega in} \tag{4.93}$$

$$B_{out-} \simeq \frac{i\mathscr{A}g_-}{\frac{\Gamma_-}{\Gamma_+^*}|\mathscr{A}|^2|g_+|^2 - |\mathscr{A}|^2|g_-|^2 + \Gamma_\Omega^*\Gamma_-}\sqrt{\gamma_-\gamma_\Omega}B_{\Omega in}^\dagger \tag{4.94}$$

A further simplification can be made if we assume that only the "+" ("-") sideband is generated. In this case, the a_- (a_+) terms are removed from the Hamiltonian, and the dynamics of the system are greatly simplified. We shall explore the realism of this simplification later on, when we calculate the values of $\Lambda^{(2)}$, which will allow us to determine g_+ and g_-. Solving the equations of motion for single sideband generation we get:

$$B_{out+} = \frac{i\mathscr{A}g_+}{|\mathscr{A}|^2|g_+|^2 + \Gamma_\Omega\Gamma_+}\sqrt{\gamma_+\gamma_\Omega}B_{\Omega in} \tag{4.95}$$

$$B_{out-} = \frac{i\mathscr{A}g_-}{-|\mathscr{A}|^2|g_-|^2 + \Gamma_\Omega^*\Gamma_-}\sqrt{\gamma_-\gamma_\Omega}B_{\Omega in}^\dagger \tag{4.96}$$

At this point we can calculate what range of parameters we need in order to have total frequency conversion between the input microwave field and the output optical sideband. We can do so by setting the absolute value of the coefficient multiplying $B_{\Omega in}$ ($B_{\Omega in}^\dagger$) equal to one.

In the case of resonance between the input fields and the corresponding cavity modes for a lossless cavity $\Gamma_i = \gamma_i/2$, and the condition for total frequency conversion for SFG is

$$|\mathscr{A}|^2|g_+|^2 = \frac{\gamma_\Omega\gamma_+}{4}. \tag{4.97}$$

Note that one to one conversion can't be obtained from the DFG process. This is because when the frequency of the pump is greater than the frequency of the converted field it is possible to obtain photons at the converted field frequency even without the presence of any microwaves in the microwave cavity due to spontaneous parametric downconversion.

4.3 Conversion Efficiency

In this section I will give an expression for the conversion efficiency between microwave and optical photons for the case in which an optical cavity is used and for the case of single pass optics in the classical regime. This will help to see how much of an effect does the optical cavity have.

4.3.1 Conversion Efficiency with an Optical Cavity

The conversion efficiency with an optical cavity can be obtained from Eq. (4.95) as

$$\eta_{OC} = \frac{|\mathscr{A}|^2|g_+|^2}{\left(|\mathscr{A}|^2|g_+|^2 + \Gamma_\Omega\Gamma_+\right)^2}\gamma_+\gamma_\Omega. \tag{4.98}$$

This expression can be written explicitly in terms of $\Lambda^{(2)}$, the cavities' quality factors $Q_i = \omega_i/2\Omega_i$ and the power of the optical pump P_0 (by noting that $|\mathscr{A}|^2 = P_0Q_0/(\hbar\omega_0^2)$) as:

$$\eta_{OC} = \frac{\frac{P_0Q_0}{\hbar\omega_0^2}\frac{\hbar}{8}\omega_+\omega_\Omega\omega_0\frac{\tilde{V}^2}{V_+V_\Omega V_0}\mu_0\left[\Lambda^{(2)}\right]^2}{\left\{\frac{P_0Q_0}{\hbar\omega_0^2}\frac{\hbar}{8}\omega_+\omega_\Omega\omega_0\frac{\tilde{V}^2}{V_+V_\Omega V_0}\mu_0\left[\Lambda^{(2)}\right]^2 + \frac{\omega_\Omega\omega_+}{4Q_\Omega Q_+}\right\}^2}\left(\frac{\omega_\Omega}{Q_\Omega} - \tilde{\gamma}_\Omega\right)\left(\frac{\omega_+}{Q_+} - \tilde{\gamma}_+\right). \tag{4.99}$$

It is worth mentioning that the quality factor of the different optical modes will in general be very similar, so at any point we can simplify the problem by setting $Q_0 = Q_+ = Q_-$.

4.3.2 Conversion Efficiency with Single Pass Optics

Next, I want to derive the conversion efficiency for the simple case with no optical cavity and compare it with the result obtained for the case in which an optical cavity is used.

From Maxwell's equations in the absence of free currents and charges one can derive the following wave equation for linearly polarised plane waves propagating along the z axis, assuming that their amplitude and phase vary slowly in time:

$$\frac{\partial E}{\partial z} - \frac{n}{c}\frac{\partial E}{\partial t} = \frac{i\mu_0\omega_0 c}{2}P. \tag{4.100}$$

In order to solve this equation we define

$$E_r(z,t) = E\left(z, t - \frac{nz}{c}\right). \tag{4.101}$$

In doing this we are defining a different origin of time for each cross section of the sample taking into account the propagation speed of the generated electromagnetic wave, so that a pulse travelling from the origin ($z = 0$) at $t = 0$ would hit each point at $t - nz/c = 0$ (as the pulse propagates with a speed c/n). Assuming an optically thin sample, we get

$$E_r \equiv E_+ = i\frac{\mu_0\omega_0 c}{2}Pl \tag{4.102}$$

where l is the total length that the light travels across the sample and $P = \epsilon_0\Lambda^{(2)}B_\Omega E_0$.

On the other hand the energy stored inside the microwave cavity can be written as

$$\hbar\omega_\Omega \langle a_\Omega^\dagger a_\Omega\rangle = 2\int_{V_\Omega} \vec{H}\cdot\vec{B}\mathrm{d}V = 2V_\Omega\frac{B^2}{\mu_0}, \tag{4.103}$$

where I have considered that the energy of a microwave photon is stored in equal parts in its electric and its magnetic fields, and that the magnetic field is homogeneous inside a volume V_Ω in the microwave resonator. We can also see from the input-output theory (see Appendix A) that the energy stored inside the microwave cavity can be written as

$$\hbar\omega_\Omega \langle a_\Omega^\dagger a_\Omega\rangle = \sqrt{|S_{21}|^2 P_{in\Omega}}\frac{2}{\Delta\omega}, \tag{4.104}$$

where $|S_{21}|^2$ is the scattering parameter that measures (power) transmission through the cavity, $P_{in\Omega}$ is the input power to the microwave cavity and $\Delta\omega$ is the FWHM of the cavity transmission peak. Using these two results we get

$$B^2 = \frac{\mu_0}{V_\Omega \Delta\omega}\sqrt{|S_{21}|^2 P_{in\Omega}}. \tag{4.105}$$

Combining Eqs. (4.102) and Eqs. (4.105) we obtain

$$|E_+|^2 = \left(\frac{\mu_0\omega_0 c}{2} z\epsilon_0 \Lambda^{(2)}\right)^2 \frac{\mu_0}{V_\Omega \Delta\omega}\sqrt{|S_{21}|^2 P_{in\Omega}}|E_0|^2. \tag{4.106}$$

The power of a collimated laser beam can be expressed as $P = A\epsilon_0 c E^2$, where A is the cross sectional area of the beam. Since the pump and the converted fields will have the same transverse spatial mode $A_+ = A_0$ and we can write the single pass conversion efficiency as:

$$\eta_{SP} = \frac{\omega_\Omega}{\omega_0}\frac{P_+}{P_{in\Omega}} = \frac{\omega_\Omega}{\omega_0}\left(\frac{\mu_0\omega_0 c}{2} z\epsilon_0 \Lambda^{(2)}\right)^2 \frac{\mu_0}{V_\Omega \Delta\omega}\sqrt{|S_{21}|^2 P_0} \tag{4.107}$$

where we have included the factor ω_Ω/ω_0 to take into account the energy difference between an input microwave photon and an output optical photon. In this way η_{SP} is not a power efficiency but a photon number efficiency.

So far, phase matching has been neglected. In order to include it's effects we will consider that both of the optical fields are plane waves propagating with a different wavevectors k_0 and k_+. The phase of the microwave field will be considered constant. This is a good approximation because the length of the sample is short compared to the wavelength of a photon at ~ 5 GHz. Then, the phase matching factor can be calculated by performing the following integral:

$$\int_0^L e^{i\Delta k z}\mathrm{d}z = \frac{e^{i\Delta k L} - 1}{i\Delta k}, \tag{4.108}$$

where $\Delta k = k_0 - k_+$, and L is the length of the sample. Eq. (4.109) shows the correction term that accompanies the generated electric field E_+. However, the conversion efficiency is proportional to $|E_+|^2$, so the correction term to the efficiency due to phase matching is

$$\left|\frac{e^{i\Delta k L} - 1}{i\Delta k}\right|^2 = \left[\frac{\sin(\Delta k L/2)}{\Delta k L/2}\right]^2. \tag{4.109}$$

Therefore, the single pass conversion efficiency from Eq. (4.107) becomes

$$\eta_{SP} = \frac{\omega_\Omega}{\omega_0}\frac{P_+}{P_{in\Omega}} = \frac{\omega_\Omega}{\omega_0}\left(\frac{\mu_0\omega_0 c}{2} z\epsilon_0 \Lambda^{(2)}\right)^2 \frac{\mu_0}{V_\Omega \Delta\omega}\sqrt{|S_{21}|^2 P_0}\left[\frac{\sin(\Delta k L/2)}{\Delta k L/2}\right]^2. \tag{4.110}$$

In order to show explicitly the effect of the microwave cavity's quality factor $Q_\Omega = \omega_\Omega/\Delta\omega$ we can rewrite the previous expression as

$$\eta_{SP} = \left(\frac{\mu_0\omega_0 c}{2} z\epsilon_0\Lambda^{(2)}\right)^2 \frac{\mu_0}{V_\Omega\omega_0} Q_\Omega \sqrt{|S_{21}|^2 P_0} \left[\frac{\sin(\Delta kL/2)}{\Delta kL/2}\right]^2 . \tag{4.111}$$

4.3.3 Optical Cavity Enhancement Factor

Now I want to compare the conversion efficiency obtained with and without an optical cavity. To do so, we can take a look at Eqs. (4.99) and (4.111). A good parameter to quantify this enhancement is the optical cavity quality factor Q_0. However, the enhancement due to the optical cavity does not only depend on Q_0 but also on the coupling factor g presented in Eq. (4.59). This is to be expected, as g contains information related to phase matching and mode overlapping. Figure (4.9) shows the enhancement due to the optical cavity normalised by g^2. The units have been chosen to be arbitrary in both axes (even though Q_0 has actually no units) because the precise values will depend on the particular values for all the parameters involved, and we are only interested in the shape of the function now. The enhancement factor can be seen to increase quadratically with Q_0 to a very good approximation in the beginning, until the absolute conversion efficiency starts to get close to one, where the enhancement factor inevitably starts to go down as efficiencies greater than one are unattainable.

4.4 Feasibility

In this section I will explore the possibility of achieving unit frequency conversion efficiency according to the theory described in Secs. 4.2 and 4.3. That is, if according to the theory described above it is possible to build a one-to-one quantum frequency converter between microwave and optical photons.

To do so I will consider a 5 GHz microwave transition. This can be achieved via Zeeman splitting of the ground state with a magnetic field of around 0.15 T, with an orientation angle $\alpha \simeq \alpha_M$ as per Fig. 3.8. According to the calculations in Sec. 4.2.3 for an Er^{3+}:Y_2SiO_5 sample doped at 100 ppm cooled down to 10 mK the value for $\Lambda^{(2)}$ can be around or greater than $5\times10^{-2}\,T^{-1}$ for a set of detunings greater than the inhomogeneous linewidths. I will consider an optical cavity with a quality factor $Q_o = 2\times10^7$ and a microwave cavity with a quality factor $Q_\Omega = 6\times10^3$. I will take a value for the microwave cavity mode volume of $V_\Omega = 200\,\text{mm}^3$ and for the optical cavity mode volume of $V_0 = V_+ = 0.9\,\text{mm}^3$. The overlapping volume, taking mode matching into account as explained in Sec. 4.2.4, will be taken as $\tilde{V} = 0.2\,\text{mm}^3$. Inserting these values into Eq. (4.99) we can calculate the conversion efficiency η_{OC} as a function of

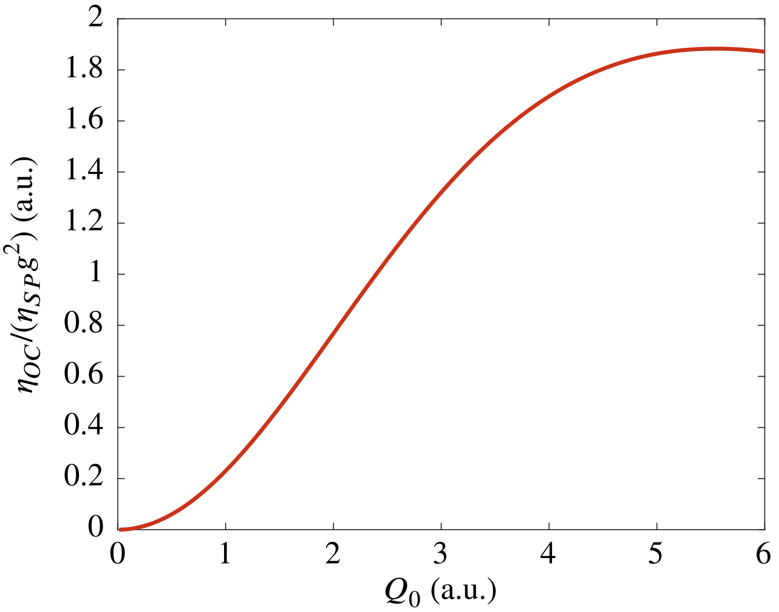

Figure 4.9: Dependence of the conversion efficiency enhancement due to the optical cavity as a function of the optical cavity's quality factor. Both axes have been scaled arbitrarily, as the enhancement factor will strongly depend on the particular values of all the parameters involved. The enhancement factor can be seen to increase quadratically until it reaches a saturation point which corresponds to an absolute value for the conversion efficiency of one.

the optical pump power for different optical and microwave cavity loss parameters, as shown in Fig. 4.10. The cavity losses in this case are characterised by $\tilde{\gamma}_i/\Gamma_i$ (with $i = \Omega, o$) which tells us what fraction of the resonators' Q factor is due to material losses ($\tilde{\gamma}_i$) as opposed to coupling losses (γ_i) (remember $Q_i = \omega_i/(2\Gamma_i)$, and on resonance $\Gamma_i = (\tilde{\gamma}_i + \gamma_i)/2$).

I would like note that the parameters mentioned in the previous paragraph are all well within current technical capabilities. Superconducting magnets can generate magnetic fields of the order of a few Tesla. Temperatures of 10 mK can be reached using dilution refrigerators. The quality factors for the optical and the microwave cavities mentioned above are of the same order as the ones that we can achieve in our experiments, as it will be discussed later on in Chs. 8 and 9. It is important to note that in our experiments V_Ω is relatively large compared to V_o, and V_o is relatively large compared to $\tilde{V}$. This is due to a design choice that was made in order to simplify the experiment in terms of optical alignment, but smaller microwave mode volumes and better mode overlap could be achieved without any drastic modification of the setup.

Fig. 4.10 shows that according to the theory described in the present chapter it is possible to achieve conversion efficiencies close to one using $Er^{3+}:Y_2SiO_5$ crystals at millikelvin temperatures. As it can be seen, for the case of dissipation-less cavities ($\tilde{\gamma}_i = 0$) perfect impedance

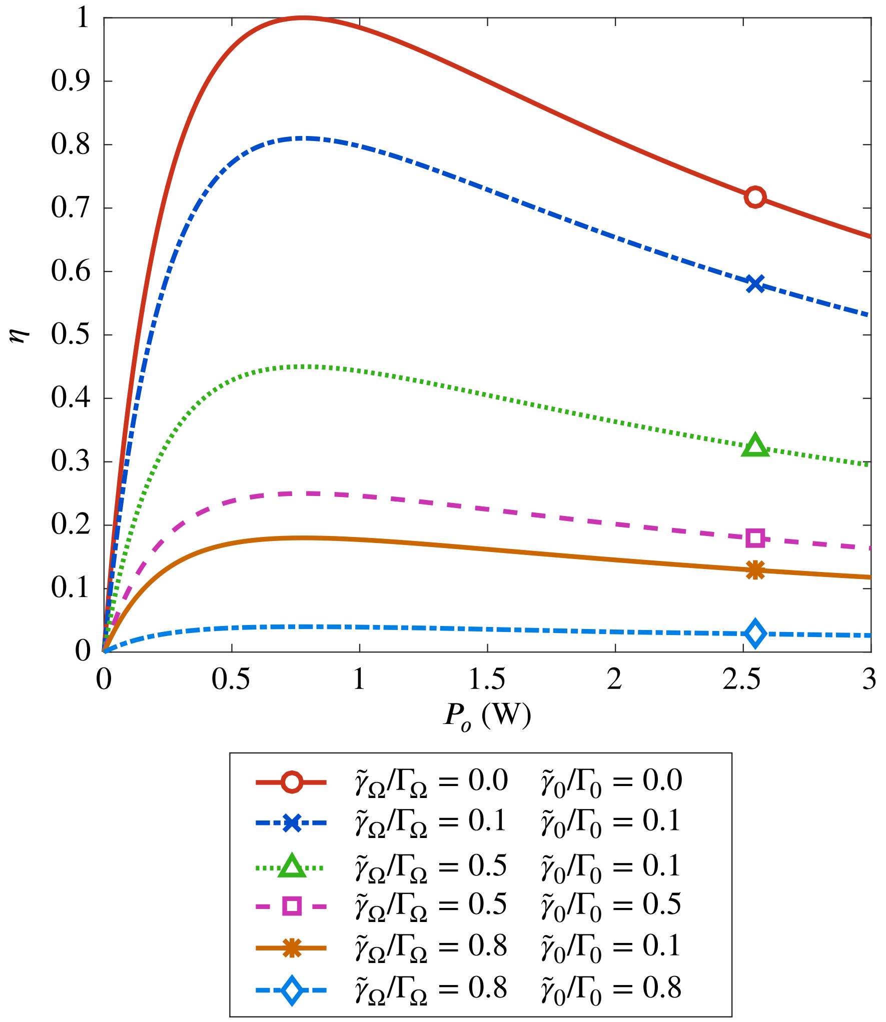

Figure 4.10: Predicted conversion efficiency as a function of the pump power for different cavity loss parameters. For the case of dissipation-less cavities ($\tilde{\gamma}_i = 0$) total conversion efficiency is achievable. Introducing parasitic losses in the resonators results in an inevitable loss of conversion efficiency, but even for relatively high intrinsic losses it is possible to achieve meaningful conversion efficiencies on the order of a few percents.

matching can be achieved and total conversion efficiency is possible. Unfortunately, in any realistic scenario the cavities will present some parasitic loss which translates into lower conversion efficiencies. However, even for relatively high contributions of the parasitic loss to the linewidths of the cavities (e.g. $\tilde{\gamma}_i/\Gamma_i = 0.8$) conversion efficiencies of a few percent are possible. Looking at the horizontal axis one can see that depending on the particular parameters maximising the conversion efficiency may require relatively high pump laser powers, on the order of a few Watt. This doesn't present a major issue, as it is well within what's technologically possible at the present time. In the experiments presented in this thesis certain technical limitations apply. The most important one is not having direct access to a dilution refrigerator. Instead, our experiments are performed at liquid helium temperatures, near 3∼4 K. The second biggest limitation is the lack of high optical power for the pump beam, as our laser currently has a modest maximum output of several tens of milliwatts.

Chapter 5

Experimental Techniques

In this chapter I will describe the three main experimental techniques that I employed during my thesis: Raman heterodyne spectroscopy, electron paramagnetic resonance, and optical absorption. These three spectroscopic techniques are well described in the literature and have been extensively utilized over the last several decades. A brief explanation will be given here to identify some key points, and to highlight several aspects that need to be treated differently in our case.

5.1 Raman Heterodyne Spectroscopy

Raman heterodyne spectroscopy (or as I like to call it in private, RHESPECT) is a spectroscopic technique based on driving Raman transitions, which generates Stokes and anti-Stokes photons, and then detecting these photons using heterodyne detection. A Raman scattering process occurs when a photon loses (gains) energy after being scattered by an atom. The energy that the photon loses is transferred to (from) a different particle or quasiparticle, usually another photon or a phonon. If the incoming photon gives part of its energy the process is called Stokes scattering, and the outgoing photon is called a Stokes photon. The opposite process is called anti-Stokes scattering, and the outgoing photon is called an anti-Stokes photon. A Raman transition can be observed in a three energy level system in which the different levels are connected to one another, as shown on the left half of Fig. 5.1. Raman transitions can be driven on and off resonance, as long as energy is conserved (in the example of Fig. 5.1 this implies $\omega_S - \omega_\xi = \omega_\mu$).

Raman heterodyne spectroscopy was first used by Mlynek et al. in 1982 to detect nuclear magnetic resonances [78, 79] but it can also be used to detect electron spin transitions. Since then Raman heterodyne spectroscopy has been employed on numerous occasions [80–83], in particular in the radio-frequency regime (ca. 0-200 MHz) in rare earth systems [84–87] but also in the microwave regime in ruby [88, 89] and metalloproteins [90].

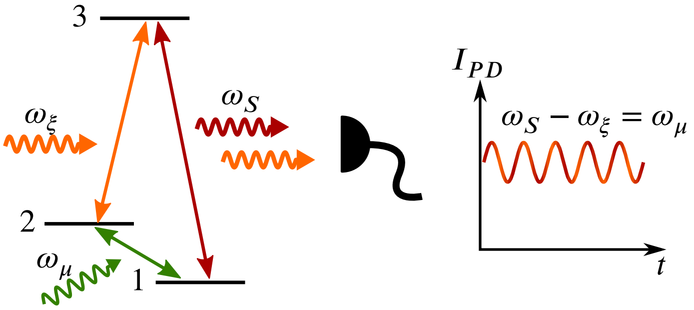

Figure 5.1: Raman heterodyne spectroscopy in a three level system.

The way Raman heterodyne spectroscopy works is schematically depicted in Fig. 5.1. In this figure a coherent microwave field at frequency ω_μ drives the 1-2 transition, while a coherent pump field at frequency ω_ξ drives the 2-3 transition. This generates a coherence between levels 1 and 3, which results in the emission of coherent light at frequency $\omega_S = \omega_\xi + \omega_\mu$. The generated signal beam is in the same transverse spatial mode as the pump beam, and the two fields travel together. When both frequencies strike a photodiode a beat note can be observed at the frequency difference $\omega_S - \omega_\xi = \omega_\mu$. This way of detecting sidebands is known as heterodyne detection. In general a beat note at the sum frequency $\omega_S + \omega_\xi$ can also be observed, but when ω_S and ω_ξ are optical frequencies this beat note is too fast for any technologically available detector to be detected.

A crucial parameter in our experiments is the photon number conversion efficiency. Following the diagram in Fig. 5.1 this means how many photons at ω_μ are converted into photons at ω_S. In order to calculate this we need to be able to determine the power of the generated optical sideband. In a heterodyne detection system, given a local oscillator power P_{LO} and a sideband power P_{SB} the total power can be written as

$$P_{tot} = P_{LO} + P_{SB} + 2\sqrt{P_{LO}P_{SB}}\cos(\omega t). \tag{5.1}$$

If this is detected with a photodiode of sensitivity d (in amperes per Watt) then the generated current will be

$$I_{tot} = dP_{tot} = I_{dc} + I_{ac}\cos(\omega t), \tag{5.2}$$

which I have explicitly split into a DC and an AC component. Comparing (5.1) and (5.2) it is clear that

$$I_{ac} = 2d\sqrt{P_{LO}P_{SB}}. \tag{5.3}$$

Note that this current is much bigger than what one would observe if the sideband was measured directly, as $P_{LO} \gg P_{SB}$. Heterodyne detection is a very useful technique when it comes to detecting small optical signals, because it makes them bigger. It also moves the signals away from DC, which means that frequency filtering can be used to increase the signal to noise ratio.

From Eq. 5.3 we can calculate the RF power coming out of the photodiode

$$P_{rf} = \frac{1}{2} R I_{ac}^2 = 2Rd^2 P_{LO} P_{SB}, \tag{5.4}$$

where R is the characteristic impedance of the photodiode (ideally $50\,\Omega$), and where the 1/2 factor takes into account the fact that the detected power is associated with the root mean square of the oscillating field rather than its peak amplitude. Rearranging terms in the previous equation we can write down the sideband power as a function of P_{rf} and P_{LO}:

$$P_{SB} = \frac{P_{rf}}{2Rd^2 P_{LO}}. \tag{5.5}$$

In any practical case P_{LO} will always be much greater than P_{SB}, and therefore P_{LO} can be taken as the total power measured in front of the photodiode with a power meter.

A more accurate way of working out P_{SB} is by calibrating the detection system by measuring P_{rf} for different known values of P_{LO} and P_{SB}. This can be done in the following way. Using an amplitude modulator one can generate symmetric sidebands around the central carrier. The size of these sidebands can be measured using a narrow frequency filter, like an optical cavity, by scanning either the frequency of the laser or the frequency of the cavity. Then it is only a matter of measuring P_{rf} for different sideband powers, keeping in mind that the power detected in the heterodyne setup coming from two sidebands equals four times the power that would correspond to each of the single sidebands. This is because when using two sidebands there is twice as much electric field at the sideband frequency, and P_{rf} is proportional to the square of the electric field. Note that this calibration can't be performed with a phase modulator, as the beat notes from symmetric phase modulated sidebands cancel each other. Calibrating is preferred over calculating because some parameters may not be very reliable, like d and R (particularly the latter). Additionally, the behaviour of the photodiode may depend on how tightly the incoming light beam is focused amongst other things. These sources of uncertainty can be ruled out if the calibration measurements are performed in the same conditions as the Raman heterodyne experiments, in particular regarding optical alignment.

5.2 Electron Paramagnetic Resonance

Electron paramagnetic resonance (EPR, sometimes also referred to as electron spin resonance or ESR) has been a widely used experimental technique since it's first observation by Yevgueni Zavoiski in 1944 [91]. The aim of EPR is to study materials with unpaired electrons. EPR works in a very similar way as nuclear magnetic resonance (NMR), but in EPR the electron spins are excited instead of the nuclear spins. In an experiment where the sample doesn't present hyperfine splittings but is susceptible to the Zeeman effect, a magnetic field $\mathbf{B}$ is applied in order to split the degenerate electronic energy levels. The size of this splitting is equal to $\Delta E = \mu_B g B$, owing to the Zeeman effect and to the fact that electrons have spin 1/2, where μ_B is the Bohr magneton and g is the g-factor or dimensionless magnetic moment. It is the value of g what one typically aims to measure in an EPR experiment. Simultaneously, an electromagnetic field (typically in the microwave region of the spectrum) is applied at a fixed frequency ω_{rf}. When $\Delta E = \hbar\omega_{rf}$ a change in the absorption properties of the sample is observed (see Fig. 5.2). By scanning the strength of the magnetic field and noting at which point the absorption becomes maximum it is possible to find the value of g. In non-isotropic materials g is usually a 3×3 tensor, and in order to determine its various components different measurements at different angles of $\mathbf{B}$ are required. Note that EPR can also be performed at zero magnetic fields by scanning the frequency of the microwave cavity instead. This allows one to measure zero field transition frequencies arising from effects like the hyperfine splitting.

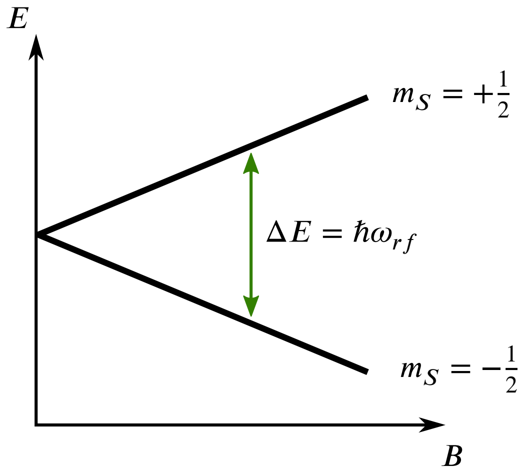

Figure 5.2: Schematic representation of EPR. The atmoic energy levels are Zeeman split under the effect of an applied magnetic field. A microwave field at frequency ω_{rf} is applied to the sample. When the energy difference between the levels equals $\hbar\omega_{rf}$ the absorptive properties of the sample change.

A very sensitive way of measuring the change in absorption of the sample is to place it inside a resonant cavity centred at ω_{rf}. As the magnetic field is scanned, when the frequency of the electronic transition approaches that of the cavity both systems become coupled, and what one observes is a frequency shift in the cavity's transmission spectrum. The frequency of the cavity is "pushed" away by the atoms, as schematically depicted in Fig. 5.3. More details of how this process works can be found in Appendix A.

In most EPR experiments the impedance matching to the cavity is tweaked in order to achieve critical coupling. Then, as the magnetic field strength is scanned, when the frequency of an atom is swept through the resonance with the cavity a change in its reflection coefficient is observed. This change in reflectivity can be measured with great sensitivity by using lock-in detection techniques, where the magnetic field is modulated at a given rate creating a modulation in the reflection signal, which can be measured using a lock-in amplifier or a similar instrument.

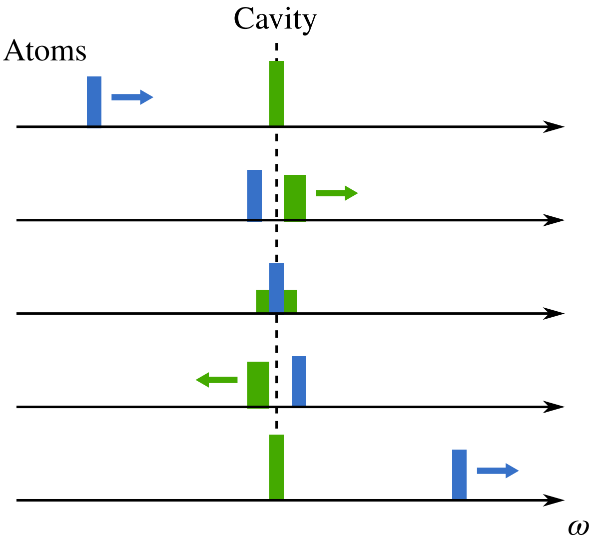

Figure 5.3: Effect of an atomic transition over a resonant cavity. When the frequency of the atoms approaches that of the cavity the frequency of the cavity is effectively "pushed" away from the atoms due to the atom-cavity coupling.

In our experiment we proceed in a different way. Instead of coupling to the cavity critically and measuring a change in reflectivity we measure the transmitted signal, for which we don't require critical coupling. Additionally, instead of modulating the magnetic field we modulate the frequency of the input signal into the cavity and measure the frequency shift using Pound locking techniques [92]. When the atomic frequency is swept through the resonance with the cavity frequency a modulation in the amplitude of the transmitted signal can be observed. This amplitude modulation is detected using a lock-in amplifier in the same way as in a conventional

EPR setup. This method has the advantage that we don't require modulation coils for the magnetic field, and that we don't require critical coupling to the cavity, which would be hard to achieve in our case.

A completely different way of measuring EPR is to measure the transmission spectrum of the microwave cavity directly using a network analyser, while scanning the magnetic field. This method offers a great advantage in its simplicity because the frequency shift can be read directly from the network analyser. It also has the advantage that it gives the full transmission spectrum of the cavity at any magnetic field. This allows one to read the cavity broadening due to the presence of the atoms on top of the frequency shift, which is particularly advantageous in cases where the coupling between the cavity and the atoms is strong, because when measuring EPR using the previously described techniques the effect of cavity broadening will give smaller measurements of the frequency shift than they really are. This is because a broader cavity has a less steep tangent at any given point than a narrower cavity (except when perfectly on resonance or when very far off resonance, where the slope of the tangent is zero). Measuring EPR directly with a network analyser, however, has the disadvantages that it is less sensitive than the alternative method, and it is also much slower. While a standard EPR measurement can be performed in a few seconds measuring EPR with a network analyser often takes several minutes, or even up to a few hours.

5.3 Optical Absorption

Optical absorption is a common spectroscopic technique, but some special considerations need to be taken into account when performing absorption measurements on rare earth doped crystals. In a typical optical absorption measurement a laser beam is shone through the sample and the output power is compared to the input power for different values of the laser frequency. In some cases the reflected power by the sample is measured too, although often this can be neglected due to the low reflectivity of many samples. This kind of experiment allow one to accurate measurements as long as the laser used to perform the measurement itself doesn't perturb the absorption properties of the sample. In rare earth doped crystals, and more particularly in the case of Er^{3+}:$\mathrm{Y}_2\mathrm{SiO}_5$, one has to put some thought to avoid this. This is because shining a laser on the sample will burn a spectral hole as explained in Sec. 3.3, which means that the absorption profile is modified.

The effect of spectral hole burning in an absorption spectrum measurement is that of giving an apparent higher transmission, or lower absorption overall. This is very pronounced in the case of Er^{3+}:$\mathrm{Y}_2\mathrm{SiO}_5$ because of the 11 ms lifetime of the excited state, which means that the spectral holes are relatively long-lived. There are several strategies that one can employ in order to avoid this effect. One of them is to use low laser power. The inconvenience of doing this is that the signals detected will be smaller, and therefore more noisy. The limit on how low a power one can use will be determined by the properties of the detectors at use. Another strategy is to set a scan in the frequency of the laser, which avoids having the laser on at a particular frequency all the time. This gives the spectral holes a certain amount of time to "heal" or disappear while the incident light is at some other frequency. Another way to look at it is that if the frequency of the laser is scanned the optical power gets distributed over a wider spectral region, thus burning shallower but wider holes. A third strategy is to use short pulses of light with a low repetition rate. Having the laser on for a shorter period of time means that the hole burnt will be less deep, and having a low repetition rate means that the hole can heal completely between shots. These three different strategies are not mutually exclusive, and in fact we have had to use them all simultaneously on occasions in order to get rid of hole burning completely, and take accurate measurements of the absorption spectrum of our samples.

Some of the samples used in the experiments described in Chs. 8 and 9 have a reflective coating on one of the ends. This means that measuring only the input and the transmitted power will not be enough to work out the absorption profile, as some of the optical power will be lost in the reflective surface. We are only interested in the absorption due to the erbium ions inside the sample. In order to compensate for reflection and for all other absorptive losses we can set the laser well off resonance with the erbium transitions and measured the transmitted power. This gives a reference of zero erbium absorption which compensates for all power losses in the setup and allows for accurate absorption measurements.

Chapter 6

Hole Burning Spectroscopy in $^{167}\mathrm{Er}^{3+}$:$\mathrm{Y_2SiO_5}$ and Usability at Zero Field

It was mentioned in Ch. 3.4 that one possibility for converting microwaves into optical photons using Er^{3+}:$\mathrm{Y_2SiO_5}$ is to use the $^{167}\mathrm{Er}$ isotope. This is the only stable isotope of erbium that has nuclear spin different from zero ($I = 7/2$) and therefore hyperfine splittings at zero magnetic field. The aim here would be to find a Δ-system within the hyperfine structure of either the ground ($^4I_{15/2}$) or the excited ($^4I_{13/2}$) state. Finding a Δ configuration of energy levels can be challenging, though, as one of the problems of working with $^{167}\mathrm{Er}^{3+}$:$\mathrm{Y_2SiO_5}$ is that its hyperfine structure for the excited state is unknown, and even the hyperfine structure for the optical ground state is not particularly well determined at zero magnetic field [70].

One of the first projects during my PhD was to try to reconstruct the $^4I_{13/2}$ excited state hyperfine structure for ions in spectroscopic site 1, using spectral hole burning spectroscopy (refer to Ch. 3.3 for details on how spectral hole burning works). In the present chapter I will talk about these experiments, and the results we obtained.

6.1 Experimental Setup

For this experiment we used an isotopically purified $^{167}\mathrm{Er}^{3+}$:$\mathrm{Y_2SiO_5}$ cylindrical sample. Its dimensions were 12 mm length by 4.95 mm diameter, with an $^{167}\mathrm{Er}$ concentration of 50 ppm. The sample was cooled to cryogenic temperatures ($\sim$4 K) in a closed cycle cryostat with optical access. We measured an optical absorption linewidth of about 2 GHz for this sample. This linewidth is a combination between hyperfine structure and inhomogeneous broadening. No individual inhomogeneously broadened peaks could be resolved, so it is hard to determine how much of it is due to inhomogeneous broadening alone.

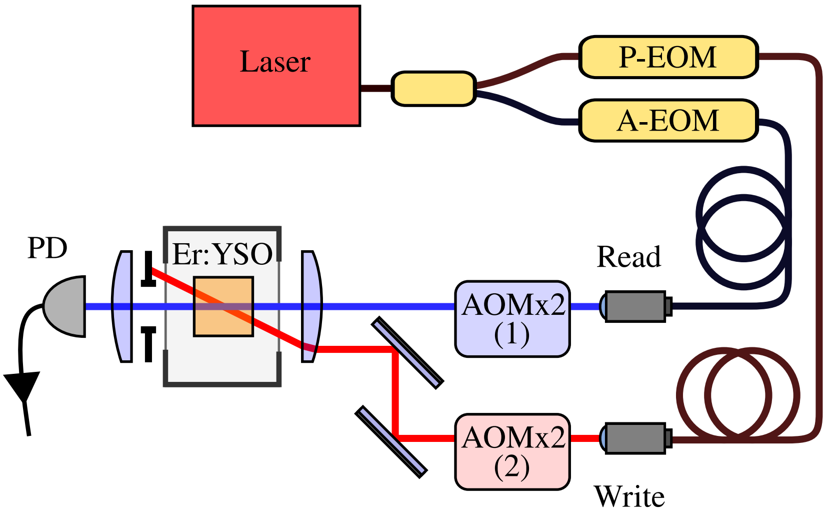

Figure 6.1: Experimental setup used for SHB spectroscopy of a ^{167}Er^{3+}:Y$_2$SiO$_5$ sample cooled at cryogenic temperatures. Light coming from the laser is split into a write and a read beam. The write beam burns a hole in the inhomogeneous line of ^{167}Er^{3+}:Y$_2$SiO$_5$, and the read beam is scanned to determine the positions of the side holes and anti-holes. The frequency of the write beam is controlled with a phase electro-optic modulator (P-EOM) while that of the read beam is is controlled with an amplitude electro-optic modulator (A-EOM). The beams are pulsed using acousto-optic modulators in double pass configuration (AOMx2). The transmission signal through the sample is measured with a photodiode (PD).

The experimental setup used for the spectral hole burning experiment is shown in Fig. 6.1. A laser beam coming from a fibre laser at around 1536 nm is split into a write and a read beam. The write beam passes through a fibre coupled phase electro optic modulator (P-EOM) while the read beam passes through an amplitude electro optic modulator (A-EOM). The role of these EOMs is to generate tunable sidebands on each beam so that we can scan the frequency of the write and the read beam independently. There was no special reason to use an amplitude or a phase modulator in either channel. The only aim of the modulators here was to produce sidebands, and we used what we had available at the moment. The RF power sent to each of the modulators was chosen to maximise the first order sideband while minimising all the other orders from each EOM, although in practice total suppression is not possible. In order to minimise the effect of the undesired laser frequency components the driving frequencies of the modulators need to be high enough so the carrier and the unwanted sidebands stay outside of the inhomogeneously broadened hyperfine line. The write and the read beams were focused in the center of the sample, but they did not share the same propagation axis. This was done in order to avoid saturating the detector with the strong light coming from the write beam.

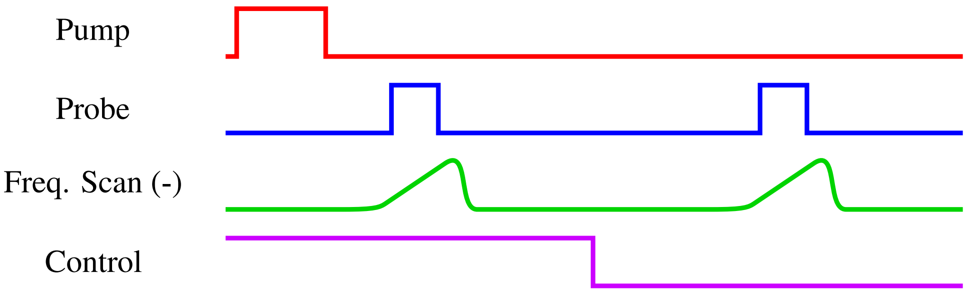

Figure 6.2: Pulse sequence used for the SHB experiments. Signal and background shots are alternated in time depending on the state of the Control channel.

The measurements were made in a pulsed regime (see Fig. 6.2), where the write beam is switched on for 30 ms and then the read beam is switched on for 0.2 ms, with a delay of 0.3 ms in between. Switching the light on and off was done using a couple of acousto-optic modulators in double pass configuration (AOMx2). The read pulse is synchronised with a frequency scan of the laser, which is generated by scanning the voltage of a piezoelectric transducer (PZT) inside the laser box, which changes the length of the fibre cavity by stretching the fibre [93]. This scan was 530 MHz wide. The scanning function sent to the PZT needs to be smooth in order to avoid high frequency components. To achieve this we programmed a function that starts with a Gaussian profile, then it is patched up with a linear region and at the end it is patched up with another Gaussian, such that at every stitching point the slopes of the Gaussians match that of the linear function. The pulse sequence also incorporates a control pulse that is used to take alternate background and signal shots, background meaning that the pump beam is off for that shot. In this way background subtraction from the signal can be performed in pseudo-real time for every shot, instead of subtracting a premeasured value equal for all the shots. This allows us to make a direct and accurate comparison of the shape of the inhomogeneously broadened hyperfine line with the pump beam on or off.

The way in which the frequencies are scanned is shown in Fig. 6.3. The P-EOM (write beam) is kept constant at 7 GHz. The A-EOM (read beam) is scanned between 100 MHz and 7.2 GHz in small steps. At each step of the A-EOM frequency scan several background and signal shots are taken (at least 40 of each), and the average of the background shots is subtracted from the average of the signal shots to get an absorption signal. We had to divide the read frequency scan in several parts because an RF amplifier broadband enough wasn't available. Once these different scans were done they were stitched together, and the frequency of the laser source was changed so that the write pulse burnt a hole in a different point of the inhomogeneous line, and the read pulse scanning process was started again. This was repeated until the write beam had scanned over the whole inhomogeneous line. Finally, we repeated the whole measurement process for several different temperatures of the sample.

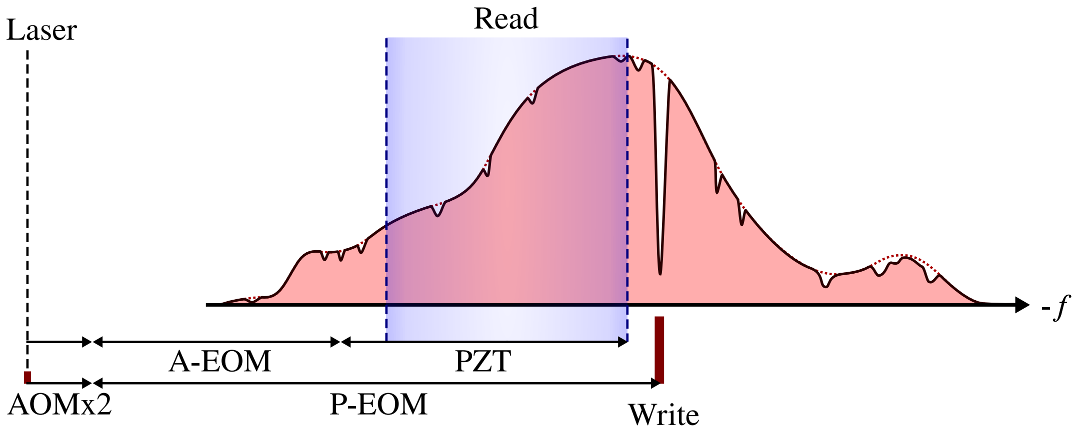

Figure 6.3: Frequency configuration used in the SHB experiments. The P-EOM that shifts the frequency of the write beam is kept at 7 GHz. The A-EOM that controls the frequency of the read beam is scanned between 0.1 and 7.2 GHz. The laser PZT provides an additional frequency shift of 80-610 MHz. The AOMx2 provides a total frequency shift of 170 MHz on each beam, in the same direction. Note the negative sign of the absolute frequency axis. Frequencies not to scale.

6.2 Experimental Results

The bulk of the experimental data obtained in these experiments can be found in Appendix C. Fig. 6.4 shows an example for the 3 K case. The different lines show the data obtained for different laser frequencies. The three blocks in which the data are divided correspond to the three different amplifiers that we needed to use to drive the A-EOM, as each of them operated in a different frequency range. Each line is composed of the data from several read scan shots, which have been averaged together. The vertical axis refers to the frequency of the write beam. The horizontal axis represent the frequency difference between read and write beams. The absolute frequency origin is taken to be roughly at the center of the inhomogeneous line.

The way to interpret the plot in Fig. 6.4 is the following: along the horizontal axis, a hole is always burned at $f_r - f_w = 0$, where f_r and f_w are the frequencies of the read and write beam respectively, with respect to the center of the inhomogeneous line. The features along the horizontal axis are the side holes and anti-holes that accompany the central hole at 0. Along the vertical axis the central hole is burnt at different positions of the inhomogeneous line. Many features can be observed in the data. Mainly a collection of side holes, although some of the features could be anti-holes. It is hard to make a judgement on whether it is one or the other due to how tightly packed the observed features are. The region around the end of each scan, near $f_r - f_w = 7$ GHz, is particularly noisy. This is because at that point the frequency of the A-EOM (read beam) is very close to zero, so the undesired frequency components of the read beam start to get in the way.

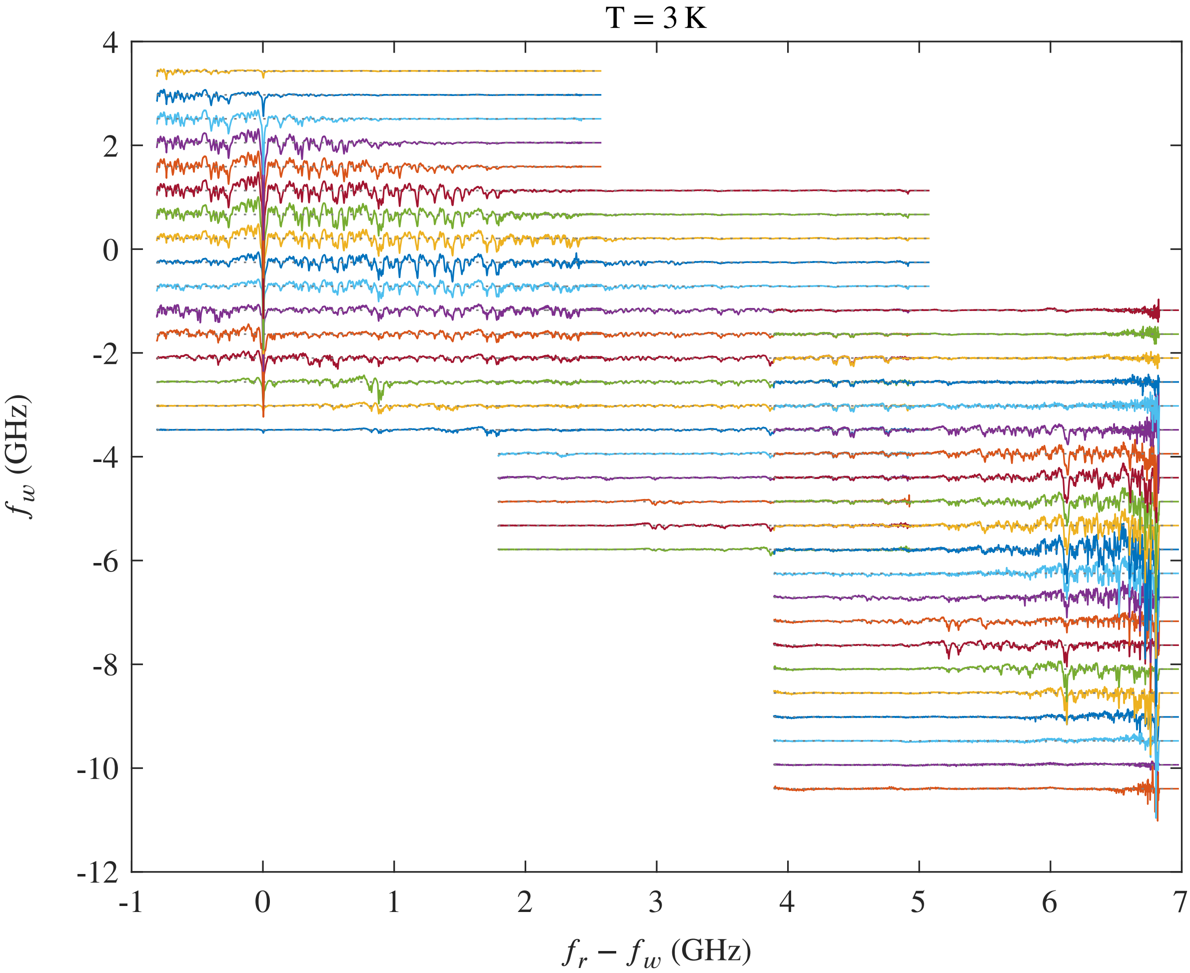

Figure 6.4: Example of SHB experimental results for a temperature of 3 K.

The width of the holes and anti-holes measured in these experiments is around 8 MHz, which is wider than what one usually measures in Er^{3+}:Y_2SiO_5. However, the laser used to burn the holes is substantially narrower than that (ca. 10 kHz), and we don't expect that the power levels we are using to be enough to cause power broadening of the holes, so we don't think that the width of the features observed is limited by the measuring setup.

Looking at how each particular feature changes when the temperature is varied should help to distinguish holes from anti-holes, but even then the task is hard. A detailed study of how side holes and specially anti-holes behave when the temperature is changed was published in Ref. [94]. In that case they studied the behaviour of side holes and anti-holes coming from the Zeeman split energy levels of the even isotopes of Er^{3+}:Y_2SiO_5. One of the things reported in that paper was the transition from side anti-holes to side holes as the temperature of the sample is increased, due to a change in the relaxation times between Zeeman states. A similar effect is likely to be happening with our sample in our zero field experiments. What determines whether a side hole or an anti-hole is created are the decay rates between the excited and the ground state manifolds and between hyperfine levels in the ground state manifold. When the write beam is on, if the decay time from the excited state to the ground state is shorter than the relaxation time between hyperfine levels, the atomic population will accumulate in the different hyperfine levels. Then, side anti-holes will be created. If the relaxation time between hyperfine levels is shorter than the decay time from excited to ground states then the atomic population will accumulate in the excited state, and side holes will be created. Looking at the plots at different temperatures (see Appendix C) one can see that as the temperature is increased the side holes get deeper. This is because at higher temperatures the relaxation process between hyperfine levels happens faster, and therefore the ratio between atomic population trapped in the excited state and in the ground hyperfine levels increases. Increasing the temperature even further degrades the quality of the side holes relatively fast, until they vanish.

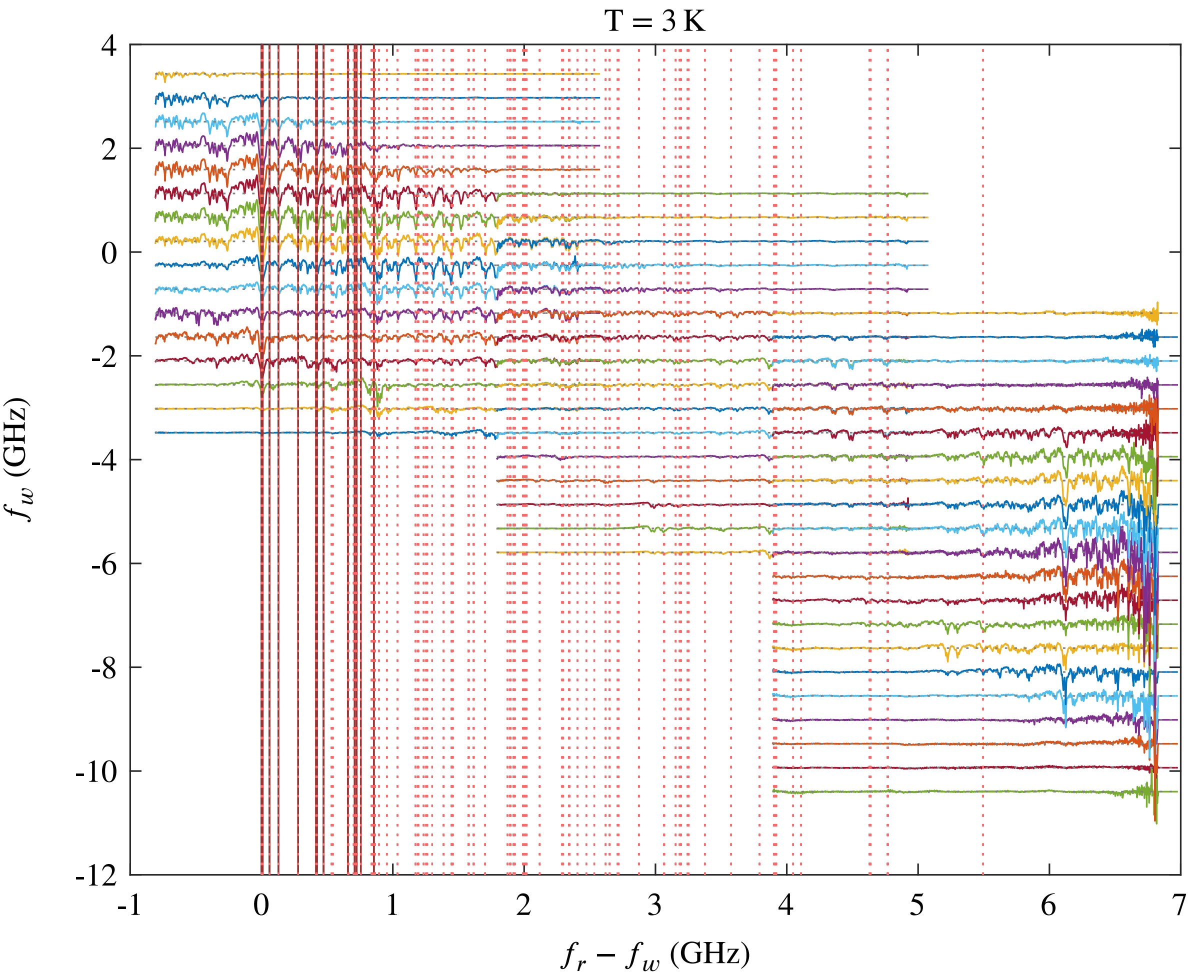

Figure 6.5: Comparison between SHB experimental results and predictions made using previously reported spin Hamiltonian parameters.

In an attempt to determine which side holes come from the hyperfine structure of the ground state and which side holes come from the hyperfine structure of the excited state the data were compared with previously published values of the spin Hamiltonian parameters [95]. These parameters were used to calculate the hyperfine energy levels of the ground state of $^{167}\mathrm{Er}^{3+}$:$\mathrm{Y}_2\mathrm{SiO}_5$ at zero magnetic field, and the positions of all side-holes and anti-holes related to the ground state were predicted. This is shown in Fig. 6.5. For an $I = 7/2$ nucleus 16 hyperfine energy levels are expected. This gives rise to 120 different transitions between these levels. These transitions are represented in Fig. 6.5 as vertical red lines. The solid lines represent transitions between immediately adjacent energy levels, and the dashed lines represent the rest of possible transitions. Note that this only gives the expected frequencies for a small fraction of the total number of side holes and anti-holes observed, but should nevertheless be a good place to start. Some of the lines are so close to one another that they are not resolved in the figure. It can be seen that some of the expected transitions match with some of the observed side holes, but it is hard to tell whether this is just a coincidence, as the whole picture is so cluttered with lines and peaks. Reported observations by Chen et al. using EPR spectroscopy in $^{167}\mathrm{Er}^{3+}$:$\mathrm{Y}_2\mathrm{SiO}_5$ [96] show discrepancies with the published spin Hamiltonian parameters.

Knowing the frequency differences between all side holes and anti-holes should in principle be sufficient to reconstruct the hyperfine structure of the ground and excited states of $^{167}\mathrm{Er}^{3+}$:$\mathrm{Y}_2\mathrm{SiO}_5$. A fair amount of effort was put towards this end. We started off by making a list of the frequencies of all the observed features, and calculated all the frequency differences between all of them. Then we tried to find frequency triplets, meaning groups of three frequencies f_1, f_2 and f_3 such that $f_3 = f_1 + f_2$. Similarly, we tried to find tetraplets too (groups of four frequencies). We could find between one and two hundred triplets and somewhere around fifty tetraplets. Then we tried to organise them in a way in which one of the frequencies of one triple/tetraplet matched one of the frequencies of another triplet/tetraplet, with the hope that this process would lead us to something resembling an energy level diagram. No conclusive results were obtained with this method.

6.3 Further Discussion and Conclusions

Reconstructing the excited state hyperfine structure of $^{167}\mathrm{Er}^{3+}$:$\mathrm{Y}_2\mathrm{SiO}_5$ using spectral hole burning data alone proved to be a non-trivial task. This is mainly due to the sheer amount of features that one can observe. It is possible that better or more spectral hole burning data may shine some light into the matter, in particular using lower sample temperatures, which would potentially allow one to distinguish side holes from anti-holes. A better way of solving this problem would be to combine these observations with other experiments, like zero field EPR and zero field Raman heterodyne spectroscopy.

At this stage we decided to use the even erbium isotopes and work with magnetic fields to Zeeman split the energy levels in order to implement our microwave to optical frequency conversion experiment. Since then Yu-Hui Chen, Sebastian Horvath and Jelena Rakonjac took over the project of characterising the hyperfine structure of $^{167}\mathrm{Er}^{3+}$:$\mathrm{Y_2SiO_5}$, both from the theoretical and from the experimental points of view. They have got some promising results, but to date none of it has yet been published.

Chapter 7

Frequency Conversion With Single Pass Optics: a Qualitative Study

In this section I will describe the first frequency conversion experiment that we realised. For this experiment we used a microwave cavity and single pass optics. The aim of this experiment was to test if the Raman conversion process in $\mathrm{Er^{3+}{:}Y_2SiO_5}$ actually exists and explore its qualitative behaviour as different parameters are changed. Most of the information contained in this chapter was published in Ref. [59]. All of the experiments presented in this chapter were performed in Professor Sven Rogge's laboratory at the University of New South Wales, in Sydney. The reason for this was that we didn't have a cryostat with a magnet at our disposal in our lab at that time.

In this experiment the ground ($^4I_{15/2}$) and the excited ($^4I_{13/2}$) states of the even isotopes of $\mathrm{Er^{3+}{:}Y_2SiO_5}$ are Zeeman split under the effect of an applied magnetic field $\mathbf{B}$ as per Fig. 7.1, making the $1 \leftrightarrow 2$ transition resonant with a microwave cavity at frequency ω_μ. An input microwave field then generates a coherence between levels 1 and 2. At the same time, an optical coupling field at frequency ω_ξ drives a second coherence between levels 2 and 3. The presence of these two coherences generates a third one between levels 1 and 3, which gives an output signal field at a frequency equal to the sum of the frequencies of the microwave and the coupling fields $\omega_S = \omega_\xi + \omega_\mu$. As long as the sample is small compared to the wavelength of the microwave field the signal field will be generated with the same transverse profile as the coupling beam. The signal field is then detected in a photodiode using heterodyne detection as a beat note at a frequency $|\omega_\xi - \omega_S| = \omega_\mu$ (as described in Ch. 5).

By looking at Fig. 7.1 one can see that the $2 \leftrightarrow 3$ optical coupling field is not the only option that will allow frequency conversion. In reality there are four possibilities for the coupling and the converted light frequencies, while keeping the input microwaves in resonance with the $1 \leftrightarrow 2$ transition: coupling $2 \leftrightarrow 3$ ($2 \leftrightarrow 4$) and converted signal $1 \leftrightarrow 3$ ($1 \leftrightarrow 4$), and the vice-

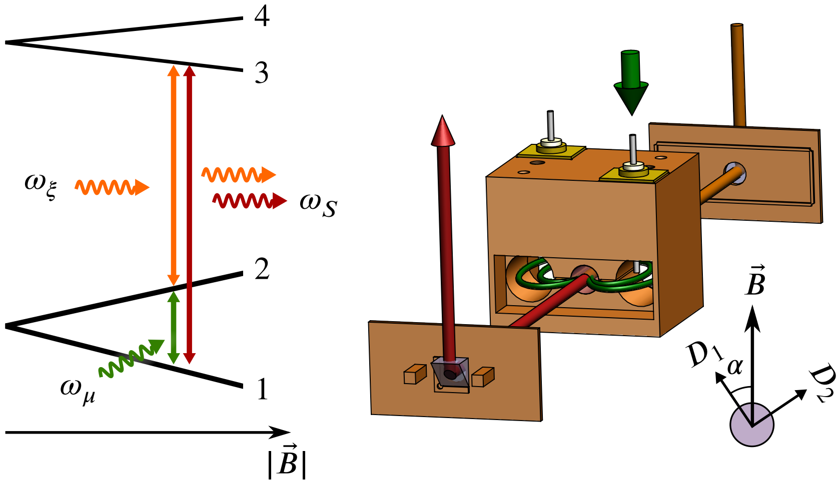

Figure 7.1: *Left:* the $^4I_{15/2}$ and $^4I_{13/2}$ levels in Er^{3+}:Y_2SiO_5 are Zeeman split under the presence of an external magnetic field $\boldsymbol{B}$. The Raman heterodyne signal is produced when a microwave field at frequency ω_μ and an optical field at frequency ω_ξ drive two transitions in a three level atom. A coherence is produced on the third transition which generates an optical signal field at frequency ω_S. *Right:* depiction of the experimental setup. A copper made loop-gap resonator holds an Er^{3+}:Y_2SiO_5 sample inside. Light is coupled in and out using a pair of prisms. Microwaves are coupled to the cavity via two straight antennas. The green loops inside the resonator represent the microwave magnetic field lines. The external magnetic field is applied in the vertical direction, parallel to the D_1-D_2 plane of the crystal, at an angle α as measured from D_1.

versa cases with coupling 1 ↔ 3 (1 ↔ 4) and converted signal 2 ↔ 3 (2 ↔ 4). For the cases in which the coupling field starts from level 2 only “pure” conversion is achieved. For the cases where the coupling field starts from level 1 parametric gain can also be present, meaning that a pump photon can be split into a signal and a microwave photon even if there is no microwave input into the system. As it will be shown later in the experimental results, however, parametric gain is negligible in these experiment since the optical depth of the sample is small. All the measurements presented in sections 7.2.2, 7.2.3 and 7.2.4 are performed in a configuration such as that presented in Fig. 7.1.

7.1 Experimental Setup

A schematic representation of the experimental setup used in this experiment is shown in Fig. 7.2. An Er^{3+}:Y_2SiO_5 crystal sits inside a loop-gap microwave resonator. We used a cylindrical Er^{3+}:Y_2SiO_5 sample of 4.95 mm diameter by 12 mm length, with an erbium concentration of 10 ppm. The optical b axis of the crystal was aligned along the length of the cylinder, and so the D_1-D_2 plane is parallel to the end faces. The orientation of the sample was chosen to make the angle α between D_1 and $\vec{B}$ as close as possible to $\alpha_M = 29°$(see

Ch. 3.4). The light fields were coupled in and out using graded index (GRIN) lens collimators and right angle prisms. The collimators were mounted in mirror mounts that could be operated at room and at cryogenic temperatures. The ensemble was suspended inside a hollow stainless steel tube of about 50 mm internal diameter. The tube was filled with helium at low pressure (ca. 1 mbar) that acted as a thermal exchange gas, and then submerged in liquid helium in a bath cryostat. The end of the tube was slid inside a superconducting solenoid that provided a magnetic field in the vertical direction of up to 0.3 T.

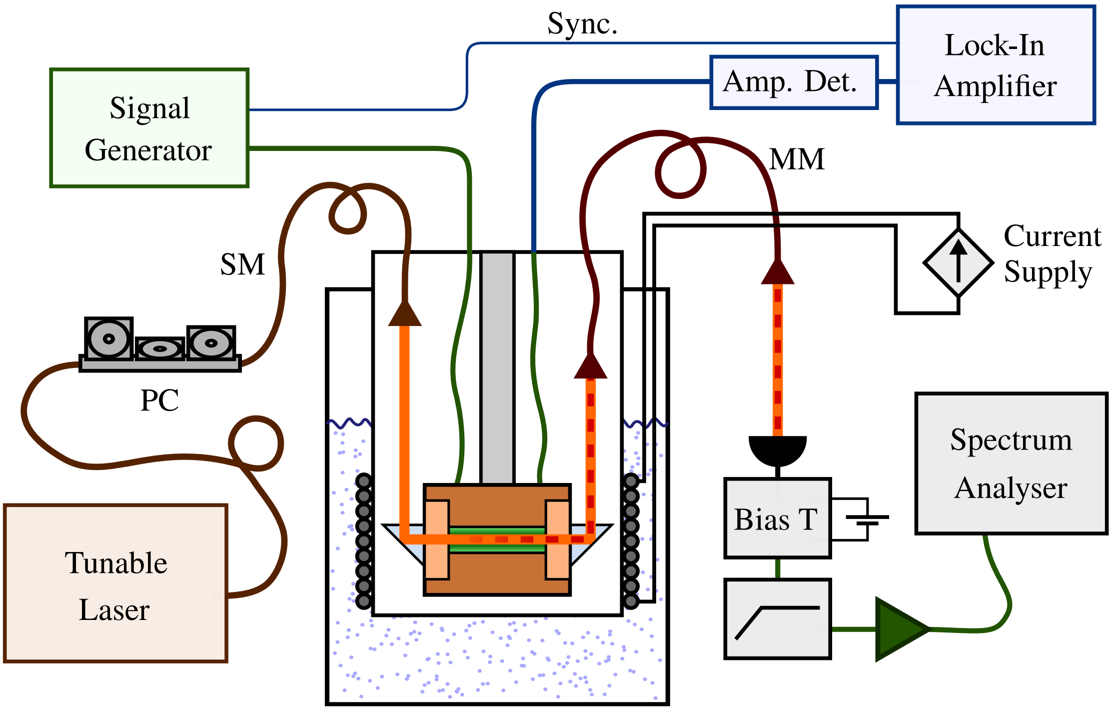

Figure 7.2: Experimental setup for the frequency conversion experiment with single pass otics. PC: polarisation controller, SM: single mode fibre, MM: multimode fibre. The Er^{3+}:Y_2SiO_5 sample (light green) sits inside a loop-gap microwave resonator (brown). The parts drawn in blue (top right) are used for EPR experiments only.

The pump laser beam was generated in a fibre-coupled external cavity diode laser at 1536 nm and amplified by an erbium doped fibre amplifier. A polarisation controller was used to maximise the heterodyne signal. While the input light comes from a single mode fibre the output light is coupled into a multimode fibre. The reason for using a multimode fibre over a single mode fibre is that coupling light into a multimode fibre is substantially easier. However this has a major drawback: since the pump and the converted field can travel in different modes inside the fibre a loss of coherence between the two fields will be seen when they reach the detector. This shows up as an effective loss of heterodyne signal. Moreover, the severity of this effect depends on how the multimode fibre is laid down at any given time. Coming out of the multimode fibre the signal was collimated into a fast photodiode (Hamamatsu G7096-03). A bias tee and a battery served the double purpose of biasing the photodiode and separating the AC from the DC components of the detected signal. The AC component was high pass filtered and amplified with a low noise amplifier, and finally analysed in a vector network analyser (FieldFox N9916A) working in spectrum analyser mode.

It was inevitable to have some optical losses in different parts of the setup. We could only fully characterise these at room temperature, with the setup taken out of the encasing stainless steel tube. The loss in power from the input fibre to the sample was practically negligible. The power loss from the sample to the detector was of about 5 dB, the main limiting factor being fibre coupling alignment. Once the system was cooled down we observed an optical loss between the input and the output of the system of around 10 dB. This additional loss only occurred when the setup was cold, which made it hard to investigate, so it still remains a mystery. It is hard to tell whether this added loss happened before or after the sample. We tried realigning the system from a misaligned state being cold and being warm, and when it was warm we could always consistently go back to a good value for the optical transmission, but not when it was cold. One possibility that would explain this loss is that the GRIN lens collimators change their properties at cryogenic temperatures. We find this the most likely explanation because we couldn't find a good reason to rule it out. Another possibility is that one of the fibres, or one of the fibre-to-fibre couplers inside the setup, stopped working when cooled down due to thermal contraction of some of the components. This is unlikely, as optical fibres are in general quite robust. A third hypothesis is that a thin layer of ice could be formed on the surface of any of the optical components (collimators, coupling mirrors, sample). We tested this hypothesis. In one experimental run we lowered the setup into the helium dewar with the tube being evacuated. In this way the sample rod with the collimators, microwave resonator and sample stayed warm, while the walls of the 50 mm tube were cold. The excess loss did occur when we added the exchange gas and the setup began to cool down. Because of this we can rule out frost or similar contamination, as any unwanted impurities in the exchange glass would have frozen out on the walls of the 50 mm tube while the setup inside was still warm. This observation further reinforces the hypothesis that some of the optical elements stopped working when they were cooled down.

On the microwave front we used a copper three-dimensional loop-gap resonator. Its resonant frequency was 4.9 GHz, with a linewidth of 16 MHz (quality factor $Q \simeq 300$). All the microwave resonators used in this thesis are loop-gap resonators, and they all have been designed by Yu-Hui Chen. Figure 7.3 displays a picture of how a typical loop-gap resonator looks like. In this case it consists of three loops (two big loops on the sides and a small one in the center) and two gaps linking the loops together. The loops act as inductors and the gaps act as capacitors, giving the equivalent of an LC circuit and therefore exhibiting a resonance frequency, which will depend on the size of the loops and the gaps. The resulting effect is an AC electric field that oscillates vertically across the gaps, accompanied by a circular current along the walls of the loops. At the same time an AC magnetic field oscillates inside the loops, its direction being parallel to the axis of the central hole, as shown by the green rings in Fig. 7.1. A copper cap was added to each end of the resonator to avoid leakage to the outside.

Loop gap resonators offer several advantages over other types of resonators. The magnetic field is very uniform in the central hole. This is where the sample sits. Additionally they have a very good filling factor, which is the parameter that determines what portion of the energy stored in the magnetic field overlaps with the sample. In the resonators that we use in our lab we typically get filling factors of around 0.8. An added advantage of this kind of resonator is that optical access to the sample is made simple by drilling a hole at the center of each of the end caps. Because the electric and magnetic fields are zero at that point the properties of the cavity are barely affected. Finally, loop gap resonators can have high Q factors, on the order of several thousands. The reason why the Q factor in this experiment is relatively low is because the cavity is highly overcoupled, meaning that most cavity loss happens through the input and output connectors.

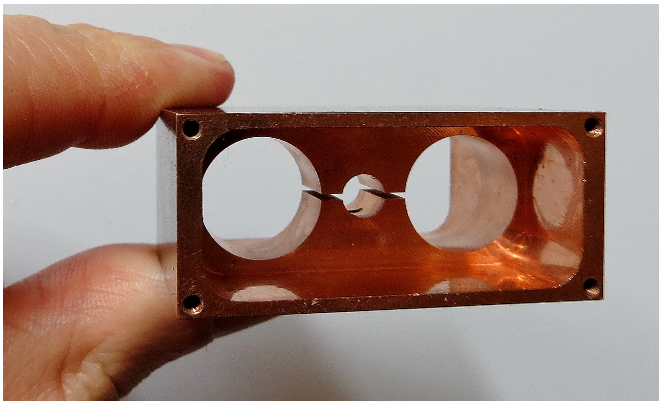

Figure 7.3: A loop-gap resonator.

To drive the microwave cavity we use an R&S SMP 22 signal generator. The signal was coupled in and out of the cavity using a pair of straight antennas. Transmission through the cavity ($|S_{21}|^2$) was measured to be -6 dB at room temperature. Microwave losses along the cables from the signal generator to the cavity input were measured to be about 8 dB. This number could be expected to change once the setup is cooled down, but this is again a quantity that we could not measure.

Because the beat frequency that we are trying to detect is at the exact same frequency that we are using to drive the microwave cavity it is unavoidable that some background signal coming directly from the signal generator gets picked up by the detector and the low noise amplifier after it. I will call this the “pick-up noise” from here on[1]. The pick-up noise could be observed even with the output of the signal generator switched off, meaning that it came straight from the oscillator inside the signal generator to either the photodiode or the low-noise amplifier. Leakage through wires and through the cavity itself only aggravated the issue. Some effort was put into shielding the detection system from the pick-up noise, but we could not get rid of it completely. The workaround in this experiment was to work at high enough microwave and optical powers so that the detected signal would be considerably higher than the pick-up noise. This noise presented a real nuisance during the early stages of the experiment when most of the parameters were not well optimised and the signal levels were low, as it was very easy to mistake one for the other. It was not until much later that we found an effective way to shield the detection apparatus by using products more commonly found in Japanese cuisine (see Ch. 8).

The part drawn in blue in Fig. 7.2 shows the bits used for EPR experiments only. This setup consists of an amplitude detector and a lock-in amplifier (SRS SR830). In the EPR experiments shown in this chapter an FM modulation at 3 kHz was added to the microwave signal. As the signal passes through the cavity the FM modulated signal turns into an AM modulated signal, where the modulation amplitude is proportional to the slope of the cavity transmission curve. This amplitude was measured with an amplitude detector connected to the lock-in amplifier, which needs to be synchronised with the FM modulation at the signal generator.

7.2 Experimental Results

7.2.1 Converted Signal vs. Laser Frequency vs. Magnetic Field

The first thing we explored was how the heterodyne signal changes as a function of laser frequency and magnetic field. These results are shown in Fig. 7.4. The power of the generated sideband P_S is plotted against the frequency detuning of the laser from the center of the inhomogeneous line at zero magnetic field $\Delta\omega_\xi$, and the magnetic field strength B. On the left side, in white, are plots of the optical absorption spectrum for $B = 0$ (dotted line) and for $B = 0.178\,\mathrm{T}$ (solid line). Due to etalon effects the background of these measurements is not constant. In the optical absorption spectrum for $B = 0.178\,\mathrm{T}$ the four optical transitions can be observed. The strong ones ($1 \leftrightarrow 3$ and $2 \leftrightarrow 4$) appear as peaks around $\Delta\omega_\xi/2\pi = \pm 1.6\,\mathrm{GHz}$, while the weak

---

[1] Technically speaking the term “noise” is inappropriate here, as this pick-up signal wasn’t random in its origin. However it was almost random to all practical effects, as the amount of signal being picked up would depend on things such as where in the lab people physically were, or how one would wave his/her hands around the setup. The reason why I call it noise is because it is an undesired background effect that obscures the level of signal.

ones (1 ↔ 4 and 2 ↔ 3) appear as smaller shoulders at about $\Delta\omega_\xi/2\pi = \pm 3.4$ GHz. The ratio between the absorption level of the weak and the strong lines matches with the expected value for $\alpha \simeq \alpha_M$. From the absorption measurements we can extract an inhomogeneous broadening of the optical lines of ~2.5 GHz at FWHM. This value is substantially higher than what we often observe in $Er^{3+}:Y_2SiO_5$ samples (see Ch. 8). We believe now this extra broadening to be caused by mechanical stress in the crystal[2]. Comparing the Raman heterodyne spectroscopy data with the absorption spectrum at $B = 0.178$ T one can see that the main four peaks in the color plot coincide with the absorption on each of the lines, as it is to be expected.

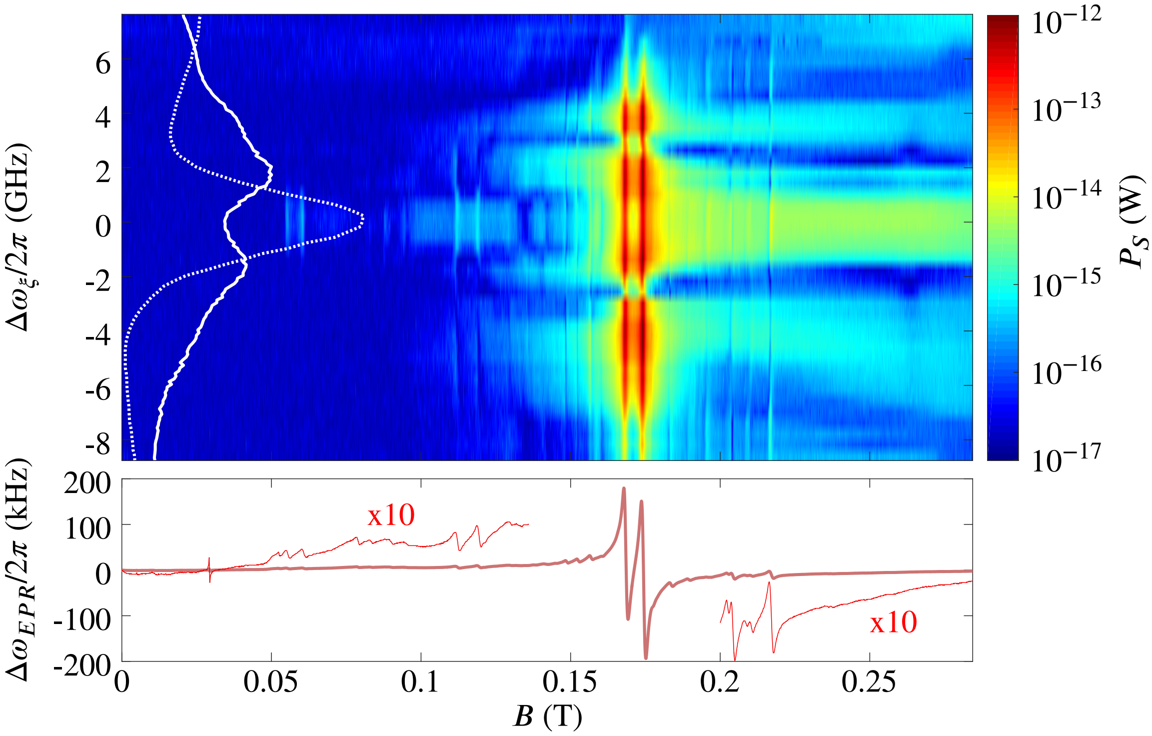

Figure 7.4: *Top*: Raman heterodyne spectroscopy on $Er^{3+}:Y_2SiO_5$, showing frequency conversion from microwaves at 4.9 GHz to optical frequencies. The strength of the magnetic field is plotted in the horizontal axis, and the coupling laser detuning is plotted in the vertical axis. The color scale indicates the power of the output signal field. On the left, the white dotted line represents the optical absorption spectrum for $B = 0$. The solid white line corresponds to the optical absorption spectrum for $B = 0.178$ T. At this magnetic field the 1 ↔ 3 and 2 ↔ 4 transitions are expected to be around $\Delta\omega_\xi/2\pi = \pm 1.6$ GHz, and the 1 ↔ 4 and 2 ↔ 3 transitions around $\Delta\omega_\xi/2\pi = \pm 3.4$ GHz. *Bottom*: EPR spectrum of the $Er^{3+}:Y_2SiO_5$ sample. The regions away from the main peaks have been magnified for clarity. In both plots the presence of double peaks along the horizontal axis is due to misalignment in the magnetic field, breaking the magnetic degeneracy of the two inequivalent orientations of Er^{+3} in Y_2SiO_5.

---

[2] In later experiments the hole in which the sample is mounted was slightly enlarged and the amount of vacuum grease used around the sample was decreased to a minimum. The optical inhomogeneous line observed in these experiments was considerably narrower, as it will be shown in Ch. 8.

Beneath the Raman heterodyne spectroscopy data is the electron EPR spectrum of the sample (see Ch. 5 for an explanation of how our EPR experiments are performed). The maximum frequency shift observed is around 180 kHz. However these measurements are taken at 0 dBm for the input microwave power which is enough to start saturating the microwave transition. For saturation-free measurements, at lower microwave powers, a maximum shift of around 260 kHz was observed. From this frequency shift one can calculate the cavity-atom cooperativity factor, which in this case is of the order of 6×10^{-2}. Comparing the Raman heterodyne and the EPR spectra one can see that most of the features present in the Raman heterodyne spectroscopy data are also replicated in the EPR data. The EPR peak at $B \approx 0.03\,\mathrm{T}$, which is not present in the Raman heterodyne data, is caused by erbium ions in Site 2 of Y_2SiO_5. Because the optical transition for these atoms is at a different wavelength (around 2 nm away) there is no Raman heterodyne signal there.

It is notable that all of the features appearing in the Raman heterodyne spectrum as well as in the EPR one are doubled in the horizontal axis. The reason for this is a slight misalignment of the magnetic field, not being completely parallel to the D_1-D_2 plane, so the degeneracy between the two inequivalent orientations in Y_2SiO_5 is no longer present. Another feature to note is the collection of additional lines at both sides of the main peaks. These are due to the ^{167}Er isotope and its hyperfine structure.

The reassuring point in Fig. 7.4 is the excellent agreement between data taken from three independent experiments. In the optical absorption experiment only optical light and optical transitions are involved. In the EPR experiment only microwaves and microwave transitions are involved. In the Raman heterodyne experiment both optical and microwave fields are involved, and all the data agree with each other. This is to be expected, but it allows us to be confident that the signal that we are detecting actually comes from a Raman transition such as the one shown in Fig. 7.1. In turn this proves that microwave to optical frequency conversion is possible in $Er^{3+}:Y_2SiO_5$, which was the main goal of this experiment.

7.2.2 Scaling with Input Powers

Next we wanted to study the dependence of the converted sideband P_S with the input optical and microwave powers P_ξ and P_μ. The results are shown in Fig. 7.5. For these measurements the laser power is measured at the output of the system, and is not corrected for optical losses between the sample and the power meter, as these are not reliably quantified. Similarly, the microwave power is the value set at the input of the setup. The dependency of P_S with P_μ follows the expected pattern for a three wave mixing process: it increases linearly until it reaches a saturation point, around $P_\mu = 20\,\mathrm{dBm}$. These measurements are taken for $P_\xi = 1.8\,\mathrm{mW}$. The dependency of P_S with P_ξ, however, doesn't follow a linear relation for large laser powers.

The faster than linear rate at which the signal increases with the pump laser power is due to optical pumping which increases the population difference between the two $I_{15/2}$ Zeeman levels, lowering the effective spin temperature. These measurements are taken for an input microwave power $P_\mu = 0\,\text{dBm}$, and with the optical and microwave fields on resonance with the atomic transitions.

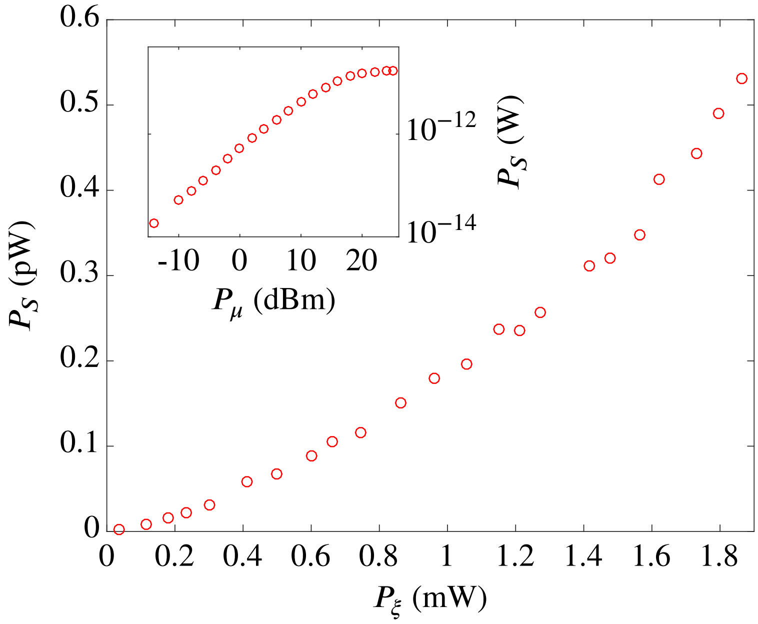

Figure 7.5: Converted sideband power as a function of detected coupling laser power (main figure) and input microwave power (inset). The faster-than-linear growth of P_S versus P_ξ shows optical cooling of the spins via optical pumping/hole burning.

7.2.3 Conversion Efficiency

By comparing the input and the sideband powers it is possible to calculate a number conversion efficiency $\eta_n = \frac{P_S}{P_\mu} \cdot \frac{\omega_\mu}{\omega_\xi}$. This efficiency η_n accounts for the fraction of microwave photons converted into optical photons. For a coupling power of ~2 mW and making the appropriate corrections for the known optical and microwave propagation losses in the system we get a conversion efficiency of $\mathcal{O}\left(10^{-12}\right)$. This value doesn't take into account microwave coupling losses into the cavity, so it is not a *process efficiency*, it is a *device efficiency*. Since the cavity is strongly overcoupled, however, these losses are small (about a factor of two). This conversion efficiency matches within reason with what the $\Lambda^{(2)}$ model predicts, although it is hard to compare since these measurements are taken with the optical and microwave fields being on resonance with the atomic transitions, where the model becomes unreliable. Also, saying something quantitative about the experimental conversion efficiency is difficult because the losses were all poorly quantified, as we were incapable to characterise them at low temperatures.

7.2.4 Coherence of the Conversion Process

While we didn't perform any direct measurement of phase preservation in the up-conversion process we can be certain that this process is a coherent one. The observed heterodyne peaks are a few tens of Hz wide. Both the optical and the microwave transitions in Er^{3+}:Y_2SiO_5 are much wider than that, hence the only explanation is that this signal is indeed generated in a Raman scattering process, which is inherently coherent. In other words: the only process in the sample that can generate such a narrow signal is a coherent process. In addition, we were performing heterodyne detection, so the measurements are only sensitive to that light which is coherent with the pump beam.

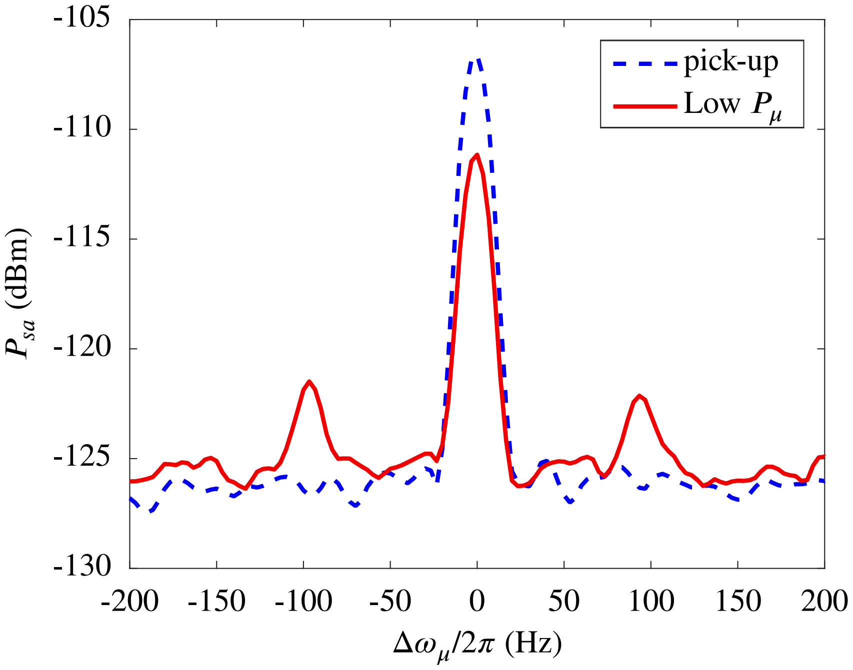

Figure 7.6: Heterodyne signal as measured by the spectrum analyser, showing interference between the generated signal and the pick-up noise from the signal generator. The sidebands are attributed to sidebands in the laser frequency due to mechanical vibrations in the laser box.

To further support our claim there is the following experimental observation related with the pick-up noise, represented in Fig. 7.6. When measuring the heterodyne signal power P_{sa} with the spectrum analyser against the input microwave power, for high microwave powers the heterodyne signal was much bigger than the pick-up noise, and the later one could be neglected. For low microwave powers, however, these were of comparable size. In this situation it was possible that the detected peak became smaller than the pick-up noise alone. This means that the detected signal and the pick-up noise were interfering destructively, which in turn means they were coherent with each other. It is safe to assume that the pick-up noise was coherent with the signal coming out of the signal generator since they came from the same source, so one can conclude that the converted signal is coherent with the input microwave signal, and therefore so is the conversion process.

7.3 Further Discussion and Conclusions

The main conclusion extracted from this experiment is that the three wave mixing process mixing optical and microwave photons in Er^{3+}:Y_2SiO_5 exists, and that it is possible indeed to coherently convert microwave signals into optical ones. This is a novel result in such a system, and it is an important step towards achieving quantum frequency conversion between optical and microwave frequencies.

At the time of performing this experiment the efficiency measurements were not completely reliable due to several factors. The loss of heterodyne signal in the multimode fibre was hard to take into account, as it depended on the particular shape in which the fibre was laid out. We could only make an estimation of how big this effect were be by twisting and bending the fibre in different ways, but getting a precise value was not possible. Another factor was the sudden loss of output light when the system was cooled down. Even though the total effect could be measured it was hard to estimate whether the loss occurred before or after the sample. These problems were solved later on when we set up a similar experiment in our lab in Dunedin, which used free space optics instead of optical fibres. This experiment is described in Ch. 8. In the Dunedin experiment there were also substantial improvements to the detection setup, greatly increasing its sensitivity and being able to suppress the pick-up noise down to noise floor levels. Additionally, a vector magnet capable of orienting the applied magnetic field in different angles was used, getting rid of the magnetic inequivalence observed in Fig. 7.4 between subclasses I and II in Er^{3+}:Y_2SiO_5.

Chapter 8

Frequency Conversion With Single Pass Optics: a Quantitative Study

After the first frequency conversion experiment performed in Sydney (see Ch. 7) we set up a similar experiment in Dunedin. The new setup needed to be able to accommodate an optical cavity which would boost the conversion efficiency dramatically. At the same time this experiment would allow us to take more data for single pass optics, which would be done in a more systematic way than in Sydney, as the constraints of lack of time and lack of our own equipment that we had there would no longer exist. Moreover, the experimental setup used in Dunedin presented several improvements with respect to the one used in Sydney, as will be described in the following sections. The experiments realised with an optical cavity will be discussed in Ch. 9. The present chapter will be devoted to single pass experiments only. The two experiments done in Dunedin use an almost identical setup with the exception of the optical cavity, so some of the things explained in this chapter will be useful for the following one.

One of the reasons to travel to Sydney was that, at that time, we did not have a suitable magnet in our lab to perform Raman heterodyne spectroscopy experiments. Moreover, none of the cryostats that we had in our lab were big enough to house a magnet that would meet our requirements. This problem was solved by building a new cryostat: the Kraken-Xavostat. The first section of this chapter talks about how this cryostat was built and some of its characteristics. Then I will move on to explaining the remaining of the experimental setup, and later on I will show the experimental results followed by a discussion and conclusions.

8.1 Building a Cryostat: The Kraken-Xavostat

Building a cryostat was a very interesting task during my PhD. It took many hours of design and many more of manufacturing, assembling and testing, adding up to at least 20-30% of my total time during my PhD. I designed the cryostat myself, with lots of advice from Jevon, Luke Taylor (a postdoctoral fellow in the group) and Peter Stroud (the mechanical engineer in the Department of Physics). The machining of most of the components was done by Peter Stroud in the mechanical workshop of the department. Some parts were too big to be machined in the university's workshop and needed to be outsourced, but it was mostly done locally in Dunedin, including several helium tight welds. More specialised components like cable feedthroughs and optical windows were bought from overseas. Finally we did all the assembly and testing process in our lab. I named it the Kraken-Xavostat. The Kraken bit comes from the mythological giant octopus-looking monster from the northern seas of Europe. With so many cables springing out of the cryostat this is what it makes me think of. Plus it is quite big. The Xavostat bit was democratically elected by the members of the group at that time.

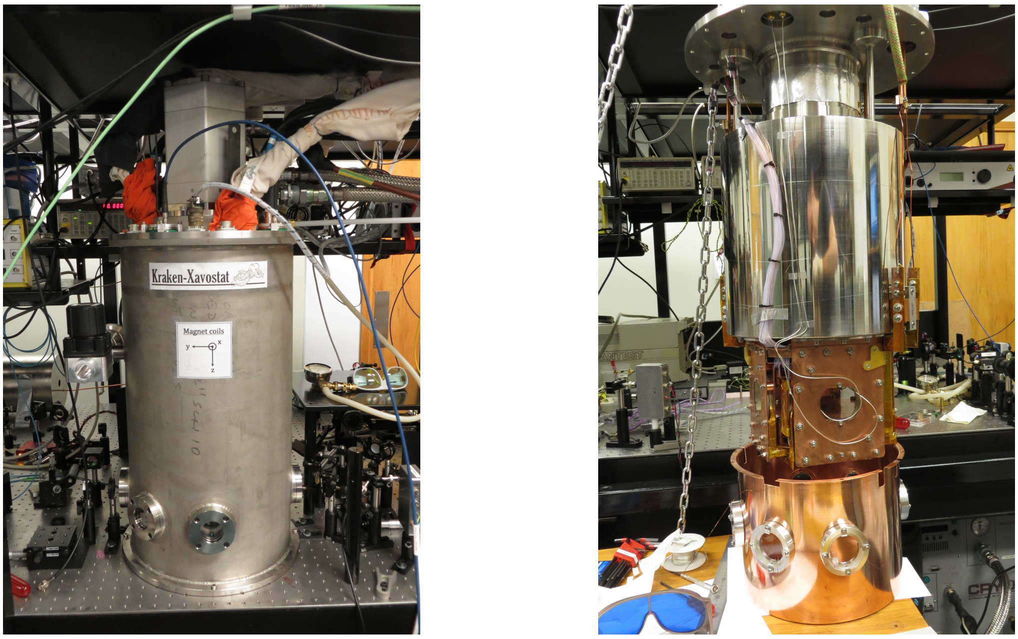

(a) (b)

Figure 8.1: (a) The Kraken-Xavostat fully operational sitting on the bench and (b) the Kraken-Xavostat being opened, displaying the LN2 Tank, the HTS Magnet and the Heat Shield. The top part of the Liquid Can can also be seen.

The cooling power comes from a helium closed cycle refrigerator (PT405). This was bought from Cryomech several years prior to my arrival to the group. The cooling head has two cooling stages. The first stage has a cooling power of 25 W at 65 K. The second stage has a cooling power of 0.5 W at 4.2 K. The minimum nominal temperature of the second stage with no load is 2.8 K.

The magnetic field is generated by a custom made high temperature superconducting magnet (from HTS-110). It has three orthogonal pairs of coils. As a function of the driving current the vertical coil (*z* coil) produces 10.4 mT/A, while the horizontal ones (*x* and *y* coils) produce 0.343 mT/A. The maximum driving current for each coil is 30 A, so the maximum attainable

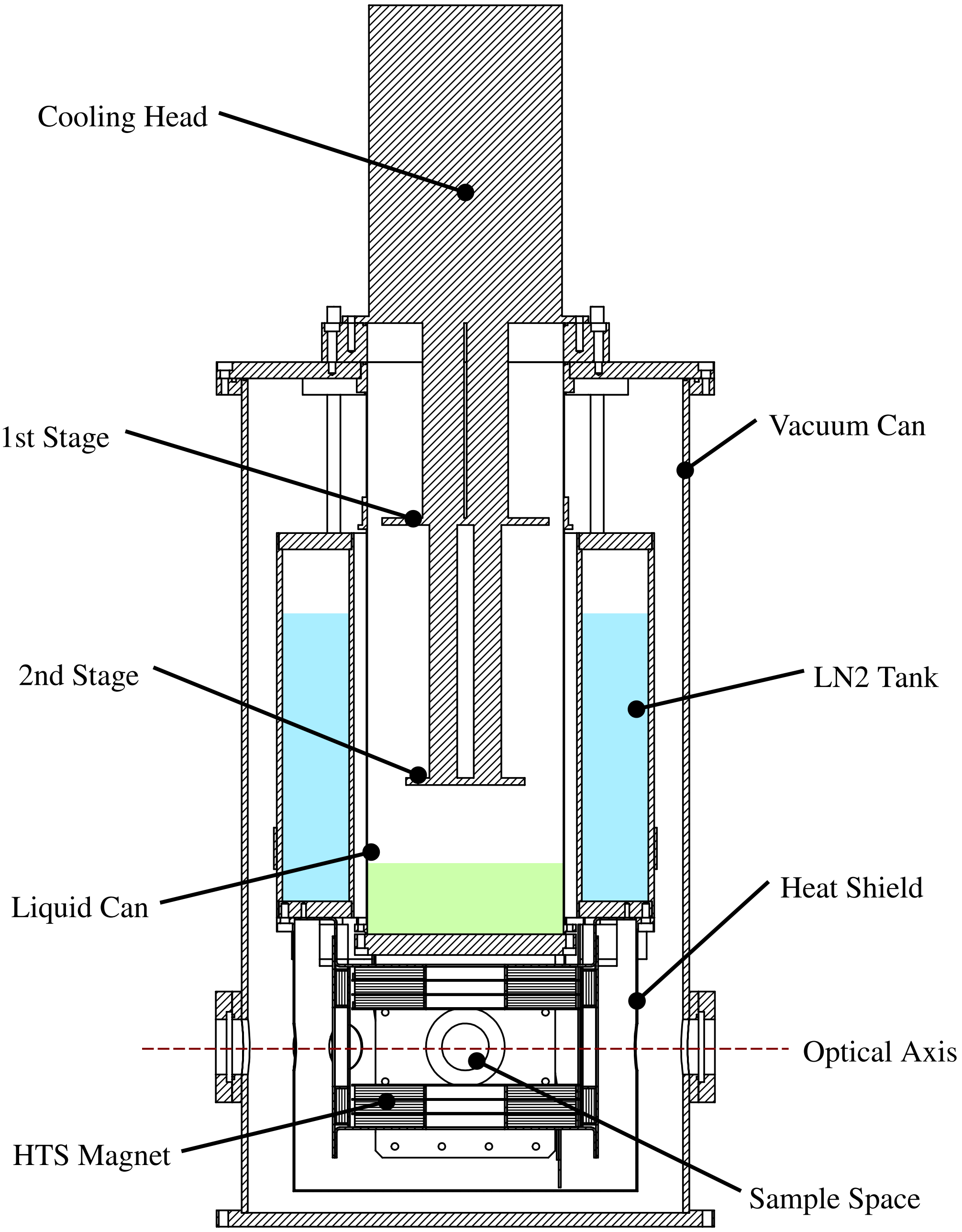

Figure 8.2: Schematic representation of the Kraken-Xavostat.

magnetic field in the z (x/y) direction is 312 mT (10.3 mT). The magnetic field inhomogeneity for the z coil is of -0.5% at 5 mm from the center radially, and +0.3% at 2.5 mm from the center axially, as specified by the manufacturer. For the x and y coils this is -0.6% at 5 mm radially and +0.4% at 2.5 mm axially. The magnet pack needs to be cooled down below 70 K before it is ready to operate.

Fig. 8.2 shows a schematic representation of the different parts of the Kraken. At the center, the Liquid Can is connected to a helium reservoir (not shown in the figure) that holds about 650 l of helium gas at room temperature. The cooling head is responsible of cooling down a fraction of this helium and condense it into liquid. This makes a puddle of liquid helium (shown in green) at the bottom of the Liquid Can. The bottom piece of the Liquid Can is a copper disk to which the sample mount can be attached. The walls of the Liquid Can are made of stainless steel, and need to be relatively thin (0.5 mm) to minimise thermal conductivity, as the top of the Liquid Can is at room temperature and the bottom is below 4 K. The seal between the walls of the Liquid Can and the bottom piece is a knife-edge seal (a sharp edge of stainless steel "biting" the softer copper).

Surrounding the liquid can there is the Liquid Nitrogen Tank (LN2 Tank). This is a hollow toroidal tank that is filled with liquid nitrogen. The magnet and the Heat Shield are directly attached to the LN2 Tank. The LN2 Tank serves a double purpose. On the one hand it shields the liquid can from thermal radiation, acting as a heat shield. On the other hand it cools the magnet down to operating temperature. In order to get the magnet below 70 K it is necessary to connect a vacuum pump to the LN2 Tank, as decreasing the pressure decreases the boiling point of a liquid. The LN2 Tank connects to the exterior through three different stalks. One is used as a liquid nitrogen inlet, another one is used as a gas nitrogen outlet, and the third one is connected to a pressure gauge and a pressure relief valve for safety. The Heat Shield, hanging from the LN2 Tank, shields the sample from thermal radiation coming from the external shell of the cryostat.

The outermost shell, the Vacuum Can, provides a sealed space inside the cryostat that can be evacuated. Having the interior of the cryostat under vacuum is critical, as any gas would act as a thermal bridge between the external world at room temperature and the cold sample below 4 K. The Vacuum Can seals are sealed using standard rubber O-rings. The Kraken has three optical axes in the horizontal plane. Two of them orthogonal to each other, and the other one at 45°. The x and y axis of the magnet are aligned with the orthogonal optical axes of the cryostat.

The design of the Kraken-Xavostat, in which the Cooling Head and the sample mount are not directly mechanically attached, helps to reduce vibrations while the cooler is running. But the principal advantage of this design is that, since there is a puddle of liquid helium at the bottom of the Liquid Can, the Cooling Head can be switched off completely, thus reducing vibrations to a minimum. An added advantage is that, by pumping on the gas inside the liquid can the boiling temperature of the helium puddle can be decreased, thus reaching temperatures even lower that liquid helium at atmospheric pressure. In contrast, in the more traditional approaches, the sample is directly attached to the second stage of the cryostat. This means that one has to choose between having the Cooling Head on to keep the sample cold, but at the same time introducing unwanted vibrations, or switching off the Cooling Head to get rid of vibrations at the expense of an increase in temperature over time (which usually happens quite fast).

Cooling down the cryostat from room temperature to operating temperature takes about three hours. Then helium condensation starts. Reaching the stationary state of helium condensation (i.e. condensing the maximum amount of helium possible) can take from 12 to 24 hours, depending on the characteristics of the sample and the thermal load it introduces (through connecting wires, thermal radiation, etc.). The pressure of the helium tank can be controlled using a gas regulator, typically set to around 0.4 bar. This corresponds to a temperature of about 3.5 K. Switching the cryostat off after maximum condensation has been reached allows for 2 to 3 hours of cold temperatures, while the helium puddle evaporates. Using a vacuum pump to decrease the temperature in the Liquid Can allows for liquid helium temperatures below 2.5 K. Warming up the cryostat to room temperature takes close to 20 hours.

8.2 Experimental Setup

In this experiment we used free space optics instead of optical fibres like we used in the Sydney experiment described in Ch. 7. A schematic drawing of the experimental setup can be found in Fig. 8.3. One of the aims of this experiment was to provide data that could be directly comparable with the data gathered from the cavity experiment (described in Ch. 9). Therefore, we used the same sample in the same orientation, and when we coupled the light into the sample we tried to mimic the same spatial profile as the cavity mode, so that we address a similar total number of atoms as in the cavity experiment. The sample used was an Er^{3+}:Y_2SiO_5 cylinder doped at 10 ppm, of 12 mm length and 4.95 mm diameter. In order to sustain a cavity mode one of the ends of the sample was cut with a curvature radius of 100 mm, and it was coated to have high reflectivity at 1536 nm. The other end of the sample was flat, and coated to have high transmission at 1536 nm. More details about the cavity mode will be given in Ch. 9. How this translates into the present experiment is by pushing us towards performing the measurements in a double pass configuration as shown in Fig. 8.3, i.e. light comes into the sample from one side, it bounces on the reflective surface of the sample and it comes out the same way it went in. In order to separate the incoming from the outgoing light we used a 50/50 beam splitter. A coupling lens of 300 mm focal length was used to shape the beam with the same spatial profile as the cavity mode discussed in Ch. 9. A linear polariser, a $\lambda/4$ and a $\lambda/2$ waveplates were used to set the polarisation of the light in order to maximise the Raman heterodyne signal.

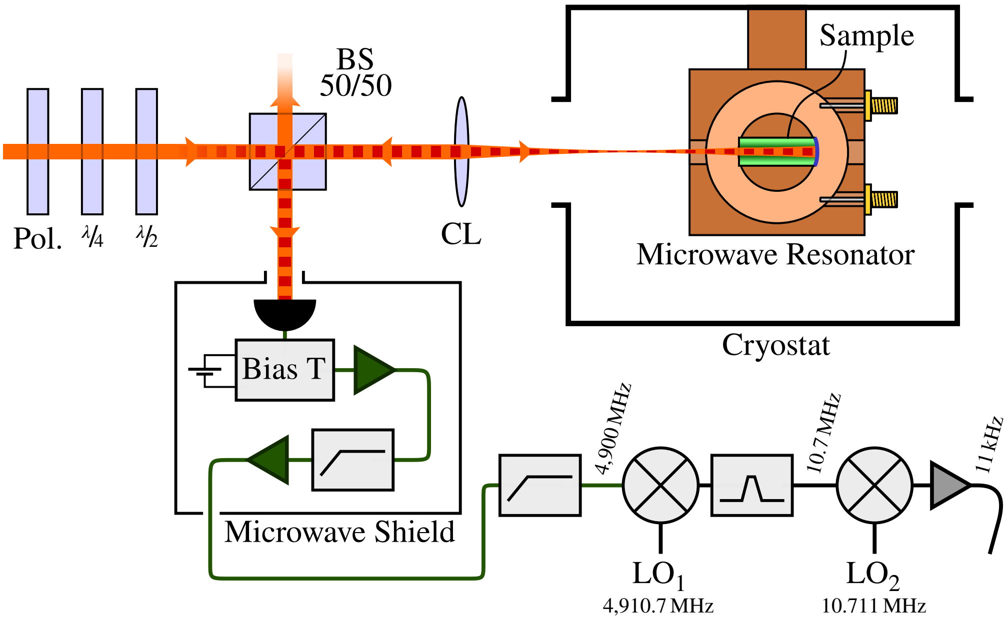

Figure 8.3: Schematic representation of the experimental setup. The microwave resonator is driven by a signal generator at 4.9 GHz. The sample (in green) sits inside a tunable microwave resonator. Light from the laser comes from the left hand side of the image, crossing a polariser, a $\lambda/4$ and a $\lambda/2$ waveplates. Then it crosses a 50/50 beamsplitter and a coupling lens which is used to give the beam the desired spatial profile. Light travels across the sample, getting reflected back on its rightmost surface. After being reflected by the 50/50 beamsplitter again it reaches the detection setup.

Another important difference between this setup and the one used in the Sydney experiment is that in this case we used a tunable microwave resonator. While this tunability will not play a major role in the present experiment it will become very relevant in the experiments described in Ch. 9. This tunable microwave resonator was made out of high quality oxygen free copper in order to minimise the microwave loss in the surface of the material. A picture showing the microwave cavity is presented in Fig. 8.4. For the double pass experiment the mirror mount on the left of the microwave resonator is taken out, so that light can be coupled in and out from that side. The copper body at the center of the image forms the bulk of the microwave cavity. The pillar in the center holds the Er^{3+}:Y$_2$SiO$_5$ sample, which is mounted using a thin layer of vacuum grease to offer good thermal contact with the copper walls. The closeness of the fit is such that if the resonator is turned on its side at room temperature the sample will slowly slide out over a period of time of several seconds, but once the setup has been cooled down the copper of the cavity shrinks more than the sample, applying enough mechanical pressure between them so that the thermal contact is good enough to keep the crystal at the required temperatures. At the right side of the picture in Fig. 8.4 there is a copper plunger that is mounted on a linear micro-mechanical actuator (attocube). The actuator is mounted on an L shaped cover that gets screwed into the main body of the resonator, so that the plunger stands directly on top of the pillar holding the sample, as shown schematically in Fig. 8.5. The gap between the pillar and the plunger forms the "gap" in the loop-gap resonator, and by changing it's size one can tune the resonance frequency of the cavity. The tunability range of this microwave resonator is between approximately 3 and 5.3 GHz.

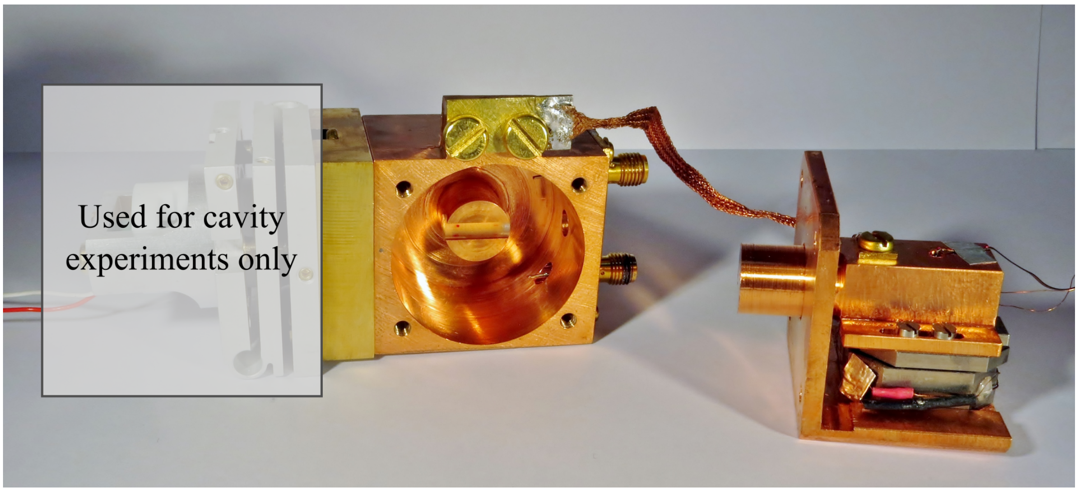

Figure 8.4: A picture of the tunable microwave cavity with the Er^{3+}:Y_2SiO_5 sample inside it. The main body of the cavity can be seen at the center of the image. The part sitting on the right of the picture is the plunger mounted on an attocube micro-translation stage, which is used to tune the frequency of the resonator. Both bodies are connected with a copper bride to facilitate thermal conductivity.

To couple microwaves in and out of the cavity we used a pair of straight antennas inserted directly into the main body, as can be seen in Fig. 8.4. The antennas are soldered into SMA connectors. The outer walls of the cavity also have holes that allow us to couple light in and out from both sides, left and right. Observed with a network analyser the transmission peak has a FWHM of around 750 kHz when the cavity is cooled down to 4 K, for a central frequency tuned around 4.9 GHz. The corresponding quality factor Q is of around 6500, which is primarily limited by intrinsic loss in the copper's surface. Under these conditions the measured transmission parameter $|S_{21}|^2$ is around -17 dBm, which has been corrected for microwave losses in the connecting wires (losses measured at room temperature). Designing and testing this microwave cavity was a combined effort between Yu-Hui Chen and myself.

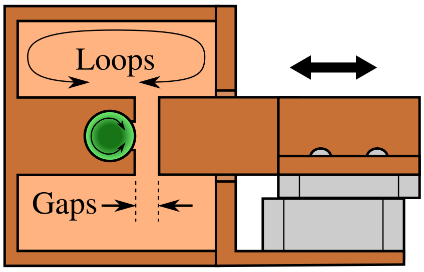

Figure 8.5: Schematic representation of a cross section of the tunable microwave resonator. The plunger moves in and out thanks to the attocube micro-translation stage changing the size of the gap, thus changing the resonance frequency of the cavity.

The detection setup used in this experiment and in the experiments presented in Ch. 9 represents an improvement over that used in our first experiments in Sydney (Ch. 7). In the Sydney experiment the heterodyne signal was detected using an amplifier and a spectrum analyser connected directly after the bias tee as shown in Fig. 7.2. In the present experiment the signal at microwave frequencies is demodulated down to a frequency of a few kHz and observed on an oscilloscope. The advantage of this method is that the signal can be read much faster. While the spectrum analyser takes tens or hundreds of milliseconds to update its received signal an average oscilloscope has a time resolution several orders of magnitude faster than that. This allows us to take faster and different kinds of measurements. An example would be a measurement in which the frequency of the laser is scanned at a rate of several hundreds of Hertz, which we would not have been able to measure with the previous detection setup. The way in which the signal is demodulated is by first using a mixer with a local oscillator frequency equal to the input microwave frequency plus 10.7 MHz (LO_1 in Fig. 8.3). This gives an output signal at 10.7 MHz which is then filtered using a narrow bandpass filter. The frequency of 10.7 MHz was chosen because of the availability of narrow bandpass filters around that frequency. A second mixer with a local oscillator frequency equal to 10.711 MHz (LO_2 in Fig. 8.3) mixes the signal down to 11 kHz. The signal is then sent to an SRS pre-amplifier that further filters and amplifies the signal, and finally measured in an oscilloscope. The 11 kHz frequency was chosen because of the available filtering stages of the SRS pre-amplifier. With this detection setup the amplitude of the 11 kHz signal seen in the oscilloscope is proportional to the square root of the microwave power coming out of the AC port of the bias tee. Additional frequency filtering can be achieved by averaging the signal in the oscilloscope. To this end a signal at 11 kHz coming from an additional signal generator is used to trigger the scope. Even though all the signal generators used in the experiment share a common time base they were not phase locked to one another, so a slight mismatch could be observed between the frequencies of the 11 kHz signal coming from the detection setup and the 11 kHz signal used to trigger the oscilloscope. This effect manifested itself as a time dependent phase shift between both signals at a constant rate. This could be compensated by adjusting the frequency of the signal generator used to trigger the oscilloscope by a small amount (usually between 0.001 $\sim$ 0.1 Hz). The detection setup can be easily calibrated by substituting the bias tee by a microwave signal generator and checking the proportionality factor between the power of the signal generated by the signal generator and the peak-to-peak amplitude squared of the signal in the oscilloscope. This detection setup offers great sensitivity, allowing us to measure RF powers as low as a few tens of attowatts (note that this value makes reference to the RF power as it would be coming from the bias tee).

The first stages of the detection system are placed inside a microwave shield in order to avoid the pick-up noise described in Ch. 7.1. This shield has two parts, a reflective one and an absorptive one. The reflective part of the shield is an aluminium box of 6 mm wall thickness. This box has two small holes. One at the front for light to be able to reach the photodiode, and one at the opposite end for several cables to go in and out. These are the power supply cables for both amplifiers and the RF output that carries the detected signal. Since the aluminium box alone wasn't enough to bring the pick-up noise down to a level at which we would be satisfied I decided to add an absorptive layer to it. It is well known that water absorbs microwave radiation, so this was my first thought. Unfortunately filling the aluminium box with water would at the very least put the detectors and amplifiers in danger, if not destroy them completely. To get around this issue I prepared several "bricks" of agar. Agar is a jelly-like substance commonly found in Japanese cooking. It is made of seaweed powder mixed with water. It is also used as a sterile culture medium in biology labs. These agar bricks were inserted in sealed plastic bags to protect the electronics, and placed inside the aluminium box, as shown in Fig. 8.6. This solution reduced the level of pick-up noise by around 40 dB, bringing it down to levels below the laser noise in the detection system.

8.3 Experimental Results

In this section I will present the data obtained from different experiments performed in the previously described setup. First I will show two experiments aimed at the characterisation of the sample and the interaction of the sample with the microwave cavity. These are an optical absorption and an electron paramagnetic resonance experiment. The data coming from these experiments will be very useful in terms of making meaningful predictions using the $\Lambda^{(2)}$ model described in Ch. 4. The EPR section will be divided in two parts. In the first one I will show EPR measurements performed with our standard EPR setup, that makes use of Pound locking techniques in order to measure the frequency shift of the microwave cavity as the magnetic field

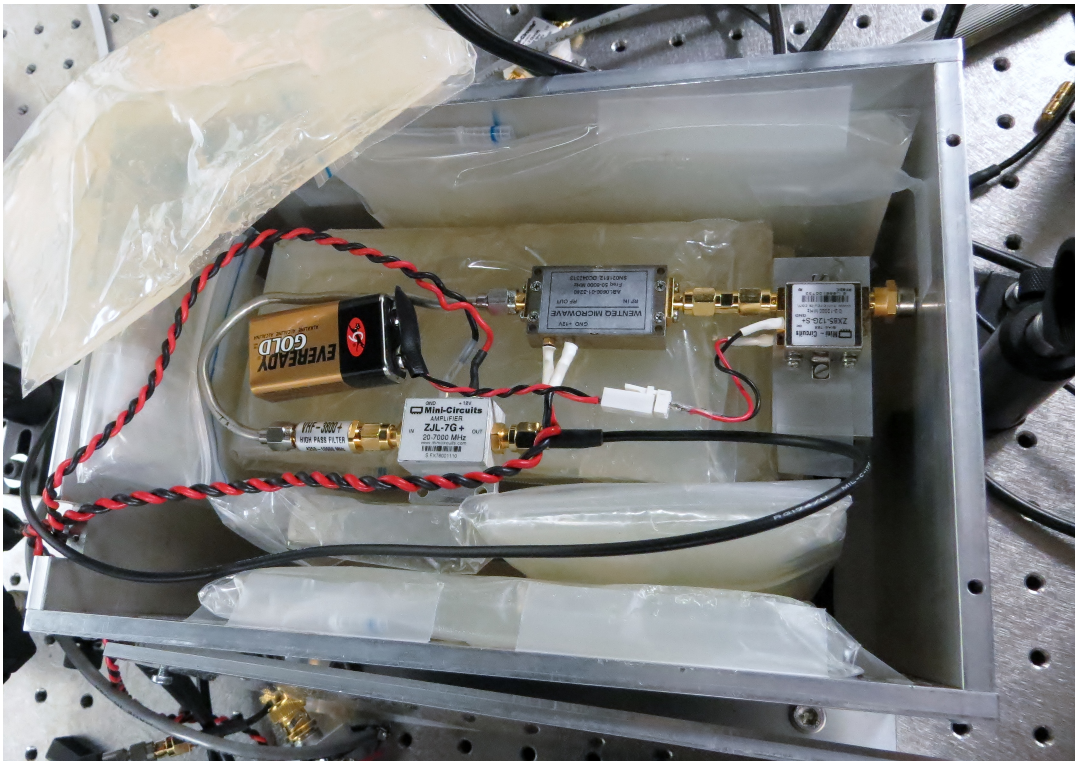

Figure 8.6: Microwave shield box used to avoid pick-up noise in the detection setup. An aluminium box with thick walls provides a reflective layer of protection, while a collection of agar bricks provides an absorptive one.

is swept. Then I will explain why the data obtained in this way can be easily misinterpreted for a system in which the coupling between the atoms and the cavity is strong. After this I will show a different set of EPR measurements in which the cavity transmission spectrum is measured directly with a network analyser as a function of the magnetic field strength, which is a less sensitive method and much more time consuming, but provides straightforward data. These data will be compared with the theoretical model explaining atom-cavity interaction (see Appendix A) in order to extract some crucial information about the sample. Finally, I will show Raman heterodyne spectroscopy measurements from which a conversion efficiency can be deduced, and I will compare the data obtained with the predictions from the $\Lambda^{(2)}$ model.

8.3.1 Optical Absorption

Knowing the optical properties of our sample is crucial in order to perform Raman heterodyne spectroscopy experiments. In the experiment presented in this section we measured the optical absorption spectrum of the crystal at zero and at non-zero magnetic field. In order to take accurate optical absorption measurements it is important to avoid burning spectral holes in the inhomogeneous profile of the atoms, as this would show a lower level of absorption than the real one. In order to avoid this we performed these measurements using very low optical power (a few microwatts), we pulsed the laser, and we scanned it's frequency in time as discussed in Ch. 5.3. The results are shown in Fig. 8.7.

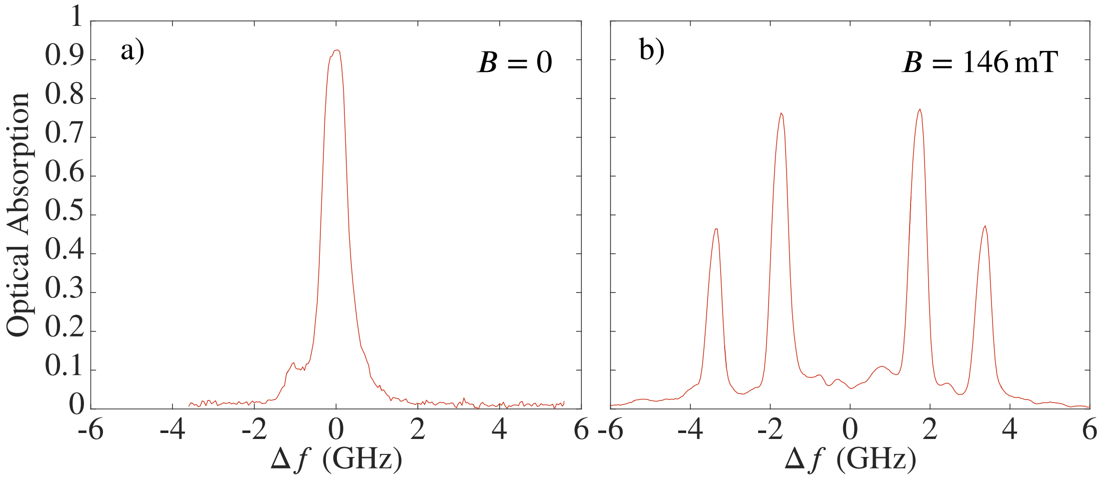

Figure 8.7: Optical absorption (calculated as one minus transmission) through the Er^{3+}:Y_2SiO_5 sample at zero magnetic field (a) and at $B = 146\,\mathrm{mT}$ (b). In order to avoid hole burning these measurements are performed with weak short pulses in synchrony with a short ranged frequency scan. The measurement at $B = 0$ can be seen to saturate near the top of the central peak. The small sidepeaks are due to the ^{167}Er isotope.

Comparing the peaks for the $B = 0$ and the $B = 146\,\mathrm{mT}$ measurements one can see that when the magnetic field is off one gets very close to full absorption, which distorts the shape of the absorption peak. Therefore the inhomogeneous linewidth is better determined by looking at the measurements when the magnetic field is on. The FWHM of the inhomogeneous line was determined to be around 0.4 GHz. This is much narrower than that measured in Ch. 7. A possible reason is the way in which the sample was mounted inside the resonator. In the Sydney experiments we used a larger amount of vacuum grease around the sample, not giving much room for thermal contraction. In the present experiment we used a minimal amount of grease, which means that the sample sits a bit more loosely inside the resonator at room temperature, but also that it doesn't get so much mechanical stress when cooled down. Note, however, that the samples used in both experiments are different, and that the inhomogeneous line shape, which is essentially a measure of the crystal quality, can change from sample to sample even for equal dopant concentrations.

From the height of the peaks in Fig. 8.7.b) we can extract two important parameters that will be required in order to calculate the value of $\Lambda^{(2)}$. These are the transition dipole moments for the different optical transitions. These dipole moments are assumed to be electric dipole moments only, as it was discussed in Ch. 4.2.3. The fitted values are $\mu_{31} = \mu_{42} = 2.6 \times 10^{-32}$ C·m for the strong transitions (second and third peaks) and $\mu_{41} = \mu_{32} = 1.7 \times 10^{-32}$ C·m for the weak transitions (first and fourth peaks).

Another feature that can be observed from the measurements in Fig. 8.7 is a collection of smaller side peaks around the main absorption peak. These are attributed to the ^{167}Er isotope. From the plot in Fig. 8.7.a) these peaks may seem rather innocuous, but in Fig. 8.7.b) it can be seen that once the magnetic field is switched on they spread throughout a wide range around the main absorption lines. This doesn't present a big problem for the double pass experiments described in the present chapter because the absorption due to ^{167}Er is relatively low, but as it will be discussed in Ch. 9 this can become a real issue once an optical cavity is added.

8.3.2 Electron Paramagnetic Resonance

Knowing the microwave properties of our sample is also crucial in order to perform Raman heterodyne spectroscopy experiments. In this section I will describe the electron paramagnetic resonance experiments that we performed in our lab. As discussed in Ch. 5.2 we employed two different techniques to perform EPR spectroscopy: a more sensitive one in which we use Pound lock techniques and a lock-in amplifier to detect the frequency shift in the cavity and a less sensitive method that in exchange offers more reliable data in which the frequency shift is measured directly with a network analyser. I will show the lock-in amplifier method first, and I will explain and show how and why the data obtained can be easily misinterpreted. The reason to show these data is because misinterpreting EPR data was the source of big problems during our experiments, and this was an exemplar mistake from which to learn things. After this I will show the data obtained with the network analyser and extract some meaningful information from them.

The setup used to perform the first EPR experiments is analogous to that shown in Ch. 7.1 and the data are taken in the same way. The results are presented in Fig. 8.8, where several measurements at different microwave powers are shown. The frequency on the horizontal axis is the frequency of the atomic transition as the magnetic field is scanned minus the frequency of the microwave cavity at zero magnetic field. On the vertical axis is the frequency shift of the cavity due to the presence of the atomic microwave transition. The microwave power P_μ represents the power right at the entrance of the microwave cavity, and it has been corrected for wire losses between the signal generator and the cavity.

It can be seen in Fig. 8.8 that the EPR signals don't have the typical dispersive shape for these kind of measurements (e.g. see the bottom plot in Fig. 7.4). Moreover, the maximum frequency shift and even the shape of the signal depends on the input microwave power. This suggests that the microwave power that we were employing was high enough to saturate the

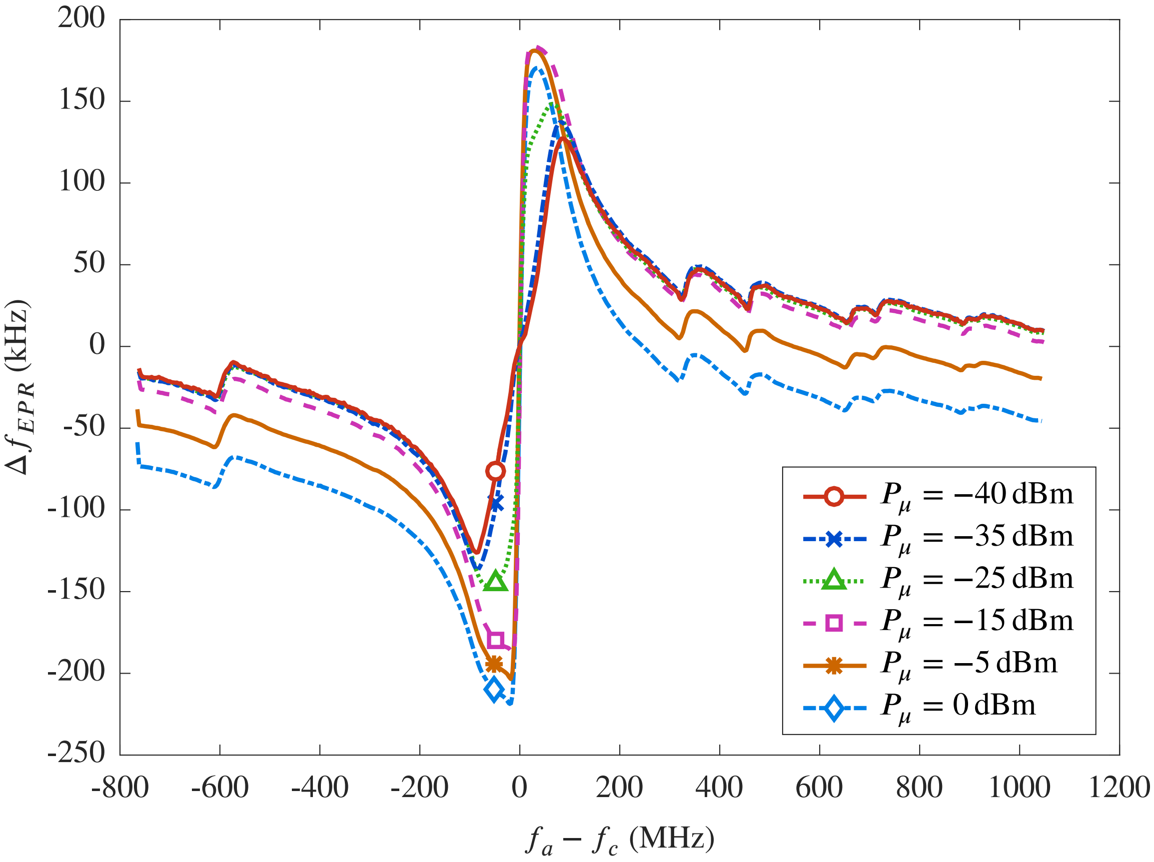

Figure 8.8: Electron paramagnetic resonance signals measured with the lock-in amplifier using Pound locking techniques at different microwave powers. In the horizontal axis the frequency of the microwave transition is displayed with respect to the central frequency of the cavity at zero magnetic field. Most of the measuremets show the effects of saturation of the atomic microwave transition. The measurement at low powers are distorted due to the strong atom-cavity interaction, which broadens the absorption peak of the resonator. Data taken in this way can be easily misinterpreted.

microwave transition of the atoms. From these data one can speculate that the start of the saturation effect happens somewhere around -40 dBm, as the measurement at -40 dBm and -35 dBm are fairly similar. The reason why the EPR signals don't look like a typical EPR signal is because the cavity that we are using in this experiment has a very high quality factor, which translates into a high atom-cavity coupling. In this experiment the microwave cavity and the atoms are not in the strong coupling regime, but they are not in the weak coupling regime either. The situation is somewhere in between. This high coupling means that on top of a frequency shift there will be a frequency broadening of the cavity's absorption peak, which happens when the atoms are set near resonance. On the other hand the vertical axis of the plot is calibrated at zero magnetic field, when the cavity is "empty", meaning that the atomic transition is far from resonance. The calibration of this axis is proportional to the slope of the cavity absorption profile at any given point. When the cavity is broadened due to the presence of the atoms the slope of the absorption profile decreases, giving the impression that the frequency shift is smaller than it really is. Special care should therefore be taken when trying to interpret the data shown in Fig. 8.8. An additional effect that can be observed is a small kink around the centre of the EPR signal (easier to see in the lower power measurements), which would usually look like a straight line. It was later discovered that this was caused because the modulation depth on the sidebands was too high.

Misinterpreting these data lead us to take Raman heterodyne measurements at high microwave power and not realise that the microwave atomic transition was saturated, which in turn

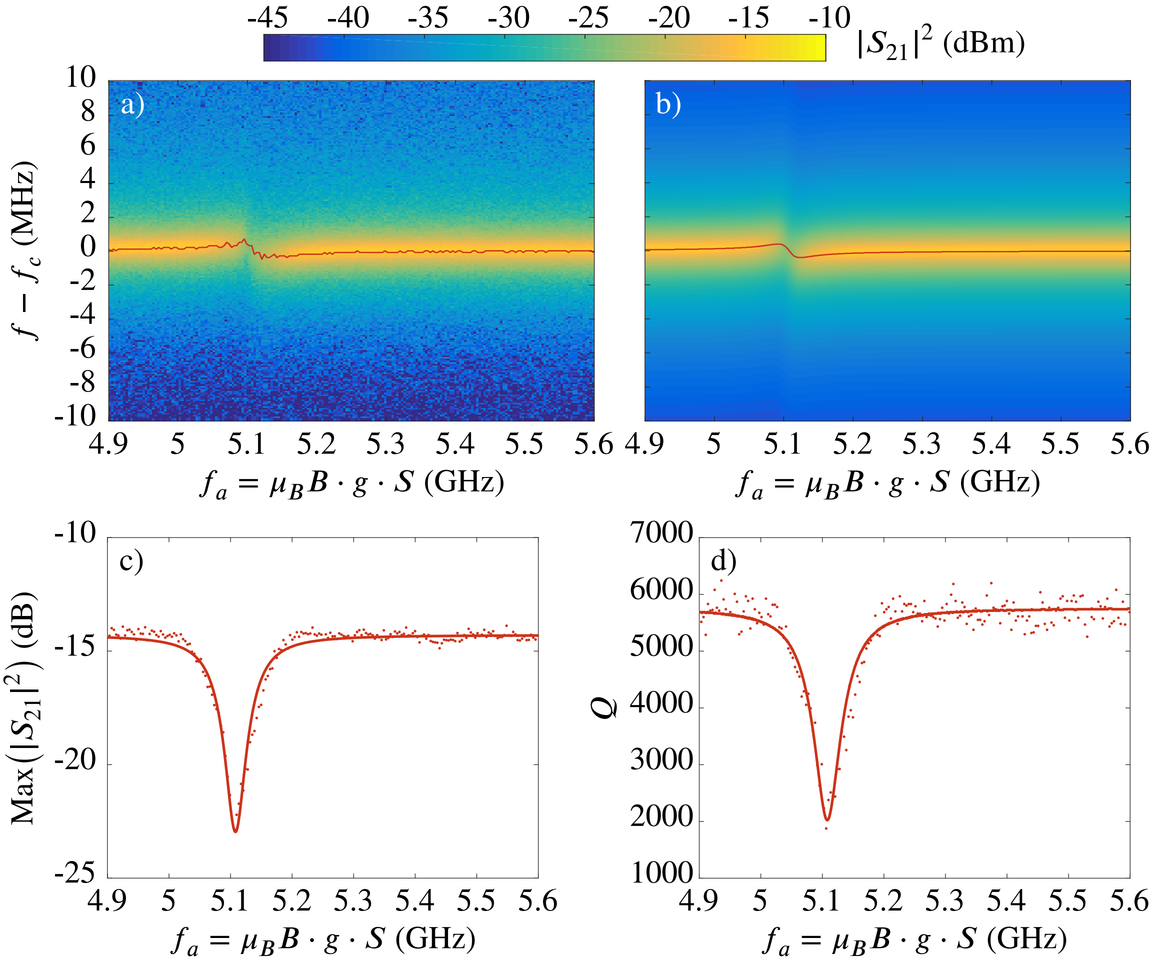

Figure 8.9: a) Electron paramagnetic resonance spectrum obtained by measuring the transmission spectrum of the cavity at different magnetic fields. The horizontal axis shows the frequency of the atomic transition f_a as the magnetic field is scanned. The vertical axis shows the frequency of the network analyser with respect to the central frequency of the microwave cavity. The red line shows the maximum $|S_{21}|^2$ at every value of f_a. b) Fit to the data displayed in a). c) Maximum value of $|S_{21}|^2$ at every step of f_a. Data are displayed with dots, while the solid lines show the values extracted from the fit shown in b). d) Quality factor of the microwave resonator at every value of f_a. Dots represent data, while the solid line is calculated from the fit in b).

lead us to wrong conclusions about frequency conversion efficiencies. The result was a much lower conversion efficiency than expected. This went undetected for a long time because saturation of the microwave transition had never been a problem in the past. For comparison, in the experiments performed in Sydney saturation of the microwave transition happened at much higher microwave powers, since the microwave cavity that we used in those experiments had a much lower quality factor than the one used in Dunedin.

In order to get rid of the saturation ambiguity we performed the following EPR experiments using a network analyser to measure the cavity transmission profile directly as a function of the magnetic field. These results are shown in Fig. 8.9, along with a fit to the data. The fit is done by calculating the transmission parameter $|S_{21}|^2$ using the input-output formalism described in Appendix A. During the fitting process the coupling (κ_1, κ_2) and intrinsic loss parameters (κ_i) are left constant and equal to the measured values at $B = 0$. Then the decoherence rate of the microwave transition γ_{21} and the cavity-atom coupling factor g are changed in order to best match a series of figures of merit. These are the $|S_{21}|^2$ parameter as a function of the microwave transition frequency f_a (shown in Fig. 8.9.a)), the maximum of $|S_{21}|^2$ at each value of f_a (shown in Fig. 8.9.c)), the quality factor Q of the cavity (shown in Fig. 8.9.d)) and its FWHM (not shown). The best fitting values are $\gamma_{21} \approx 2\pi \cdot 35\,\text{MHz}$ and $g \approx 2\pi \cdot 0.115\,\text{Hz}$.

The data shown in Fig. 8.9 were taken at a microwave power P_{rf} of -40 dBm. To ensure that this level of power is low enough to not saturate the microwave transition we checked the EPR signal as a function of power, while keeping the magnetic field constant at the point in which the frequency of the microwave transition matches that of the cavity. These data can be seen in Fig. 8.10. As it can be seen saturation starts to appear when the input microwave power approaches -35 dBm. This agrees with the results presented in Fig. 8.8. From the point of view of the transmission spectrum of the cavity the situation where the microwave transition is saturated due to excessive microwave power is similar to the situation in which the cavity is empty (or $B = 0$). Note that the power levels given here refer to the power at the input of the microwave cavity, and are not compensated for the coupling efficiency into it (most of the power gets actually reflected instead of entering the cavity).

8.3.3 Conversion Efficiency and Comparison with the $\Lambda^{(2)}$ Model

In this section I will present a series of measurements of microwave to optical conversion efficiency. These measurements will then be compared with the theoretical predictions from the $\Lambda^{(2)}$ model described in Ch. 4. These experiments were performed with a relatively large detuning between the microwave cavity and the microwave transition. The input microwave field was always kept on resonance with the microwave cavity. The microwave detuning with the atomic transition serves a double purpose. On the one hand it allows us to use higher levels of microwave power than we would be able to use on resonance while still not saturating the microwave transition. On the other hand, one of the limitations of the $\Lambda^{(2)}$ model is that it requires both microwave and optical fields to be off-resonance with the atomic transitions, so working with the microwave fields off-resonance is a requirement when it comes to comparing theory with experiment.

The microwave detuning chosen was $\Delta_\mu = 200\,\text{MHz}$. Then, the conversion efficiency was measured for different values of the optical detuning Δ_o, which is the frequency difference between the pump laser and the lowest frequency optical transition (2-3 transition by looking at Fig. 4.3). The microwave power used for these measurements was -20 dBm, and the power of the optical pump was around 25 mW. The obtained results are displayed in Fig. 8.11, where the red circles represent the data obtained from the experiment and the dash-dotted blue line represents the theoretical predictions from the $\Lambda^{(2)}$ model.

The expected conversion efficiency was calculated from Eq. (4.110), which assumes that only one sideband is generated (i.e. only the SFG process is taken into account, and not the DFG). The atomic spectroscopic parameters used are summarised in Tab. 4.1. The mode vo-

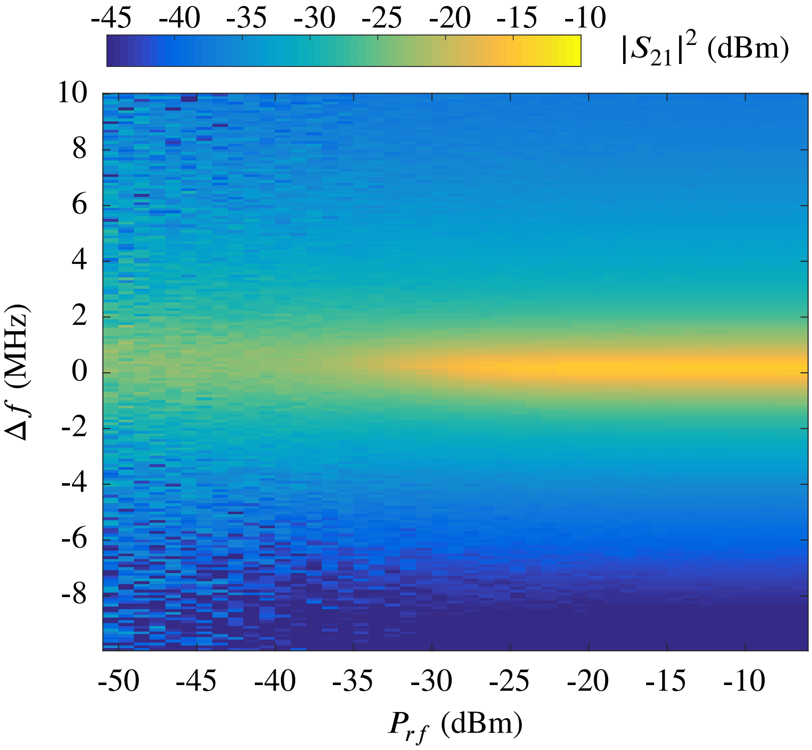

Figure 8.10: Cavity transmission spectrum as a function of input microwave power P_{rf}. In these measurements the magnetic field is kept constant at the value in which the microwave transition is on resonance with the microwave cavity. Saturation of the microwave transition starts to appear near $P_{rf} = -35\,\text{dBm}$.

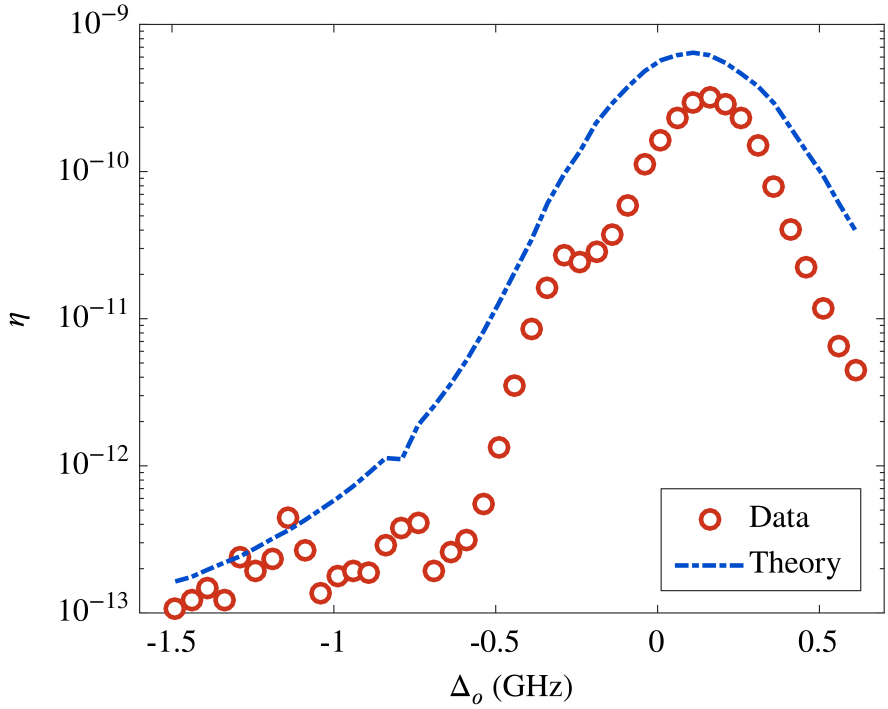

Figure 8.11: Microwave to optical frequency conversion efficiency as a function of optical detuning for a fixed microwave detuning $\Delta_\mu = 200\,\mathrm{MHz}$. Red dots show experimental data while the blue dash-dotted line shows the theoretical predictions from the $\Lambda^{(2)}$ model. The discrepancy between model and experiment is higher for measurements close to optical resonance, and it decreases to below a factor of two for measurements with an optical detuning near 1.5 GHz.

lume for the microwave cavity can be calculated from FDTD (Finite-Difference Time-Domain) simulations of the electromagnetic field inside the resonator, which was done by Yu-Hui Chen. This is $V_\Omega = 200\,\mathrm{mm}^3$. During these experiments the linewidth of the microwave cavity (FWHM) was measured to be $\Delta\omega/(2\pi) = 947\,\mathrm{kHz}$, and the transmission scattering parameter was $|S_{21}|^2 = -18.3\,\mathrm{dB}$ (note that the microwave cavity parameters may vary for different resonance frequencies).

Looking at Fig. 8.11, the maximum conversion efficiencies can be achieved near optical resonance. However, the theoretical description provided by the $\Lambda^{(2)}$ model is more inaccurate in this region because on resonance the assumption that the only the second order nonlinear term is relevant may not becomes less realistic. The general shape of the experimental points approximately follows the theoretical curve, showing a peak of similar width centred around $\Delta_o = 0$. A series of dips occur at several values of the optical detuning, which could be explained due to optical absorption from ^{167}Er in the sample. The absorption line shape for this isotope at a given magnetic field can be extracted from measurements like the ones presented in Fig. 8.7. However with the power levels used in most Raman heterodyne measurements the absorption spectrum will be modified due to hole burning.

What is most uncertain is the effect that ^{167}Er will have in the Raman heterodyne signal on itself, i.e. what kind of Raman heterodyne signal will the ^{167}Er isotope generate. If this is a signal in phase with the one generated by the even isotopes the conversion efficiency should be higher than predicted. If the signal generated by ^{167}Er is out of phase then the conversion efficiency will be lower than predicted. The main problem is that without knowing the energy level structure of ^{167}Er in detail one can not use the $\Lambda^{(2)}$ model to make predictions about the heterodyne signal that this isotope will generate. The agreement between the data points and the theoretical predictions gets significantly better at higher optical detunings, where the $\Lambda^{(2)}$ model works better and where optical absorption due to ^{167}Er can be expected to be lower.

8.4 Further Discussion and Conclusions

In this chapter I have presented an evolutionary step forward of the experimental setup used in the first Raman heterodyne experiments in Sydney. The experimental data obtained hold a lot of value. The optical absorption and the electron paramagnetic resonance experiments provide us with some crucial information about our sample, such as the inhomogeneous linewidths, the optical transition's dipole moment and the microwave transition's decoherence rate. These values allow us to calculate fairly accurate values of $\Lambda^{(2)}$, which together with some other known experimental parameters we can use to make realistic predictions about the microwave to optical frequency conversion efficiency. This sets up the basis for performing Raman heterodyne experiments with an optical resonator added to the system, which will be discussed in the following chapter.

The maximum experimental conversion efficiency values presented here are of the order of $10^{-10} \sim 10^{-9}$. This is a rather low value for any quantum computation or quantum information device. However, these values are measured with the microwave field largely detuned with respect to the microwave transition, which lowers the conversion efficiency. The predicted enhancement factor due to the optical cavity in our experiment is around 10^4 (see Ch. 9). This would set the efficiency around 10^{-6}, even with the microwave field off-resonance. A very important factor that determines the conversion efficiency is temperature. The population difference between the two ground states at 4 K is of a few percent. At temperatures around 10 mK, where our experiment is intended to operate, almost all of the population is in the lowest ground state. This makes a difference in the value of $\Lambda^{(2)}$ by about a factor of 30. This would translate into a factor of $30^2 \approx 10^3$ when it comes to calculating conversion efficiencies, setting a hypothetical conversion efficiency of 10^{-3}. Using a sample with a higher dopant concentration $\bar{N}$ would also increase the conversion efficiency. Because $\Lambda^{(2)}$ is proportional to $\bar{N}$ and the conversion efficiency is proportional to $[\Lambda^{(2)}]^2$, an increase in the dopant concentration of a factor of 10 would give an increase in conversion efficiency of a factor of 10^2. This would increase the conversion efficiency up to 10^{-1}, which is already a very respectable number. Another thing to note is that the power that we are using for the optical pump is rather low, of around 25 mW. The conversion efficiency is proportional to this power, and this could be at least 10 times higher, if not more (although this would only be a viable approach for experiments performed off resonance, because higher pump powers on resonance would increase the dominance of higher order nonlinear terms). Therefore, theoretically, unit conversion efficiency is achievable.

Due to technical and material limitations some of the hypothesis mentioned in the previous paragraph can not be tested at the time of writing this thesis. The one we can and we did test is the addition of an optical cavity, which is described in Ch. 9.

Chapter 9

Frequency Conversion With an Optical and a Microwave Cavity: Experiment

In this chapter I will explore and discuss the effects of adding an optical cavity to the setup, as compared with the experiments presented in Ch. 8. The requirements for the optical cavity are to be in resonance with both the pump mode and the signal mode simultaneously. For a given microwave frequency ω_μ this determines the free spectral range (FSR) of the optical cavity, the requirement being that $\omega_\mu/2\pi = n\times\text{FSR}$ where n is an integer number. I will refer to this as the triple resonance condition. For the first approach to using an optical cavity we decided to use a Fabry-Perot resonator, as they are well understood and easy to deal with. This was a hemilithic cavity (half monolithic), with one of the mirror surfaces coated in one of the ends of the sample and the other mirror being an off the shelf mirror bought from Thorlabs that was custom cut to the size we needed. The choice of n will then determine the optical length of the cavity, and therefore it's physical size. This is important, as we want to have a small optical cavity in order to maximise mode overlapping with the microwave cavity mode, yet at the same time we don't want the external mirror to be inside of the microwave resonator, so this sets a limit on how small the optical cavity can be.

In the first section of the chapter I will discuss the experimental setup with particular attention to the design and properties of the optical cavity, as many of the other parts of the setup are identical to the ones described in Ch. 8. After this I will present the experimental results obtained, and discuss them. I will start by showing how the optical cavity and the erbium ions interact with each other. Then I will present a study on how the frequency converted signal depends on the various frequencies involved in the system. After that I will show a set of data demonstrating the enhancement effect of the optical cavity regarding conversion efficiency. To finalise I will show a study on how the converted signal scales with the power of the input fields, where some interesting non-linear behaviour can be observed.

9.1 Experimental Setup

The experimental setup used in this experiment is based on the one presented in Ch. 8. The main difference is the presence of an optical cavity, and a subsequent modification in the optical coupling to the sample. A schematic representation of the experimental setup can be found in Fig. 9.1. An Er^{3+}:Y_2SiO_5 crystal (in green) sits inside a microwave loop-gap resonator (in brown) and a Fabry-Perot optical resonator. One of the boundary mirrors of the optical resonator (in dark blue) is one of the ends of the sample, which has been reflection coated. The other mirror is mounted on the microwave cavity using a mirror mount and a PZT actuator (in beige). This assembly sits inside the cryostat at around 4 K. Light is coupled into the optical cavity using a coupling lens (CL). The polarisation of the input light is controlled with a linear polariser, a half-wave plate and a quarter-waveplate. A 50/50 beam splitter is used to separate a fraction of the reflected light from the incident light on the optical cavity. The sample used in this experiment is the same used in Ch. 8. The reflective end of the sample is spherically cut with a curvature radius of 100.305 mm, and coated with a reflectivity of 98.8%. The other end is cut flat and anti-reflection coated with a reflectivity lower than 0.8%. The linewidth of the optical cavity was around 10 MHz, with a corresponding quality factor of $\sim 2 \times 10^7$. This was

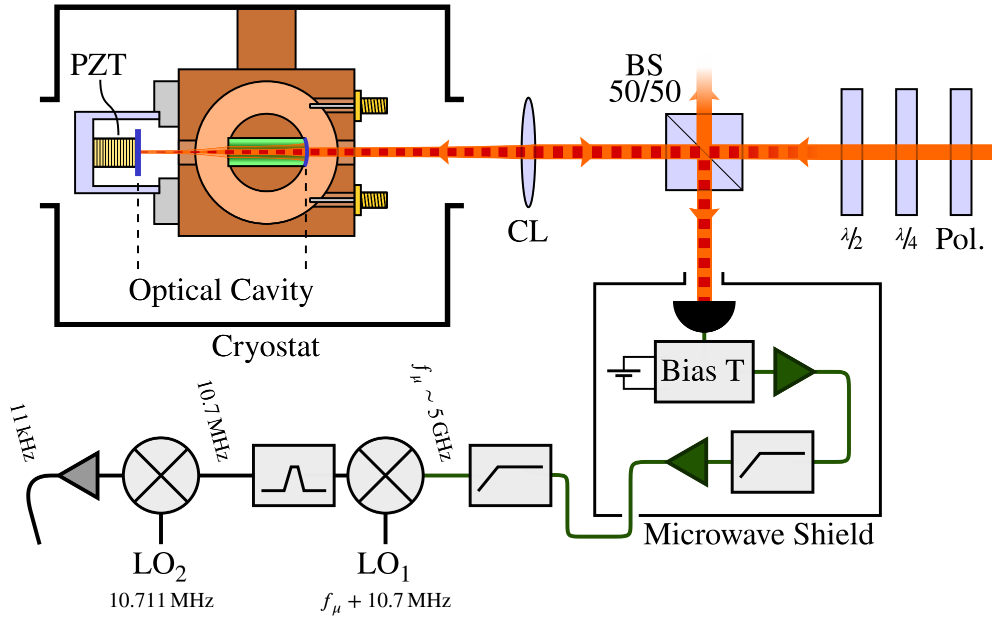

Figure 9.1: Schematic representation of the experimental setup. Light from the laser source comes from the right hand side of the image. A linear polariser, a $\lambda/4$ and a $\lambda/2$ waveplates are used to control the polarisation of the beam. A 50/50 beam splitter is used to separate the input from the output beams. The optical cavity is formed between one of the ends of the sample, which is reflection-coated and a Thorlabs mirror that sits on a piezo actuator (both shown with dark blue lines). In order to match the mode profile a coupling lens is used. The detection setup is described in Ch. 8.

limited by optical losses in Y_2SiO_5. The detection setup is the same as described in Ch. 8. A picture of the cavities can be seen in Fig. 9.2.

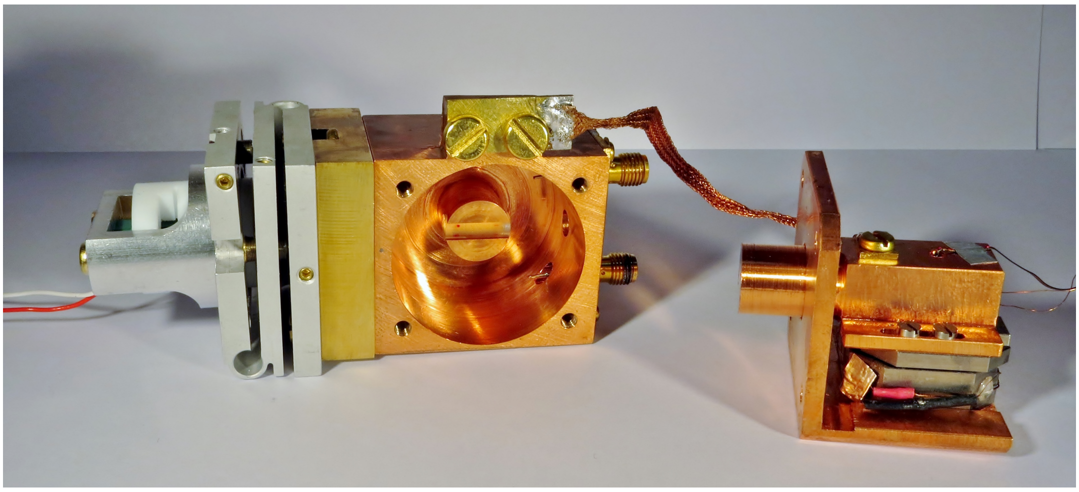

Figure 9.2: A picture of the tunable microwave cavity with the Er^{3+}:Y_2SiO_5 sample inside it and the other half of the optical cavity attached to it. The right bit is the plunger mounted on an attocube micro-translation stage.

The optical cavity was designed to have a FSR around 2.2 GHz. This means that, when performing cavity enhanced frequency conversion, two optical modes spaced by twice the FSR are used in order to ensure the triple resonance condition where the frequency of the optical pump is on resonance with one of the optical cavity modes, the frequency of the input microwaves is on resonance with the microwave cavity mode, and the corresponding frequency of the converted signal is also on resonance with one of the optical cavity modes. The design of the optical cavity was done using the ABCD matrix formalism [97]. A picture of the cavity design can be seen in Fig. 9.3. In this figure the transverse profile of a beam propagating towards and inside the cavity is plotted, as well as the curvature radius of its phase front. A collimated beam is incident from the right, passing through the coupling lens (solid line) and into the cryostat (dashed line). Then it enters the optical cavity, for which several round trips are plotted (these can not be seen in the figure, as they overlap with one another). A detailed calculation shows that the stability condition [97]

$$-1 < \frac{1}{2}(A + D) < 1 \tag{9.1}$$

is satisfied, as $\frac{1}{2}(A+D) = -0.876$ for the cavity design shown. The size of the mode inside the cavity can be slightly adjusted by changing the position of the flat mirror. Making the cavity shorter shrinks the size of the mode, and vice versa. If the flat mirror is moved too far away from the curved one then the cavity becomes concentric and therefore unstable. For a concentric cavity the spot size on the curved mirror is maximum. Any changes on the intracavity distance require a consequent adjustment of the position (or curvature radius) of the coupling lens.

The distance between the flat mirror and the closest edge of the sample is 46.6 mm, which added to the length of the sample (12 mm) makes for a total optical path of 67.72 mm for half a round trip (the refractive index of Y_2SiO_5 at 1536 nm is $n_{YSO} \simeq 1.76$). This gives a FSR of 2.212 GHz. The focal distance of the coupling lens is 400 mm. As it can be seen in Fig. 9.3 the beam diameter is relatively small compared to the diameter of the sample. This means that the mode overlap between the microwave and the optical modes will be small. A bigger effort could have been done in this regard in order to obtain a higher mode overlap and hence

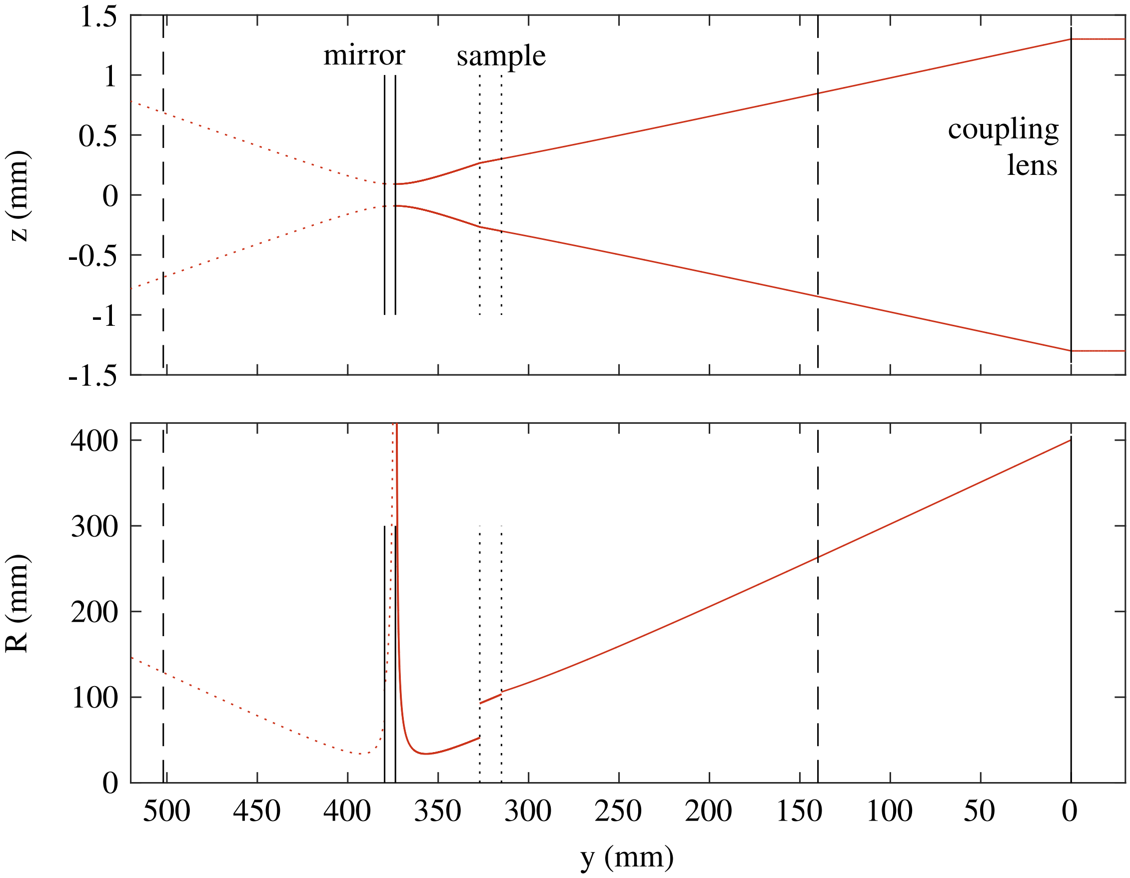

Figure 9.3: Diagram of a collimated laser beam incident on the optical cavity. The beam is incident from the right hand side of the image, it passes through the coupling lens (vertical solid line at $y = 0$) which has a focal length of 400 mm and then it enters the cryostat (limits shown by dashed lines). The dotted lines near 320 mm represent the Er^{3+}:Y_2SiO_5 sample with the rightmost surface being curved and reflection coated, while the two vertical solid lines near 380 mm represent the flat mirror of the cavity. Light exits the cavity the same way it goes in. *Top:* transverse profile of the beam. *Bottom:* curvature radius of the phase front.

higher conversion efficiencies, but a thicker beam would have been more prone to clipping on the edges of the sample, and we opted for a more conservative approach, using a smaller beam.

During the Raman heterodyne spectroscopy experiments it is important to keep the laser and the cavity frequencies locked to one another. The frequency of the optical cavity can be scanned using the piezo actuator on which the flat mirror is mounted. This provides a tunability range greater than the FSR of the optical cavity even at low temperatures. However, in our experiments we could never lock the cavity to the laser. The reason for this is that in order to have a tunability range greater than the FSR of the optical cavity the cavity's PZT

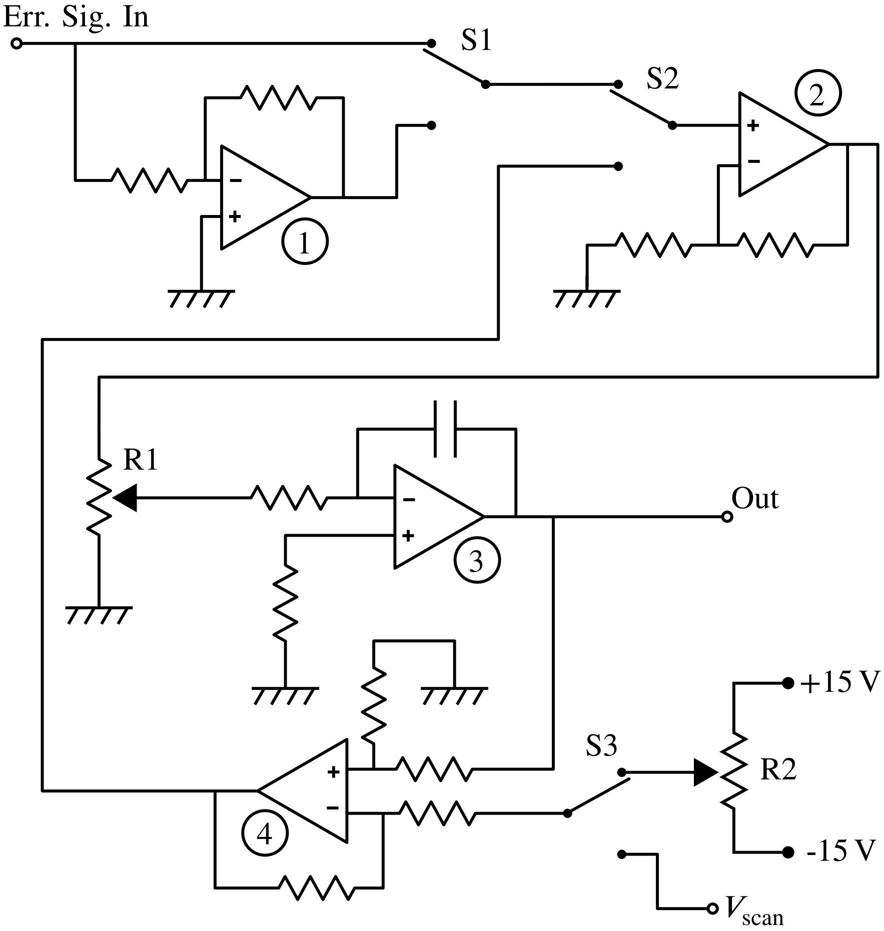

Figure 9.4: Schematic of the electronics inside the Lock-Box. The box takes an error signal as an input and provides an output voltage to the laser's PZT (this voltage requires external amplification). The circuitry inculdes four operational amplifier standard circuits: 1 is an inverter circuit with unity gain, 2 is an amplifier circuit, 3 is an integrator circuit and 4 is a difference amplifier with unity gain. A series of switches (S1, S2 and S3) allows to set the Lock-Box in the desired operation mode. The variable resistor R1 is used to adjust the gain of the servo loop. The variable resistor R2 is used to set the voltage level when operating in constant voltage mode.

actuator needs to be relatively large (in our case around 20 mm) and, in general, the bigger the actuator the slower it is. To this factor one has to add the fact that the capabilities of PZTs are considerably reduced once cooled down to cryogenic temperatures. These two factors made the particular actuator we were using at that time not fast enough to lock the cavity to the laser. On the other hand, the laser could be locked to the cavity with ease. This was achieved using the Lock-Box, which I designed and built specifically for this experiment.

The electronic schematic of the Lock-Box is shown in Fig. 9.4. The Lock-Box takes an error signal as an input, and provides an output voltage towards the laser's PZT. This voltage is amplified using an external DC amplifier so the full range of the PZT can be utilised. The system is based in the use of four standard operational amplifier circuits, labelled 1, 2, 3 and 4 in the figure. Circuit 1 is an inverter circuit with unity gain. This is used to flip the sign of the input error signal in case of need. If the switch S1 is in the upper position the sign is not flipped, while if the S1 is in the lower position the sign of the error signal is flipped. Circuit 2 is a non-inverting amplifier circuit. The gain of this circuit is determined by the values of the resistors. In our case the gain was 17. The variable resistor R1 is used to tune the overall gain of the feedback loop. Circuit 3 is an integrator, and it's time constant will be determined by the values of the resistors and the capacitor. The output of circuit 3 is then amplified and sent to the laser's PZT. This tunes the frequency of the laser, which in turn changes the value of the error signal, thus closing the feedback loop.

The Lock-Box can also be used to send a predetermined voltage to the laser's PZT. This is achieved by setting the switch S2 in the lower position. In this situation, a voltage between -15 V and +15 V can be set by adjusting the variable resistor R2 (at the bottom right corner of Fig. 9.4). Circuit 4 is a difference amplifier with unity gain. This circuit cancels the effect of the integrator (circuit 3), ensuring that in the stationary state the output voltage will be proportional to the voltage set by R2 (one needs to account for the amplification of circuit 2, the attenuation due to R1 and the gain in circuit 3). The advantage of this system is that one can manually scan the frequency of the laser using R2 to set it close to or on resonance with one of the cavity modes, and then by switching S2 back to the upper position lock the laser to that mode. Alternatively to set a constant voltage using R2, one can use an external voltage V_{scan}. This is useful in case one wants to scan the frequency of the laser with a given periodic voltage, which one can use to observe the cavity modes in the vicinity of the central laser frequency.

One of the main difficulties in the Raman heterodyne spectroscopy experiments presented in this chapter is the fact that the frequency of the optical cavity can be shifted by a relatively large amount when near the optical atomic transitions due to a strong atom-cavity interaction. In order to get high cavity enhancement it is important that the triple resonance condition is satisfied. In order to maximise conversion efficiency we will want the frequencies of the cavities to be close to the atomic transitions, both for the light and for the microwaves. As explained in Appendix A the frequency of a cavity mode shifts when the frequency of an atomic transition is tuned nearby. This makes setting up the experiment a challenge, but a lot of the parameters are tunable, which is a great advantage. Setting the magnetic field to a given value sets the frequency of the atomic transitions. Then we can adjust the frequency of the optical cavity to match the optical transitions. This, in turn, will change the FSR of the optical cavity due to the atom-cavity interaction. Then the frequency of the microwave cavity needs to be readjusted. If we want the microwave atomic transition to be near the microwave cavity we need then to change the magnetic field. But this changes the frequency of the optical transitions, so the optical cavity frequency needs to be adjusted again. A repeating cycle of parameter adjustments. However, in many cases we will not want to be totally on resonance with the atomic transitions. In these cases, and as long as one does not want to impose a particular value for the optical and/or microwave detunings, the cycle of parameter adjustments can be broken with ease, because the only hard requirement then is that the frequency difference between the two modes of interest of the optical cavity matches the frequency of the microwave resonator.

9.2 Experimental Results

In this section I will present the results we obtained in the frequency conversion experiment using an optical cavity. The first results I will show are about how the optical cavity frequency changes as the atomic transition frequencies are scanned. Next I will explore how the Raman heterodyne signal scales when changing the different parameters in the experiment, such as the frequency of the optical and microwave cavities and fields, as well as the magnetic field. Then I will make a comparison of the conversion efficiency with the case in which the optical cavity is removed from the setup. Finally I will show the behaviour of the Raman heterodyne signal when the optical and microwave fields are set close to or on resonance with the atomic transitions. This behaviour was found to be surprisingly non-linear, but an explanation for it will be given.

9.2.1 Coupling Between Erbium Ions and the Optical Cavity

The first thing we wanted to investigate is how the optical atomic transitions interact with the optical cavity, and in particular how the frequency of the latter changes when the former ones are scanned. In order to do so we checked the optical cavity modes as a function of the applied magnetic field. Initially we used a sample with a higher erbium concentration, of

200 ppm. These results are shown in Fig. 9.5. For these measurements the cryostat cooler was kept on. This made the cavities vibrate. While the effect on the microwave cavity was unnoticeable the cryostat vibrations could clearly be seen in the optical cavity's spectrum. The central frequencies of the optical cavity modes could be seen to oscillate (vibrate) within a couple of hundreds of megahertzs. During the measurements presented in Fig. 9.5 we scanned the frequency of the laser by changing its temperature (slow scan) and at each frequency we scanned the magnetic field. In Fig. 9.5 the standard deviation of the reflected signal from the cavity is plotted, instead of plotting the reflected signal directly. This is because the cryostat vibrations made it hard to measure the peak reflectivity, but measuring how the peak reflectivity oscillates up and down was much easier. As it can be seen in the plot this value gives a good indication of where the cavity modes are, although it doesn't represent properly the width of said modes.

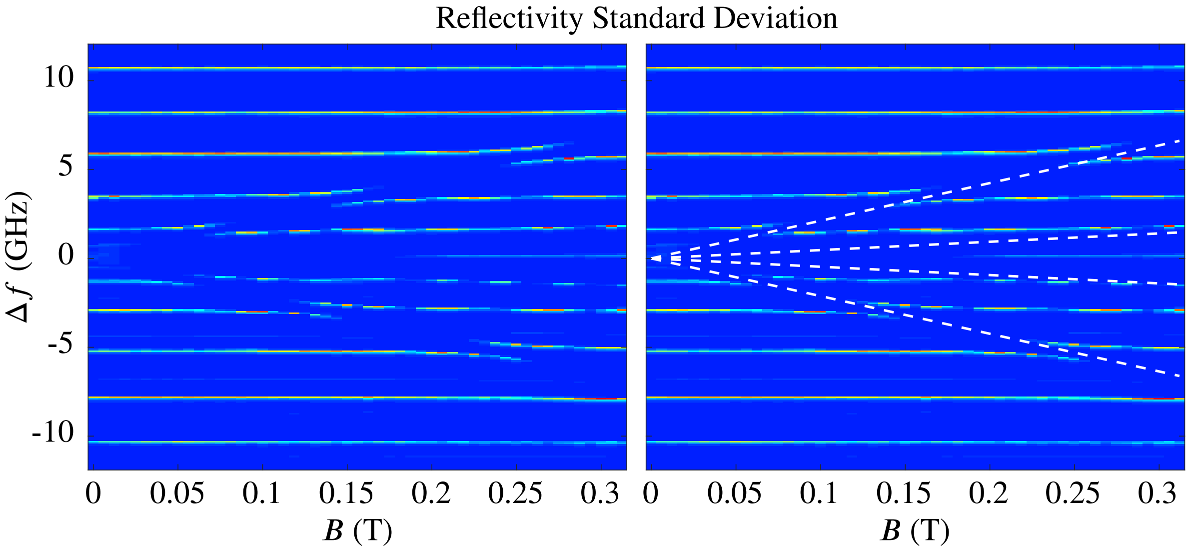

Figure 9.5: Effect of the atomic transitions on the optical cavity modes for an Er^{3+}:Y_2SiO_5 sample with 200 ppm dopant concentration. Avoided crossings can be seen for several cavity modes as the magnetic field is scanned. The plot on the right shows the same data but the white dashed lines have been added, representing the expected atoimc transition frequencies calculated from the measured g-factors.

On the right hand side of Fig. 9.5, superimposed to the cavity modes in dashed white lines, are the expected frequencies of the four atomic transitions, which can be calculated from the g-factors of the ground and the excited state. The effect of the atoms on the cavity frequency can be seen as a split in the cavity frequency every time there is a crossing with the frequency of the atoms. The fact that at the crossing points the optical cavity is bistable indicates strong coupling between the atoms and the cavity (keep in mind the sample used for these measurements contains 20 times more erbium than the samples used in the rest of the experiments).

We repeated the measurements with the 10 ppm doped sample. The results obtained with this sample are presented in Fig. 9.6, and as it can be seen they are noticeably different. The cavity doesn't exhibit bistability around the crossing point, but tristability instead, and a Z shape can be observed instead of the usual avoided crossing. A key point in understanding this behaviour is the fact that the laser is scanned *slowly* for this measurement. In fact, compared with any of the relevant atomic time scales the laser is not being scanned at all, as it sits at a fixed frequency for several minutes during the time that B is scanned.

In order to understand this behaviour and how the Z shape arises we can look at the atom-cavity interaction theory described in Appendix A. By checking Eq. (A.19) one can see that an atomic transition will effectively *push away* the cavity frequency from it's own frequency, which is what gives rise to avoided crossings in a normal situation. In our case we are dealing with an inhomogeneously broadened ensemble of ions. If the inhomogeneous absorption profile of the ions is unperturbed we will observe a usual avoided crossing, as the ions will collectively push the frequency of the cavity away. In this case the ions with lower transition frequencies in the inhomogeneous line will push the cavity towards lower frequencies, and the ions with higher transition frequencies in the inhomogeneous line will push the cavity towards higher frequencies. However, if a spectral hole is burnt there will be a narrow spot in the in-

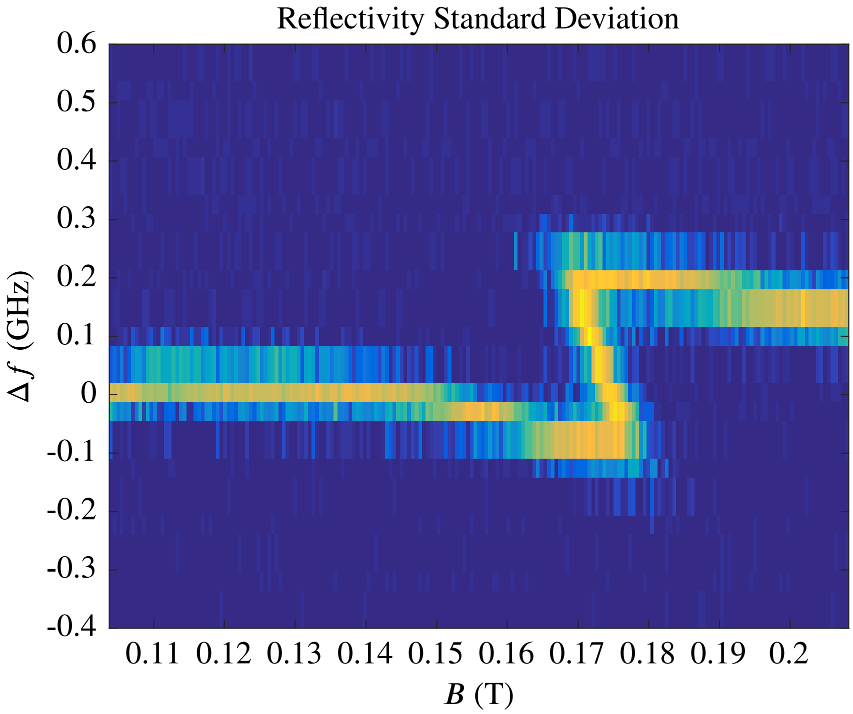

Figure 9.6: Effect of the atomic transitions on the optical cavity modes for an Er^{3+}:Y_2SiO_5 sample with 10 ppm dopant concentration. In this case the frequency of the laser is scanned *slowly*, and tristability can be observed, giving a very characteristic Z shape.

homogeneous line where the frequency of the cavity is pushed in the opposite directions, as it can be seen in the simulations shown in Fig. 9.7. In this simulation an inhomogeneously broadened gaussian profile with a FWHM of 400 MHz is shown. A spectral hole is burnt 50 MHz away from the center of the inhomogeneous line. The absorption from the ions is plotted in blue, while the shift in the cavity's central frequency, which can be calculated by integrating Eq. (A.19) over the inhomogeneous line, is plotted in red. In the close vicinity of the spectral hole the ions of lower frequency push the cavity towards higher frequencies, while the ions of higher frequency push the cavity towards lower frequencies. This adds to the pushing of the rest of the ions not in the vicinity of the spectral hole. The final result is that, if the spectral hole is deep enough, there will be a point in the inhomogeneous line where the cavity frequency is pushed to either side with equal strengths, giving rise to the characteristic tristability observed in Fig. 9.6.

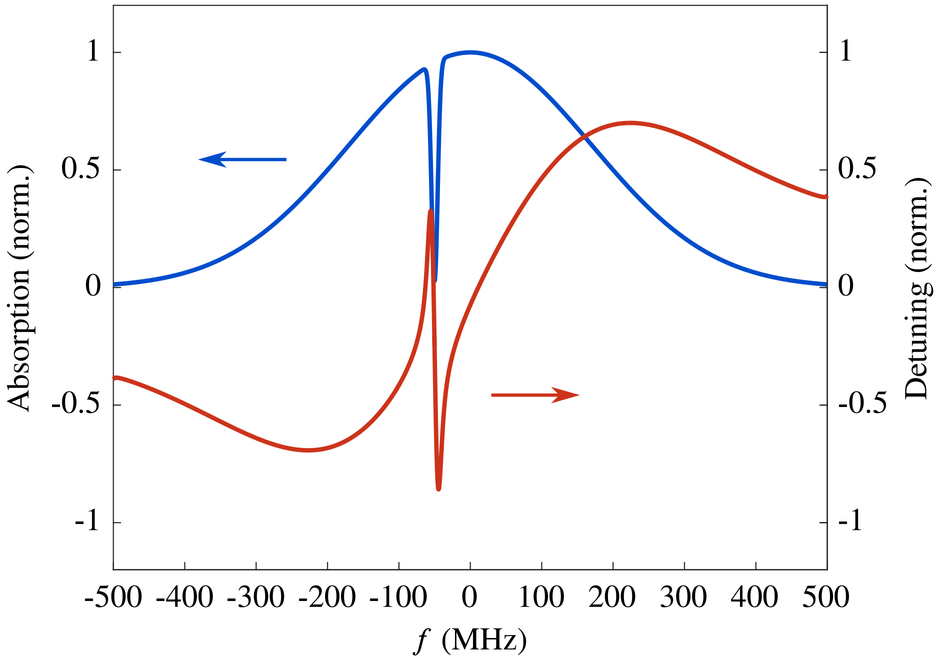

Figure 9.7: Simulated cavity detuning due to the atom-cavity interaction described in Appendix A. The blue line shows an inhomogeneously broadened absorption profile with a deep spectral hole burnt in it. The red line represents the corresponding shift in the cavity's central frequency as it would be scanned across the inhomogeneous line. Negative signs for this frequency shift mean that the cavity is being pushed towards the left and vice versa. A point of zero pushing is found close to where the spectral hole is burnt, giving rise to a tristable behaviour and the Z shape observed in Fig. 9.6.

The Z-like behaviour was not observable with the previous sample, which contained twenty times more erbium dopants (200 ppm versus 10 ppm). The reason behind this is that in that case the higher erbium concentration inhibited the appearance of deep spectral holes. If the spectral hole burnt in the inhomogeneous line is not deep enough the effect of the ions in the vicinity of the hole pushing the cavity towards a stable point will not be strong enough to overcome the push of the rest of the ions in the inhomogeneous line, that are pushing the cavity outwards, and the Z shape will therefore not be observed.

The experiment presented in Fig. 9.6 was repeated, but this time using the piezo actuator inside the laser to scan the frequency. This allows for a *fast* frequency scan (the complete frequency scan was of about 720 MHz, and the scanning rate was 128 Hz), which inhibits the formation of spectral holes in the inhomogeneous profile, as the time spent at each inhomogeneous class of ions is smaller than the reciprocal of the Rabi frequency associated to the optical transition. The results of this experiment are presented in Fig. 9.8. In this case the measurements were taken with the cryostat switched off, and so the reflectivity from the cavity could be accurately measured. The fact that the Z shape disappears when the laser frequency is scanned fast provides further evidence that this effect is related with spectral hole burning.

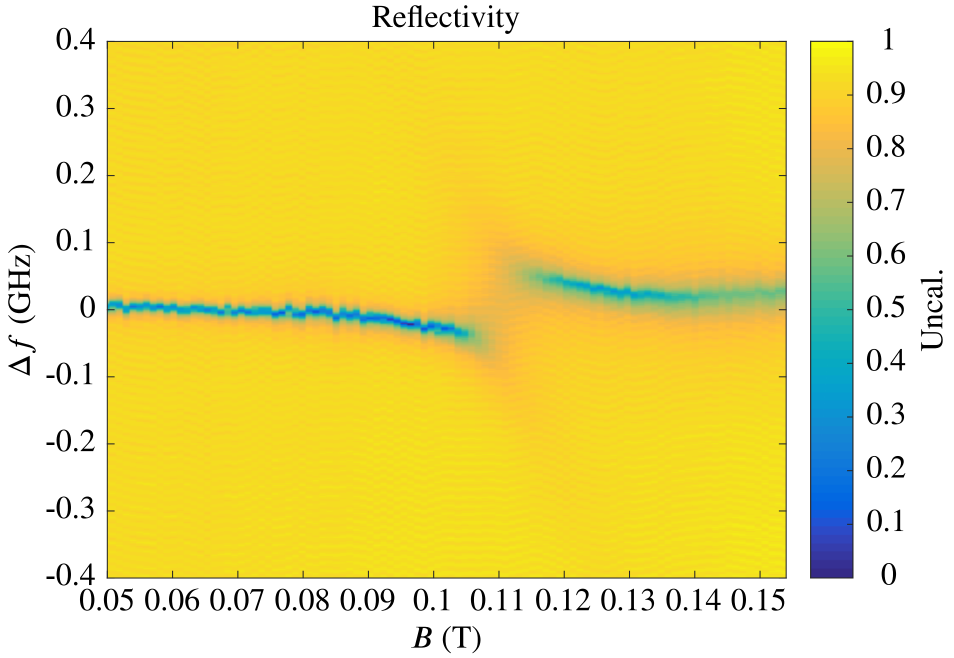

Figure 9.8: Effect of the atomic transitions on the optical cavity modes for an $Er^{3+}:Y_2SiO_5$ sample with 10 ppm dopant concentration. In this case the frequency of the laser is scanned *fast* (ca. 180 GHz/s), and tyical avoided crossings can be observed.

Finally, we wanted a way to measure how the FSR of the optical cavity changes as its resonance frequency is scanned. This helps in making sure that the FSR matches the frequency of the microwave cavity and the triple resonance condition is satisfied. In order to make this measurement we used a fibre coupled EOM to generate sidebands on the laser at a frequency close to the expected FSR. Then we scanned the laser's frequency using its built-in PZT, and looked for the reflected signal on an oscilloscope. If the frequency of the sidebands is close enough to the FSR and the frequency scan is large enough it is possible to see on the oscilloscope's screen the reflected signal from three different cavity modes. These will be the two modes we are interested in plus a third one, that will not be used in the frequency conversion experiment but that is nonetheless useful to have on the screen as a reference. Additionally, the frequency of the optical cavity was scanned over a range big enough to overlap with the frequency of the optical atomic transitions. One of such measurements is presented in Fig. 9.9. This data was taken for a magnetic field strength $B = 0.150\,\mathrm{T}$ and the EOM frequency used was $f_{EOM} = 4.91\,\mathrm{GHz}$. Along the vertical axis there is the detuning in the laser frequency Δf_{las}, with respect to an arbitrary origin. Along the horizontal axis the detuning of the optical cavity Δf_{cav} is represented, also with respect to an arbitrary origin. The three main cavity modes observed are labelled (a) and (b) for the two cavity modes that are intended to be used for frequency conversion, and (c) for the third mode. In this figure mode (b) is probed with the central carrier of the laser, and modes (a) and (c) are probed with the two sidebands. The line from (a) comes from the optical cavity mode at higher laser frequencies than (b) (it "comes from the top") while the line from (c) comes from the optical cavity mode at lower laser frequencies than (b) (it "comes from the bottom"). The frequency separation between (a) or (c) and (b) can be obtained by reading the vertical separation from the plot, and then adding f_{EOM} to it. Since mode (c) is far from the atomic resonances it helps to calibrate the horizontal and vertical frequency axes with one another, as an unperturbed mode will look like a straight line of slope one. The weaker lines that appear in Fig. 9.9 come from modes of the optical cavity that are spaced further away, and that are being probed by the higher order sidebands generated by the EOM. These can also be used as a calibration reference.

From the data in Fig. 9.9 we can see that for the value chosen for the magnetic field, and for a given cavity frequency (near $\Delta f_{cav} = 0.5\,\mathrm{GHz}$), modes (a) and (b) can be set close to resonance with two of the optical atomic transitions simultaneously. In the case shown mode (a) is on resonance with one of the strong transitions, while mode (b) is on resonance with one of the weak transitions. From Fig. 9.9 one can also see how the distance between modes (a) and (b) varies due to the cavity-atom interaction as a function of the central cavity frequency.

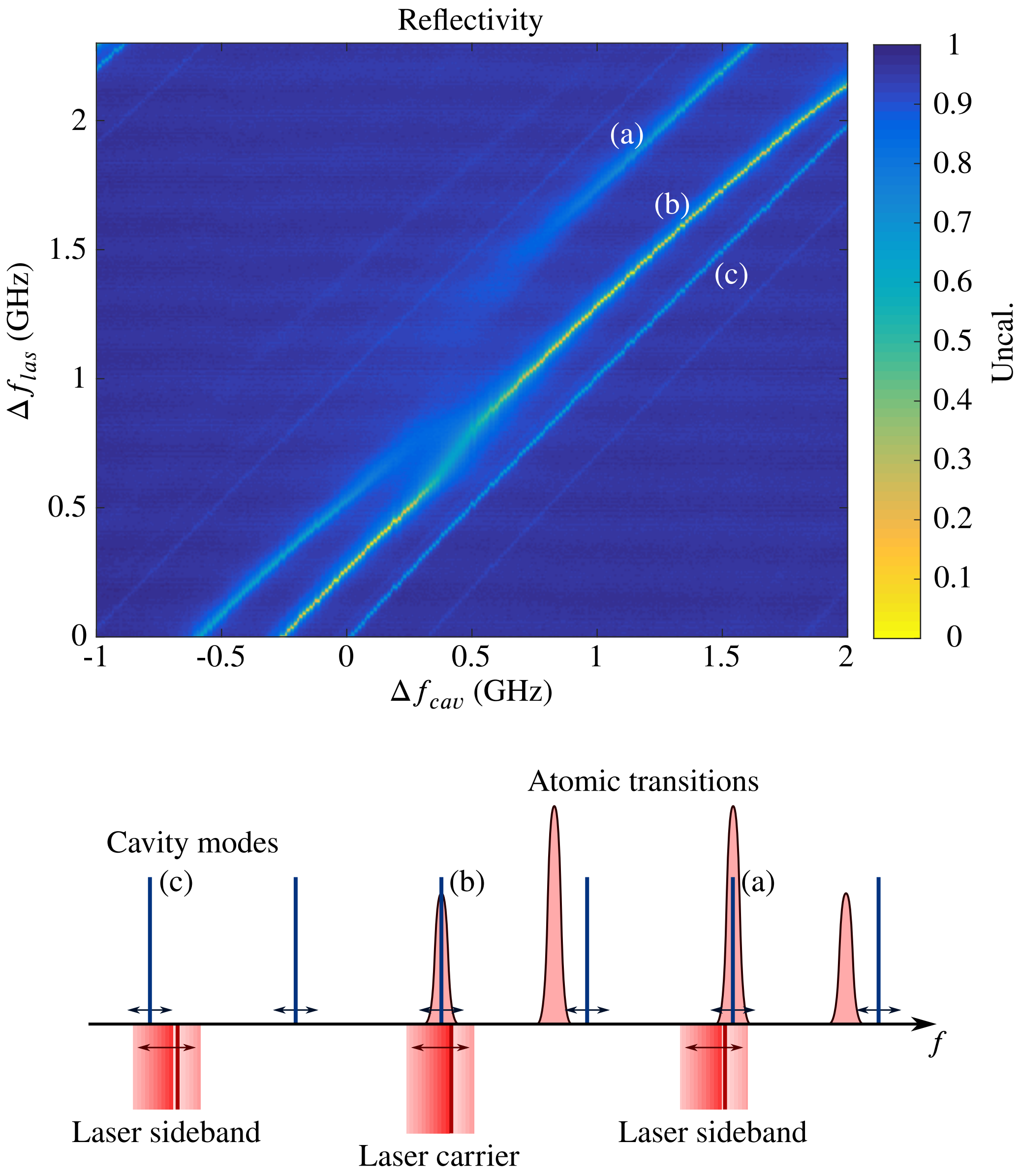

Figure 9.9: Measurement of the variable FSR of the optical cavity as a function of the cavity frequency. This particular measurement was taken at $B = 0.150\,\mathrm{T}$. Frequency sidebands on the laser are generated using an EOM at frequency $f_{EOM} = 4.91\,\mathrm{GHz}$. This allows seeing three cavity modes in a single laser frequency scan. Mode (b) is scanned through resonance with the lowest frequency atomic transition. The atom-cavity interaction can be seen as a wiggle of the cavity frequency as it is scanned. Mode (a) is scanned through resonance with one of the strong atomic transitions, which gives rise to an avoided crossing. Mode (c) is always far from the atomic transitions, and therefore it looks like a straight line of slope one. The faint lines are modes of the optical cavity that are being probed by the higher order sidebands of the laser.

9.2.2 Frequency Conversion vs. Optical and Microwave Frequencies

The next thing I want to look at is how the Raman heterodyne signal changes as a function of the input microwave and laser frequencies. To measure this we locked the laser to the optical cavity and scanned the cavity frequency while looking at the amplitude of the heterodyne signal. Then we moved the microwave cavity frequency (and adjusted the frequency of the input microwave signal accordingly) and repeated the measurement. In this way the input fields are always on resonance with the cavities. We performed these measurements for several values of the magnetic field. One of these measurements is shown in Fig. 9.10, together with a reflectivity spectrum of the optical cavity for comparison.

The measurements shown are taken for $B = 0.150\,\mathrm{T}$, as in Fig. 9.9. The two measurements were taken independently in different runs. For the Raman heterodyne measurements the frequency of the optical cavity (and therefore the pump laser) was scanned at a relatively slow rate. This made hole burning effects to be observable. One characteristic effect is the fact that the signal observed was slightly different whether the frequency was scanned upwards or downwards, where the main difference was the ratio between the upwards and downwards scanning peaks. Another consequence of hole burning is the tristable behaviour explained in Sec. 9.2.1. The measurements presented in Fig. 9.10 were performed for an input microwave power of -10 dBm and an optical pump power of 7.4 mW.

The vertical axis in the Raman heterodyne signal plot has been calibrated to match the vertical axis in the reflectivity plot in regards to mode (b). This allows to identify how far or how close is the frequency of the optical modes to the atomic transitions. The frequency of the converted optical signal will be equal to the frequency of the optical pump plus the frequency of the input microwaves, which can be read in the horizontal axis in the Raman heterodyne signal plot. The corresponding frequency in the reflectivity plot with regards to mode (a) can be obtained by taking the laser frequency as referred to mode (b), adding the microwave frequency to it, and subtracting the EOM sideband frequency of $f_{EOM} = 4.91\,\mathrm{GHz}$ from it. This is represented by the solid red vertical lines. The circles in the reflectivity plot show where the pump frequency is (I.b and II.b) and where the signal frequency is (I.a and II.a) for the two peaks shown in the Raman heterodyne signal plot.

It can be seen that peak I corresponds to a situation where the optical cavity modes are close but not directly on resonance with the atomic transitions. In contrast peak II corresponds to a situation where the optical fields are on resonance with the atomic transitions. What happens in this situation is hard to interpret (see Sec. 9.2.3) and hard to predict, as our theoretical models are incapable of making accurate predictions when the fields are on resonance with the atomic transitions.

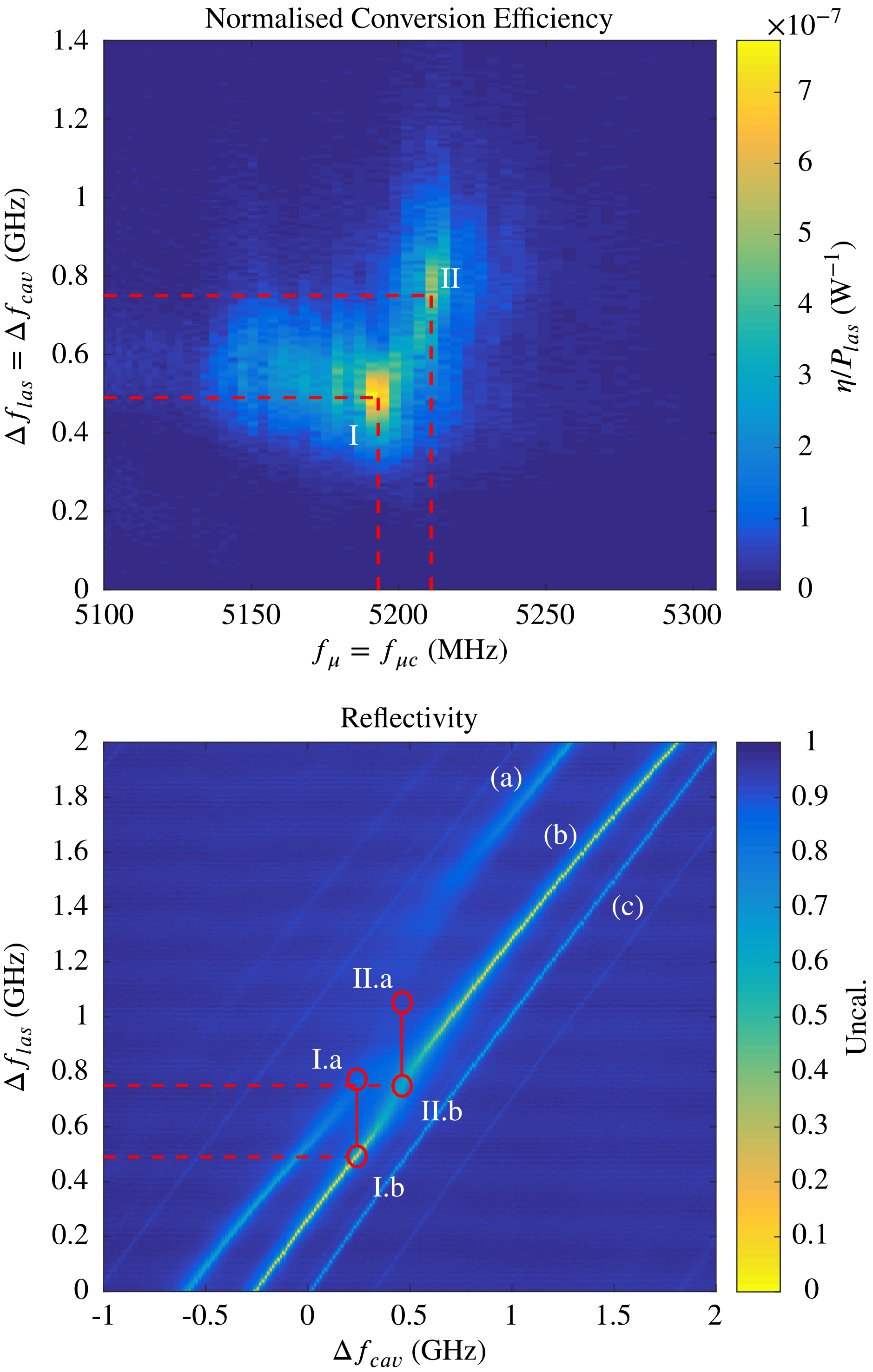

Figure 9.10: *Top:* Raman heterodyne signal as a function of the microwave and optical input and cavity frequencies. *Bottom:* Optical cavity modes as the frequency of the cavity is scanned around the frequency of the optical atomic transitions. I(II).a and I(II).b correspond to the optical frequencies of peak I (II) in the top figure. The situation for peak I is considered to be close to resonance, while the situation for peak II is considered to be on resonance.

9.2.3 Non-Linear Behaviour of the Heterodyne Signal

In this section I will discuss the unexpected behaviour of the Raman heterodyne signal when one or all of the fields are close to resonance with the atomic transitions. What happens in this case is not explained by either of our theoretical approaches discussed in Ch. 4. The measurements show a highly non-linear behaviour of the converted signal with respect to the input microwave and optical powers. Additionally, the non-linear behaviour observed as a function of one of the input powers appears to depend on the power of the other field. The measurements presented in this section were performed at the position of peak I in Fig. 9.10 unless otherwise specified, with the same magnetic field $B = 0.150\,\mathrm{T}$. In this configuration the microwave field is on resonance with the atomic microwave transition, but the optical fields are about -200 MHz off resonance with respect to the center of the inhomogeneous line. This optical detuning is not enough to consider all the erbium ions to be off resonance, though. With these detunings the theoretically calculated value of the nonlinear coefficient for our sample is $\Lambda^{(2)} \simeq 3 \times 10^{-3}\,\mathrm{T}^{-1}$ at 4 K.

The first observation I want to show is how the conversion efficiency η scales with the optical pump power P_{las} for different values of the input microwave power P_{rf}, which can be seen in Fig. 9.11. For comparison, a measurement with the optical fields completely off-resonance is also shown in the figure. The conversion efficiency has been normalised by the power of the pump beam so that a direct comparison can be made for the different cases presented. Notice the logarithmic scales on both axes. The expected value for the conversion efficiency is plotted using a black dashed line. This value has been calculated using Eq. (4.99) and the theory described in Ch. 4.

The first thing one can see from Fig. 9.11 is that η doesn't scale linearly with the pump power, which is what one would expect for a three wave mixing process. If the conversion efficiency scaled linearly with the power of the pump beam one would observe horizontal lines, and the three measurements performed on resonance with the optical transitions should be at the same level. The observations are quite different. For low microwave powers (green triangles) and for measurements totally off-resonance with the optical lines (blue crosses) the behaviour is almost linear, although a slight upwards tendency can be observed. For higher microwave powers (red circles) the slope increases dramatically, but for even higher microwave powers (pink squares) the slope appears to decrease. Another way to interpret the data is to say that for the two highest microwave power measurements the efficiency flattens out near $\eta/P_{las} = 10^{-4}\,\mathrm{W}^{-1}$. It is possible that the measurements taken at the highest microwave power are partially saturated from the beginning, which can give the impression of a line with a different slope. In order to test this more measurements at higher and lower laser powers would be useful, but taking measurements at lower optical powers than the ones presented here becomes quite hard, as the signal level decreases below what we can detect, and we could not perform measurements at higher powers with the available laser. A possible explanation for this non-linear behaviour will be given later. Note that in all the measurements presented in Fig. 9.11 the microwave power is beyond the saturation point determined in Ch. 8.3.2.

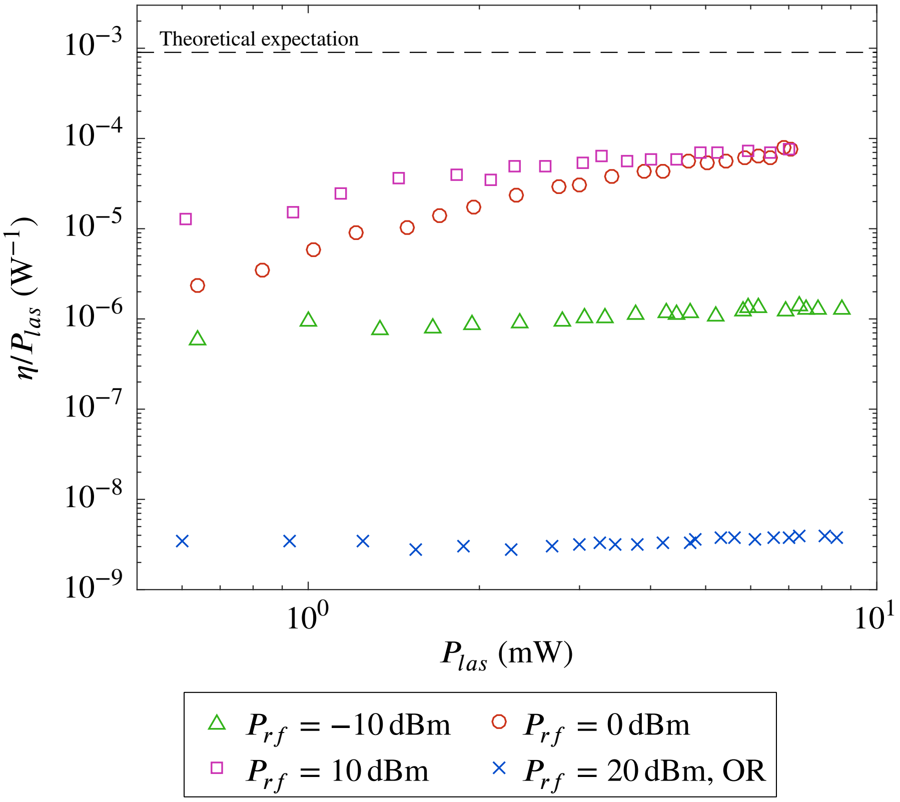

Figure 9.11: Conversion efficiency per Watt of pump laser power as a function of pump laser power for the case in which the optical and microwave fields are on resonance with the atomic transitions. Several measurements taken for different input microwave powers are presented. A measurement with the optical fields off-resonance with respect to the atomic transitions is shown for comparison (OR). The expected value of the normalised conversion efficiency is shown using a black dashed line.

In the next measurement that I want to discuss we measured the normalised conversion efficiency as a function of the input microwave power for different values of the pump laser power. A series of these kind of measurements is presented in Fig. 9.12. A measurement with the optical fields completely off-resonance with the atomic inhomogeneous line is also presented here for comparison (blue crosses). The off-resonance measurement starts at higher microwave powers because at low powers the level of noise is very high, as the levels of heterodyne signals are quite low in this region for off-resonance optical fields.

In this case the non-linear behaviour is even more exaggerated than in the measurements shown in Fig. 9.11. First, the measurement with off-resonance optical fields seems to preserve a slight upwards tendency as the microwave power is increased, in a similar way as it can be observed in Fig. 9.11 when the optical power is increased. For the measurements with the optical fields on resonance the situation is quite interesting. At lower powers a near linear increase in normalised conversion efficiency can be observed. Then the conversion efficiency per Watt of pump power rapidly increases, until it reaches a saturation point and it starts to decrease. In Fig. 9.12 one can see again how the behaviour of the normalised conversion efficiency as a function of one of the input powers depends on the level of the other input power. Namely, one can see here how the point of maximum efficiency occurs at different microwave powers for different pump laser powers. It can be seen that the top of the curves at higher optical powers nearly reaches the theoretical expectations for the conversion efficiency.

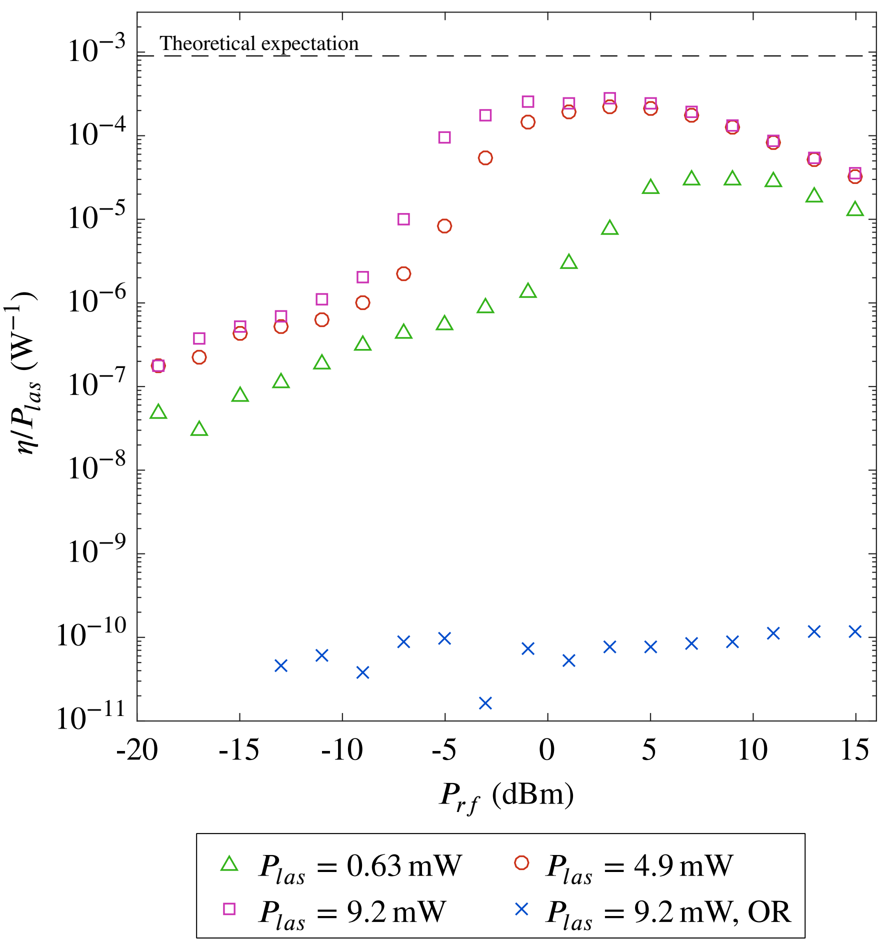

Figure 9.12: Conversion efficiency per Watt of pump laser power as a function of input microwave power for the case in which the optical and microwave fields are on resonance with the atomic transitions. Several measurements are presented at different pump laser powers. A measurement with the optical fields off-resonance (OR) is shown for comparison.

A possible explanation for the non-linear behaviour of the conversion efficiency has to do with hole burning and stray absorption in the inhomogeneous line, in particular due to ^{167}Er. As it can be seen from Fig. 8.7.b) the absorption spectrum of the ^{167}Er isotope spreads over a very long range of frequencies. This means that the frequency of the converted signal will most likely overlap with an absorptive region in its spectrum. Only at very large optical detunings ($> 3 \sim 4$ GHz) can one picture a situation in which the up-converted signal will fall outside the absorption region of ^{167}Er. Furthermore, when performing experiments optically on resonance absorption from the even isotopes will also be present. For experiments without an optical cavity this stray absorption has the effect of an apparent lower level of the conversion efficiency, as the converted signal gets absorbed by some of the ions. For the experiments in which an optical cavity is used the situation is different, because the cavity will enhance the absorption. In this situation most of the converted signal will get lost inside the cavity, unless it is strong enough to start burning a spectral hole in the inhomogeneous line. We suspect this might be what we are observing in our measurements: as the power of the converted signal increases it burns a deeper hole in the inhomogeneous line, which allows it to escape the optical cavity instead of getting absorbed. This explains the fact that for higher optical powers one needs less microwave powers in order to attain similar levels of efficiency and vice versa. In order to further test this hypothesis a purified sample with much smaller amounts of ^{167}Er could be used, and experiments with the optical fields off resonance with the atomic transitions could be performed. In this way one could perform experiments close enough to the inhomogeneous line to see big signals but at the same time not have any stray absorption from the 167 isotope. Another possible explanation for this behaviour is that there is some dynamic effect in the atomic populations within the different energy levels that alters the value of $\Lambda^{(2)}$. It could be that this effect initially sets the population levels in an unfavourable way for low input powers, and then the situation becomes more favourable as the powers are increased. Also, since these experiments are performed on resonance with both fields saturation of the microwave line may happen at higher microwave power levels, because the effect of both fields needs to be taken into account simultaneously, as one can not treat the transitions independently any more when all the fields are on resonance. Confirming this hypothesis would likely require a more complete theoretical model in which the dynamics of the atomic populations are taken into account. However, the fact that the measured conversion efficiency approaches the theoretical expectation at its peak reinforces the hypothesis involving optical absorption of the generated sideband.

9.2.4 Cavity Enhancement

Quantifying the effect that the optical cavity has in the microwave to optical conversion efficiency is a very important aspect of our experiment. In order to determine the enhancement factor we measured the conversion with and without the optical cavity for a given set of parameters, and compared both cases. In this case the optical field was set well off-resonance, with a detuning from the center of the inhomogeneous line of 0.8 GHz. The microwave field was kept on resonance with the microwave atomic transition. We also measured the dependency of the heterodyne signal with respect to the input laser and microwave powers in this situation. This helps to determine whether the experiment is working in the linear regime or not (see Sec. 9.2.3), and if not, helps to give an estimate of how much of the non-linear behaviour arises from the fact that we are using an optical cavity and how much comes from other effects. The measurements without the optical cavity were performed in the same way as the experiments presented in Ch. 8. The enhancement factor expected from the theory presented in Ch. 4 is around 1.5×10^4 for our setup.

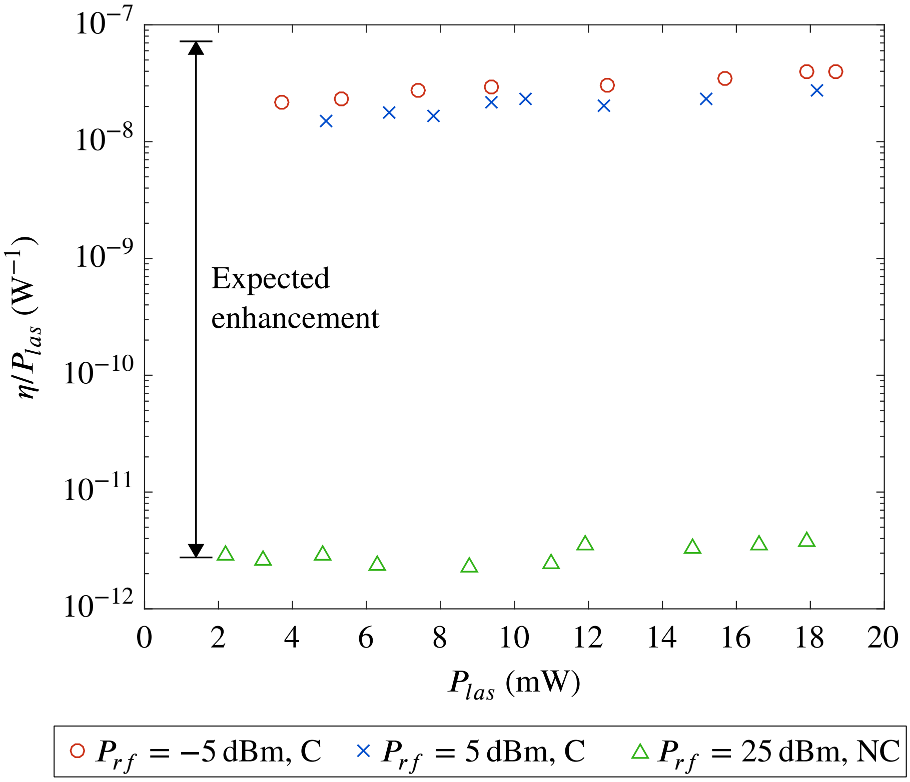

Figure 9.13: Conversion efficiency per Watt of pump laser power as a function of the pump laser power. Two measurements at different microwave powers are shown for the case in which the optical cavity is used (C) and one measurement is shown for the case in which the optical cavity is not used (NC).

Fig. 9.13 shows the conversion efficiency η per Watt of pump power as a function of the pump laser power P_{las}. Two measurements making use of the optical cavity (C) are shown for two different input microwave powers P_{rf}. A measurement without the optical cavity (NC) at high microwave powers is also shown. The three measurements show a slight upwards tendency with the laser power, which fits with what has been discussed in Sec. 9.2.3. The measurement without the optical cavity was performed at high microwave powers in order to get the best signal to noise ratio possible for this measurement. High microwave powers were required because with an optical detuning of 0.8 GHz from the atomic transitions much lower conversion efficiencies are achieved. However, the behaviour of the conversion efficiency with respect to microwave power for the case in which an optical cavity is not used is linear as it will be shown in Fig. 9.14, so the fact we are using high microwave powers for this measurement doesn't interfere when it comes to comparing with the case in which the optical cavity is used. An enhancement of 10^4 can be observed at any laser power, which fits well with the theoretical expectations.

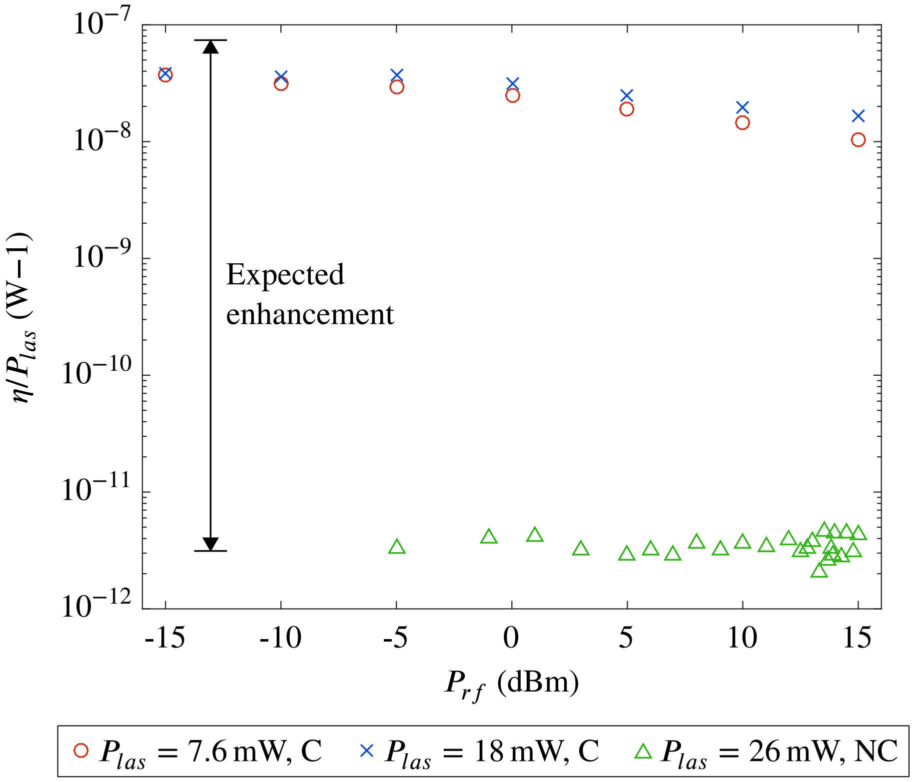

Figure 9.14: Conversion efficiency per Watt of pump laser power as a function of the input microwave power. Two measurements at different pump laser powers are shown for the case in which an optical cavity is used (C) and one measurement is shown for the case in which no optical cavity is used (NC).

A similar measurement as the one in Fig. 9.13 was performed, with the difference that a higher optical detuning was used. In that case the frequency difference between the optical fields and the center of the optical inhomogeneous line was of 1.5 GHz. The conversion efficiency showed a linear dependence with the pump laser power when using the cavity. However, at such a high detuning measurements without the optical cavity could not be performed, as the signal levels were well below the background noise, so no comparison could be made.

Fig. 9.14 shows the normalised conversion efficiency as a function of the input microwave power P_{rf}. Two measurements using the optical cavity are presented, and a single one is shown for the case without the optical cavity. The conversion efficiency for the cases in which the optical cavity is used shows a slow decay starting around $P_{rf} = -5$ dBm as the microwave power is increased. This decay is consistent with the saturation effect observed in Fig. 9.12 for the laser powers shown. However, the rapid increase in conversion efficiency is not seen in Fig. 9.14. A possible explanation for this is that the combination of magnetic field and optical detuning that we used for these measurements put the converted signal field in a region in the spectrum of ^{167}Er where the absorption is lower than it was in the measurements shown in Fig. 9.12. The measurement without the optical cavity shows a linear dependence between the conversion efficiency and the microwave power. This measurement is noisy because without the optical cavity the signal levels are low, even though the maximum laser power available was used. Comparing the measurements with and without the optical cavity we can see an enhancement of 10^4, which is consistent with the measurements in Fig. 9.13 and with the theoretical expectation.

9.3 Further Discussion and Conclusions

In this chapter I have discussed a series of experiments aimed at microwave to optical frequency conversion using an optical together with a microwave resonator. The experiments presented here were based on the experimental setup presented in Ch. 8, and in some sense they are an evolutionary step forward from that experiment. The first thing to do with the new setup was to characterise the interaction between the optical cavity and the optical atomic transitions. This study shows that the atoms are strongly coupled to the optical cavity. Some interesting tristable behaviour arising from the spectral hole burning phenomenon could be observed. The atom-cavity interaction is also responsible for a shift in the central frequency of the optical cavity modes near an atomic transition, which makes the experiments difficult since it adds a new effect to take into account. I have presented the ability to measure the spacing between optical modes at any given frequency of the optical cavity.

I have also presented a study of how the conversion efficiency scales with the input microwave power and with the optical pump power for the case in which the microwave and the optical fields are set on resonance with the atomic transitions. This shows an unexpected nonlinear behaviour, where the normalised conversion efficiency increases rapidly until it reaches a maximum and then falls off. This maximum is notably close to the expected conversion efficiency calculated from the theory presented in Ch. 4. This fact reinforces the hypothesis that the converted signal gets absorbed in the inhomogeneous lines of $^{2n}\mathrm{Er}^{3+}$:$\mathrm{Y_2SiO_5}$ and $^{167}\mathrm{Er}^{3+}$:$\mathrm{Y_2SiO_5}$. The presence of the optical cavity enhances this absorption, and the signal gets attenuated greatly. However, as the signal increases in power it reaches a state in which it can burn a spectral hole in the inhomogeneous line, which allows it to escape the cavity. At this point the measured conversion efficiency increases rapidly. The fact that the maximum of conversion efficiency is close to the theoretical value that we can calculate also reinforces the validity of the theory in Ch. 4.

In order to test the absorption hypothesis a purified sample with smaller amounts of the 167 isotope could be used. Then, experiments off resonance with the inhomogeneous line but still close enough to the atomic transitions to provide detectable signals could be performed. Alternatively, the experiments could be performed at lower temperatures; low enough to condense the atomic population in the ground state. In such a case only two absorption peaks would be observed for the even isotopes of erbium, and up to sixteen for the 167 isotope. In this situation, and in particular if using a sample with low amounts of ^{167}Er, one could set the pump on resonance with one of the absorption peaks, but then the generated signal would come out at a frequency where there is no absorption.

Lastly, a set of measurements performed with the microwave fields on resonance with the atomic transitions but with the optical fields set off resonance with the optical inhomogeneous line shows the enhancement in conversion efficiency that we obtained from the optical cavity. This was of four orders of magnitude, in good agreement with the theoretical expectations.

The maximum normalised conversion efficiency observed overall has been of about 3×10^{-4} per Watt of pump laser power. This particular measurement was performed with a pump laser power of near 10 mW, setting the maximum observed number efficiency to 3×10^{-6}. This value is about six orders of magnitude greater than what was observed in the first frequency conversion experiments, and admittedly also almost six orders of magnitude away from the idealised target value of 1. In order to increase the conversion efficiency further there are several possibilities, which can all be combined. The most critical improvement would come from performing the experiment inside a dilution refrigerator. This could bring the temperature of the sample down to around 10 mK, which would mean an increase in the nonlinear coefficient $\Lambda^{(2)}$ of a factor of 30. In turn, this would translate into an increase in conversion efficiency of $30^2 \approx 10^3$. Using samples with a higher erbium concentration would also increase the conversion efficiency, where a factor of 10 more erbium would mean a factor of 10^2 increase in efficiency. Another possibility is to use higher pump laser powers, with which the efficiency scales linearly. One more option is to use a narrower sample. By doing this we could achieve better overlapping between the microwave and the optical cavity modes.

Chapter 10

Conclusions and Future Work

This thesis explores the possibility of performing frequency conversion of microwave fields into optical ones for quantum information related applications using an erbium doped yttrium orthosilicate crystal as a nonlinear medium in an optical and a microwave cavity. The project is motivated by an earlier theoretical work by Williamson et al. [57] where they predict that high efficiencies are achievable in this kind of system with current technologies. In this thesis a new, more complete, theoretical background is developed. This theoretical work is based in calculating the nonlinear coefficient $\Lambda^{(2)}$ of the medium (analogous to the usual $\chi^{(2)}$ in nonlinear optics), and then solving the equations of motion that result from the Hamiltonian describing a system in which microwave and optical cavity modes interact with one another through the aforementioned nonlinearity of the medium. The theory developed in this thesis predicts, again, that high conversion efficiencies can be achieved under a set of realistic parameters.

A series of experiments are presented. First of all the possibility of using the 167 isotope of erbium for microwave to optical frequency conversion was explored. This isotope is the only stable one that shows hyperfine splitting in its energy level structure. The hyperfine levels of the ground state of $^{167}\mathrm{Er}^{3+}$:$\mathrm{Y_2SiO_5}$ span over about 5 GHz, which is particularly convenient as this frequency falls in the microwave region of the electromagnetic spectrum. The arrangement of the hyperfine energy levels is loosely known for the ground state, but almost completely unknown for the excited state. A hole burning spectroscopy experiment was performed in an attempt to reconstruct the hyperfine structure of the excited state, but the problem was too complex to achieve this goal. It was decided then to perform the frequency conversion experiments using the even isotopes of erbium, which don't show hyperfine splittings but on which a microwave transition can be seen by Zeeman splitting their ground and excited energy states using an external magnetic field.

Three more experiments followed. The first experiment showed that the frequency conversion process in Er^{3+}:Y_2SiO_5 actually exists, and served as a testing ground for the experimental techniques that would be used in later experiments. This initial experiment didn't incorporate an optical cavity (only a microwave resonator was used). The sample and the microwave cavity were cooled in a bath cryostat, and light was coupled in and out of the sample using optical fibres and fibre coupled collimators. Some conversion efficiency data was obtained, but several experimental complications compromised the accuracy of this data: namely, the inability to quantify the microwave and optical losses in a reliable way.

The second experiment was an improved version of the first experiment, which provided much more accurate data. A new cryostat was built in order to house a new superconducting magnet, fibre optics were substituted by free space optics, a microwave with a much higher quality factor was used, and a very much improved detection system was used. In this second experiment the interaction between the microwave cavity and the erbium ions was fully characterised. Regarding conversion efficiency, a comparison between the experimental data and the developed theory showed a discrepancy of a factor of between 2 and 5 when the optical fields were set on resonance with the atomic transitions. However, the model is not expected to work in this regime. When the optical fields were set off resonance with the atomic transitions the agreement between theory and experiment was good. The highest frequency conversion efficiency measured was of 1.5×10^{-8} per Watt of pump laser power.

In the third and last experiment an optical cavity was added to the setup. This complicated the experimental work substantially, in particular because of the interaction between the cavity modes and the erbium optical transitions. While studying this interaction a tri-stable behaviour of the optical cavity frequency was observed, which arose from spectral hole burning effects in the inhomogeneous line of Er^{3+}:Y_2SiO_5. During the characterisation of the frequency conversion efficiency a highly non-linear dependence of the converted signal with respect to the input microwave and laser powers was observed. This was not observed without the optical cavity. The effect was attributed to stray optical absorption of the converted signal inside the sample due to the 167 isotope of erbium, which has an absorption profile that extends through a wide region of the spectrum when a magnetic field is applied, and also due to the even isotopes of erbium in the case in which the optical fields are set on resonance with the atomic transitions. At higher powers of the converted signal, however, a spectral hole is burnt in the inhomogeneous line, which results in a rapid increase in the conversion efficiency measured. The reason why this effect was only relevant when an optical cavity was used is because it is the cavity itself that enhances the absorption of the converted signal in the sample. A comparison between experiments performed with and without the optical cavity showed a conversion efficiency enhancement of 10^4, in good agreement with the theoretical predictions. The maximum conversion efficiency measured while using the optical cavity was of 2×10^{-4} per Watt of pump laser power.

The two main objectives for the future development of our experiment are to get a better understanding and find a way to suppress the loss of converted signal that occurs at low powers when an optical cavity is used, and to increase the overall conversion efficiency. In order to get rid of the loss at low powers an isotopically purified sample with low amounts of ^{167}Er could be used, and then experiments could be performed with the optical fields off resonance with the transitions of the even erbium isotopes. Alternatively, a scheme in which a spectral hole is burnt around the frequency of the converted signal could be devised so that one gets rid of that region of the absorption profile. This would have the effect of shifting the populations among the energy levels of ^{167}Er, which would in turn change the value of $\Lambda^{(2)}$ for ions from this particular isotope, but the natural abundance of ^{167}Er is of about 23% so this wouldn't change the total conversion efficiency dramatically. In order to increase the conversion efficiency there are several improvements to make. The first, and most important one, is to decrease the operating temperature of the experiment. In all the experiments shown in this thesis the temperature of the sample was between 2 and 4 K. The projected working temperature is of around 10 mK. Cooling the sample down from 4 K to 10 mK would imply an increase in the nonlinear coefficient $\Lambda^{(2)}$ of around a factor of 30. Since the conversion efficiency is proportional to $[\Lambda^{(2)}]^2$ this would mean an increase of near three orders of magnitude, setting the conversion efficiency at values on the order of 10^{-1} per Watt of pump laser power. Additionally, cooling the sample down to ~10 mK would simplify the optical absorption spectrum, which would help in getting rid of the stray absorption in the sample. Another immediate way to increase the conversion efficiency is to use a sample with a higher concentration of erbium. The conversion efficiency scales quadratically with the density of erbium ions, so increasing the concentration by a factor of 10 would mean a conversion efficiency 100 times higher. However, the dopant concentration can not be increased unlimitedly because at some point the optical inhomogeneous line will start to broaden, which increases the detuning between the erbium ions and the optical fields, thus decreasing the conversion efficiency. This would be less of a problem for experiments performed off resonance. A third way to increase the conversion efficiency is to get better filling factors between the optical and the microwave modes in the resonators. In the experiment we performed we opted for a rather conservative design in which the optical cavity mode is relatively small compared to the microwave cavity mode, giving a not so good overlap between the two. A more aggressive approach would be possible in this sense. The frequency conversion efficiency scales linearly with the filling factor, but a further factor of between 2 and 5 could be easily achieved. Regarding the quality factor of the resonators we are already operating close to the limit. The quality factor of the optical cavity will ultimately be limited by optical losses in YSO, and we believe we are working close to that limit already. With respect to the microwave resonator its quality factor will ultimately be limited by losses in the surface of the material it is made from. In our experiments we used high quality oxygen free copper, and we believe to be close to that limit too. Lastly, the conversion efficiency could be increased by using higher pump laser powers. In our experiments we were limited to powers of a few tens of milliwatts, but much higher powers can be achieved. A possible caveat with this approach is that higher pump powers will translate into a higher thermal load on the sample, but one could always perform these experiments in a pulsed regime, where the pump laser is only switched on for brief periods of time, thus decreasing the heating effects.

In Ch. 2 a mention was made about the different approaches to quantum frequency conversion between microwave and optical fields. Where does the work presented in this thesis fit in the wider context? Optomechanical devices [40–45] have been shown to achieve much greater efficiencies ($\sim$10%), but in order to get low noise frequency conversion they need to be cooled down to their ground state. This is currently very challenging as they operate at frequencies in the order of kilohertzs, which means that they need to be cooled down to very low temperatures. In comparison, the three wave mixing process exploited in this thesis is naturally noise free. Experiments using nonlinear crystals in optical and microwave resonators [46–50] have shown high efficiencies too ($\sim$0.1%), but they are already exploiting the highest nonlinearities of typical nonlinear crystals. Additionally, keeping the process single-sideband is much more challenging than in the approach presented here. Brillouin scattering between magnons and photons in YIG[51–53] and Rydberg gasses [54–56] are other proposed alternatives, but either no experimental demonstration has been shown yet (Rydberg gasses), or the conversion efficiencies achieved have been extremely low (YIG). The main shortcoming of the approach discussed in this thesis is low conversion efficiency, but as it has been discussed there are multiple ways in which this can be increased, potentially to values close to unit. In conclusion, Er^{3+}:Y_2SiO_5 is, at the very least, a worthy competitor in the race towards quantum frequency conversion between microwave and optical fields.

Appendix A

Atom-Cavity Coupling and Cavity Pushing

In this appendix I will present the formalism that explains some of the effects derived from having a collection of atoms coupled to a resonator. In particular I want to give an explanation for the frequency shift that a cavity experiences when the frequency of the atoms it is coupled to is tuned close to its own. I will refer to this effect as *cavity pushing*, as the experimental observations show that the resonance frequency of the cavity shifts away from the atomic resonance frequency as they are moved towards each other. I need to mention Yu-Hui Chen in this section, as he helped me a lot in understanding this phenomenon and the mathematical equations behind it. A way to explain this effect is by looking at the Input-Output theory for resonators, which can be referred to e.g. in Ref. [74] or Ref. [98]. Note that this problem is equivalent to the study of two coupled oscillators, which can be done in a purely classical way, and which was explored in the semiclassical approach by W. E. Lamb [99].

We consider the system of an ensemble of degenerate two energy level atoms coupled with a resonant cavity mode. The Hamiltonian of this system can be written as[1]

$$H = \omega_c a^\dagger a + \omega_a b^\dagger b + \sqrt{N} g b^\dagger a + \sqrt{N} g a^\dagger b, \tag{A.1}$$

where N is the number of atoms, ω_c and ω_a are the cavity and the atomic transition frequencies respectively, a is the annihilation operator associated to a single excitation in the cavity mode, b is the annihilation operator associated with a single excitation in the atomic ensemble, and g is the atom-cavity coupling strength. For a cavity with two coupling channels the equations of

---

[1] There is a factor of $\hbar$ multiplying everything on the right hand side of Eq. (A.1). In order to keep the writing tidy the standard substitution $\hbar \rightarrow 1$ has been made in this appendix.

motion for *a* and *b* can be written as

$$\dot{a} = -i[a, H] - \frac{\kappa_i + \kappa_1 + \kappa_2}{2} a - \sqrt{\kappa_1} A_{in1} - \sqrt{\kappa_2} A_{in2}, \tag{A.2}$$

$$\dot{b} = -i[b, H] - \frac{\gamma}{2} b - \sqrt{\gamma} B_{in}, \tag{A.3}$$

where κ_i represents the intrinsic loss of the cavity, $\kappa_{1,2}$ represents the coupling loss through channels 1 and 2, γ is the linewidth of the atomic transition, and $A_{in1,2}$ and B_{in} are the input fields through the different channels. If we assume that the only input in our system is through A_{in1} we can set A_{in2} and B_{in} equal to zero. Computing the commutators in the previous equations yields

$$\dot{a} = -i\omega_c a - i\sqrt{N} g b - \frac{\kappa_i + \kappa_1 + \kappa_2}{2} a - \sqrt{\kappa_1} A_{in1} \tag{A.4}$$

$$\dot{b} = -i\omega_a b - i\sqrt{N} g a - \frac{\gamma}{2} b. \tag{A.5}$$

In order to solve this system of differential equations it is convenient to take the Fourier transform of *a* and *b* as

$$a(t) = \frac{1}{\sqrt{2\pi}} \int_{-\infty}^{+\infty} a(\omega) e^{-i\omega t} \mathrm{d}t \tag{A.6}$$

$$b(t) = \frac{1}{\sqrt{2\pi}} \int_{-\infty}^{+\infty} b(\omega) e^{-i\omega t} \mathrm{d}t. \tag{A.7}$$

Then, Eqs. (A.4) and (A.5) become

$$-i\omega a(\omega) = -i\omega_c a(\omega) - i\sqrt{N} g b(\omega) - \frac{\kappa_i + \kappa_1 + \kappa_2}{2} a(\omega) - \sqrt{\kappa_1} A_{in1}(\omega) \tag{A.8}$$

$$-i\omega b(\omega) = -i\omega_a b(\omega) - i\sqrt{N} g a(\omega) - \frac{\gamma}{2} b(\omega), \tag{A.9}$$

from which we can see that

$$b(\omega) = \frac{-i\sqrt{N} g}{\frac{\gamma}{2} - i\left(\omega - \omega_s\right)} a(\omega) \tag{A.10}$$

and

$$a(\omega) = \frac{-\sqrt{\kappa_1}}{-i\left(\omega - \omega_c\right) + \frac{\kappa_i + \kappa_1 + \kappa_2}{2} + \frac{N g^2}{\frac{\gamma}{2} - i\left(\omega - \omega_a\right)}}. \tag{A.11}$$

The input-output relationships for the cavity are

$$A_{out1}(\omega) - A_{in1}(\omega) = \sqrt{\kappa_1}a(\omega) \tag{A.12}$$

$$A_{out2}(\omega) - A_{in2}(\omega) = \sqrt{\kappa_2}a(\omega), \tag{A.13}$$

so the output fields from each channel can be written as a function of the input field in channel 1 as

$$A_{out1}(\omega) = \left[1 + \frac{-\kappa_1}{-i\left(\omega - \omega_c\right) + \frac{\kappa_i+\kappa_1+\kappa_2}{2} + \frac{Ng^2}{\frac{\gamma}{2}-i\left(\omega-\omega_a\right)}}\right] A_{in1}(\omega) \tag{A.14}$$

$$A_{out2}(\omega) = \frac{-\sqrt{\kappa_1\kappa_2}}{-i\left(\omega - \omega_c\right) + \frac{\kappa_i+\kappa_1+\kappa_2}{2} + \frac{Ng^2}{\frac{\gamma}{2}-i\left(\omega-\omega_a\right)}} A_{in1}(\omega). \tag{A.15}$$

The scattering parameters are defined as $S_{ij} = A_{out,i}(\omega)/A_{in,j}(\omega)$. It is straightforward to see from Eq. (A.15) that the reflection parameter S_{11} is

$$S_{11}(\omega) = 1 + \frac{-\kappa_1}{-i\left(\omega - \omega_c\right) + \frac{\kappa_i+\kappa_1+\kappa_2}{2} + \frac{Ng^2}{\frac{\gamma}{2}-i\left(\omega-\omega_a\right)}}. \tag{A.16}$$

Similarly, the transmission parameter through the cavity S_{21} is

$$S_{21}(\omega) = \frac{-\sqrt{\kappa_1\kappa_2}}{-i\left(\omega - \omega_c\right) + \frac{\kappa_i+\kappa_1+\kappa_2}{2} + \frac{Ng^2}{\frac{\gamma}{2}-i\left(\omega-\omega_a\right)}}. \tag{A.17}$$

The denominator in Eqs. (A.16) and (A.17) has three terms. The first term is completely imaginary, and it determines where the resonance frequency is ($\omega = \omega_c$). The second term is completely real, and it determines the total loss in the cavity. The third term contains the information about the atom cavity coupling (Ng^2), and it has a real and an imaginary part. The real part of the third term will then make some contribution to the cavity loss, or in other words, it will change the height and width of the transmission peak. The imaginary part of the third term will make a contribution to the resonance frequency of the cavity, i.e. it will change the position of the transmission peak. It is worth noting here that what one measures experimentally with a network or a spectrum analyser is usually $|S_{ij}|^2$.

By decomposing the third term into its real and imaginary parts we can write an expression for the extra broadening in the transmission peak induced by the atoms as

$$\Gamma = \frac{Ng^2}{\left(\omega - \omega_a\right)^2 + \frac{\gamma^2}{4}} \cdot \frac{\gamma}{2}. \tag{A.18}$$

Similarly, we can write an expression for the frequency shift on the cavity frequency induced by the atoms as

$$\Delta = \frac{Ng^2}{\left(\omega - \omega_a\right)^2 + \frac{\gamma^2}{4}} \cdot \left(\omega - \omega_a\right). \tag{A.19}$$

This frequency shift will only be relevant in the case where the input frequency is close to the cavity frequency, so we can replace ω for ω_c in the previous expression to get

$$\Delta = \frac{Ng^2}{\left(\omega_c - \omega_a\right)^2 + \frac{\gamma^2}{4}} \cdot \left(\omega_c - \omega_a\right). \tag{A.20}$$

The maximum and the minimum of Eq. (A.20) are for $\omega_a - \omega_c = \pm\gamma/2$, and the maximum frequency shift attainable will be given by $\Delta_M = Ng^2/\gamma$.

Appendix B

Integration of $\Lambda^{(2)}$

In this appendix I will explain how I solved the difficulties of performing the integrals of the $\Lambda^{(2)}$ function over the optical and the microwave inhomogeneous lines. The main problem is that the $\Lambda^{(2)}$ function has very narrow features. This can be seen in Fig. 4.4, where a series of sharp lines can be observed. The widths of these lines are the different γ_{ij}, which are taken to be $2\pi \times 0.1\,\text{MHz}$ for the optical transitions and $2\pi \times 35\,\text{MHz}$ for the microwave one. In order to obtain a value for $\Lambda^{(2)}$ for a given set of optical and microwave detunigs we need to perform an integral over the contribution from all the atoms in the inhomogeneous lines. The optical inhomogeneous broadening is taken to be of 400 MHz at FWHM, and the microwave one is taken to be of 35 MHz. The inhomogeneous profiles are simulated to be gaussian. In order to make sure that the contribution from all the atoms is taken into account the integral is performed over a range of frequencies equal to four times the inhomogeneous linewidths. This two dimensional integral was solved numerically using MATLAB.

Because the $\Lambda^{(2)}$ function is mostly flat but has sharp features in different places the built-in integration functions of MATLAB sometimes encounter problems when trying to integrate it. Other times these integration functions will return a number for the integral, but it will be far from the real value. In order to solve this problem I divided the two dimensional space into different sections and integrated them separately. In this way I could tell MATLAB to integrate the narrow features of the $\Lambda^{(2)}$ function separately from the flat areas, which MATLAB can do without issues. The first thing to do was to find an equation for each of the lines observed in Fig. 4.4 (1.a, 1.b, 2.a, 2.b, etc.). Then I defined a rectangular region around each of these lines. These rectangles would span around twenty times the width of each of the lines, making sure that the sharp parts of $\Lambda^{(2)}$ were contained inside these regions. At this point integrating these rectangles one by one and adding the results is possible using the built-in integration functions of MATLAB, but this would not return the right results. This is because the different lines intersect with one another at different points, and therefore so do the rectangular regions around them. If we integrated the rectangles as they are we would be counting some regions twice. On top of that we would still need a way to integrate all the flat regions outside the rectangles.

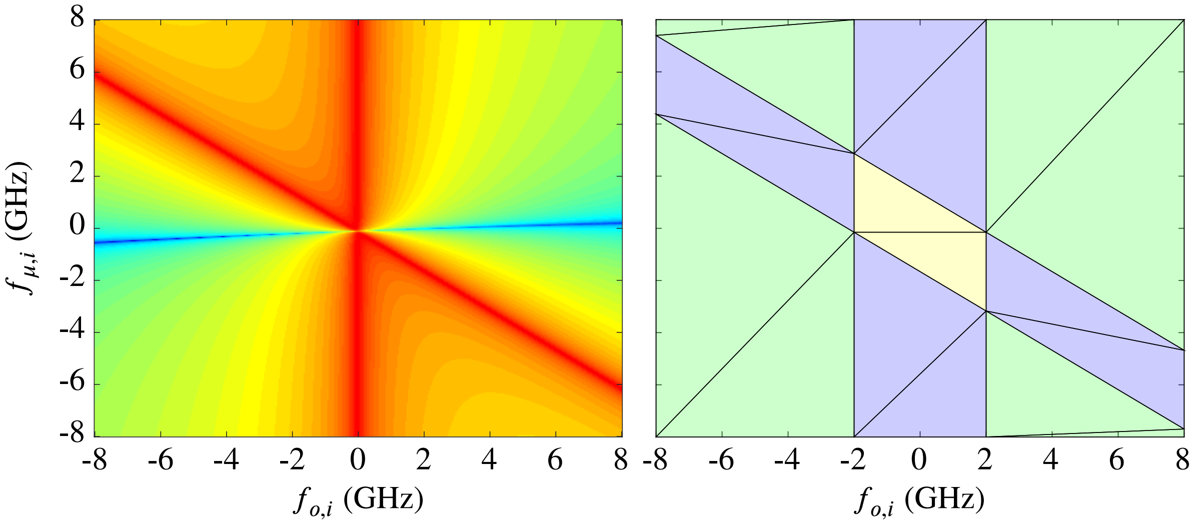

Figure B.1: Example of how the integration of the $\Lambda^{(2)}$ function is divided into different zones. *Left:* a region in the two dimensional space that needs to be integrated. The $\Lambda^{(2)}$ function is plotted as a function of the optical frequency (horizontal axis) and the microwave frequency (vertical axis) of a given atom i. *Right:* the two dimensional space is split into three different zones. Each of these zones is then triangulated and each of the triangles is integrated separately, and then the results are added.

In order to solve the problem of the rectangles overlapping with one another I divided the whole two dimensional integration space into three zones. This can be seen in Fig. B.1. Zone 1 (in green) contains the relatively flat regions, where no rectangles are present. Zone 2 (in blue) contains the regions inside the rectangles that do not intersect with any other rectangle. Zone 3 (in yellow) contains the regions where at least two rectangles intersect one another. This method provides a good separation for the different regions, mapping all the integration space with no intersections between the different zones. These zones have the shape of arbitrary polygons in two dimensions. Some of them look like quadrilaterals, some like triangles, but some others have more complicated star-like shapes, especially when three rectangles intersect at the same time. I could not find a readily available solution in MATLAB for integration of arbitrary two dimensional functions over arbitrary polygons. What I did was to triangulate each of the zones, i.e. I split the different polygons into a collection of triangles. There are several possible methods for doing this. The one I used is called Delaunay triangulation, which is a triangulation method that tries to avoid “thin” triangles with small angles. What is left after triangulating is to find a way to integrate an arbitrary two dimensional function over an arbitrary triangle, but I could not find a function in MATLAB for that. What I did was to write a function that maps the area of a triangle into the area of a square of unit length sides, and use a standard MATLAB function to integrate over the square domain.

In order to map the problem function from a triangular domain into a square one we require a change of variables given by the following transformations:

$$x = x(u, v) = (1 - u)x_1 + u[(1 - v)x_2 + vx_3] \tag{B.1}$$

$$y = y(u, v) = (1 - u)y_1 + u[(1 - v)y_2 + vy_3], \tag{B.2}$$

$$\tag{B.3}$$

where (x_1, y_1), (x_2, y_2) and (x_3, y_3) are the positions of the three vertices of the triangle that we want to integrate over. Then, we have that

$$\int_T f(x, y)\mathrm{d}x\mathrm{d}y = \int_S f[x(u, v), y(u, v)]\, |\det(J)|\, \mathrm{d}u\mathrm{d}v, \tag{B.4}$$

where the integral over T symbolises the integral over the arbitrary triangle and the integral over S represents an integral over the unit square, and J is the Jacobian matrix of the change of variables defined by

$$J = \begin{pmatrix} \frac{\partial x}{\partial u} & \frac{\partial x}{\partial v} \\ \frac{\partial y}{\partial u} & \frac{\partial y}{\partial v} \end{pmatrix}. \tag{B.5}$$

Appendix C

Spectral Hole Burning in $^{167}\mathrm{Er}^{3+}$:$\mathrm{Y_2SiO_5}$: Additional Plots

The plots shown in this appendix make reference to the experiments presented in Ch. 6, and a full description of their meaning shall be found there.

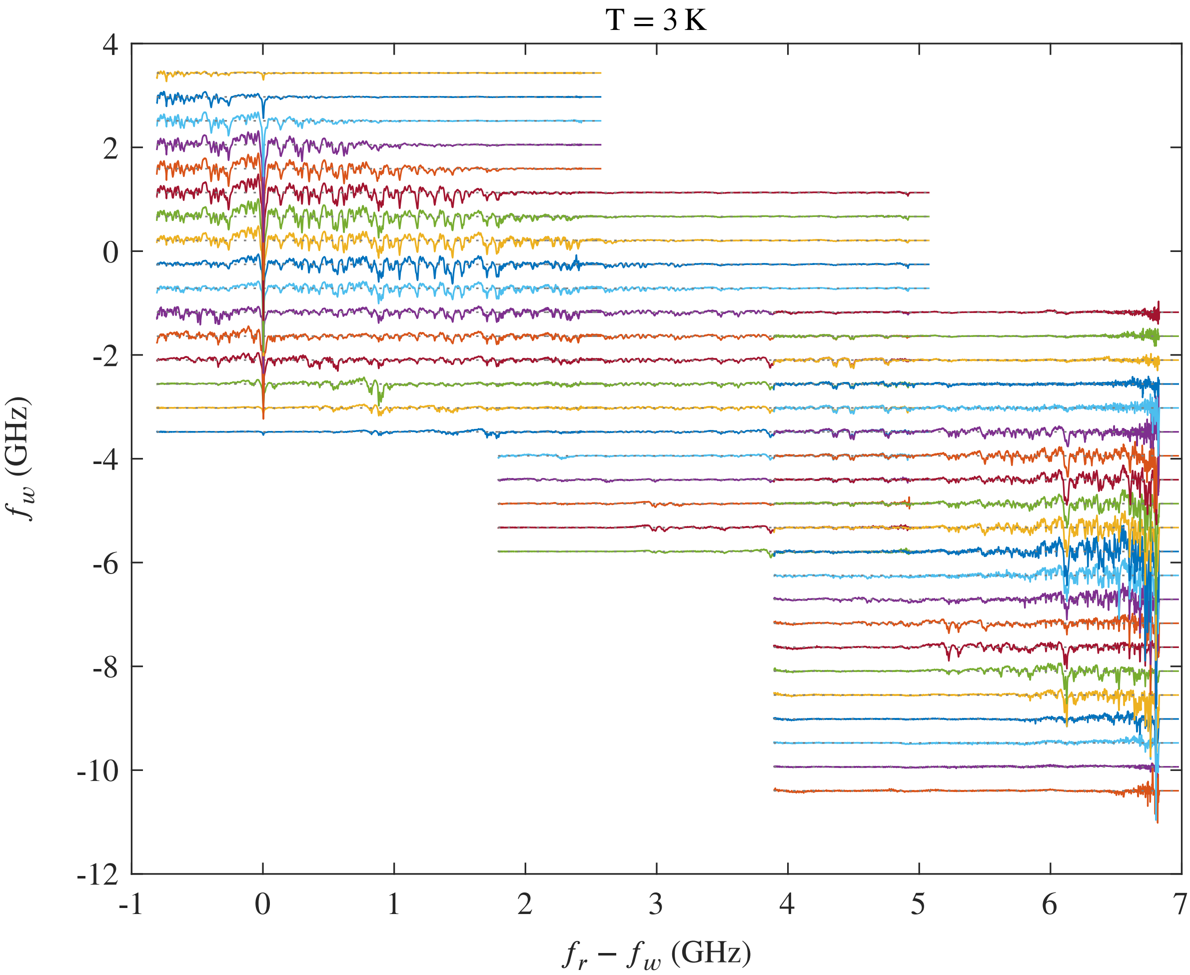

Figure C.1: SHB experimental results for a temperature of 3 K.

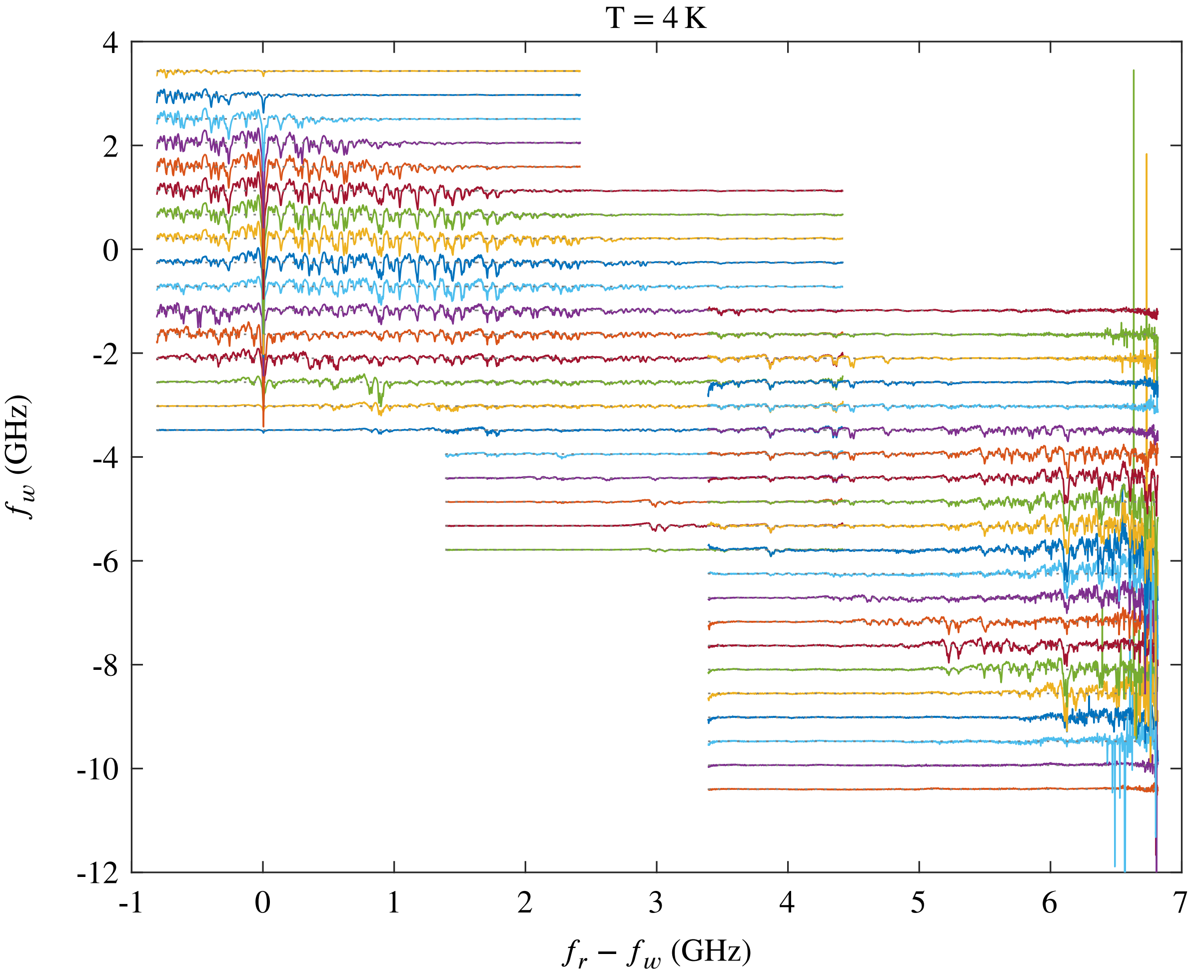

Figure C.2: SHB experimental results for a temperature of 4 K.

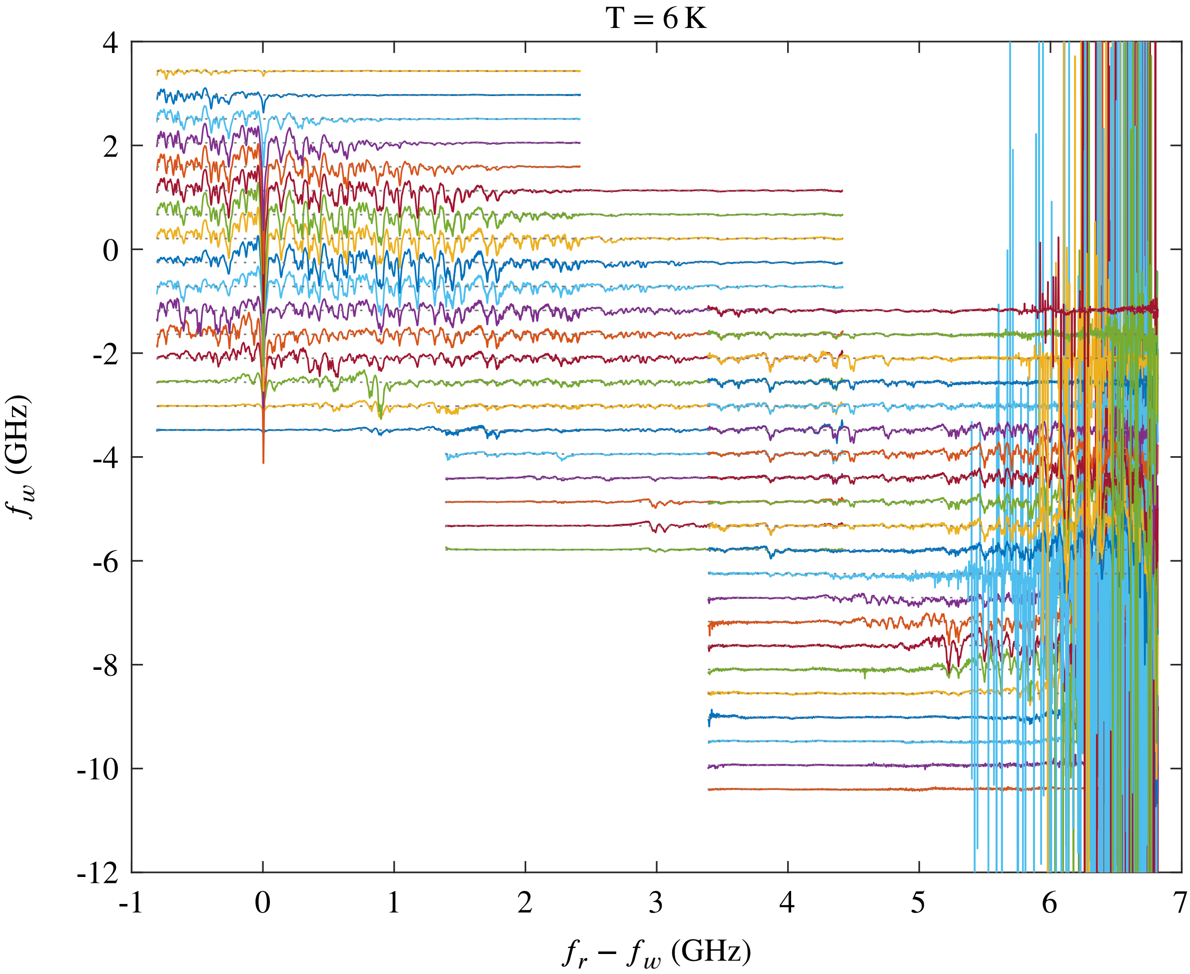

Figure C.3: SHB experimental results for a temperature of 6 K.

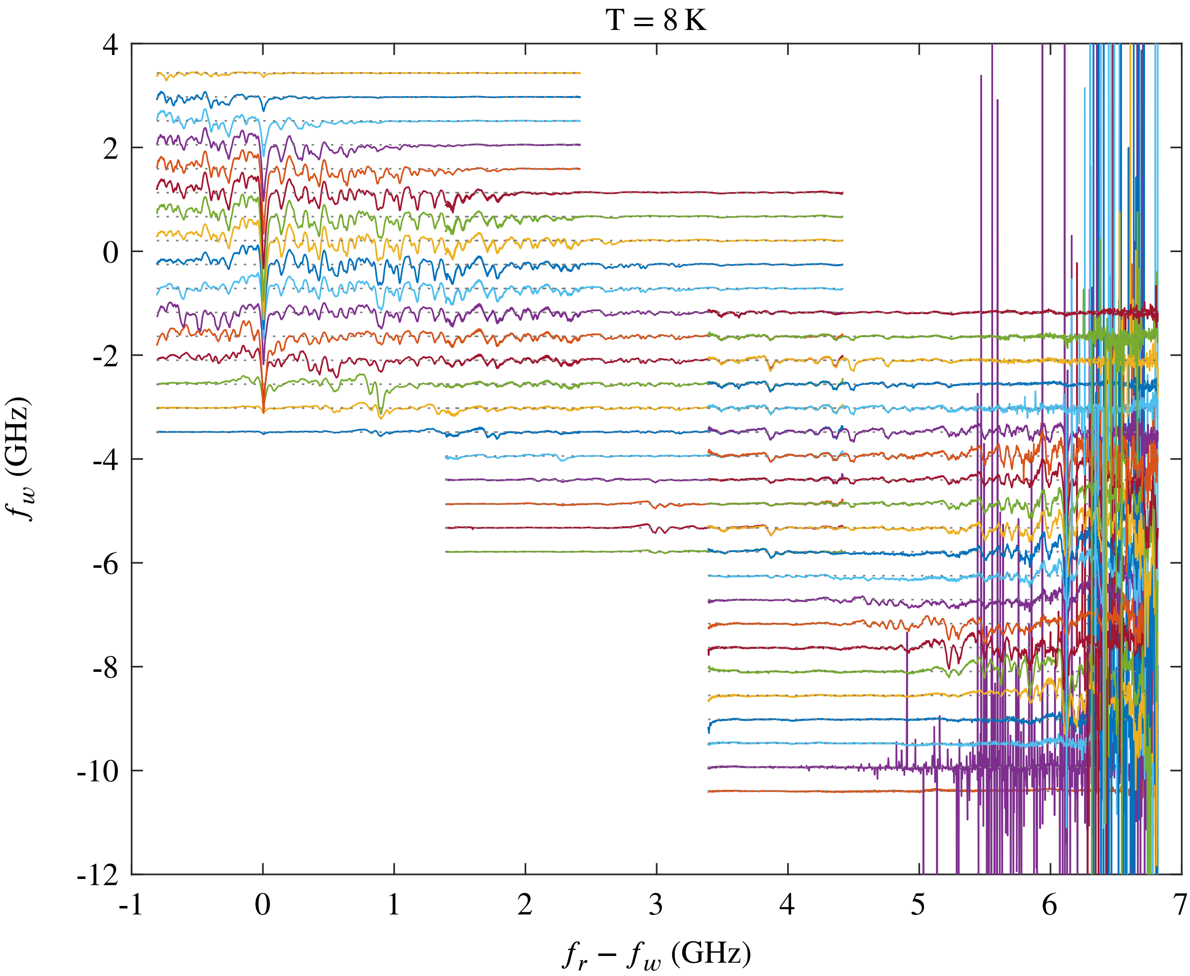

Figure C.4: SHB experimental results for a temperature of 8 K.

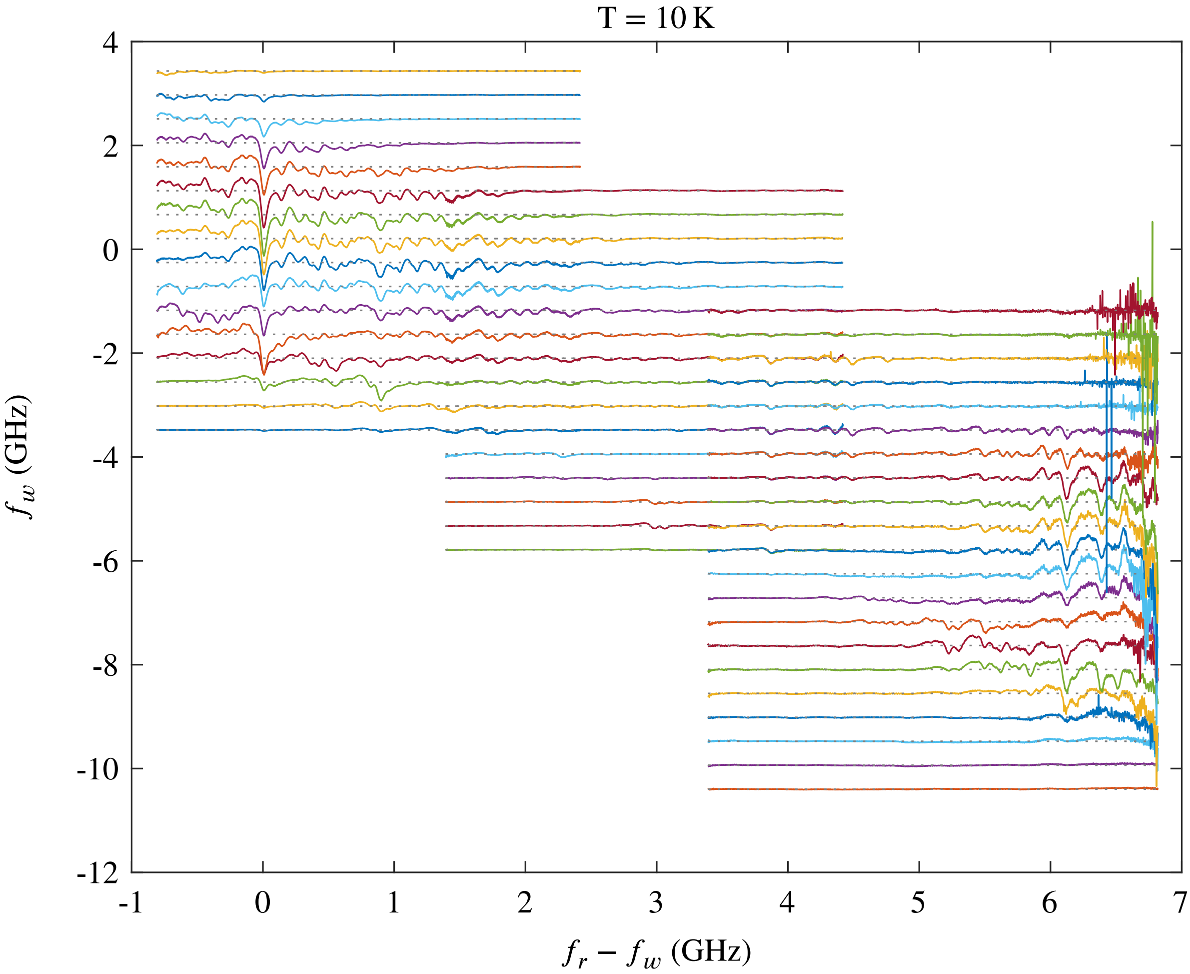

Figure C.5: SHB experimental results for a temperature of 10 K.

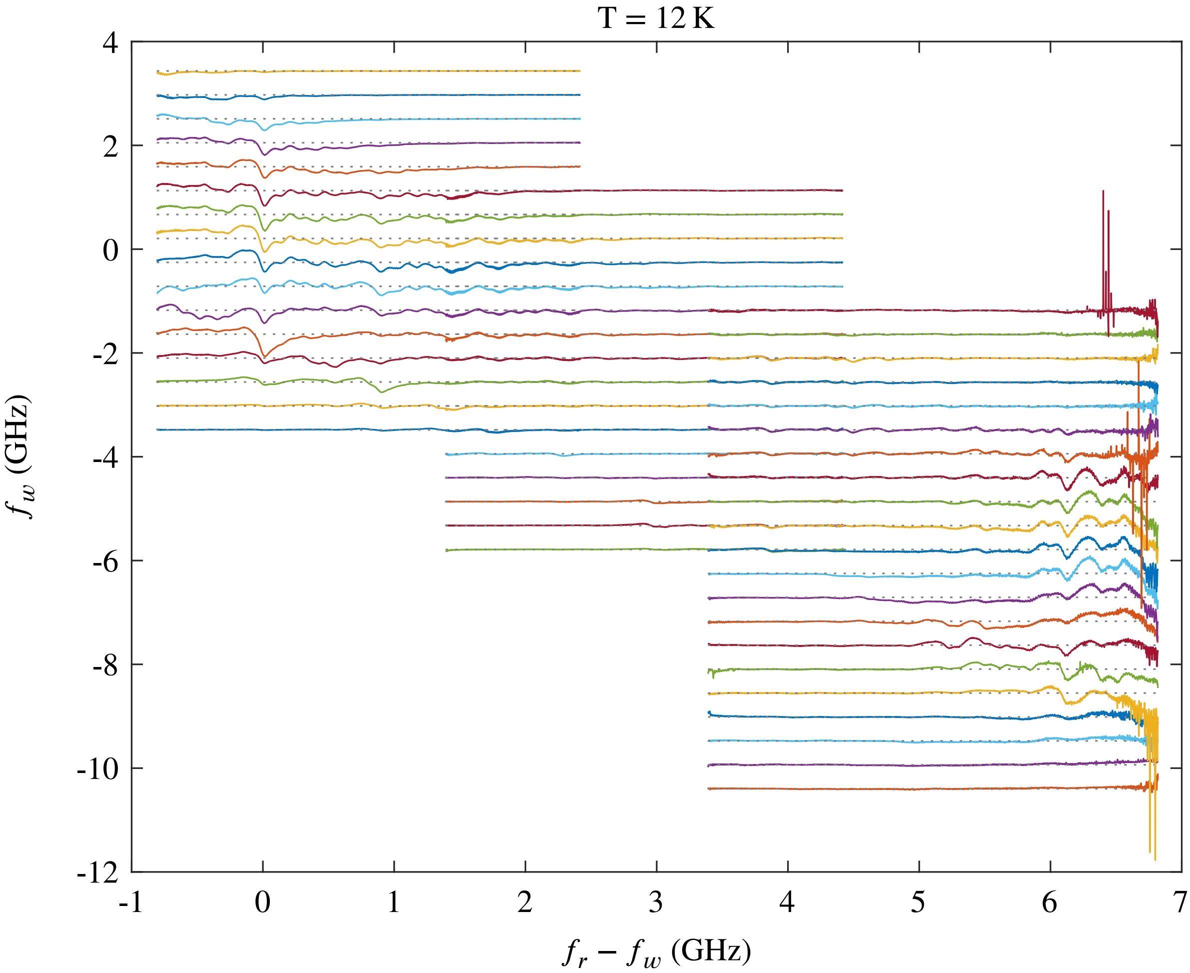

Figure C.6: SHB experimental results for a temperature of 12 K.

Appendix D

List of Publications

Papers

- Xavier Fernandez-Gonzalvo, Yu-Hui Chen, Chunming Yin, Sven Rogge, and Jevon J. Longdell. *Coherent frequency up-conversion of microwaves to the optical telecommunications band in an Er:YSO crystal.* Phys. Rev. A, 92:062313 (2015).

- Yu-Hui Chen, Xavier Fernandez-Gonzalvo, and Jevon J. Longdell. *Coupling erbium spins to a three-dimensional superconducting cavity at zero magnetic field.* Phys. Rev. B, 94:075117 (2016).

Oral Presentations

- Conference on Optics, Atoms and Laser Applications (IONS-KOALA). Adelaide, Australia, November 2014. *Frequency up-conversion of microwave photons into optical photons via Raman processes in an Er:YSO crystal.* Xavier Fernandez-Gonzalvo, Yu-Hui Chen, Chunming Yin, Sven Rogge, and Jevon J. Longdell.

- Conference on Lasers and Electro-Optics (CLEO/Europe). Munich, Germany, June 2015. *Frequency Up-Conversion of Microwave Photons to the Telecommunications Band in an Er:YSO Crystal.* Xavier Fernandez-Gonzalvo, Yu-Hui Chen, Chunming Yin, Sven Rogge, and Jevon J. Longdell.

- Matariki Workshop on Quantum Science (MQS). Dunedin, New Zealand, March 2016. *Frequency Up-Conversion of Microwave Signals to the Telecommunications Band in an Er:YSO Crystal.* Xavier Fernandez-Gonzalvo, Yu-Hui Chen, Chunming Yin, Sven Rogge, and Jevon J. Longdell.

- Dodd-Walls Center Symposium (DWCS). Queenstown, New Zealand, June 2016. *Frequency Up-Conversion of Microwave Signals to the Telecommunications Band in an Er:YSO Crystal.* Xavier Fernandez-Gonzalvo, Yu-Hui Chen, Chunming Yin, Sven Rogge, and Jevon J. Longdell.

Poster Presentations

- Dodd-Walls Center Symposium (DWCS). Dunedin, New Zealand, November 2013. *Exploring the Hyperfine Structure of* $^{167}Er{:}Y_2SiO_5$ *via Spectral Hole Burning.* Xavier Fernandez-Gonzalvo, and Jevon J. Longdell.
- Australian and New Zealand Conference on Optics and Photonics (ANZCOP). Perth, Australia, December 2013. *Exploring the Hyperfine Structure of* $^{167}Er{:}Y_2SiO_5$ *via Spectral Hole Burning.* Xavier Fernandez-Gonzalvo, and Jevon J. Longdell.
- Dodd-Walls Center Symposium (DWCS). Dunedin, New Zealand, February 2015. *Frequency conversion from microwave to telecom photons in an Er:YSO crystal.* Xavier Fernandez-Gonzalvo, Yu-Hui Chen, Chunming Yin, Sven Rogge, and Jevon J. Longdell.
- Conference on Optics, Atoms and Laser Applications (IONS-KOALA). Auckland, New Zealand, November 2015. *Frequency Up-Conversion of Microwave Signals to the Optical Telecommunications Band in an Er:YSO Crystal.* Xavier Fernandez-Gonzalvo, Yu-Hui Chen, Chunming Yin, Sven Rogge, and Jevon J. Longdell.
- Asia-Pacific Conference & Workshop on Quantum Information Science (APCWQIS). Auckland, New Zealand, November 2015. *Exploring the Hyperfine Structure of* ^{167}*Er:YSO via Spectral Hole Burning.* Xavier Fernandez-Gonzalvo, and Jevon J. Longdell.

Bibliography

[1] M. A. Nielsen and I. L. Chuang. *Quantum Computation and Quantum Information*. Cambridg Univ. Press, 1st edition, 2000.

[2] L. K. Grover. Quantum mechanics helps in searching for a needle in a haystack. *Phys. Rev. Lett.*, 79:325–328, 1997.

[3] P. W. Shor. Polynomial-time algorithms for prime factorization and discrete logarithms on a quantum computer. *SIAM Journal on Computing*, 26(5):1484–1509, 1997.

[4] C.H. Bennet and G. Brassard. Quantum cryptography: Public key distribution and coin tossing. *Proceedings of IEEE International Conference on Computers, Systems and Signal Processing*, pages 175–179, 1984.

[5] W. K. Wootters and W. H. Zurek. A single quantum cannot be cloned. *Nature*, 229:802–803, 1982.

[6] D. Dieks. Communication by EPR devices. *Physics Letters A*, 92(6):271 – 272, 1982.

[7] H. J. Kimble. The quantum internet. *Nature*, 453:1023–1030, 2008.

[8] M. Zhong, M. P. Hedges, R. L. Ahlefeldt, J. G. Bartholomew, S. E. Beavan, S. M. Wittig, J. J. Longdell, and M. J. Sellars. Optically addressable nuclear spins in a solid with a six-hour coherence time. *Nature*, 517(7533):177–180, 2015.

[9] L.-M. Duan, M. D. Lukin, J. I. Cirac, and P. Zoller. Long-distance quantum communication with atomic ensembles and linear optics. *Nature*, 414:413–418, 2001.

[10] E. Knill, R. Laflamme, and G. J. Milburn. A scheme for efficient quantum computation with linear optics. *Nature*, 409(6816):46–52, 2001.

[11] I. Buluta, S. Ashhab, and F. Nori. Natural and artificial atoms for quantum computation. *Reports on Progress in Physics*, 74(10):104401, 2011.

[12] J. J. Longdell, E. Fraval, M. J. Sellars, and N. B. Manson. Stopped light with storage times greater than one second using electromagnetically induced transparency in a solid. *Physical Review Letters*, 95(6):063601, 2005.

[13] M. Hosseini, B. M. Sparkes, G. Hetet, J. J. Longdell, P. K. Lam, and B. C. Buchler. Coherent optical pulse sequencer for quantum applications. *Nature*, 461(7261):241–245, 2009.

[14] I. Usmani, M. Afzelius, H. de Riedmatten, and N. Gisin. Mapping multiple photonic qubits into and out of one solid-state atomic ensemble. *Nat. Commun.*, 1:12, 2010.

[15] M. P. Hedges, J. J. Longdell, Y. Li, and M. J. Sellars. Efficient quantum memory for light. *Nature*, 465(7301):1052–1056, 2010.

[16] N. Timoney, I. Usmani, P. Jobez, M. Afzelius, and N. Gisin. Single-photon-level optical storage in a solid-state spin-wave memory. *Physical Review A*, 88(2):022324, 2013.

[17] A. Cleland and M. Geller. Superconducting qubit storage and entanglement with nanomechanical resonators. *Physical Review Letters*, 93(7):070501, 2004.

[18] M. A. Sillanpaa, J. I. Park, and R. W. Simmonds. Coherent quantum state storage and transfer between two phase qubits via a resonant cavity. *Nature*, 449(7161):438–442, 2007.

[19] H. Wu, R. E. George, J. H. Wesenberg, K. Mø lmer, D. I. Schuster, R. J. Schoelkopf, K. M. Itoh, A. Ardavan, J. J. L. Morton, and G. A. D. Briggs. Storage of multiple coherent microwave excitations in an electron spin ensemble. *Physical Review Letters*, 105(14):140503, 2010.

[20] N. Timoney, I. Baumgart, M. Johanning, A. F. Varon, M. B. Plenio, A. Retzker, and C. Wunderlich. Quantum gates and memory using microwave-dressed states. *Nature*, 476(7359):185–188, 2011.

[21] Z.-L. Xiang, S. Ashhab, J. Q. You, and F. Nori. Hybrid quantum circuits: Superconducting circuits interacting with other quantum systems. *Rev. Mod. Phys.*, 85:623–653, 2013.

[22] G. Kurizki, P. Bertet, Y. Kubo, K. Mølmer, D. Petrosyan, P. Rabl, and J. Schmiedmayer. Quantum technologies with hybrid systems. *Proceedings of the National Academy of Sciences*, 112(13):3866–3873, 2015.

[23] M. G. Raymer and K. Srinivasan. Manipulating the color and shape of single photons. *Physics Today*, 65(11):32–37, 2012.

[24] S. Tanzilli, W. Tittel, M. Halder, O. Alibart, P. Baldi, N. Gisin, and H. Zbinden. A photonic quantum information interface. *Nature*, 437(7055):116–120, 2005.

[25] H. McGuinness, M. Raymer, C. McKinstrie, and S. Radic. Quantum frequency translation of single-photon states in a photonic crystal fiber. *Phys. Rev. Lett.*, 105:093604, 2010.

[26] A. G. Radnaev, Y. O. Dudin, R. Zhao, H. H. Jen, S. D. Jenkins, A. Kuzmich, and T. A. B. Kennedy. A quantum memory with telecom-wavelength conversion. *Nature Physics*, 6(11):894–899, 2010.

[27] R. Ikuta, Y. Kusaka, T. Kitano, H. Kato, T. Yamamoto, M. Koashi, and N. Imoto. Wide-band quantum interface for visible-to-telecommunication wavelength conversion. *Nature Communications*, 2:1544 EP –, 2011.

[28] S. Zaske, A. Lenhard, C.n Keßler, J. Kettler, C. Hepp, C. Arend, R. Albrecht, W.-M. Schulz, M. Jetter, P. Michler, and C. Becher. Visible-to-telecom quantum frequency conversion of light from a single quantum emitter. *Phys. Rev. Lett.*, 109:147404, 2012.

[29] M. T. Rakher, L. Ma, O. Slattery, X. Tang, and K. Srinivasan. Quantum transduction of telecommunications-band single photons from a quantum dot by frequency upconversion. *Nat. Photon.*, 4(11):786–791, 2010.

[30] B. Albrecht, P. Farrera, X. Fernandez-Gonzalvo, M. Cristiani, and H. de Riedmatten. A waveguide frequency converter connecting rubidium-based quantum memories to the telecom C-band. *Nat. Commun.*, 5(3376), 2014.

[31] J. Clarke and F. K. Wilhelm. Superconducting quantum bits. *Nature*, 453(7198):1031–42, 2008.

[32] M. H. Devoret and R. J. Schoelkopf. Superconducting circuits for quantum information: an outlook. *Science*, 339(6124):1169–1174, 2013.

[33] R. J. Schoelkopf and S. M. Girvin. Wiring up quantum systems. *Nature*, 451(7179):664–669, 2008.

[34] C. Rigetti, J. M. Gambetta, S. Poletto, B. L. T. Plourde, J. M. Chow, A. D. Córcoles, J. A. Smolin, S. T. Merkel, J. R. Rozen, G. A. Keefe, M. B. Rothwell, M. B. Ketchen, and M. Steffen. Superconducting qubit in a waveguide cavity with a coherence time approaching 0.1 ms. *Phys. Rev. B*, 86:100506, 2012.

[35] S.-Y. Huang and H.-S. Goan. Optimal control for fast and high-fidelity quantum gates in coupled superconducting flux qubits. *Phys. Rev. A*, 90:012318, 2014.

[36] M. Hatridge, S. Shankar, M. Mirrahimi, F. Schackert, K. Geerlings, T. Brecht, K. M. Sliwa, B. Abdo, L. Frunzio, S. M. Girvin, R. J. Schoelkopf, and M. H. Devoret. Quantum back-action of an individual variable-strength measurement. *Science*, 339(6116):178–181, 2013.

[37] T. Hime, P. A. Reichardt, B. L. T. Plourde, T. L. Robertson, C.-E. Wu, A. V. Ustinov, and J. Clarke. Solid-state qubits with current-controlled coupling. *Science*, 314(5804):1427–1429, 2006.

[38] A. O. Niskanen, K. Harrabi, F. Yoshihara, Y. Nakamura, S. Lloyd, and J. S. Tsai. Quantum coherent tunable coupling of superconducting qubits. *Science*, 316(5825):723–726, 2007.

[39] K. Inomata, K. Koshino, Z. R. Lin, W. D. Oliver, J. S. Tsai, Y. Nakamura, and T. Yamamoto. Microwave down-conversion with an impedance-matched Λ system in driven circuit QED. *Phys. Rev. Lett.*, 113:063604, 2014.

[40] A. H. Safavi-Naeini and O. Painter. Proposal for an optomechanical traveling wave phonon–photon translator. *New Journal of Physics*, 13:013017, 2011.

[41] J. T. Hill, A. H. Safavi-Naeini, J. Chan, and O. Painter. Coherent optical wavelength conversion via cavity optomechanics. *Nature Communications*, 3:1196, 2012.

[42] S. McGee, D. Meiser, C. Regal, K. Lehnert, and M. Holland. Mechanical resonators for storage and transfer of electrical and optical quantum states. *Phys. Rev. A*, 87:053818, 2013.

[43] J. Bochmann, A. Vainsencher, D. D. Awschalom, and A. N. Cleland. Nanomechanical coupling between microwave and optical photons. *Nature Photonics*, 9:712–716, 2013.

[44] R. W. Andrews, R. W. Peterson, T. P. Purdy, K. Cicak, R. W. Simmonds, C. A. Regal, and K. W. Lehnert. Bidirectional and efficient conversion between microwave and optical light. *Nature Physics*, 10:321–326, 2014.

[45] T. Bagci, A. Simonsen, S. Schmid, L. G. Villanueva, E. Zeuthen, J. Appel, J. M. Taylor, A. Sorensen, K. Usami, A. Schliesser, and E. S. Polzik. Optical detection of radio waves through a nanomechanical transducer. *Nature*, 507(7490):81–85, 2014.

[46] V.S. Ilchenko, A. A. Savchenkov, A. B. Matsko, and L. Maleki. Sub-microwatt photonic microwave receiver. *IEEE Photonics Technology Letters*, 14(11):1602–1604, 2002.

[47] D. Strekalov, H. Schwefel, A. Savchenkov, A. Matsko, L. Wang, and N. Yu. Microwave whispering-gallery resonator for efficient optical up-conversion. *Phys. Rev. A*, 80:033810, 2009.

[48] M. Tsang. Cavity quantum electro-optics. *Phys. Rev. A*, 81:063837, 2010.

[49] M. Tsang. Cavity quantum electro-optics. II. Input-output relations between traveling optical and microwave fields. *Phys. Rev. A*, 84:043845, 2011.

[50] A. Rueda, F. Sedlmeir, M. C. Collodo, U. Vogl, B. Stiller, G. Schunk, D. V. Strekalov, C. Marquardt, J. M. Fink, O. Painter, G. Leuchs, and H. G. L. Schwefel. Efficient microwave to optical photon conversion: an electro-optical realization. *Optica*, 3(6):597–604, 2016.

[51] J. A. Haigh, S. Langenfeld, N. J. Lambert, J. J. Baumberg, A. J. Ramsay, A. Nunnenkamp, and A. J. Ferguson. Magneto-optical coupling in whispering-gallery-mode resonators. *Phys. Rev. A*, 92:063845, 2015.

[52] A. Osada, R. Hisatomi, A. Noguchi, Y. Tabuchi, R. Yamazaki, K. Usami, M. Sadgrove, R. Yalla, M. Nomura, and Y. Nakamura. Cavity optomagnonics with spin-orbit coupled photons. *Phys. Rev. Lett.*, 116:223601, 2016.

[53] X. Zhang, N. Zhu, C.-L. Zou, and H. X. Tang. Optomagnonic whispering gallery microresonators. *Phys. Rev. Lett.*, 117:123605, 2016.

[54] J. Verdú, H. Zoubi, Ch. Koller, J. Majer, H. Ritsch, and J. Schmiedmayer. Strong magnetic coupling of an ultracold gas to a superconducting waveguide cavity. *Phys. Rev. Lett.*, 103:043603, 2009.

[55] M. Hafezi, Z. Kim, S. L. Rolston, L. A. Orozco, B. L. Lev, and J. M. Taylor. Atomic interface between microwave and optical photons. *Phys. Rev. A*, 85:020302, 2012.

[56] M. Kiffner, A. Feizpour, K. T. Kaczmarek, D. Jaksch, and J. Nunn. Two-way interconversion of millimeter-wave and optical fields in Rydberg gases. *New Journal of Physics*, 18(9):093030, 2016.

[57] L. A. Williamson, Y.-H. Chen, and J. J. Longdell. Magneto-optic modulator with unit quantum efficiency. *Phys. Rev. Lett.*, 113:203601, 2014.

[58] C. O'Brien, N. Lauk, S. Blum, G. Morigi, and M. Fleischhauer. Interfacing superconducting qubits and telecom photons via a rare-earth-doped crystal. *Phys. Rev. Lett.*, 113:063603, 2014.

[59] X. Fernandez-Gonzalvo, Y.-H. Chen, C. Yin, S. Rogge, and J. J. Longdell. Coherent frequency up-conversion of microwaves to the optical telecommunications band in an Er:YSO crystal. *Phys. Rev. A*, 92:062313, 2015.

[60] J. H. L. Voncken. *The Rare Earth Elements: An Introduction.* Springer, 2016.

[61] G. Liu and B. Jacquier. *Spectroscopic Properties of Rare Earths in Optical Materials.* Springer, 2005.

[62] E. C. Ridley. Self-consistent fields without exchange for Pr^{3+} and Tm^{3+}. *Mathematical Proceedings of the Cambridge Philosophical Society*, 56(1):41–54, 1960.

[63] W. B. Jensen. The origin of the s, p, d, f orbital labels. *J Chem Educ*, 84(5):757–758, 2007.

[64] Y. Sun, C.W. Thiel, R.L. Cone, R.W. Equall, and R.L. Hutcheson. Recent progress in developing new rare earth materials for hole burning and coherent transient applications. *Journal of Luminescence*, 98(1–4):281 – 287, 2002.

[65] C. W. Thiel, T. Böttger, and R. L. Cone. Rare-earth-doped materials for applications in quantum information storage and signal processing. *Journal of Luminescence*, 131(3):353 – 361, 2011.

[66] D. M. Boye, R. M. Macfarlane, Y. Sun, and R. S. Meltzer. Spectral hole burning of Eu^{2+} in CaF_2. *Phys. Rev. B*, 54:6263–6271, 1996.

[67] N. M. Strickland, R. L. Cone, and R. M. Macfarlane. Persistent spectral hole burning in deuterated $CaF_2 : Tm^{3+}$. *Phys. Rev. B*, 59:14328–14335, 1999.

[68] R. J. Beach, G. F. Albrecht, R. W. Solarz, W. F. Krupke, B. J. Comaskey, S. C. Mitchell, C. D. Brandle, and G. W. Berkstresser. Ground-state depleted laser in neodymium-doped yttrium orthosilicate. *Proc. SPIE*, 1223:160–180, 1990.

[69] I. N. Kurkin and K. P. Chernov. EPR and spin-lattice relaxation of rare-earth activated centres in Y_2SiO_5 single crystals. *Physica B+C*, 101(2):233 – 238, 1980.

[70] Y. Sun, T. Böttger, C. Thiel, and R. Cone. Magnetic g tensors for the $^4I_{15/2}$ and $^4I_{13/2}$ states of Er^{3+}:Y_2SiO_5. *Phys. Rev. B*, 77:3376, 2008.

[71] M. Afzelius. Private communication.

[72] E. Brion, L. H. Pedersen, and K. Mølmer. Adiabatic elimination in a lambda system. *Journal of Physics A: Mathematical and Theoretical*, 40(5):1033, 2007.

[73] C. Cohen-Tannoudji, J. Dupont-Roc, and G. Grynberg. *Atom-photon interactions: basic processes and applications*. Wiley, 1992.

[74] C. W. Gardiner and P. Zoller. *Quantum Noise*. Springer, 2nd edition, 2000.

[75] R. W. Boyd. *Nonlinear Optics*. Elsevier, 3rd edition, 2008.

[76] V. S. Ilchenko, A. A. Savchenkov, A. B. Matsko, and L. Maleki. Whispering-gallery-mode electro-optic modulator and photonic microwave receiver. *J. Opt. Soc. Am. B*, 20(2):333–342, 2003.

[77] M. Hogg. Investigation of monolithic erbium-doped resonators for applications in cavity quantum electrodynamics. Master thesis.

[78] J. Mlynek, N. Wong, R. DeVoe, E. Kintzer, and R. Brewer. Raman heterodyne detection of nuclear magnetic resonance. *Phys. Rev. Lett.*, 50:993–996, 1983.

[79] N. Wong, E. Kintzer, J. Mlynek, R. DeVoe, and R. Brewer. Raman heterodyne detection of nuclear magnetic resonance. *Phys. Rev. B*, 28:4993–5010, 1983.

[80] K. Holliday, X.-F. He, P. T. H. Fisk, and N. B. Manson. Raman heterodyne detection of electron paramagnetic resonance. *Opt. Lett.*, 15:983, 1990.

[81] T. Blasberg and D. Suter. Interference of scattering pathways in raman heterodyne spectroscopy of multilevel atoms. *Phys. Rev. B*, 51:12439–12450, 1995.

[82] R. Neuhaus, M. J. Sellars, S. J. Bingham, and D. Suter. Breaking the Stokes□anti-Stokes symmetry in Raman heterodyne detection of magnetic-resonance transitions. *Phys. Rev. A*, 58:4961–4966, 1998.

[83] B. Börger, S. J. Bingham, J. Gutschank, M. O. Schweika, D. Suter, and A. J. Thomson. Optically detected electron paramagnetic resonance by microwave modulated magnetic circular dichroism. *The Journal of Chemical Physics*, 111(18):8565–8568, 1999.

[84] L. E. Erickson. A low-magnetic-field Raman heterodyne study of the Van Vleck paramagnet $YAlO_3$:Eu^{3+}. *Journal of Physics C: Solid State Physics*, 20(2):291, 1987.

[85] J. J. Longdell, M. J. Sellars, and N. B. Manson. Hyperfine interaction in ground and excited states of praseodymium-doped yttrium orthosilicate. *Phys. Rev. B*, 66:035101, 2002.

[86] J. J. Longdell, A. L. Alexander, and M. J. Sellars. Characterization of the hyperfine interaction in europium-doped yttrium orthosilicate and europium chloride hexahydrate. *Phys. Rev. B*, 74:195101, 2006.

[87] M. Lovrić, P. Glasenapp, D. Suter, B. Tumino, A. Ferrier, P. Goldner, M. Sabooni, L. Rippe, and S. Kröll. Hyperfine characterization and spin coherence lifetime extension in Pr^{3+}:$La_2(WO_4)_3$. *Phys. Rev. B*, 84:104417, 2011.

[88] S. J. Bingham, D. Suter, A. Schweiger, and A. J. Thomson. Optical detection of transition metal ion electron paramagnetic resonance by coherent Raman spectroscopy. *Chemical Physics Letters*, 266(5–6):543 – 547, 1997.

[89] M. O. Schweika-Kresimon, J. Gutschank, and D. Suter. Magneto-optical and EPR transitions in Raman heterodyne spectroscopy. *Phys. Rev. A*, 66:043816, 2002.

[90] S. J. Bingham, B. Börger, J. Gutschank, D. Suter, and A. J. Thomson. Probing the electronic structure of transition metal ion centres in proteins by coherent Raman-detected electron paramagnetic resonance spectroscopy. *JBIC Journal of Biological Inorganic Chemistry*, 5(1):30–35, 2000.

[91] Y. K. Zavoisky. Paramagnetic relaxation of liquid solutions for perpendicular fields. *Zhur. Eksperiment. i Theoret. Fiz.*, 15:344–350, 1944.

[92] R. V. Pound. Electronic frequency stabilization of microwave oscillators. *Review of Scientific Instruments*, 17(11):490, 1946.

[93] Koheras Adjustik E15 User Manual.

[94] S. R. Hastings-Simon, B. Lauritzen, M. U. Staudt, J. L. M. van Mechelen, C. Simon, H. de Riedmatten, M. Afzelius, and N. Gisin. Zeeman-level lifetimes in $\mathrm{Er}^{3+}:\mathrm{Y}_2\mathrm{SiO}_5$. *Phys. Rev. B*, 78:085410, 2008.

[95] O. Guillot-Noël, Ph. Goldner, Y. Du, E. Baldit, P. Monnier, and K. Bencheikh. Hyperfine interaction of Er^{3+} ions in $\mathrm{Y}_2\mathrm{SiO}_5$: An electron paramagnetic resonance spectroscopy study. *Phys. Rev. B*, 74:214409, 2006.

[96] Y.-H. Chen, X. Fernandez-Gonzalvo, and J. J. Longdell. Coupling erbium spins to a three-dimensional superconducting cavity at zero magnetic field. *Phys. Rev. B*, 94:075117, 2016.

[97] H. Kogelnik and T. Li. Laser beams and resonators. *Appl. Opt.*, 5(10):1550–1567, 1966.

[98] D. F. Walls and G. J. Milburn. *Quantum Optics*. Springer, 1st edition, 1994.

[99] W. E. Lamb. Theory of an optical maser. *Phys. Rev.*, 134:A1429–A1450, Jun 1964.